Measurement of Neutral B Meson Mixing in Electron-Muon Events in 1.8-TeV Proton-Antiproton Collisions

January 1996

Hisafumi Mitsushio

A dissertation submitted to the Doctoral Program
in Physics, the University of Tsukuba
in partial fulfillment of the requirements for the
degree of Doctor of Philosophy (Science)

Abstract

The $B^0\bar{B}^0$ mixing parameter, χ, has been measured in $e\mu$ events in proton-antiproton collisions at a center of mass energy of 1800 GeV. The experiment has been performed at the Fermi National Accelerator Laboratory in the United States using the Tevatron accelerator. The data were collected with the Collider Detector at Fermilab (CDF) during the 1992-1993 Tevatron collider run. The corresponding integrated luminosity is 20 pb^{-1}.

The $B^0\bar{B}^0$ mixing is a process by which neutral B-mesons oscillate into their anti-particles ($B^0 \leftrightarrow \bar{B}^0$). In the absence of mixing, the direct semileptonic decay of a $b\bar{b}$ pair produced in $p\bar{p}$ collisions results in a pair of leptons with opposite charge. The B^0 or $\bar{B}^0$ may undergo mixing, resulting in a like-sign (LS) lepton pair. The magnitude of mixing is determined from the ratio of like-sign dilepton pairs to opposite-sign (OS) dilepton pairs. In this thesis, electron-muon pairs were used as the dilepton pairs.

The CDF detector is a general purpose detector built to explore $p\bar{p}$ collisions. It covers almost the full solid angle around the $p\bar{p}$ interaction point. The CDF detector consists of tracking detectors and calorimeters for measurements of the particle momentum and energy. In order to identify muons, muon detectors are installed at the outside of the detector. Electrons, photons, muons, neutrinos, hadrons and jets are identified using these detector components.

We describe identification of muons and electrons, and then event selection of $b\bar{b}$ events. To remove events in which both leptons are produced by one B meson, it is required that an opening angle of the electron and muon is large enough. We apply the requirement that the transverse momentum of leptons to jet axis, P_T^{rel}, is large enough for $b\bar{b}$ events. This requirement significantly reduces background and systematic uncertainty. 1710 opposite-sign and 861 like-sign $e\mu$ events are found after the event selection.

Then the estimation of the background is described. We estimate the fraction of fake $e\mu$ events using J/ψ, K_s and ϕ samples, minimum bias data and Monte Carlo simulation. Most of the background for $e\mu$ events are pairs of real-electron and fake-muon. The main source of the fake muons is decay-in-flight of hadrons. The systematic uncertainty in estimating the fake muon fraction is substantially reduced by using a newly installed muon detector.

Like-sign lepton pairs are also produced by semileptonic sequential decays of B^0 or $\bar{B}^0$ mesons. The fraction of sequential decays is estimated from Monte Carlo $b\bar{b}$ events by taking into consideration the uncertainties in the structure functions and fragmentation functions. The fraction of direct $c\bar{c}$ production is estimated directly from data by fitting the Monte Carlo P_T^{rel} distribution of leptons from direct and sequential decays as well as from $c\bar{c}$ production to the observed spectra.

From the above analysis, we obtain

$$\chi = 0.130 \pm 0.010(stat.) \pm 0.010(syst.).$$

This result improves the previous CDF result by a factor of 3 and is one of the most accurate measurements of χ at the present time. It is consistent with other measurements and also with the expectations from the standard model.

Since both neutral B mesons, B_d^0 and B_s^0, are produced in $p\bar{p}$ collisions, the mixing parameter for B_s, χ_s, is estimated by using the mixing parameter for B_d measured by the ARGUS and the CLEO groups in e^+e^- collisions and by assuming the fractions of B_d^0 and B_s^0 mesons produced in $b\bar{b}$ events.

Acknowledgements

I would like to thank my advisor, Professor Koji Takikawa, for his guidance and encouragement throughout my graduate career. I want to thank Professor Kunitaka Kondo who gave me the opportunity to work at CDF and constant support through my graduate student career.

I wish to express my deepest appreciation to Itsuo Nakano and Yoshihiro Seiya who have discussed on physics and other various things with me. I could not have finished this work without their continuous help.

Manfred Paulini, Joe Kroll, Paris Sphicas and Fritz Dejongh gave me a lot of help as the CP-MIXING and B physics group convener. They gave me useful suggestions and chances to present my analysis result at the meetings. Intae Yu and Malie Yin gave me useful information for my analysis. Jonathan Lewis, John Marriner, Phil Schlabach, Tony Liss, Randy Keup, Alain Gauthier, Mark Vondracek, Andrew Martin, Yoshiki Teramoto, Takuo Yoshida and Yukihiro Kato collaborated with me during my detector work. G. P. Yeh and Lingfeng Song gave me useful suggestions and encouragements at Fermilab. Conversations with Luc Demortier, Shuichi Kunori, Shoji Mikamo, Nobuaki Oshima, Susumu Igarashi, Taiji Yamanouchi, Masanori Mishina and Hidemi Akimoto are unforgettable during my stay at Fermilab.

Discussions on physics and other various things with Shinhong Kim, Kazuhiko Hara, Kiyoshi Yasuoka, Shige Miyashita, Takeshi Chikamatsu, Makoto Shimojima, Tomohiro Kaneko and Fumihiko Ukegawa were very beneficial for me. I also wish to thank other members of the Tsukuba high energy physics group for their constant help. They include Takashi Ino, Masahiko Yokoyama, Mikio Takano Nobuyuki Uemura, Shinichi Funaki, Masakazu Okabe, Hiroyuki Sato, Eiichiro Hayashi, Toshiharu Uchida, Tsuyoshi Takano, Mariko Ninomiya, Housai Nakata, Shin Aota, Hirofumi Ikeda, Tomoko Kuwabara, Junichi Suzuki and other colleagues.

I want to express my thanks to Carol Picciolo and Dee Hahn for their secretary works at Fermilab. I thank Japanese secretary Kyoko Kunori who has always been giving us kind support at Fermilab. I thank Kazuko Kumashiro and Mutsumi Uenishi for their secretary work at University of Tsukuba.

Members of Ballroom Dance Club of University of Tsukuba gave me a lot of continuous encouragements.

Finally, I would like to thank my parents, sister, brother and grandmother for their continuous support.

We thank the Fermilab staff and the technical staffs of the participating institutions for their vital contributions. This work was supported by the U.S. Department of Energy and National Science Foundation; the Italian Istituto Nazionale di Fisica Nucleare; the Ministry of Education, Science and Culture of Japan; the Natural Sciences and Engineering Research Council of Canada; the National Science Council of the Republic of China; the A. P. Sloan Foundation; and the Alexander von Humboldt-Stiftung.

Contents

List of Tables

List of Figures

CDF Collaboration

F. Abe,[13] M. G. Albrow,[7] S. R. Amendolia,[23] D. Amidei,[16] J. Antos,[28] C. Anway-Wiese,[4] G. Apollinari,[26] H. Areti,[7] M. Atac,[7] P. Auchincloss,[25] F. Azfar,[21] P. Azzi,[20] N. Bacchetta,[18] W. Badgett,[16] M. W. Bailey,[18] J. Bao,[35] P. de Barbaro,[25] A. Barbaro-Galtieri,[14] V. E. Barnes,[24] B. A. Barnett,[12] P. Bartalini,[23] G. Bauer,[15] T. Baumann,[9] F. Bedeschi,[23] S. Behrends,[3] S. Belforte,[23] G. Bellettini,[23] J. Bellinger,[34] D. Benjamin,[31] J. Benlloch,[15] J. Bensinger,[3] D. Benton,[21] A. Beretvas,[7] J. P. Berge,[7] S. Bertolucci,[8] A. Bhatti,[26] K. Biery,[11] M. Binkley,[7] F. Bird,[29] D. Bisello,[20] R. E. Blair,[1] C. Blocker,[29] A. Bodek,[25] W. Bokhari,[15] V. Bolognesi,[23] D. Bortoletto,[24] C. Boswell,[12] T. Boulos,[14] G. Brandenburg,[9] C. Bromberg,[17] E. Buckley-Geer,[7] H. S. Budd,[25] K. Burkett,[16] G. Busetto,[20] A. Byon-Wagner,[7] K. L. Byrum,[1] J. Cammerata,[12] C. Campagnari,[7] M. Campbell,[16] A. Caner,[7] W. Carithers,[14] D. Carlsmith,[34] A. Castro,[20] Y. Cen,[21] F. Cervelli,[23] H. Y. Chao,[28] J. Chapman,[16] M.-T. Cheng,[28] G. Chiarelli,[8] T. Chikamatsu,[32] C. N. Chiou,[28] S. Cihangir,[7] A. G. Clark,[23] M. Cobal,[23] M. Contreras,[5] J. Conway,[27] J. Cooper,[7] M. Cordelli,[8] C. Couyoumtzelis,[23] D. Crane,[1] J. D. Cunningham,[3] T. Daniels,[15] F. DeJongh,[7] S. Delchamps,[7] S. Dell'Agnello,[23] M. Dell'Orso,[23] L. Demortier,[26] B. Denby,[23] M. Deninno,[2] P. F. Derwent,[16] T. Devlin,[27] M. Dickson,[25] J. R. Dittmann,[6] S. Donati,[23] R. B. Drucker,[14] A. Dunn,[16] K. Einsweiler,[14] J. E. Elias,[7] R. Ely,[14] E. Engels, Jr.,[22] S. Eno,[5] D. Errede,[10] S. Errede,[10] Q. Fan,[25] B. Farhat,[15] I. Fiori,[2] B. Flaugher,[7] G. W. Foster,[7] M. Franklin,[9] M. Frautschi,[18] J. Freeman,[7] J. Friedman,[15] H. Frisch,[5] A. Fry,[29] T. A. Fuess,[1] Y. Fukui,[13] S. Funaki,[32] G. Gagliardi,[23] S. Galeotti,[23] M. Gallinaro,[20] A. F. Garfinkel,[24] S. Geer,[7] D. W. Gerdes,[16] P. Giannetti,[23] N. Giokaris,[26] P. Giromini,[8] L. Gladney,[21] D. Glenzinski,[12] M. Gold,[18] J. Gonzalez,[21] A. Gordon,[9] A. T. Goshaw,[6] K. Goulianos,[26] H. Grassmann,[6] A. Grewal,[21] G. Grieco,[23] L. Groer,[27] C. Grosso-Pilcher,[5] C. Haber,[14] S. R. Hahn,[7] R. Hamilton,[9] R. Handler,[34] R. M. Hans,[35] K. Hara,[32] B. Harral,[21] R. M. Harris,[7] S. A. Hauger,[6] J. Hauser,[4] C. Hawk,[27] J. Heinrich,[21] D. Cronin-Hennessy,[6] R. Hollebeek,[21]

L. Holloway,[10] A. Hölscher,[11] S. Hong,[16] G. Houk,[21] P. Hu,[22] B. T. Huffman,[22] R. Hughes,[25] P. Hurst,[9] J. Huston,[17] J. Huth,[9] J. Hylen,[7] M. Incagli,[23] J. Incandela,[7] H. Iso,[32] H. Jensen,[7] C. P. Jessop,[9] U. Joshi,[7] R. W. Kadel,[14] E. Kajfasz,[7a] T. Kamon,[30] T. Kaneko,[32] D. A. Kardelis,[10] H. Kasha,[35] Y. Kato,[19] L. Keeble,[8] R. D. Kennedy,[27] R. Kephart,[7] P. Kesten,[14] D. Kestenbaum,[9] R. M. Keup,[10] H. Keutelian,[7] F. Keyvan,[4] D. H. Kim,[7] H. S. Kim,[11] S. B. Kim,[16] S. H. Kim,[32] Y. K. Kim,[14] L. Kirsch,[3] P. Koehn,[25] K. Kondo,[32] J. Konigsberg,[9] S. Kopp,[5] K. Kordas,[11] W. Koska,[7] E. Kovacs,[7a] W. Kowald,[6] M. Krasberg,[16] J. Kroll,[7] M. Kruse,[24] S. E. Kuhlmann,[1] E. Kuns,[27] A. T. Laasanen,[24] N. Labanca,[23] S. Lammel,[4] J. I. Lamoureux,[3] T. LeCompte,[10] S. Leone,[23] J. D. Lewis,[7] P. Limon,[7] M. Lindgren,[4] T. M. Liss,[10] N. Lockyer,[21] C. Loomis,[27] O. Long,[21] M. Loreti,[20] E. H. Low,[21] J. Lu,[30] D. Lucchesi,[23] C. B. Luchini,[10] P. Lukens,[7] P. Maas,[34] K. Maeshima,[7] A. Maghakian,[26] P. Maksimovic,[15] M. Mangano,[23] J. Mansour,[17] M. Mariotti,[23] J. P. Marriner,[7] A. Martin,[10] J. A. J. Matthews,[18] R. Mattingly,[15] P. McIntyre,[30] P. Melese,[26] A. Menzione,[23] E. Meschi,[23] G. Michail,[9] S. Mikamo,[13] M. Miller,[5] R. Miller,[17] T. Mimashi,[32] S. Miscetti,[8] M. Mishina,[13] H. Mitsushio,[32] S. Miyashita,[32] Y. Morita,[13] S. Moulding,[26] J. Mueller,[27] A. Mukherjee,[7] T. Muller,[4] P. Musgrave,[11] L. F. Nakae,[29] I. Nakano,[32] C. Nelson,[7] D. Neuberger,[4] C. Newman-Holmes,[7] L. Nodulman,[1] S. Ogawa,[32] S. H. Oh,[6] K. E. Ohl,[35] R. Oishi,[32] T. Okusawa,[19] C. Pagliarone,[23] R. Paoletti,[23] V. Papadimitriou,[31] S. Park,[7] J. Patrick,[7] G. Pauletta,[23] M. Paulini,[14] L. Pescara,[20] M. D. Peters,[14] T. J. Phillips,[6] G. Piacentino,[2] M. Pillai,[25] R. Plunkett,[7] L. Pondrom,[34] N. Produit,[14] J. Proudfoot,[1] F. Ptohos,[9] G. Punzi,[23] K. Ragan,[11] F. Rimondi,[2] L. Ristori,[23] M. Roach-Bellino,[33] W. J. Robertson,[6] T. Rodrigo,[7] J. Romano,[5] L. Rosenson,[15] W. K. Sakumoto,[25] D. Saltzberg,[5] A. Sansoni,[8] V. Scarpine,[30] A. Schindler,[14] P. Schlabach,[9] E. E. Schmidt,[7] M. P. Schmidt,[35] O. Schneider,[14] G. F. Sciacca,[23] A. Scribano,[23] S. Segler,[7] S. Seidel,[18] Y. Seiya,[32] G. Sganos,[11] A. Sgolacchia,[2] M. Shapiro,[14] N. M. Shaw,[24] Q. Shen,[24] P. F. Shepard,[22] M. Shimojima,[32] M. Shochet,[5] J. Siegrist,[29] A. Sill,[31] P. Sinervo,[11] P. Singh,[22] J. Skarha,[12] K. Sliwa,[33] D. A. Smith,[23] F. D. Snider,[12] L. Song,[7] T. Song,[16] J. Spalding,[7] L. Spiegel,[7]

P. Sphicas,[15] A. Spies,[12] L. Stanco,[20] J. Steele,[34] A. Stefanini,[23] K. Strahl,[11] J. Strait,[7] D. Stuart,[7] G. Sullivan,[5] K. Sumorok,[15] R. L. Swartz, Jr.,[10] T. Takahashi,[19] K. Takikawa,[32] F. Tartarelli,[23] W. Taylor,[11] P. K. Teng,[28] Y. Teramoto,[19] S. Tether,[15] D. Theriot,[7] J. Thomas,[29] T. L. Thomas,[18] R. Thun,[16] M. Timko,[33] P. Tipton,[25] A. Titov,[26] S. Tkaczyk,[7] K. Tollefson,[25] A. Tollestrup,[7] J. Tonnison,[24] J. F. de Troconiz,[9] J. Tseng,[12] M. Turcotte,[29] N. Turini,[2] N. Uemura,[32] F. Ukegawa,[21] G. Unal,[21] S. van den Brink,[22] S. Vejcik, III,[16] R. Vidal,[7] M. Vondracek,[10] R. G. Wagner,[1] R. L. Wagner,[7] N. Wainer,[7] R. C. Walker,[25] C. H. Wang,[28] G. Wang,[23] J. Wang,[5] M. J. Wang,[28] Q. F. Wang,[26] A. Warburton,[11] G. Watts,[25] T. Watts,[27] R. Webb,[30] C. Wendt,[34] H. Wenzel,[14] W. C. Wester, III,[14] T. Westhusing,[10] A. B. Wicklund,[1] E. Wicklund,[7] R. Wilkinson,[21] H. H. Williams,[21] P. Wilson,[5] B. L. Winer,[25] J. Wolinski,[30] D. Y. Wu,[16] X. Wu,[23] J. Wyss,[20] A. Yagil,[7] W. Yao,[14] K. Yasuoka,[32] Y. Ye,[11] G. P. Yeh,[7] P. Yeh,[28] M. Yin,[6] J. Yoh,[7] T. Yoshida,[19] D. Yovanovitch,[7] I. Yu,[35] J. C. Yun,[7] A. Zanetti,[23] F. Zetti,[23] L. Zhang,[34] S. Zhang,[16] W. Zhang,[21] and S. Zucchelli[2]

[1] *Argonne National Laboratory, Argonne, Illinois 60439*

[2] *Istituto Nazionale di Fisica Nucleare, University of Bologna, I-40126 Bologna, Italy*

[3] *Brandeis University, Waltham, Massachusetts 02254*

[4] *University of California at Los Angeles, Los Angeles, California 90024*

[5] *University of Chicago, Chicago, Illinois 60637*

[6] *Duke University, Durham, North Carolina 27708*

[7] *Fermi National Accelerator Laboratory, Batavia, Illinois 60510*

[8] *Laboratori Nazionali di Frascati, Istituto Nazionale di Fisica Nucleare, I-00044 Frascati, Italy*

[9] *Harvard University, Cambridge, Massachusetts 02138*

[10] *University of Illinois, Urbana, Illinois 61801*

[11] *Institute of Particle Physics, McGill University, Montreal H3A 2T8, and University of Toronto, Toronto M5S 1A7, Canada*

[12] *The Johns Hopkins University, Baltimore, Maryland 21218*

[13] *National Laboratory for High Energy Physics (KEK), Tsukuba, Ibaraki 305, Japan*

[14] *Lawrence Berkeley Laboratory, Berkeley, California 94720*

[15] *Massachusetts Institute of Technology, Cambridge, Massachusetts 02139*

[16] *University of Michigan, Ann Arbor, Michigan 48109*

[17] *Michigan State University, East Lansing, Michigan 48824*

[18] *University of New Mexico, Albuquerque, New Mexico 87131*

[19] *Osaka City University, Osaka 588, Japan*

[20] *Universita di Padova, Instituto Nazionale di Fisica Nucleare, Sezione di Padova, I-35131 Padova, Italy*

[21] *University of Pennsylvania, Philadelphia, Pennsylvania 19104*

[22] *University of Pittsburgh, Pittsburgh, Pennsylvania 15260*

[23] *Istituto Nazionale di Fisica Nucleare, University and Scuola Normale Superiore of Pisa, I-56100 Pisa, Italy*

[24] *Purdue University, West Lafayette, Indiana 47907*

[25] *University of Rochester, Rochester, New York 14627*

[26] *Rockefeller University, New York, New York 10021*

[27] *Rutgers University, Piscataway, New Jersey 08854*

[28] *Academia Sinica, Taiwan 11529, Republic of China*

[29] *Superconducting Super Collider Laboratory, Dallas, Texas 75237*

[30] *Texas A&M University, College Station, Texas 77843*

[31] *Texas Tech University, Lubbock, Texas 79409*

[32] *University of Tsukuba, Tsukuba, Ibaraki 305, Japan*

[33] *Tufts University, Medford, Massachusetts 02155*

[34] *University of Wisconsin, Madison, Wisconsin 53706*

[35] *Yale University, New Haven, Connecticut 06511*

Chapter 1

Introduction

1.1 Standard Model

The Standard model is a model which can explain well all the observed phenomena at high energies in the present time. In the model, matter interacts with each other through three force mediators. The matter consists of quarks and leptons which are spin 1/2 particles and are called fermions. The mediators are spin 1 particles and are called gauge bosons. Correspondingly to the gauge bosons, there are three types of interactions: the strong (gluon), electromagnetic (photon) and weak (W's and Z) interactions. The standard model does not include gravitational interaction, but the observed phenomena are explained well without it because the effect of the gravitational interaction is negligibly small.

The quarks and leptons form sequential doublets as shown in Table 1.1. The common sequential structure of leptons and quarks is often called the family structure. The quarks and leptons of the three families are directly and/or indirectly confirmed experimentally. The top quark was observed by CDF and D0 experiments in last spring [1, 2]. The mass of the top quark is measured to be $176 \pm 8 \pm 10$ GeV/c^2 by the CDF experiment.

The weak isospin eigenstates of quarks (q') are not identical to the mass eigenstates (q). They are related by a unitary mixing matrix called Cabibbo-Kobayashi-Maskawa

$$
\begin{array}{ll}
\text{Leptons} & \begin{pmatrix} \nu_e \\ e^- \end{pmatrix} \quad \begin{pmatrix} \nu_\mu \\ \mu^- \end{pmatrix} \quad \begin{pmatrix} \nu_\tau \\ \tau^- \end{pmatrix} \\[2ex]
\text{Quarks} & \begin{pmatrix} u \\ d \end{pmatrix} \quad \begin{pmatrix} c \\ s \end{pmatrix} \quad \begin{pmatrix} t \\ b \end{pmatrix}
\end{array}
$$

Table 1.1: Leptons and quarks of the Standard Model

(CKM) matrix [3] by

$$
\begin{pmatrix} d' \\ s' \\ b' \end{pmatrix} = \begin{pmatrix} V_{ud} & V_{us} & V_{ub} \\ V_{cd} & V_{cs} & V_{cb} \\ V_{td} & V_{ts} & V_{tb} \end{pmatrix} \begin{pmatrix} d \\ s \\ b \end{pmatrix}. \tag{1.1}
$$

The values of the matrix elements are not calculable in the standard model but must be determined experimentally. The 90% confidence limits on the magnitude of the matrix elements are listed below [4].

$$
|V_{ij}| = \begin{pmatrix} 0.9747 \text{ to } 0.9759 & 0.218 \text{ to } 0.224 & 0.002 \text{ to } 0.005 \\ 0.218 \text{ to } 0.224 & 0.9738 \text{ to } 0.9752 & 0.032 \text{ to } 0.048 \\ 0.004 \text{ to } 0.015 & 0.030 \text{ to } 0.048 & 0.9988 \text{ to } 0.9995 \end{pmatrix} \tag{1.2}
$$

Due to the unitarity, the elements can be parameterized [3, 5] in terms of three angles and one phase:

$$
\begin{pmatrix} c_1 & -s_1c_3 & -s_1s_3 \\ s_1c_2 & c_1c_2c_3 - s_2s_3e^{i\delta} & c_1c_2s_3 + s_2c_3e^{i\delta} \\ s_1s_2 & c_1s_2c_3 + c_2s_3e^{i\delta} & c_1s_2s_3 - c_2c_3e^{i\delta} \end{pmatrix} \tag{1.3}
$$

where $c_i = \cos\theta_i, s_i = \sin\theta_i$ for $i = 1, 2, 3$.

1.2 Basic formalism of mixing mechanism

In this section we describe basic formulas of neutral B meson mixing [6]. The mixing proceeds by a second order weak interaction as described by the "Box-diagrams" (Figure 1.1). The $B^0\bar{B}^0$ system is given by the phenomenological Hamiltonian matrix H:

$$H\begin{pmatrix} B^0 \\ \bar{B}^0 \end{pmatrix} = \begin{pmatrix} M - i\Gamma/2 & M_{12} - i\Gamma_{12}/2 \\ M_{12}^* - i\Gamma_{12}^*/2 & M - i\Gamma/2 \end{pmatrix} \begin{pmatrix} B^0 \\ \bar{B}^0 \end{pmatrix}. \tag{1.4}$$

The diagonal terms describe the decay of the neutral B mesons with M being the mass of the flavor eigenstates B^0 and $\bar{B}^0$ and Γ their decay width. The off-diagonal terms are responsible for the $B^0\bar{B}^0$ transition. M_{12} and Γ_{12} can be determined from theory by evaluating the box-diagrams. M_{12} corresponds to virtual $B^0\bar{B}^0$ transitions while Γ_{12} describes real transitions due to decay modes which are common to the B^0 and $\bar{B}^0$, such as B^0, $\bar{B}^0 \to \pi^+\pi^-$ or D^+D^-. In contrast to the case of the $K^0\bar{K}^0$ system, these common decay modes are Cabibbo suppressed and therefore represent only a very small fraction of the total B decay rate. The term Γ_{12} in the $B^0\bar{B}^0$ system can therefore be neglected in practical calculation. Diagonalization of the Hamiltonian matrix leads to the CP eigenstates B_1 and B_2 which are linear combinations of the flavor eigenstates. Neglecting CP violation, we obtain:

$$|B_1\rangle = \frac{1}{\sqrt{2}}(|B^0\rangle + |\bar{B}^0\rangle) \tag{1.5}$$

$$|B_2\rangle = \frac{1}{\sqrt{2}}(|B^0\rangle - |\bar{B}^0\rangle) \tag{1.6}$$

with masses $M_{1,2}$ and $\Gamma_{1,2}$:

$$M_{1,2} = M \pm \frac{\Delta M}{2} \tag{1.7}$$

$$\Gamma_{1,2} = \Gamma \pm \frac{\Delta\Gamma}{2} \tag{1.8}$$

The mass difference ΔM and the decay rate difference $\Delta\Gamma$ are given by:

$$\Delta M = 2Re\sqrt{(M_{12} - i\Gamma_{12}/2)(M_{12}^* - i\Gamma_{12}^*/2)} \tag{1.9}$$

and

$$\Delta\Gamma = -4Im\sqrt{(M_{12} - i\Gamma_{12}/2)(M_{12}^* - i\Gamma_{12}^*/2)}. \tag{1.10}$$

The mass difference ΔM is a measure of the oscillation frequency to change from a B^0 to a $\bar{B}^0$ and vice versa. This is easily seen from the time evolution of one particle which at time $t = 0$ is a B^0. The probability to find a B^0 ($\bar{B}^0$) at a time t is given by $W_{B^0}(t)$ ($W_{\bar{B}^0}(t)$):

$$W_{B^0}(t) = \frac{1}{4}[exp(-\Gamma_1 t) + exp(-\Gamma_2 t) + 2exp(-\Gamma t)\cos\Delta M t] \tag{1.11}$$

$$W_{\bar{B}^0}(t) = \frac{1}{4}[exp(-\Gamma_1 t) + exp(-\Gamma_2 t) - 2exp(-\Gamma t)\cos\Delta M t] \tag{1.12}$$

The measurements of these time dependences allow us to extract the values of ΔM, Γ_1 and Γ_2. From time integrated rates $N(B^0)$ and $N(\bar{B}^0)$

$$N(B^0) = \int_0^\infty W_{B^0}(t)dt = \frac{1}{4}[\frac{1}{\Gamma_1} + \frac{1}{\Gamma_2} + \frac{2\Gamma}{\Gamma^2 + (\Delta M)^2}] \tag{1.13}$$

$$N(\bar{B}^0) = \int_0^\infty W_{\bar{B}^0}(t)dt = \frac{1}{4}[\frac{1}{\Gamma_1} + \frac{1}{\Gamma_2} - \frac{2\Gamma}{\Gamma^2 + (\Delta M)^2}] \tag{1.14}$$

we can determine the parameter r:

$$r = \frac{N(\bar{B}^0)}{N(B^0)} = \frac{(\Delta M)^2 + (\frac{\Delta\Gamma}{2})^2}{2\Gamma^2 + (\Delta M)^2 - (\frac{\Delta\Gamma}{2})^2} \tag{1.15}$$

With $\Delta\Gamma \approx 0$ as a consequence of $\Gamma_{12} \approx 0$ for $B^0\bar{B}^0$ system, the determination of r gives a measurement of the ratio of the oscillation frequency and the decay width:

$$r = \frac{x^2}{2 + x^2} \tag{1.16}$$

with

$$x = \frac{\Delta M}{\Gamma} \tag{1.17}$$

The $p\bar{p}$ colliding experiments can measure the ratio r and the time dependent probabilities. The ratio is measured by using events in which both bottom quarks decay to leptons without knowing secondary vertex points. The time dependent probabilities are able to be measured by measuring the secondary vertex in events in which both bottom quarks decay to leptons.

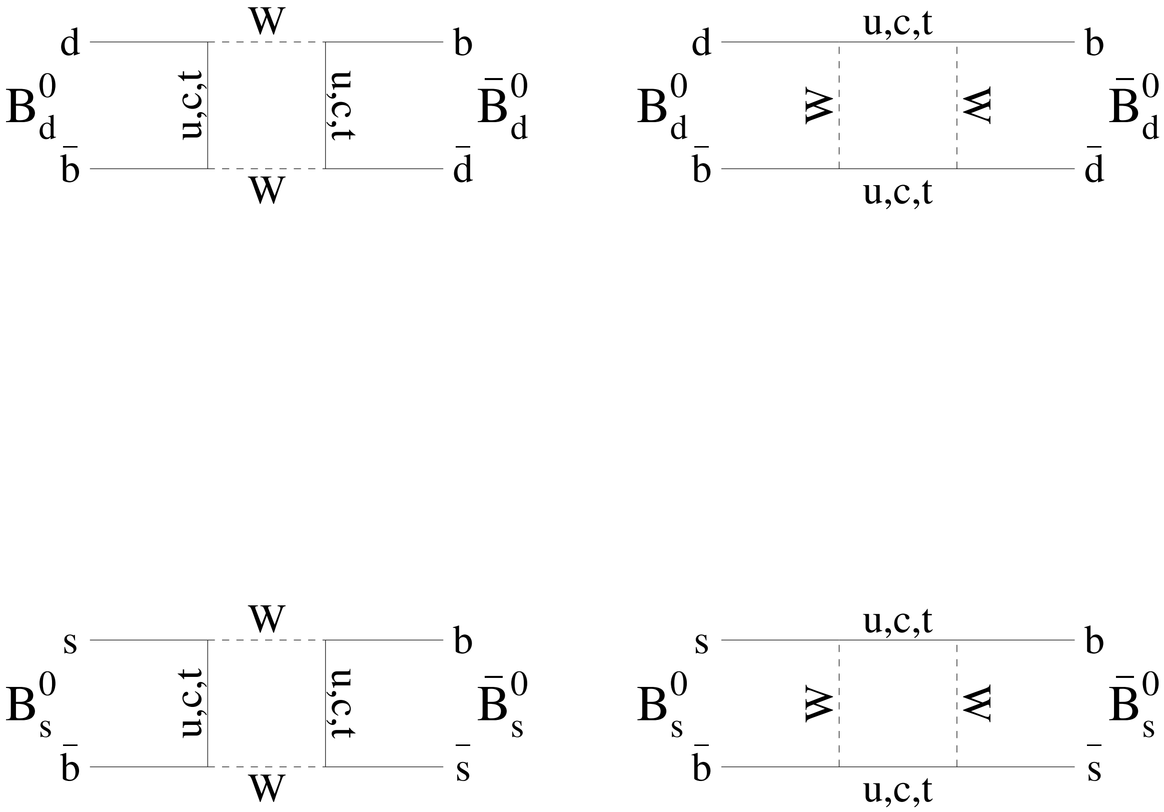

Figure 1.1: Feynman diagrams for the $B^0\bar{B}^0$ mixing process.

Chapter 2

Mixing in Neutral B Mesons

2.1 B meson production

2.1.1 $b\bar{b}$ production

In lowest order QCD, bottom quarks can be produced via gluon or a quark fusion mechanism, as shown in Fig. 2.1. Since the strong production process conserves flavor quantum number, b and $\bar{b}$ quarks are always produced in pairs. The gluon fusion processes dominate at the Tevatron collider energy.

In the c and b quark productions, we have to take into consideration next-to-leading order diagrams, as shown in Fig. 2.2. The reason why higher order processes are as important as the lowest order ones is due to the large gluon-gluon scattering cross section. The process $gg \to gg$ has a cross section about 100 times that of $gg \to b\bar{b}$. Even though the $g \to b\bar{b}$ branching fraction is only 1%, the $b\bar{b}$ production from the gluon splitting process is competitively as large as the lowest order contribution.

2.1.2 b quark fragmentation

When heavy quark Q hadronizes, the heavy quark fragmentation function can be written as

$$D_Q^H(z) = \frac{N_H}{z(1-\frac{1}{z}-\frac{\epsilon}{1-z})^2} \tag{2.1}$$

where E^H and E^Q are the energies of the hadron H and the quark Q, $P_{||}^H$ is the momentum component of the hadron H parallel to the quark momentum (P^Q) direction and $z = (E^H + P_{||}^H)/(E^Q + P^Q)$. The $D_Q^H(z)$ is the probability that the heavy quark Q fragments to hadron H with value z, where ϵ is a constant proportional to $1/M_Q^2$. The normalization constant N_H is determined by

$$\sum_H \int D_Q^H(z)dz = 1, \tag{2.2}$$

where the summation is over all hadrons containing the heavy quark Q. This formula agrees well with experimental measurements for b and c quarks. The measured value of ϵ for b quarks [7] is

$$\epsilon_b = 0.006 \pm 0.001 \pm 0.002, \tag{2.3}$$

where the first is a statistical uncertainty and the second is systematic. The fragmentation function $D_Q^H(z)$ for b and c quarks are shown in Fig. 2.3. We can see that the bottom quark fragmentation is much harder than that of the charm quark. The hard fragmentation for b quark clearly favors the detection of its daughter leptons at high P_T.

2.2 B^0 $\bar{B}^0$ mixing

Especially in the case of B_q mesons where q stands for either an s or d quark, Eq. (1.17) is written by

$$r_q = \frac{x_q^2}{2 + x_q^2}. \tag{2.4}$$

Another parameter describing time-integrated mixing is χ_q. This parameter describes the probability that a produced B_q^0 will have mixed into a $\bar{B}_q^0$ by the time it decays.

$$\chi_q = \frac{N(\bar{B}^0)}{N(\bar{B}^0)+N(B^0)} \tag{2.5}$$

$$= \frac{N(B_q^0 \to \bar{B}_q^0)}{N(B_q^0 \to \bar{B}_q^0)+N(B_q^0 \to B_q^0)} \tag{2.6}$$

$$= \frac{r_q}{1+r_q} \tag{2.7}$$

$$= \frac{x_q^2}{2(1+x_q^2)} \tag{2.8}$$

The possible range of these parameters are

$$0 \leq \; r_q \; \leq 1 \tag{2.9}$$

$$0 \leq \; \chi_q \; \leq \frac{1}{2}. \tag{2.10}$$

The time dependence of the $(B^0 \to \bar{B}^0)$ probabilities is rewritten as

$$W_{B^0}(t) = \frac{1}{4}[exp(-\Gamma_1 t) + exp(-\Gamma_2 t) + 2exp(-\Gamma t)\cos\Delta M t] \tag{2.11}$$

$$W_{\bar{B}^0}(t) = \frac{1}{4}[exp(-\Gamma_1 t) + exp(-\Gamma_2 t) - 2exp(-\Gamma t)\cos\Delta M t] \tag{2.12}$$

Figure 2.4 shows the probabilities of finding B^0 and $\bar{B}^0$ in an initially pure B^0 state for B_d^0 and B_s^0 mesons.

When B meson mixing occurs by the second order W exchange, as shown in Fig. 1.1, any of the quarks t, c, u can participate in the box diagram but the t quark is expected to be dominant due to its high mass. When the matrix elements are evaluated [8], one find

$$x_q \equiv (\Delta M/\Gamma)_{B_q} = \frac{G_F^2}{6\pi^2} m_t^2 \tau_{B_q} B_{B_q} f_{B_q}^2 M_{B_q} |V_{tq} V_{tb}^*|^2 \frac{A(z_t)}{z_t} \eta_{QCD} \tag{2.13}$$

where q stands for either an s or d quark, G_F is the Fermi constant, τ_B is the B^0 lifetime and η_{QCD} is a correction from the mass scale dependence of the strong coupling constant.

Taking B_d^0 as an example, we review the current knowledge of these parameters:

- τ_{B_d}

$$\tau_{B_d} = 1.29 \pm 0.5 \text{ psec } [4] \tag{2.14}$$

- M_{B_d}

$$M_{B_d} = 5.278 \text{ GeV } [4] \tag{2.15}$$

- $A(z_t)/z_t$ is a slowly decreasing monotonic function varying from 1 at $m_{top} = 0$ to about 0.6 at $m_{top} = 150$ GeV, where $z_t = m_t^2/m_W^2$.

- η_{QCD} is a QCD correction and is estimated to be about 0.85.

- $B_B \cdot f_B^2$ describes the uncertainty about the hadronic matrix elements. The QCD coupling becomes large for low momentum transfer and thus perturbation theory is not applicable. This means that the value cannot be directly calculated. However, calculations using lattice QCD can estimate an approximate number. The standard value, combining the available theoretical and experimental information [8] is;

$$B_{B_d} f_{B_d}^2 = 140 \pm 40 \text{ MeV} \tag{2.16}$$

The $|V_{td}|$ is estimated to be ~ 0.004 by putting the above values, the top mass measured by CDF and the x_d measured by ARGUS and CLEO [9, 10].

There are many uncertainties in the calculation of χ_q but they all cancel when we look at the ratio of B_d^0 mixing and B_s^0 mixing. If we assume that the above five parameters are the same for B_d^0 and B_s^0 mesons, we find

$$\beta \equiv \frac{x_d}{x_s} = \left|\frac{V_{td}}{V_{ts}}\right|^2 \tag{2.17}$$

The only factor that remains is the ratio between the CKM matrix elements. From the unitarity of the CKM matrix, the ratio is estimated to be [8]

$$\beta \leq 0.17 \tag{2.18}$$

If we use this parameter to make a relationship between χ_d and χ_s we find

$$\chi_d < \beta^2 \chi_s/[1 - 2\chi_s(1-\beta^2)] \leq 0.0289/(1 - 1.9422\chi_s) \tag{2.19}$$

Since B_d^0 and B_s^0 mesons are produced in $p\bar{p}$ collisions and since flavor tagging is made by looking at the charge of leptons, we define the mixing parameter, χ, by

$$\chi = \frac{N(b \to \bar{B}^0 \to B^0 \to l^+)}{N(b \to l^\pm)}, \tag{2.20}$$

where $N(b \to l^\pm)$ is the number of b quarks directly decaying to leptons and $N(b \to \bar{B}^0 \to B^0 \to l^+)$ is the number of b quarks directly decaying to leptons via $B^0\bar{B}^0$ mixing process. The denominator includes all possible hadrons formed with the b quark, i.e, $\bar{B}_d^0$, $\bar{B}_u^-$, $\bar{B}_s^0$, etc. Since we do not distinguish between B_d^0 and B_s^0, the mixing parameter is written as

$$\chi = \frac{N(b \to \bar{B}^0 \to B^0 \to l^+)}{N(b \to l^\pm)} \tag{2.21}$$

$$\begin{aligned} = & \frac{N(b)prob(b \to \bar{B}_u^-)prob(\bar{B}_u^- \to B_u^+)Br(B_u^+ \to l^+)}{N(b)prob(b \to \bar{B}_u^-)[prob(\bar{B}_u^- \to B_u^+)Br(B_u^+ \to l^+) + prob(\bar{B}_u^- \to \bar{B}_u^-)Br(\bar{B}_u^- \to l^-)]} \\ & \frac{+N(b)prob(b \to \bar{B}_d^0)prob(\bar{B}_d^0 \to B_d^0)Br(B_d^0 \to l^+)}{+N(b)prob(b \to \bar{B}_d^0)[prob(\bar{B}_d^0 \to B_d^0)Br(B_d^0 \to l^+) + prob(\bar{B}_d^0 \to \bar{B}_d^0)Br(\bar{B}_d^0 \to l^-)]} \\ & \frac{+N(b)prob(b \to \bar{B}_s^0)prob(\bar{B}_s^0 \to B_s^0)Br(B_s^0 \to l^+)}{+N(b)prob(b \to \bar{B}_s^0)[prob(\bar{B}_s^0 \to B_s^0)Br(B_s^0 \to l^+) + prob(\bar{B}_s^0 \to \bar{B}_s^0)Br(\bar{B}_s^0 \to l^-)]} \\ & \frac{+N(b)prob(b \to Baryon_b)prob(Baryon_b \to Baryon_{\bar{b}})Br(Baryon_{\bar{b}} \to l^+)}{+N(b)prob(b \to Baryon_b)[prob(Baryon_b \to Baryon_{\bar{b}})Br(Baryon_{\bar{b}} \to l^+)} \\ & \overline{+prob(Baryon_b \to Baryon_b)Br(Baryon_b \to l^-)]}. \end{aligned} \tag{2.22}$$

where $N(b)$ is the number of b quarks, $prob(b \to \bar{B}_q)$ is the production probability for

$\bar{B}_q$, $prob(\bar{B}_q \to B_q)$ is the probability that a produced $\bar{B}_q$ will have mixed into a B_q and $Br(B_q \to l)$ is a branching ratio for $B_q \to l$ decays. Since

$$prob(\bar{B}_u^- \to B_u^+) = prob(Baryon_b \to Baryon_{\bar{b}}) = 0, \tag{2.23}$$

$$prob(\bar{B}_d^0 \to B_d^0) = \chi_d, \tag{2.24}$$

$$prob(\bar{B}_s^0 \to B_s^0) = \chi_s \tag{2.25}$$

and

$$prob(\bar{B}_q \to B_q) + prob(\bar{B}_q \to \bar{B}_q) = 1 \qquad \text{for } b \text{ hadrons}, \tag{2.26}$$

we obtain

$$\begin{aligned}
\chi &= \frac{N(b)prob(b \to \bar{B}_d^0)\chi_d Br(B_d^0 \to l^+) + N(b)prob(b \to \bar{B}_s^0)\chi_s Br(B_s^0 \to l^+)}{N(b)Br(b \to l^\pm)} && (2.27)\\
&= \frac{N(b)prob(b \to \bar{B}_d^0)\chi_d Br(B_d^0 \to l^+)}{N(b)Br(b \to l^\pm)} + \frac{N(b)prob(b \to \bar{B}_s^0)\chi_s Br(B_s^0 \to l^+)}{N(b)Br(b \to l^\pm)} && (2.28)\\
&= prob(b \to \bar{B}_d^0)\frac{Br(B_d^0 \to l^+)}{Br(b \to l^\pm)}\chi_d + prob(b \to \bar{B}_s^0)\frac{Br(B_s^0 \to l^+)}{Br(b \to l^\pm)}\chi_s && (2.29)\\
&= P_d\chi_d + P_s\chi_s && (2.30)
\end{aligned}$$

where

$$\begin{aligned}
&Br(b \to l^\pm) = \\
&\quad prob(b \to \bar{B}_u^-)Br(\bar{B}_u^- \to l^-) + \\
&\quad prob(b \to \bar{B}_d^0)[prob(\bar{B}_d^0 \to B_d^0)Br(B_d^0 \to l^+) + prob(\bar{B}_d^0 \to \bar{B}_d^0)Br(\bar{B}_d^0 \to l^-)] + \\
&\quad prob(b \to \bar{B}_s^0)[prob(\bar{B}_s^0 \to B_s^0)Br(B_s^0 \to l^+) + prob(\bar{B}_s^0 \to \bar{B}_s^0)Br(\bar{B}_s^0 \to l^-)] + \\
&\quad prob(b \to Baryon_b)Br(Baryon_b \to l^-), && (2.31)
\end{aligned}$$

$$\chi_{d(s)} \equiv \frac{N(\bar{B}_{d(s)}^0 \to B_{d(s)}^0)}{N(\bar{B}_{d(s)}^0 \to \bar{B}_{d(s)}^0) + N(\bar{B}_{d(s)}^0 \to B_{d(s)}^0)} \tag{2.32}$$

$$= \frac{N(B^0_{d(s)} \to \bar{B}^0_{d(s)})}{N(B^0_{d(s)} \to B^0_{d(s)}) + N(B^0_{d(s)} \to \bar{B}^0_{d(s)})} \tag{2.33}$$

and

$$P_{d(s)} = \text{prob}(b \to \bar{B}^0_{d(s)}) \frac{Br(B^0_{d(s)} \to l^+X)}{Br(b \to l^{\pm}X)}. \tag{2.34}$$

When a pair of $b\bar{b}$ quarks is generated and both directly decay to leptons ($b \to l + X$), there are three different cases: (1) neither b nor $\bar{b}$ quark undergoes mixing, (2) either b or $\bar{b}$ quark undergoes mixing, and (3) both b and $\bar{b}$ quarks undergo mixing. The fraction of case (1), (2) and (3) are $(1-\chi)^2$, $2\chi(1-\chi)$ and χ^2, respectively. Taking into account the fact that the lepton charge flipps if the mixing occurs, one can easily find that a ratio of the number of like-sign (LS) dilepton event to that of opposite-sign (OS) dilepton events is expressed by the mixing parameter χ as

$$\frac{\text{the number of LS dilepton events}}{\text{the number of OS dilepton events}} = \frac{2\chi(1-\chi)}{\chi^2 + (1-\chi)^2}. \tag{2.35}$$

Therefore, the mixing parameter can be derived by measuring the ratio of LS to OS dilepton events.

The mixing parameter, χ, can be estimated from Eq. (2.35) in principle, but some complications arise in actual analysis, due to sequential decay processes and background contributions.

2.2.1 Previous measurements of mixing in the B^0_d and B^0_s system

Observation of $B^0_d\bar{B}^0_d$ mixing at $\Upsilon(4S)$ [6]

The study of the $B^0_d\bar{B}^0_d$ mixing phenomenon is particularly simple at the $\Upsilon(4S)$ which decays about a half of the time into a $B^0\bar{B}^0$ pair.

Since no other particles are produced besides this pair, the $\Upsilon(4S)$ is a clean source of B^0_d mesons which can be reconstructed or efficiently tagged. Background from e^+e^-

continuum contributions under the $\Upsilon(4S)$ can be studied experimentally at the center-of-mass energies below the $\Upsilon(4S)$ mass. The investigation of the $B_d\bar{B}_d$ mixing phenomenon on the $\Upsilon(4S)$ has led to its observation by ARGUS and CLEO.

On the $\Upsilon(4S)$ the straightforward strategy to study $B\bar{B}$ mixing is to reconstruct completely the two neutral B_d mesons in the $\Upsilon(4S)$ decay. This, however, is not trivial because of the small reconstruction efficiency. Nevertheless, the approach of fully reconstructing $\Upsilon(4S)$ decays into $B_d^0 B_d^0$ or $\bar{B}_d^0 \bar{B}_d^0$ pairs led to the discovery of $B_d\bar{B}_d$ mixing. ARGUS succeeded in reconstructing a decay $\Upsilon(4S) \rightarrow B_d^0 B_d^0$ completely, where both B_d^0 mesons decayed into $D^{*-}l^+\nu$ with the following decay chains:

$$\begin{array}{llllcllll}
B^0 \rightarrow & D_1^{*-} & \mu_1^+ & \nu_1 & \text{and} & B^0 \rightarrow & D_2^{*-} & \mu_2^+ & \nu_2 \\
 & \hookrightarrow & \bar{D}^0 & \pi_{1s}^- & & & \hookrightarrow & D^- & \pi^0 \\
 & & \hookrightarrow & K_1^+\pi_1^- & & & & \hookrightarrow & K_2^+\pi_2^-\pi_2^-
\end{array}$$

In this simple event (Fig. 2.5) all particles were well identified and the masses of the intermediate states agreed well with the particle data table values. Kinematic considerations showed that the event is complete. The background for this event was considered to be completely negligible.

This one event demonstrated that the phenomenon of $B_d^0\bar{B}_d^0$ mixing must exist. However, a determination of the $B_d^0\bar{B}_d^0$ mixing strength needed other methods which provide much better statistics. One of the most efficient methods is the flavor tagging of B mesons through their semileptonic decays. A B meson will decay into an e^+ or μ^+ plus a neutrino and hadrons with a branching ratio of about 10%. Likewise a $\bar{B}_d$ meson will yield an e^- or μ^- in its semileptonic decays. A search for mixing can thus be made by looking for events of: $\Upsilon(4S) \rightarrow l^\pm l^\pm + X$. Besides the tagging of B mesons through leptons, other particles which originate frequently in the weak decay of the b quark can be used to tag the b flavour of the decaying B meson. For example, D^{*+}, Λ_c and D_s^- from b quark decay products can be used as the tagging particles since they can be fully reconstructed.

ARGUS and CLEO have investigated events containing lepton pairs originating from

$\Upsilon(4S)$ decays. Due to the fact that the B_d mesons were nearly at rest, two leptons from different mesons were uncorrelated. The dilepton events still included backgrounds from J/ψ decays.

$B^0\bar{B}^0$ mixing is studied by tagging the flavor of the other B^0 mesons by a fast lepton. The B^0 mesons were most efficiently reconstructed in the channel $B^0 \to D^{*-}l^+\nu$ where the undetectable neutrino was inferred from the missing mass squared against the $D^{*-}l^+$ system, MM^2, which had to be consistent with zero for B^0 mesons originating from $\Upsilon(4S)$ decays. The quantity MM^2 was given by the beam energy and the known energies and momenta of the D^{*-} mesons and the l^+ lepton:

$$MM^2 = (E_{beam} - (E_{D^{*-}} + E_{l^+}))^2 - (\vec{p}_{D^{*-}} + \vec{p}_{l^+})^2 \tag{2.36}$$

As signature for the decay $B^0 \to D^{*-}l^+\nu$ they obtained a prominent peak at $MM^2 = 0$. The momenta of D^{*-} meson can be estimated by the pion momentum, in the decay $D^{*-} \to \bar{D}^0\pi^-$. When $B^0 \to D^{*-}l^+\nu \to \bar{D}^0\pi^-l^+\nu$, right-sign combination of lepton and pion is $l^+\pi^-$.

The MM^2 spectra for events with $(l^-\pi^+)l^-$ and $(l^-\pi^+)l^+$ are shown in Fig. 2.6 and the momentum spectra of the additional leptons are shown in Fig. 2.7. The mixing parameter χ is given by:

$$\chi_d = \frac{N(\bar{B}_d^0l^-) + N(B_d^0l^+)}{(N(\bar{B}_d^0l^-) + N(B_d^0l^+)) + (N(\bar{B}_d^0l^+) + N(B_d^0l^-))} \tag{2.37}$$

where $N(\bar{B}_d^0l^-)+N(B_d^0l^+)$ are given by the contents in the peak at $MM^2 = 0$ in Fig. 2.6 a) and $N(\bar{B}_d^0l^+) + N(B_d^0l^-)$ by the corresponding one in Fig. 2.6 b).

From these measurements, they estimated $\chi_d = 0.162 \pm 0.043 \pm 0.039$ (ARGUS) [9] and $\chi_d = 0.149 \pm 0.023 \pm 0.021$ (CLEO) [10].

Observation of $B\bar{B}$ mixing on Z^0 and in $p\bar{p}$ colliders [6].

In $p\bar{p}$ colliders, the $B\bar{B}$ mixing were observed with the like-sign dimuon events by UA1. At LEP, the $B\bar{B}$ mixing has been studied using the $Z^0 \rightarrow b\bar{b}$ process. In this case b quarks fragment into a mixture of B hadrons containing B_d^0 and B_s^0 mesons for which mixing can occur, which is a different point from the $B_d\bar{B}_d$ mixing at the $\Upsilon(4S)$.

The fractions P_d and P_s of these incoherently produced B_d^0 and B_s^0 mesons are estimated from measurements of B_s^0 and Λ_b^0 production in Z^0 decays and were found to be: $P_s = 0.152 \pm 0.042$ and $P_{baryon} = 0.146 \pm 0.033$ [6]. Assuming $P_d = P_u$, we gets $P_d = 0.351 \pm 0.027$.

In time integrated measurements the B mesons are tagged by their semileptonic decays and experimental signature for $B_d^0\bar{B}_d^0$ or $B_s^0\bar{B}_s^0$ mixing is given by an excess of like sign lepton pairs over the predicted number of like sign lepton pairs from background processes.

The leptons which are used to tag the b flavor are again subject to backgrounds from other lepton sources like charm decays, converted photons or hadrons faking leptons. These backgrounds can be suppressed by requiring large momenta and large transverse momenta p_T for both leptons with respect to the jet axis. The cut on large p_T exploits the heaviness of the B mesons compared to charm particles.

The amount of $B_d^0\bar{B}_d^0$ and $B_s^0\bar{B}_s^0$ mixing is determined from the like-sign and opposite-sign lepton pairs by

$$\frac{N(l^{\pm}l^{\pm})}{N(l^{+}l^{-}) + N(l^{\pm}l^{\pm})} = \frac{2\chi(1-\chi)N_o + [(1-\chi)^2 + \chi^2]N_l}{N_o + N_l} \tag{2.38}$$

where N_o (N_l) is the predicted opposite-sign (like-sign) dilepton rate in the case of no mixing. N_o is given by the number of primary lepton pairs originating from $b \rightarrow l^-X$, $\bar{b} \rightarrow l^+X$ decays, while N_l is given by the like-sign lepton pairs from $b \rightarrow l^-X$, $\bar{b} \rightarrow \bar{c}X$, $\bar{c} \rightarrow l^-X$ decays.

The ALEPH and DELPHI used the jet charge technique for tagging b flavor. The

Experiment	Year	Value of mixing parameter (χ)
ALEPH [11]	1994	$0.114 \pm 0.014 \pm 0.008$
L3 [12]	1994	$0.123 \pm 0.012 \pm 0.008$
D0 [13]	1993	$0.13 \pm 0.02 \pm 0.05$
OPAL [14]	1993	$0.143^{+0.022}_{-0.021} \pm 0.007$
DELPHI [15]	1993	$0.121 \pm 0.016 \pm 0.004 \pm 0.004$
UA1 [16]	1991	$0.148 \pm 0.029 \pm 0.017$
CDF [17]	1991	$0.176 \pm 0.027(stat.) \pm 0.022(syst.) \pm 0.032(model)$

Table 2.1: Mixing parameter, χ.

jet charge Q_{jet} is defined by

$$Q_{jet} = \frac{\sum_i q_i |\vec{p}_i \vec{e}_j|^\kappa}{\sum_i |\vec{p}_i \vec{e}_j|^\kappa} \tag{2.39}$$

where $\vec{p}$ is the particle momentum, q_i its charge and $\vec{e}_j$ the unit vector in the direction of the jet. κ is a calibration constant of the order of unity and was obtained from Monte Carlo studies. The resulting mixing parameter χ using the jet charge technique are consistent with the ones using dilepton events but have larger uncertainties.

Results of the mixing parameter, χ, from different experiments are summarized in Table 2.1.

The previous CDF result [17] is based on $e\mu$ events in 2.7 pb^{-1} of data collected during 1988-89 run. The major improvement of the present analysis from the previous one are:

- Almost three times e-μ events are collected in this experiment. This reduces the statistical uncertainty by $1/\sqrt{3}$.

- Background e-μ events from direct $c\bar{c}$ production and also sequential semileptonical decays are reduced by requiring large transverse momenta for leptons with respect to the jet axis.

- By using data from the new muon detector, the uncertainty in estimating the fake lepton event fraction is reduced.

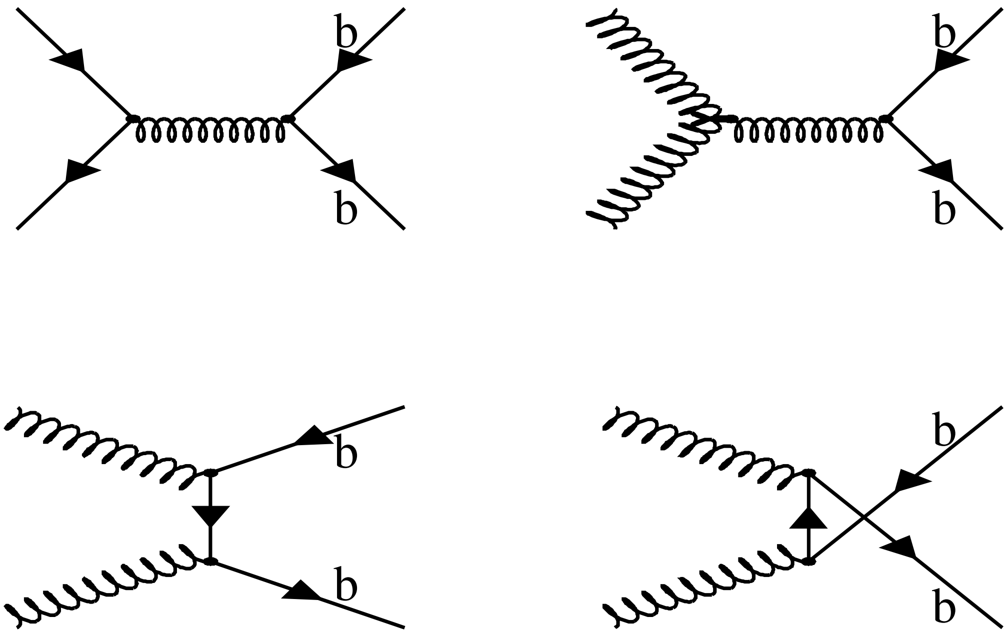

Figure 2.1: Feynman diagrams for lowest order $b\bar{b}$ production

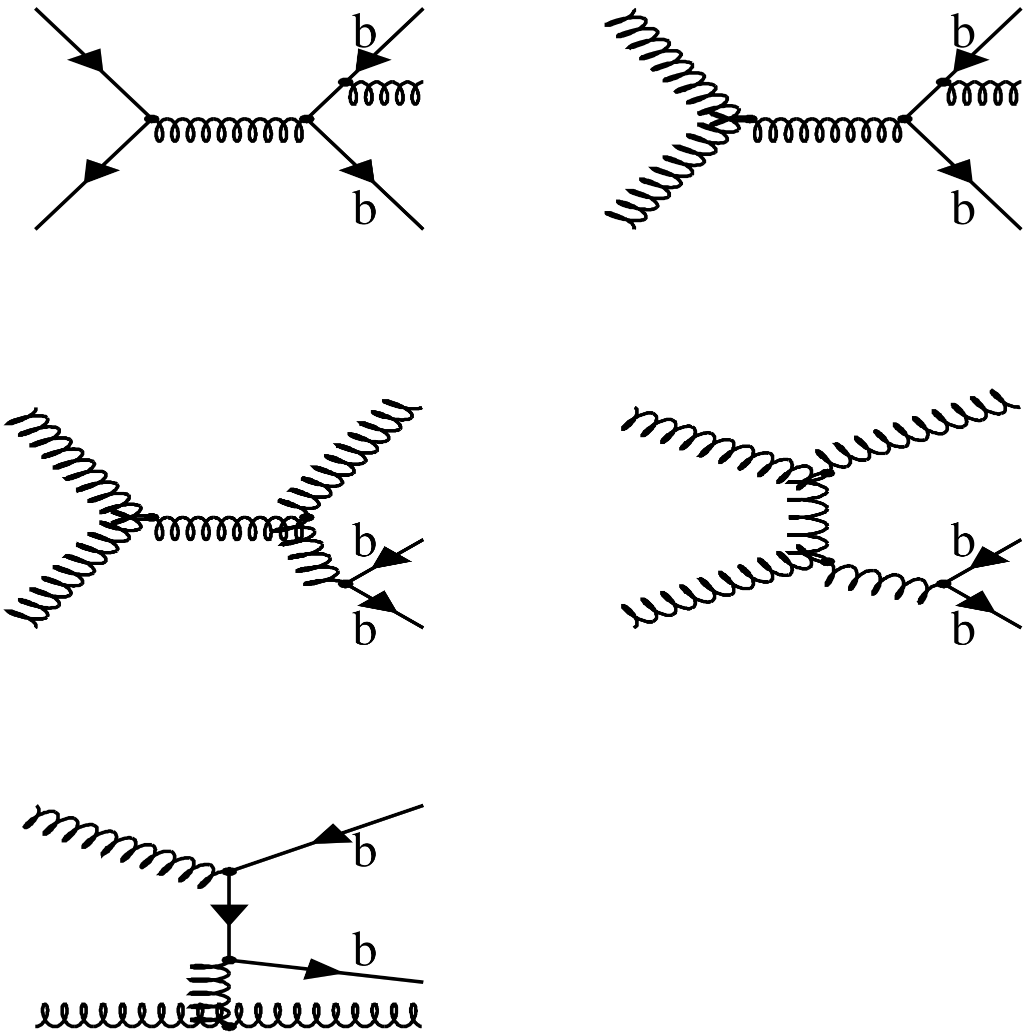

Figure 2.2: The example of Feynman diagrams for next leading order $b\bar{b}$ production

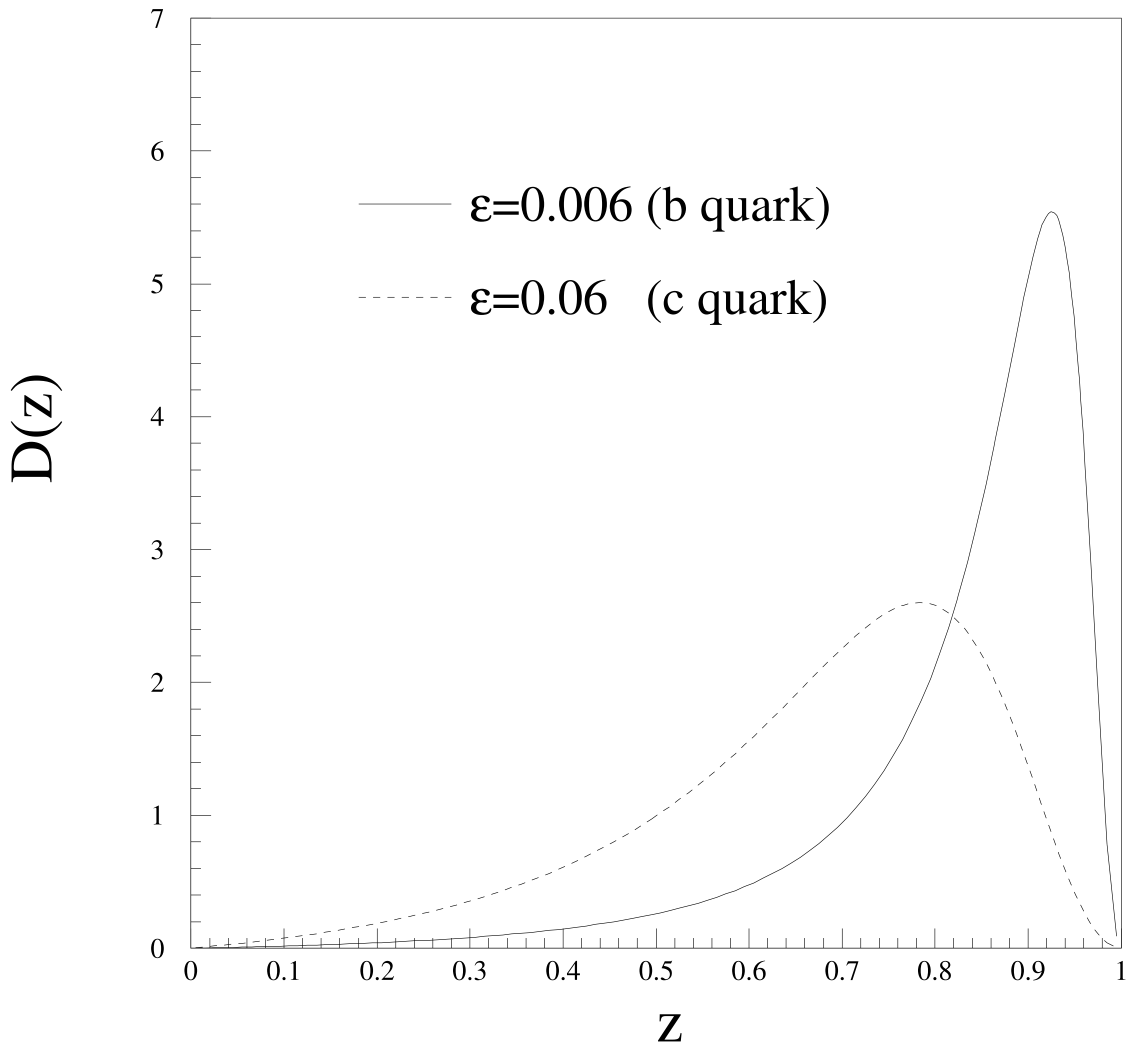

Figure 2.3: Fragmentation functions for b and c quarks.

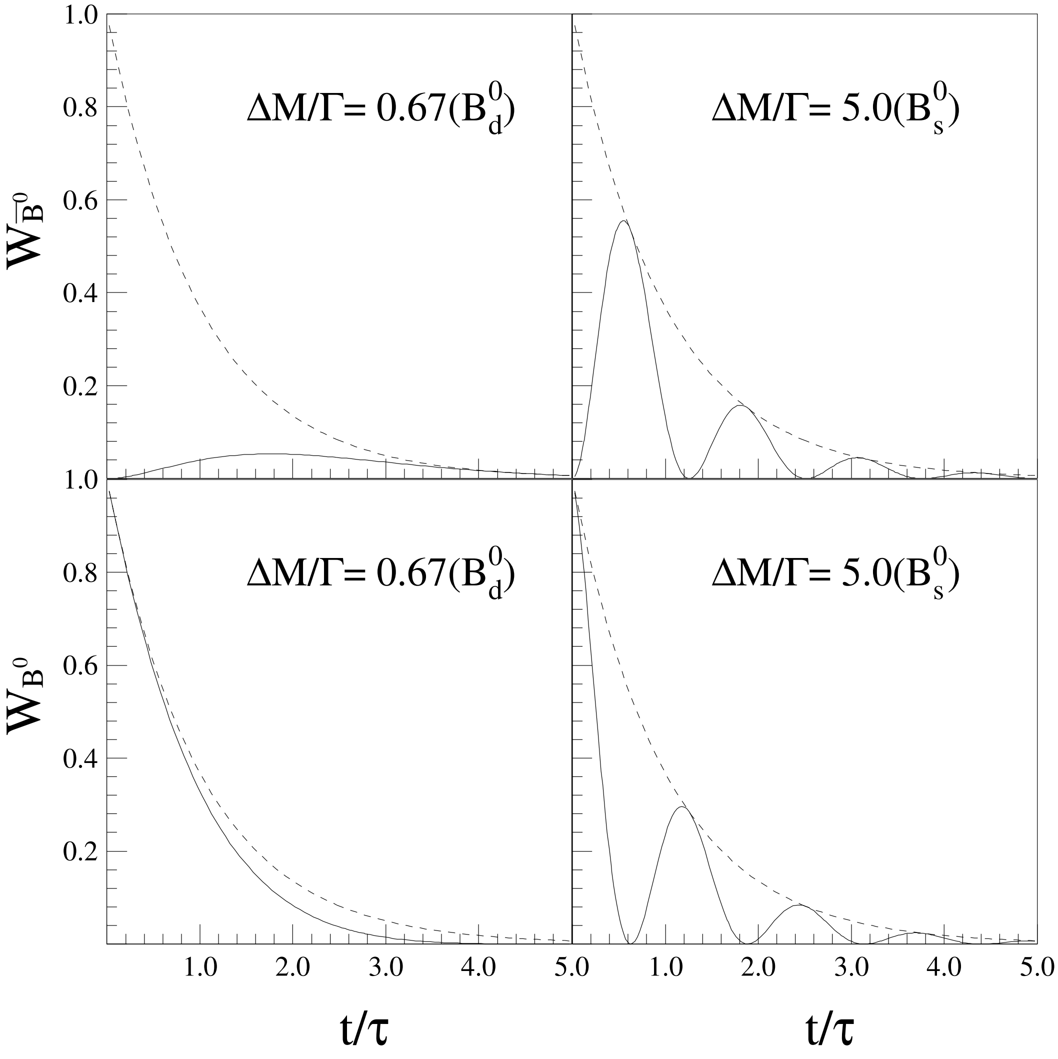

Figure 2.4: The solid lines show time dependent probabilities of finding B^0 and $\bar{B}^0$ in an initially pure B^0 state for B_d and B_s mesons. The dotted lines show the total decay probabilities. We assume $\Delta M/\Gamma = 0.67$ (5.0) for the B_d^0 (B_s^0) meson.

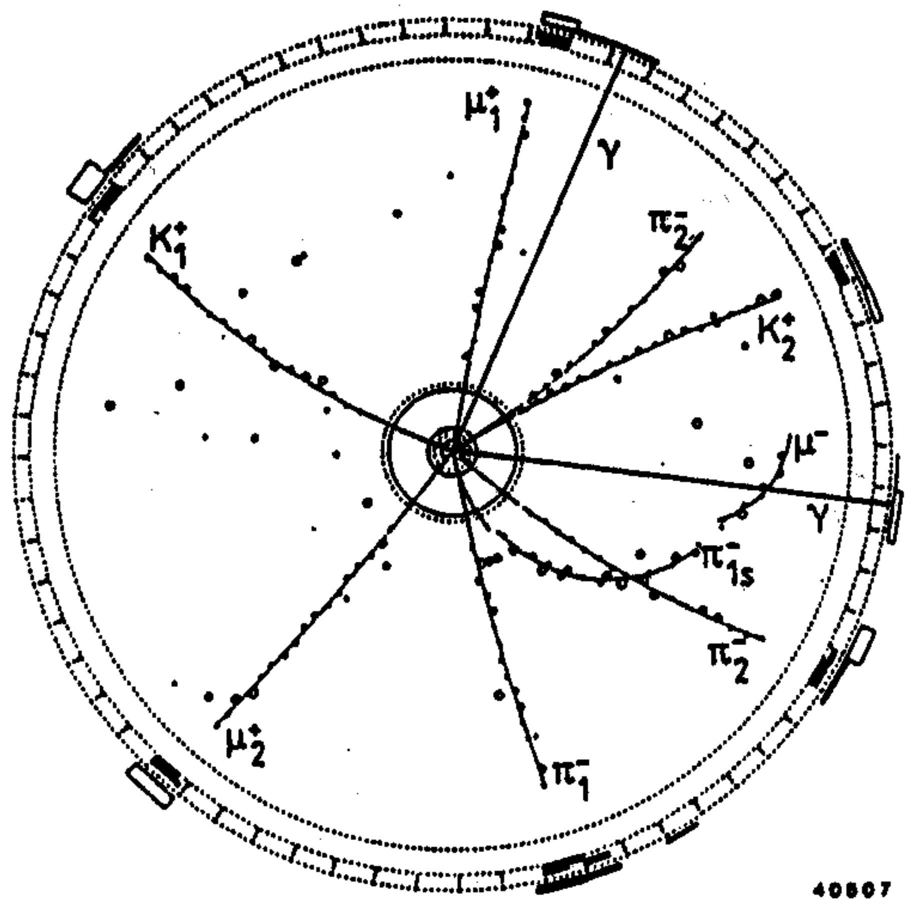

Figure 2.5: The completely reconstructed event consisting of the decay $\Upsilon(4S) \rightarrow B^0B^0$.

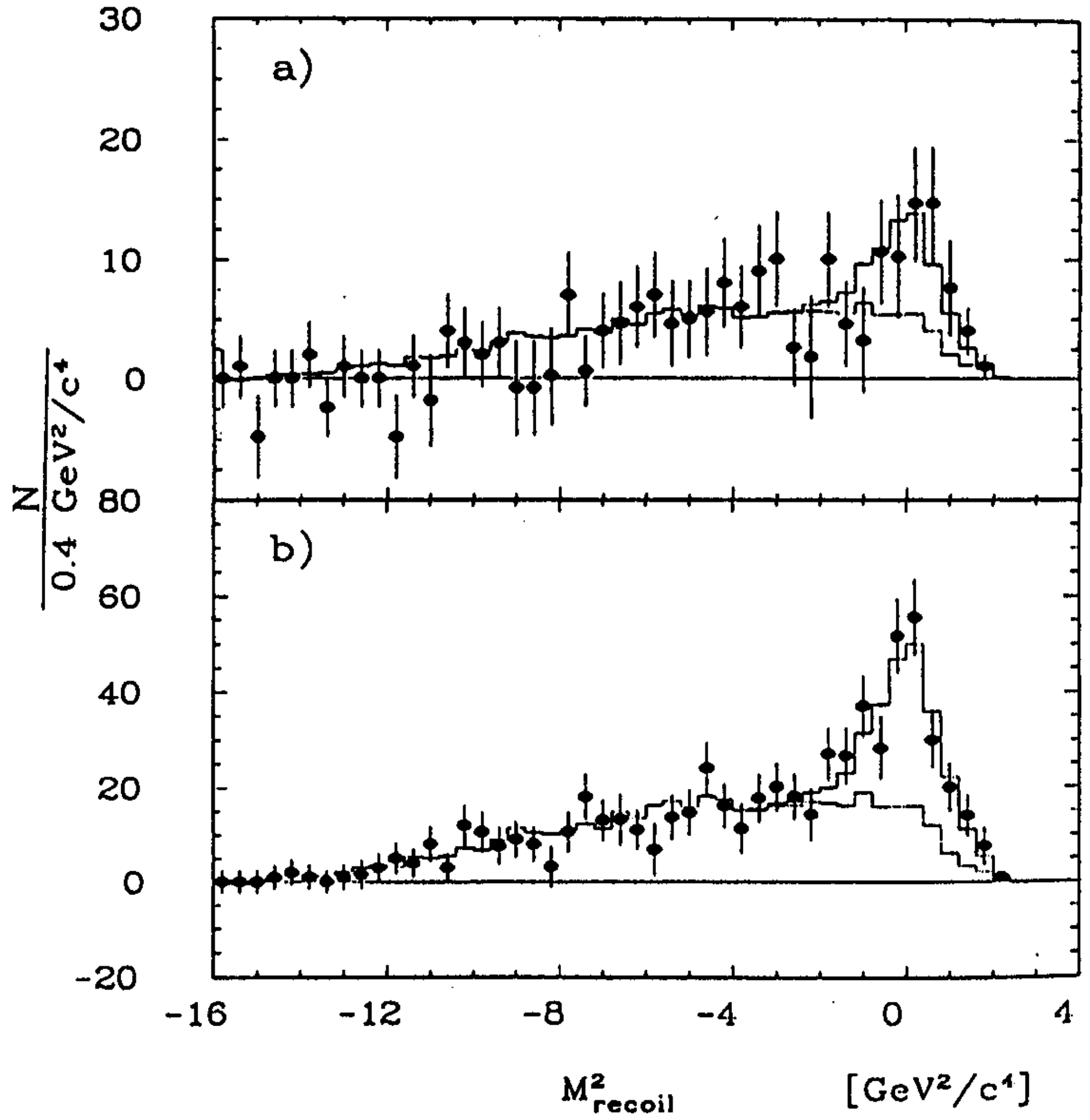

Figure 2.6: MM^2 spectra for $l^+\pi^-$ (points with error) for events with an additional lepton with momentum $1.4 < p_l < 2.5$: background (dotted histogram) and the result of the fit (full histogram) *a*) for like-sign leptons; *b*) for opposite-sign leptons.

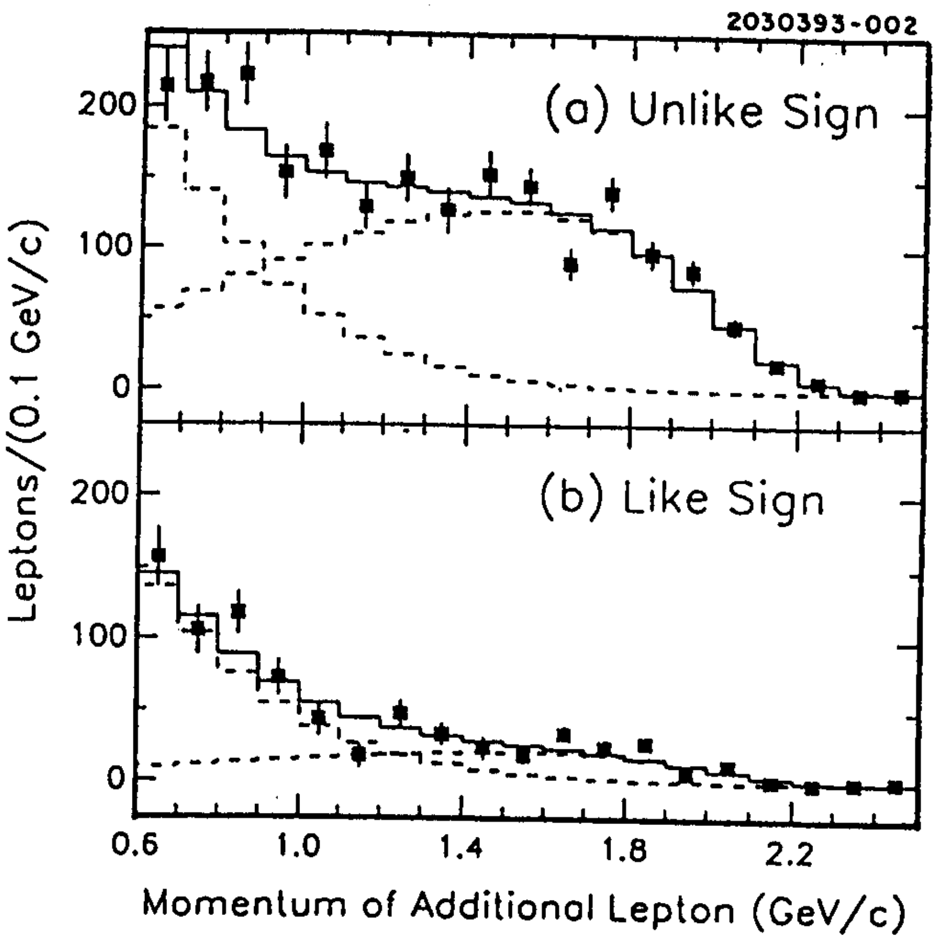

Figure 2.7: Efficiency corrected spectrum of additional leptons in tag events, for *a*) opposite-sign and *b*) same-sign leptons. Superimposed are fits (solid) to a primary lepton spectrum (dashed) plus a secondary spectrum (dash-dot).

Chapter 3

Apparatus

This experiment was performed at the Fermi National Accelerator Laboratory (Fermilab) in Batavia, Illinois, U.S.A. using the Tevatron accelerator which gave proton-antiproton collisions at a center-of-mass energy of 1.8 TeV. Particles which were produced by the collisions were detected by the Collider Detector at Fermilab (CDF). The Tevatron accelerator and CDF detector are described below emphasizing what we used in our analysis.

3.1 Tevatron

The Tevatron accelerator produces the world highest energy proton-antiproton collisions at a center-of-mass energy of 1.8 TeV. Six accelerators of which the Tevatron accelerator consists are illustrated in Fig. 3.1. First, negatively charged hydrogen ions are injected to a DC voltage accelerator, Cockcroft-Walton electrostatic accelerator (C-W), and are accelerated to 750 keV. These particles are accelerated to 200 MeV in 500 foot-length linear accelerator (LINAC). The two electrons are then stripped off the hydrogen ions, leaving bare protons, which are injected into the booster ring, a synchrotron with a diameter of 500 feet. The protons are accelerated up to 8 GeV in the booster ring and are injected to the main ring. The main ring, a synchrotron with a diameter of two kilometers, is composed of water-cooled magnets. After being accelerated to 150 GeV in the main ring, protons are injected to the Tevatron ring which is the same diameter with the main ring. The Tevatron ring is composed of superconducting magnets and can accelerate protons to 900 GeV.

Protons accelerated to 150 GeV in the main ring are also used to initiate production of antiprotons. Every two seconds, approximately two trillion protons are accelerated to 120 GeV in the main ring and then directed to an antiproton production target. Of the many particles and antiparticles of different types produced in collisions the protons make in the target, about ten million antiprotons are collected in a debuncher ring. The captured beam of antiprotons, circulating in the debuncher ring, is then made more dense by a process called stochastic cooling. The antiprotons are then transferred to the accumulator ring. The antiprotons merged into a single beam, cooled further, and stored in the accumulator ring. The debuncher and accumulator rings operate at 8 GeV. The antiprotons are accelerated by the main ring and the Tevatron ring in the opposite direction against the protons. Protons and antiprotons are collected into 6 bunches, so that a beam crossing occurs every 3.5 μsec.

The 1992-1993 run (RUN-Ia) started in April 1992 and ended in May 1993. The Tevatron provided about 25 pb^{-1} and the CDF has collected an integrated luminosity of $\int L dt = 20\ \mathrm{pb}^{-1}$.

3.2 Collider Detector at Fermilab

The Collider Detector at Fermilab (CDF) is a general purpose detector located at the $B0$ interaction region of the Tevatron ring, where collisions between protons and antiprotons occur. A perspective view of the CDF detector is shown in Fig. 3.2. The detector consists of 2 parts: the central detector and the forward and backward detectors. Figure 3.3 shows the location of each detector component. The tracking chambers consist of the silicon vertex detector (SVX), the vertex chamber (VTX) and the central tracking chamber (CTC). They are azimuthally symmetric around the beam axis. The solenoidal magnet which surrounds the tracking chambers generates 1.4 T magnetic field along the beam axis. The calorimeter used to measure energy of particles surrounds the solenoidal magnet. The calorimeter consists of the central electromagnetic calorimeter (CEM), the central hadronic calorimeter (CHA), the endwall hadron calorimeter (WHA), the plug electromagnetic calorimeter (PEM), the plug hadronic calorimeter (PHA), the forward electromagnetic calorimeter (FEM) and the forward hadron calorimeter (FHA). The muons which passed through the calorimeters reach muon chambers. The muon detectors consists of the central muon system (CMU), the central muon upgrade (CMP), the central muon extension (CMX) and the forward muon system (FMU). The beam-beam counters (BBC) are placed in front of the forward and backward calorimeters and are used for luminosity monitor and trigger. The detectors and detector components most relevant to this analysis are briefly reviewed in the following sections.

The CDF coordinate system is taken as follows. The origin is the center of detector, the nominal collision point, and the z-axis is the proton beam direction. The x-axis points to the outside of the Tevatron ring and the y-axis points toward vertically upward, so as to make a right-handed coordinate system. The azimuthal angle ϕ is an angle measured from the positive x-axis toward the positive y-axis. The pseudo-rapidity η is defined by $\eta \equiv -\ln(\tan\theta/2)$, where the polar angle θ is an angle from the proton beam direction (the positive z-axis). The radius r is a distance from the beam axis in x-y plane. The central detector and the forward (backward) detector cover regions $10^\circ < \theta < 170^\circ$ and $\theta < 10^\circ$ ($\theta > 170^\circ$), respectively.

3.2.1 Beam-beam counters

The beam-beam counters (BBC) are planes of scintillation counters which are located at the front face of each of the forward and the backward calorimeters. A beam's-eye view of the one of the BBC's is shown in Fig. 3.5. They provide a minimum-bias trigger for the detector in addition to a role of the luminosity monitor. The timing resolution of the counters is less than 200 psec. They cover the polar angle region from 0.32° to 4.47° along either the horizontal or vertical directions, corresponding to a pseudo-rapidity range of 3.24 to 5.90.

3.2.2 Tracking detectors

Silicon Vertex detector (SVX) [18]

The SVX consists of two cylindrical modules placed end-to-end with their axes coincident with the beamline. The total longitudinal coverage is 51 cm (2×25.5 cm with 2.15 cm gap). Because $p\bar{p}$ interactions are spread along the beamline with standard deviation $\sigma \sim 30$ cm, the geometrical acceptance of the SVX is about 60% for $p\bar{p}$ interactions. Each module consists of four radial layers (numbered 0-3 from beam pipe) of silicon strip detector. The inner and outer layers are at radii of 3.005 cm and 7.866 cm, respectively. Figure 3.6 shows a view of one cylindrical module of the SVX. For layers 0, 1 and 2 of the silicon strip detector, the strips are on a 60 μm pitch along the beam axis. For layer 3 they are on a 55 μm pitch. The resolution for high p_T tracks is ~ 10 μm after correction of the alignment of the SVX geometry by using real track data.

Vertex chamber (VTX)

The VTX is designed primarily to determine the event vertex position in the longitudinal z direction. The VTX provides tracking information up to a radius of 22 cm and $|\eta| < 3.25$. The VTX consists of vertical planes of drift chambers along the z direction, with each individual z slice being radially divided into octants. The individual chamber octants have sense wires arranged tangentially to the beam, providing track hit information mainly in (r, z) coordinates. The typical resolution of vertex point turned out to be about 1 mm in the z direction.

Central Tracking Chamber (CTC) [19]

The CTC is a 1.3 m radius and 3.2 m long cylindrical drift chamber which gives precise momentum measurements in the angular region $40^\circ < \theta < 140^\circ$ ($-1 < \eta < 1$). In this region the momentum resolution is better than $\delta p_T/p_T^2 \leq 0.002$ (GeV/c)$^{-1}$. The chamber contains 84 layers of the sense wires grouped into 9 "superlayers". Five of the superlayers consist of 12 axial sense wires; four stereo superlayers consist of 6 sense wires tilted by $\pm 3^\circ$ relative to the beam direction. Figure 3.7 shows an endplate of the chamber displaying the 45° tilt of the superlayers to the radial direction to correct for the Lorentz angle of the electron drift in the magnetic field.

Leading electrons drift into the azimuthal direction with a maximum drift distance being less than 40 mm, corresponding to a drift time 800 ns. The axial superlayer signals give a picture of the event in $r - \phi$ plane. The stereo superlayer signals give a picture of the event in $r - z$ plane in cooperation with the axial superlayer signals.

3.2.3 Calorimeters

In order to contain showers produced by particles from $p\bar{p}$ collision at the nominal interaction point a "tower" geometry was chosen for all calorimeters as shown in Fig 3.4. The coverage of the calorimeter towers in $\eta - \phi$ space is shown in Fig 3.8. Each tower has an electromagnetic shower counter in front of a corresponding hadron calorimeter, so that one can make a detailed comparison of electromagnetic to hadronic energy on a tower-by-tower basis. The towers are projective, i.e., they point at the interaction region, and are 0.1 units of η wide by 15° (central region) or 5° (plug and forward regions) in ϕ. The physical size of a tower ranges from about 24.1 cm (η) $\times$ 46.2 cm (ϕ) in the central region to 1.8 cm $\times$ 1.8 cm in the forward region. Geometric coverages in η direction and absorption thickness for calorimeters are summarized in Table 3.1. The absorption thicknesses in Table 3.1 are given in radiation lengths, X_0, for the electromagnetic calorimeters or in pion absorption lengths, Λ_{abs}, for the hadron calorimeters.

Calorimeter component	Geometric coverage in η direction	Absorption thickness
CEM	$0.0 < \lvert\eta\rvert < 1.1$	$18X_0$
PEM	$1.2 < \lvert\eta\rvert < 2.4$	$18 - 21X_0$
FEM	$2.4 < \lvert\eta\rvert < 4.2$	$18X_0$
CHA	$0.0 < \lvert\eta\rvert < 0.8$	$4.7\Lambda_{abs}$
WHA	$0.8 < \lvert\eta\rvert < 1.3$	$4.5\Lambda_{abs}$
PHA	$1.3 < \lvert\eta\rvert < 2.4$	$5.7\Lambda_{abs}$
CHA	$2.4 < \lvert\eta\rvert < 4.2$	$7.7\Lambda_{abs}$

Table 3.1: Geometric coverage in η direction and absorption thickness for calorimeter components.

Central calorimeters: Central electromagnetic calorimeter (CEM), Central hadron calorimeter (CHA) and Endwall hadron calorimeter (WHA)

The central calorimeters cover a polar angle region of $39° < \theta < 141°$ ($|\eta| < 1.1$). It is azimuthally segmented into 15° wedges. There are 48 wedges in all, 24 on each side of the $z = 0$ plane. A perspective view of one central calorimeter wedge is shown in Fig. 3.9. Each wedge has an electromagnetic part and a hadronic calorimeter part, and is subdivided along the z-axis into ten projective towers, numbered from 0 to 9, where tower 0 is at 90° polar angle. The size of the central calorimeter tower is approximately 15° in ϕ and 0.11 units in η.

The CEM [20] consists of 31 layers of 5 mm polystyrene scintillator interleaved with 30 layers of 1/8 inch lead. Total thickness of CEM module is approximately eighteen radiation lengths. Using the test beam electron with an energy range of 15-100 GeV, the energy resolution of the CEM was measured [21] as

$$\frac{\Delta E}{E} = \frac{13.5\%}{\sqrt{E sin\theta}} \qquad (E \text{ in GeV}), \tag{3.1}$$

where the $sin\theta$ reflects the change of the sampling thickness seen by the electron emitted at a polar angle θ.

The CEM has a gas proportional wire chamber with cathode strip embedded approximately at the EM shower maximum, 5.9 radiation lengths including the solenoid. The central strip chamber (CES) consists of wires along the beam direction for ϕ measurements and cathode strips perpendicular to wires for z measurements. The CES provides a precise determination of shower center and shower shape. The position resolution is about 2.2 mm in the wire (ϕ) view and 1.4 mm in the strip view for 50 GeV/c electrons.

The CHA [22] consists of 32 layers of 10 mm plastic scintillator interleaved with 32 layers of 25 mm iron. The WHA consists of 15 layers of 10 mm plastic scintillator interleaved with 15 layers of 50 mm iron. Total material thickness is 4.7 units of pion absorption lengths for CHA and 4.5 units for the WHA. The CHA has 9 projective towers numbered from 0 to 8 along z-axis. The WHA has 6 projective towers numbered from 6 to 11 along z-axis. The number 6 (7, 8) tower of the CHA occupies the same tower in $\eta - \phi$ plane as the number 6 (7, 8) of WHA in the same wedge. The energy resolution for the CHA is given by

$$\frac{\Delta E}{E} = \frac{75\%}{\sqrt{E sin\theta}} \qquad (\ E \text{ in GeV}) \tag{3.2}$$

from test beam pion data with an energy range of 10-150 GeV [23]. From the same beam test, the energy resolution for WHA is given by

$$\frac{\Delta E}{E} = \frac{80\%}{\sqrt{E}} \qquad (\ E \text{ in GeV}). \tag{3.3}$$

Plug calorimeters: plug electromagnetic calorimeter (PEM) and plug hadronic calorimeter (PHA)

The PEM [24] is an annular shaped detector which covers a polar angles region of $10^\circ < \theta < 32^\circ$. This polar angle region covers the end of the CTC. The PEM is a gas-based calorimeter using conductive plastic proportional tube arrays (7×7 mm) interleaved with 0.27 cm$\times$34 lead absorber panels and read out by cathode pads. Shower profiles can be measured with a resolution of 2 mm by this calorimeter [24, 25]. The tower segmentation in the plug calorimeter region is $\Delta\eta \sim 0.9$ and $\Delta\phi \sim 5^\circ$, finer than that in the central region. The energy resolution was measured in an electron test beam with an energy range of 20-200 GeV to be [26]

$$\frac{\Delta E}{E} = \frac{28\%}{\sqrt{E}} \qquad (\ E \text{ in GeV}). \tag{3.4}$$

The PHA is located behind the PEM, forming a partial conical shape. The PHA uses steel plates as absorber, with similar conductive plastic proportional tubes. Total material thickness is 5.7 units of pion absorption lengths. The energy resolution for the PHA was measured as

$$\frac{\Delta E}{E} = \frac{132\%}{\sqrt{E}} \tag{3.5}$$

by the test beam pions with an energy range of 40-200 GeV [27].

Forward calorimeters: Forward electromagnetic calorimeter (FEM) and forward hadron calorimeter (FHA)

The FEM is located behind the BBC's on both sides of the detector. The FEM's employ a gas-based calorimeter very similar to the PEM, with 0.48 cm $\times$ 30 lead absorber panels and tower segmentation $\Delta\phi \sim 5^\circ$ and $\Delta\eta \sim 0.1$. The coverage extends from 2.2 to 4.2 in η. The FEM position resolution ranges from 1 mm to 4 mm, depending on the location.

The FHA covers the forward region from 2.3 to 4.2 in η with an additional 7.7 pion absorption lengths behind the FEM. The FHA preserves the tower geometry of the FEM.

3.2.4 Muon detectors

The central muon detectors are located behind the calorimeters because electrons, photons and hadrons are absorbed inside calorimeters. The central muon detectors are divided into several components, each covering a different section. The central muon system (CMU) and central muon upgrade (CMP) cover a pseudo-rapidity region of $|\eta| < 0.6$. The central muon extension (CMX) covers a pseudo-rapidity region of $0.65 < |\eta| < 1.0$.

The coverage of the muon chambers is shown in the Fig. 3.10. The CMP and CMX were added just before RUN-Ia. The CMP is used for confirmation of muon track stubs in the CMU and it also fills up crack in $\eta = 0$ and wedge gaps of the CMU. The CMX extends the coverage of the CMU to about $\eta \sim 1.0$.

Central muon system (CMU) [28]

The CMU is divided into 24 wedges ($\Delta\phi = 15°$) forming an approximate cylinder around the beamline. The CMU is divided into 2 parts at $\eta = 0$. Each CMU wedge contains a total of 48 drift chambers, each 2.3 m long, arranged axially along the z direction. Figure 3.11 shows the layout of a CMU wedge; note there are significant cracks in acceptance between the wedges. The diagram in Fig. 3.12 shows a cross sectional view of a 5° section of the CMU, with a typical muon track passing through the four layers of drift cells.

The individual drift cells shown in Fig. 3.12 measure 63.5 mm $\times$ 26.8 mm in cross section, with a sense wire in the center, and are operated with a 50%/50% $Ar - C_2H_6$ gas mixture. A muon track stub is formed by measuring the drift time for each of the four sense wires along the muon path. The left-right ambiguity of the track is resolved by staggering the wires along the radial line. The chambers were operated in limited stream mode, allowing a measurement of the z position by measuring the relative charge deposited at both ends of the sense wire.

Central muon upgrade (CMP) [29]

The CMP is mounted on four flat planes around the central barrel detector, with a layer of steel ($\sim$ 3 absorption lengths) beyond the CMU. On the top and bottom of the detector, the CMP is attached to the steel of the solenoid return yoke. On both side of the detector, the CMP planes are attached to walls of steel. The tubes are continuous across the CMU $\eta = 0$ crack. The chambers are of fixed length in z and form the box around the central detector, therefore the actual pseudo-rapidity coverage varies with azimuth as shown in Fig. 3.10.

The CMP consists of 864 drift tubes with the size of 2.5 cm $\times$ 15 cm $\times$ 640 cm. The CMP drift tubes are half cell staggered and use the same argon/ethane gas mixture as used in the CMU. Figure 3.13 shows a schematic view of a CMP tube. Like the CMU, there are four layers of drift cells, and muon track stubs can be reconstructed in the $r-\phi$ plane by measuring the drift times in the four layers. However, no z information on the muon track is available from the CMP unlike CMU. The position resolution of the tube is about 300 μm.

Central muon extension (CMX) [29]

The CMX occupies the surface of a cone (see Fig 3.2). The CMX are free standing, just beyond the central barrel region. The CMX extends pseudo-rapidity coverage from 0.65 to 1.0.

The CMX consists of 864×2 drift tubes, which are of the same structure as the CMP tube. The tubes are sandwiched between two layers of scintillation counters which are used for triggering.

3.2.5 Trigger

The CDF trigger system consists of three levels [30, 31, 32]. The level 1-3 triggers reduce the high rate of $\sim$280 kHz in the 1992-1993 CDF run of $p\bar{p}$ interactions to a rate of $\sim$ 6 Hz at which events could be recorded on tape. The level 1-3 triggers consist of a logical OR of several requirements of electrons, photons, muons, missing energy, jets, taus, and select events based on physics interests. The level 3 trigger is made up of 48 Silicon Graphics computers, each containing two event buffers, plus an array of service hardware to push the data into and out of 96 buffers. Each event is sent to a single buffer, and so that level 3 triggers can be processed up to 48 separate events in parallel, with another 48 events meanwhile being loaded to the secondary buffers. Here we describe a low P_T dilepton trigger, which is called "JPSI STREAM 1". We used events which passed this trigger in this analysis.

Level 1 trigger

All level 1 triggers require a coincidence between hits in the forward and backward BBC scintillators to select physical reactions.

The level 1 trigger for low P_T dilepton events consists of level 1 dielectron trigger, level 1 dimuon trigger and level 1 electron-muon trigger. The level 1 dielectron (dimuon) trigger is made by a pair of level 1 electron (muon) triggers. The level 1 triggers for electron-muon events are generated by a pair of a level 1 low-E_T calorimeter trigger and a level 1 muon trigger.

The level 1 low-E_T calorimeter trigger is produced from analog signals coming from phototubes in the central calorimeters. The trigger is segmented in detector $\eta - \phi$ plane by $\Delta\phi = 15°$ and $\Delta\eta = 0.2$. The actual segmentation provided by the calorimeters is reduced by summing fast analog signals in order to reduce the large quantity of signals to a manageable level, resulting in a total of 2048 trigger towers, half electromagnetic and half hadronic. The analog calorimeter signals are corrected for pedestal offsets and gain variations. The level 1 low-E_T calorimeter trigger required that a trigger tower have the transverse EM energy above 4 GeV. No correction is made for possible variations in the z vertex position at this stage.

The level 1 muon trigger is produced from a fast analog measurement of momentum of muons in the CMU and a coincidence signal between chambers in alternate layers in the CMP. The momentum of muons is measured by a difference of drift times between layer 2 and layer 4 of CMU chambers (See Fig. 3.12). The difference of the drift time is a function of momentum of muons. The level 1 muon trigger requires the momentum to be greater than 3.3 GeV/c.

Level 2 trigger

The level 2 trigger for low P_T dilepton events consists of a level 2 dielectron trigger, a level 2 dimuon trigger and a level 2 electron-muon trigger. The level 2 dielectron (dimuon) trigger is made by a pair of level 2 electron (muon) triggers. The level 2 trigger for electron-muon events is generated by a pair of a level 2 low-E_T calorimeter trigger and a level 2 muon trigger.

Electromagnetic energy clusters are formed from trigger towers by hardware processors at this stage. The clustering algorithm used is that, first, a trigger tower with transverse EM energy greater than 4 GeV is searched, then four adjacent towers are examined one by one to be added to the seed tower if its transverse EM energy is greater than 3.6 GeV, and each attached trigger tower is taken as a seed tower and the same procedure is repeated until no more trigger tower is found to be added. A ratio of total (EM + HAD) transverse energy to transverse EM energy is calculated from electromagnetic and hadronic energies in the clusters. The level 2 electron trigger requires the ratio be less than 1.125.

The CTC tracks are reconstructed in two dimensions by a hardware processor called Central Fast Tracker (CFT) [33]. The CFT processes fast timing information from the CTC to identify a high P_T track in the $r - \phi$ plane by comparing the CTC hits with predetermined patterns. The CFT has a momentum resolution of $\Delta P_T/P_T^2 \sim 0.035$ $(\mathrm{GeV/c})^{-1}$, with a high efficiency [33]. The level 2 electron trigger requires the momentum of an associated track with the EM cluster to be greater than 4.8 GeV/c.

The level 2 muon trigger requires matching between the CFT track and a stub in the muon detectors. The momentum of the CFT track for the level 2 muon trigger is required to be greater than 3 GeV/c.

Level 3 trigger

The level 3 trigger for electron and muon requires the following.

- Level 3 electron

- Transverse energy: $E_T > 5$ GeV
- Transverse momentum: $P_T > 3$ GeV/c
- Lateral shower sharing: $L_{\text{shr}} > 0.3$
- Lateral shower shape: $\chi^2_{\text{strip}} < 15$
- Difference between a measured shower position in the CES and an extrapolated CTC track at the CES: $\Delta X < 6$ cm and $\Delta Z < 10$ cm

• Level 3 muon

- Transverse momentum: $P_T > 3$ GeV/c
- Difference between a CMU stub position and an extrapolated CTC track at the entrance of the CMU chambers: $\Delta X < 16$ cm and $\Delta Z < 16$ cm

Because the level 3 trigger uses same code as offline analysis, the lateral shower sharing, lateral shower shape, position matching will be defined and described later.

The level 3 trigger for low P_T dilepton events consists of a level 3 dielectron, a level 3 dimuon trigger and a level 3 electron-muon trigger. The level 3 dielectron (muon) trigger is generated by a pair of the electron (muon) triggers. The level 3 electron-muon trigger is generated by a pair of a level 3 electron and a level 3 muon trigger.

3.2.6 Data acquisition system

The CDF data aquisition system (DAQ) [34] employs a FASTBUS-based multi-level network. The CDF DAQ has multiple partitions each of which covers one or more independent detector sections so that the DAQ for different detector components can proceed in parallel. At the lowest level of the DAQ system, there are two major types of front end system. When an event is accepted by both level 1 and level 2, the data from front end crates are digitized and read by scanner modules. All the calorimeters and the central muon system use the redundant analog bus-based information transfer (RABBIT) which are read by MX scanner [35]. Most tracking detectors use FASTBUS

TDCs which are read by SSP scanners [36]. A few CAMAC modules are included in the event data stream and are read by an SSP scanner using a FASTBUS to CAMAC interface. Each scanner can buffer four events. This step in the DAQ pipeline is managed by the trigger supervisor (TS) FASTBUS module. The TS uses a combination of FASTBUS messages and dedicated control lines to provide flexible and efficient control of front end systems. Each partition is allocated a unique set of scanners and a trigger supervisor.

When all MX and SSP scanners have finished reading and buffering data for one event, the TS module sends a FASTBUS message to buffer manager (BFM) indicating that an event is available in a specified buffer. The BFM supervises dataflow from scanner modules to host VAX computers. The BFM initiates this dataflow by sending a FASTBUS message to event builder (EVB) instructing it to "Pull" an event from the same buffer in all scanners of a specified detector partition. The EVB is a group of FASTBUS modules which can read, buffer and reformat complete events from any allowed partition of detector components. When the EVB has finished reading data from scanner buffer N, it sends a "Pull OK" message to the BFM which in turn notifies the TS that buffer N is available for a new level 1 and level 2 trigger.

Under direction of the BFM, the EVB writes a complete event into a specified node in the level 3 processor farm (Silicon Graphics computers). Events accepted by the level 3 trigger are read by the buffer multiplexer executing on one or more computers in the VAX cluster. Event data can be logged to disk or tape.

3.2.7 Luminosity measurement

The luminosity can be obtained by counting the rate of a certain process of which cross section is known. We use inelastic $p\bar{p}$ events, and the BBC's to detect them. That is, we have

$$L = \frac{R_{BBC}}{\sigma_{BBC}}, \tag{3.6}$$

where L is the luminosity, R_{BBC} is the BBC event rate, and σ_{BBC} is the effective cross section visible to the BBC's. We estimate σ_{BBC} at 1800 GeV as follows.

We first calculate the corresponding quantity for the UA4 experiment at 546 GeV [37, 38], using their absolute measurements of the total and elastic $p\bar{p}$ cross sections, to be 38.9 ± 1.8 mb. A small correction due to the difference in the geometry of the trigger counters at CDF and UA4 is made in order to convert the above quantity into the corresponding CDF quantity at 546 GeV, σ_{BBC}^{546}. We then relate it to the value at 1800 GeV, σ_{BBC}^{1800}, by using the measurements of the Tevatron luminosities (L_{acc}) based on accelerator parameters, and the observed BBC rates R_{BBC} at the two energies. They have a relation

$$\frac{\sigma_{BBC}^{1800}}{\sigma_{BBC}^{546}} = \frac{R_{BBC}(1800)}{R_{BBC}(546)} \cdot \frac{L_{acc}(546)}{L_{acc}(1800)}. \tag{3.7}$$

We obtain [39]

$$\sigma_{BBC}^{1800} = 46.8 \pm 3.2 \text{ mb}. \tag{3.8}$$

With recent direct measurements of elastic and total cross sections by CDF collaboration [40], we are able to measure a direct measurement of the BBC cross section of

$$\sigma_{BBC} = 51.2 \pm 1.7 \text{ mb}. \tag{3.9}$$

After accounting for possible backgrounds in the BBC's, we have a total uncertainty of 3.6% on the integrated luminosity.

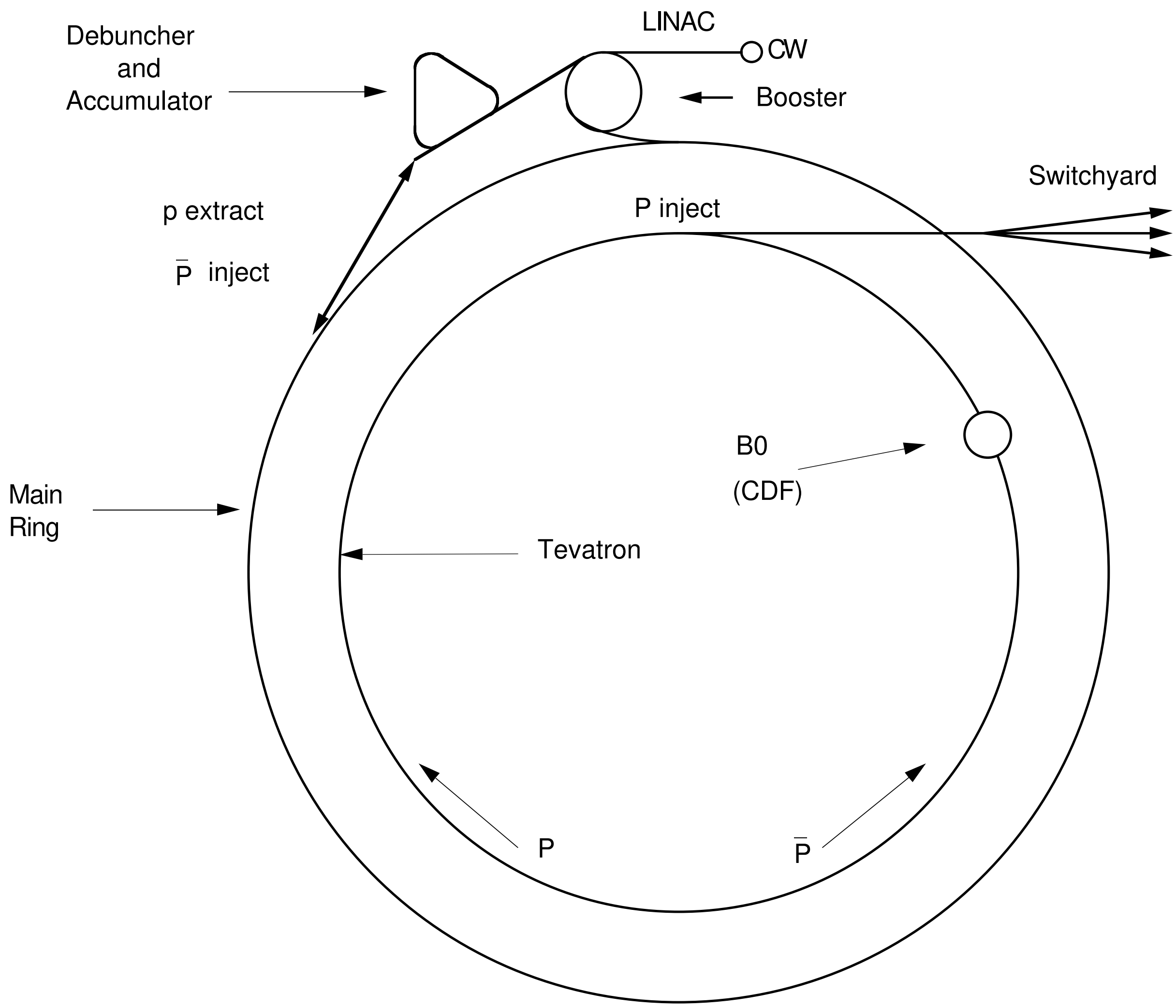

Figure 3.1: Diagram of the Tevatron accelerator complex.

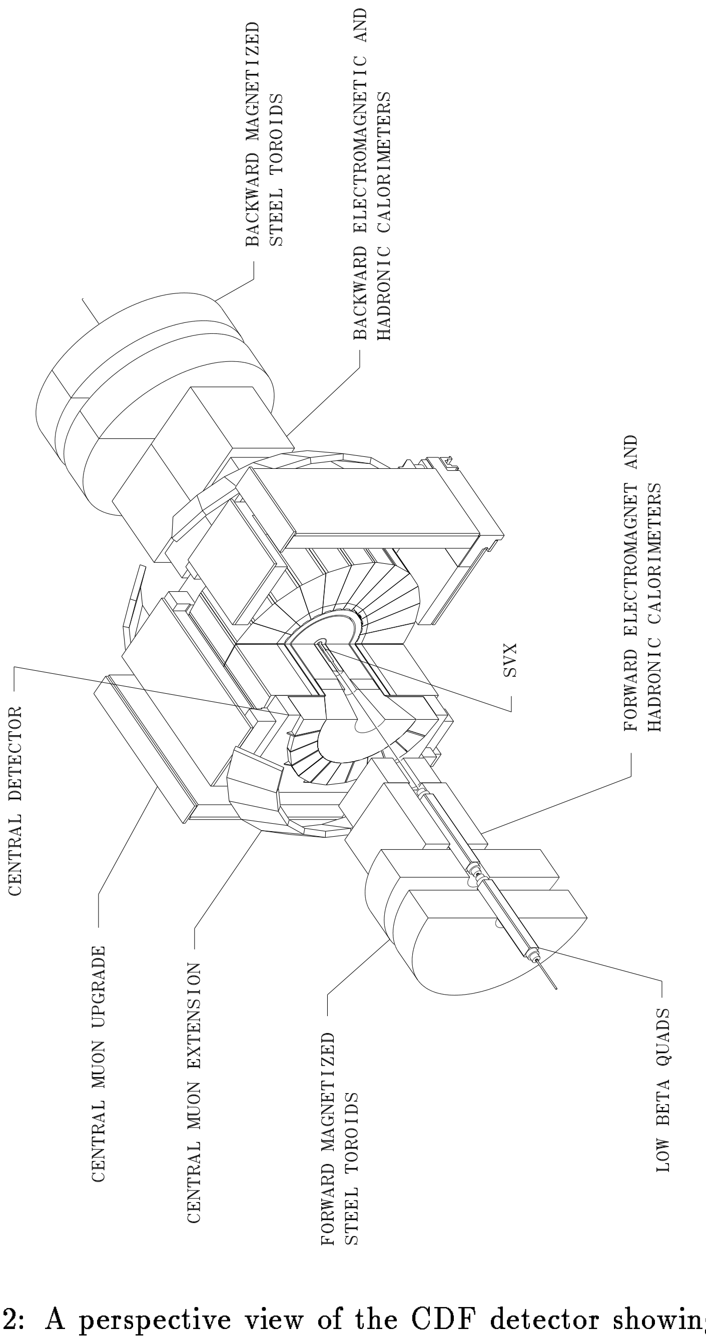

Figure 3.2: A perspective view of the CDF detector showing the central detector, the forward and the backward detectors.

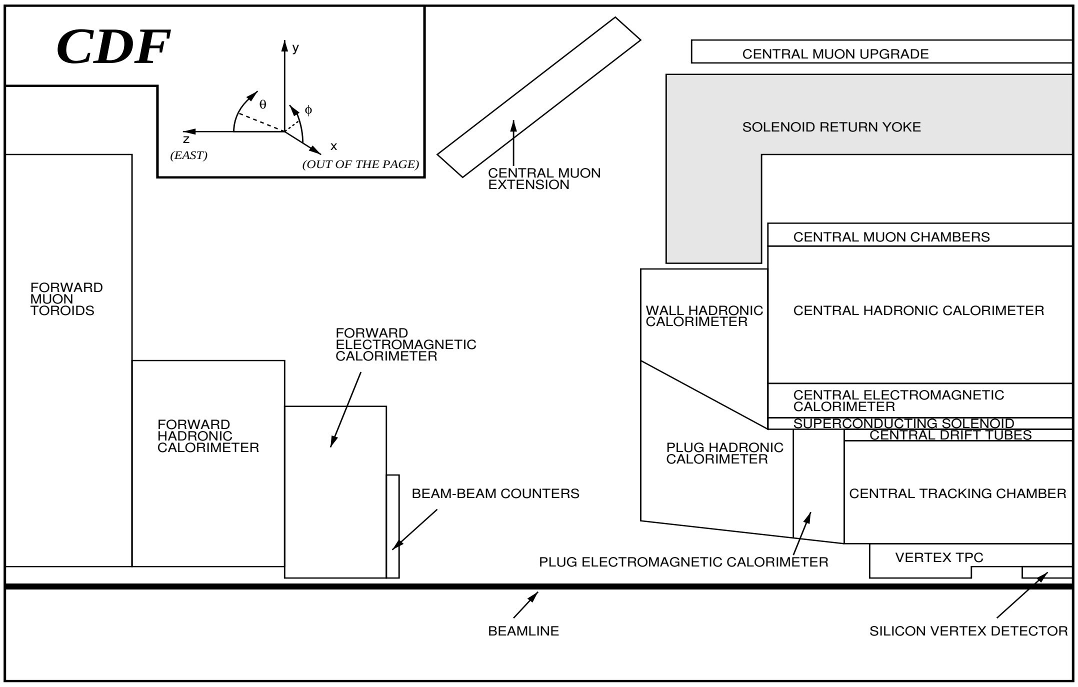

Figure 3.3: A side-view cross section of the CDF detector. The detector is forward-backward symmetric about the interaction point.

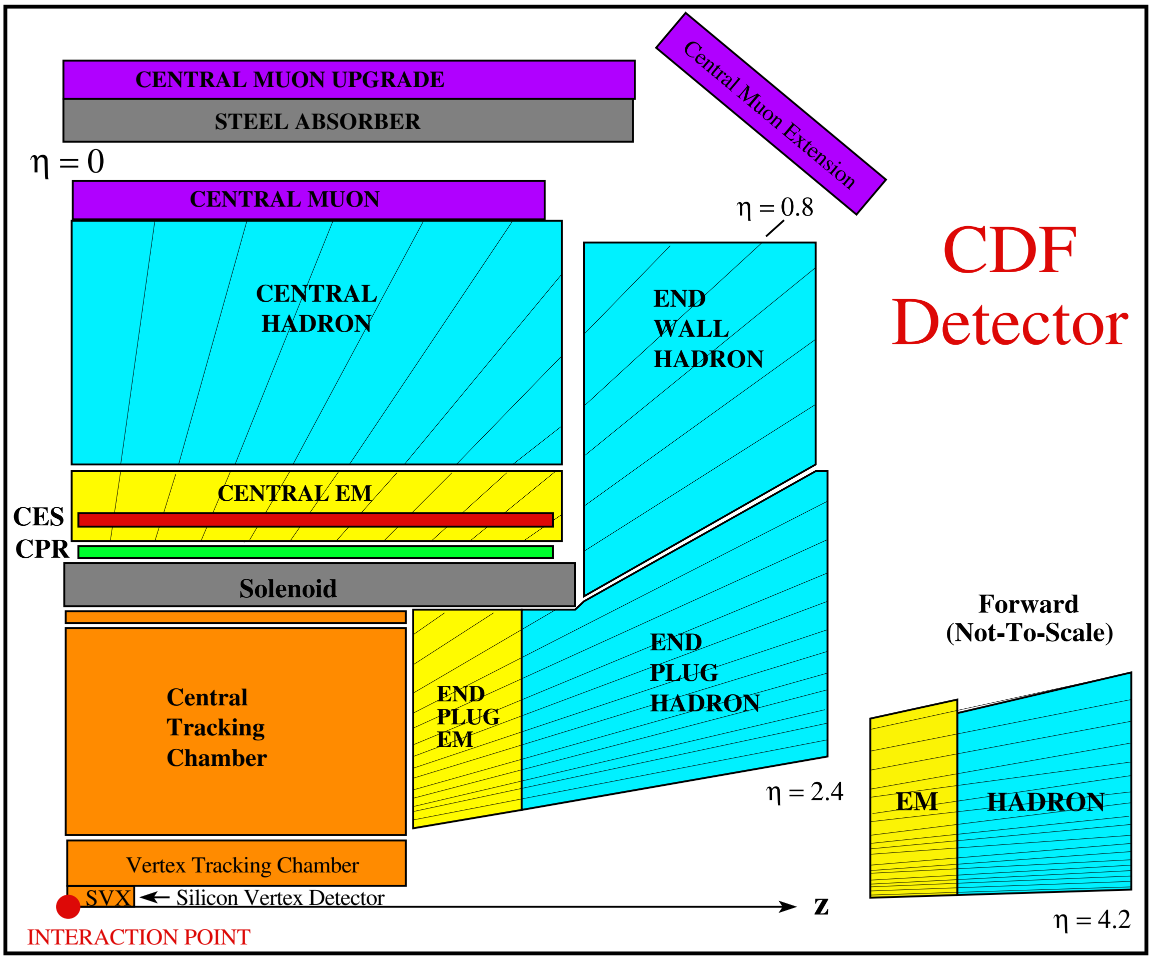

Figure 3.4: Cross-sectional view of the central detectors.

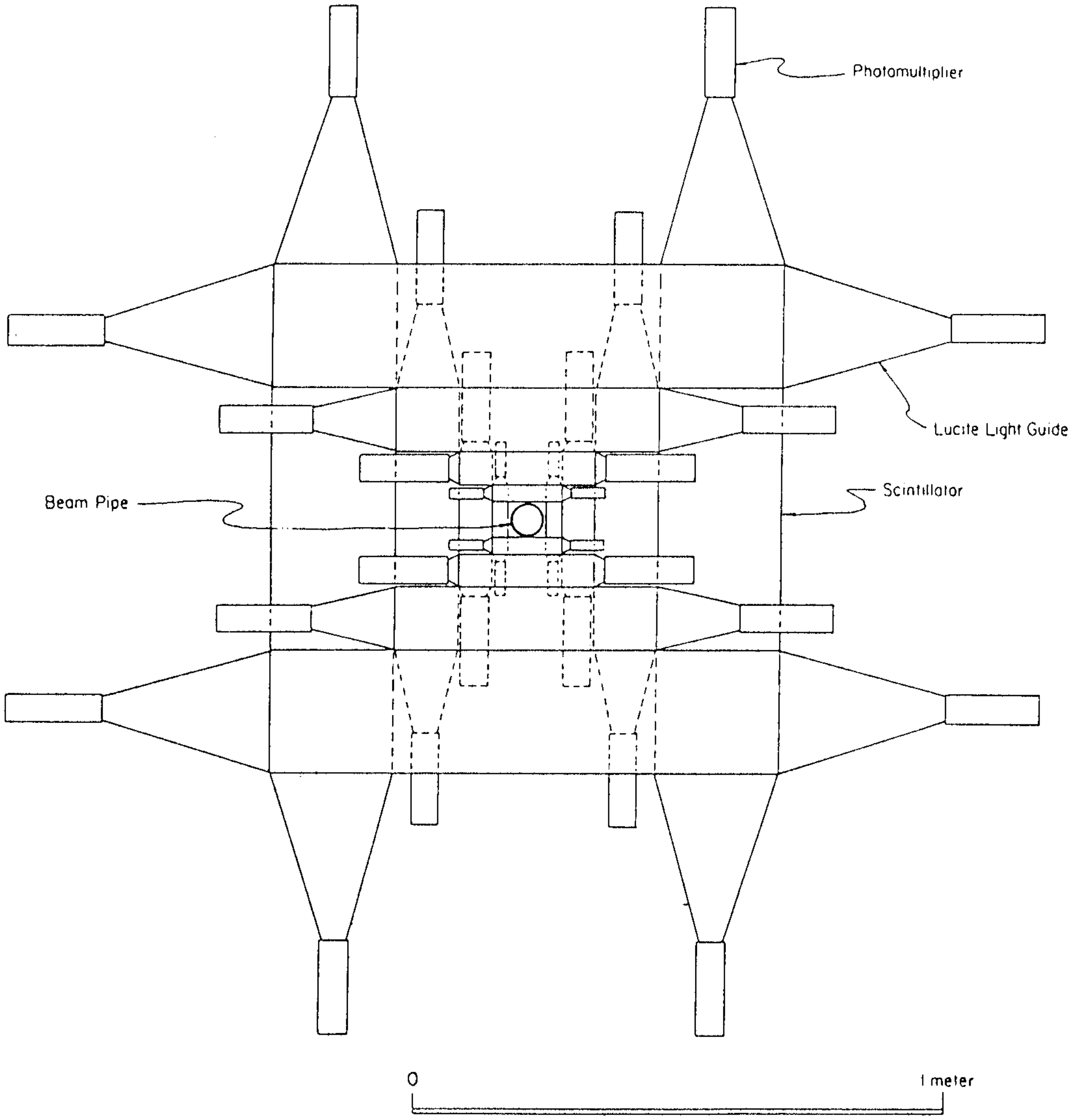

Figure 3.5: A beam's eye view of one of the beam-beam counter planes.

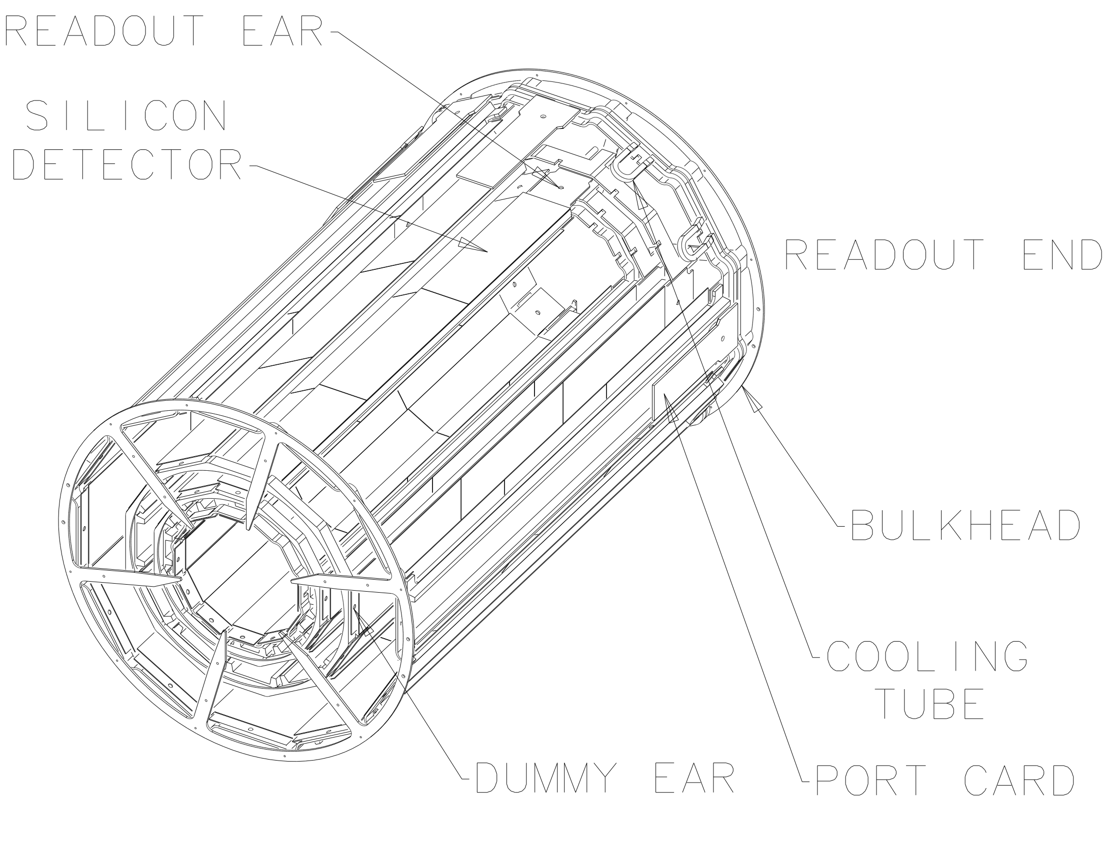

Figure 3.6: A perspective view of the SVX barrel.

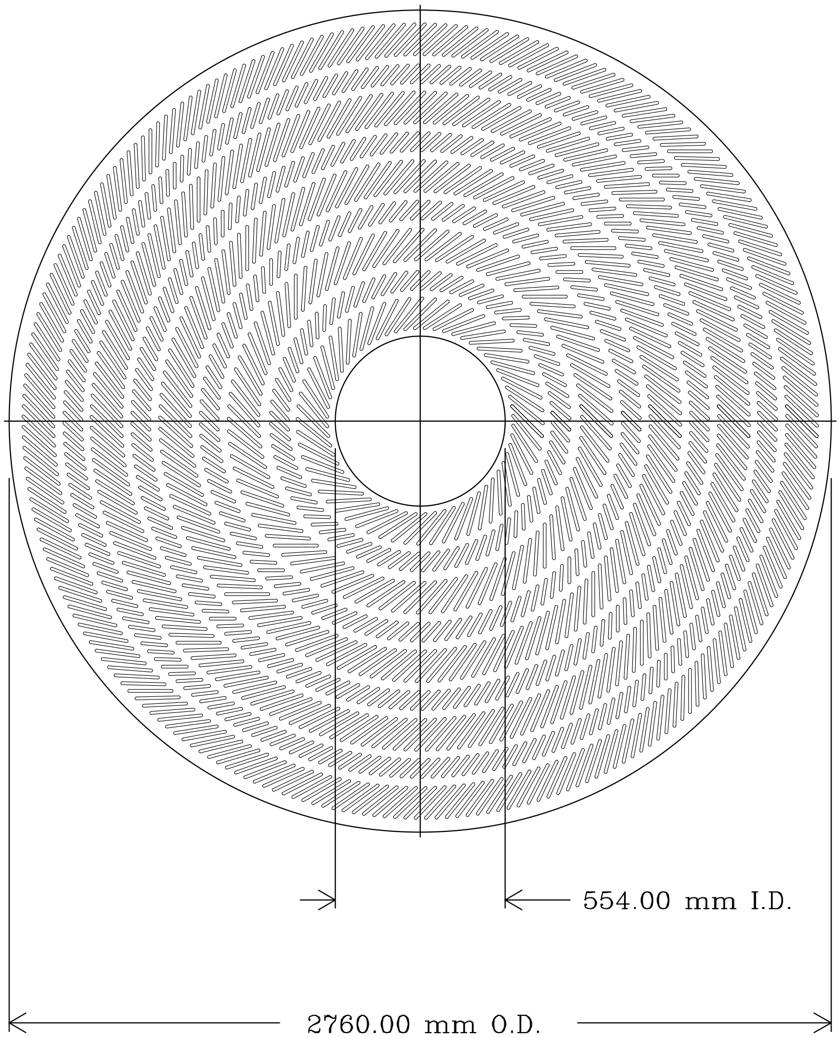

Figure 3.7: An endplate of the CTC showing the arrangement of the blocks which hold the 84 layers of sense wires.

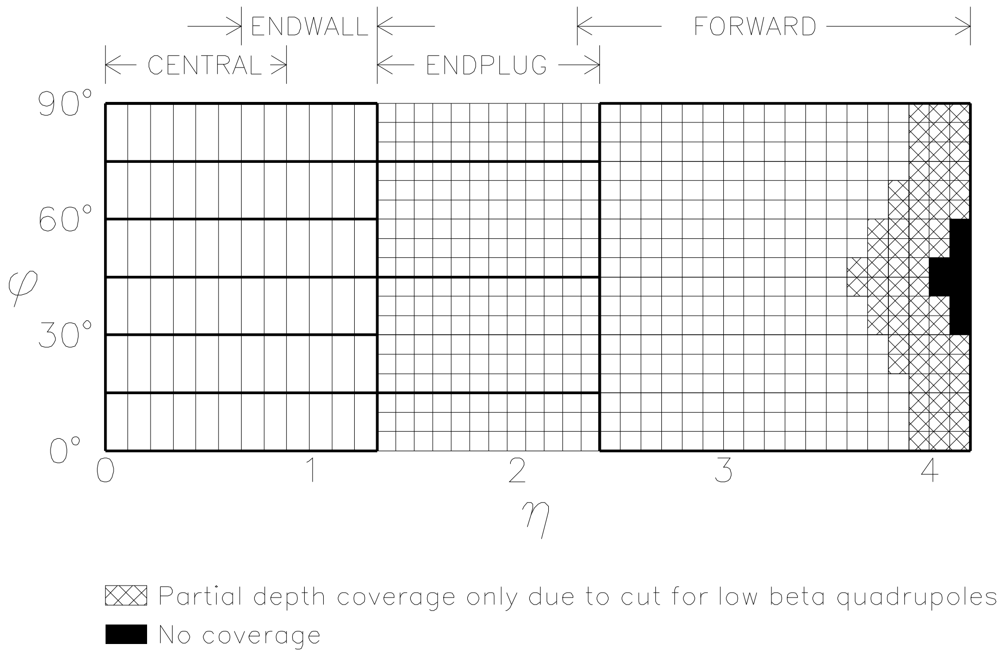

Figure 3.8: Hadron calorimeter tower in one of eight identical $\eta - \phi$ quadrants ($\Delta\phi = 90°, \eta > 0$). The heavy lines indicate module or chamber boundaries. The EM calorimeters have complete ϕ coverage out to $\eta = 4.2$.

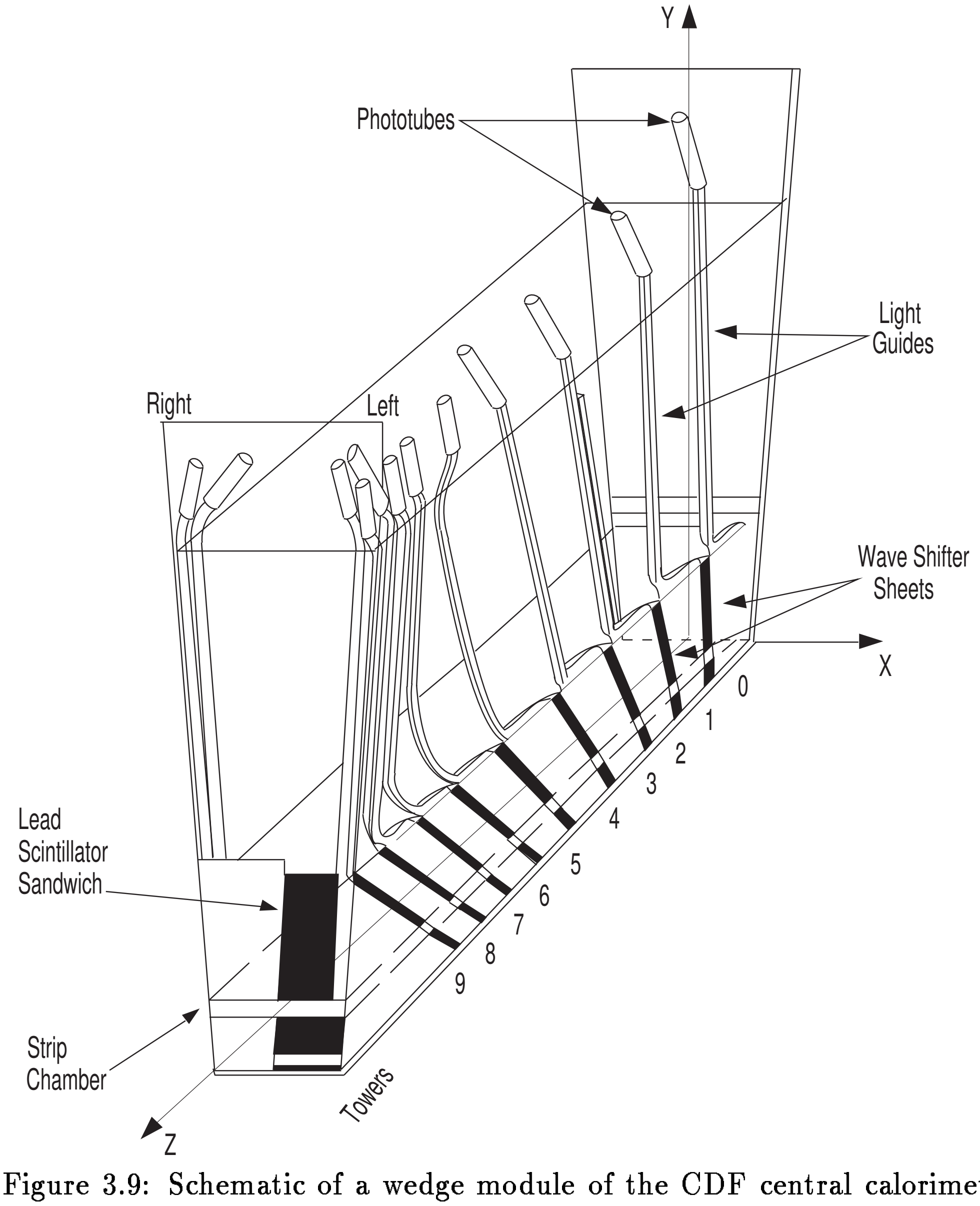

Figure 3.9: Schematic of a wedge module of the CDF central calorimeter showing the coordinate system as measured by the strip chamber used for test beam energy and mapping measurements. The 45° end plate is in the $+z$ direction; the "left" of the module was defined as being in the $+x$ direction.

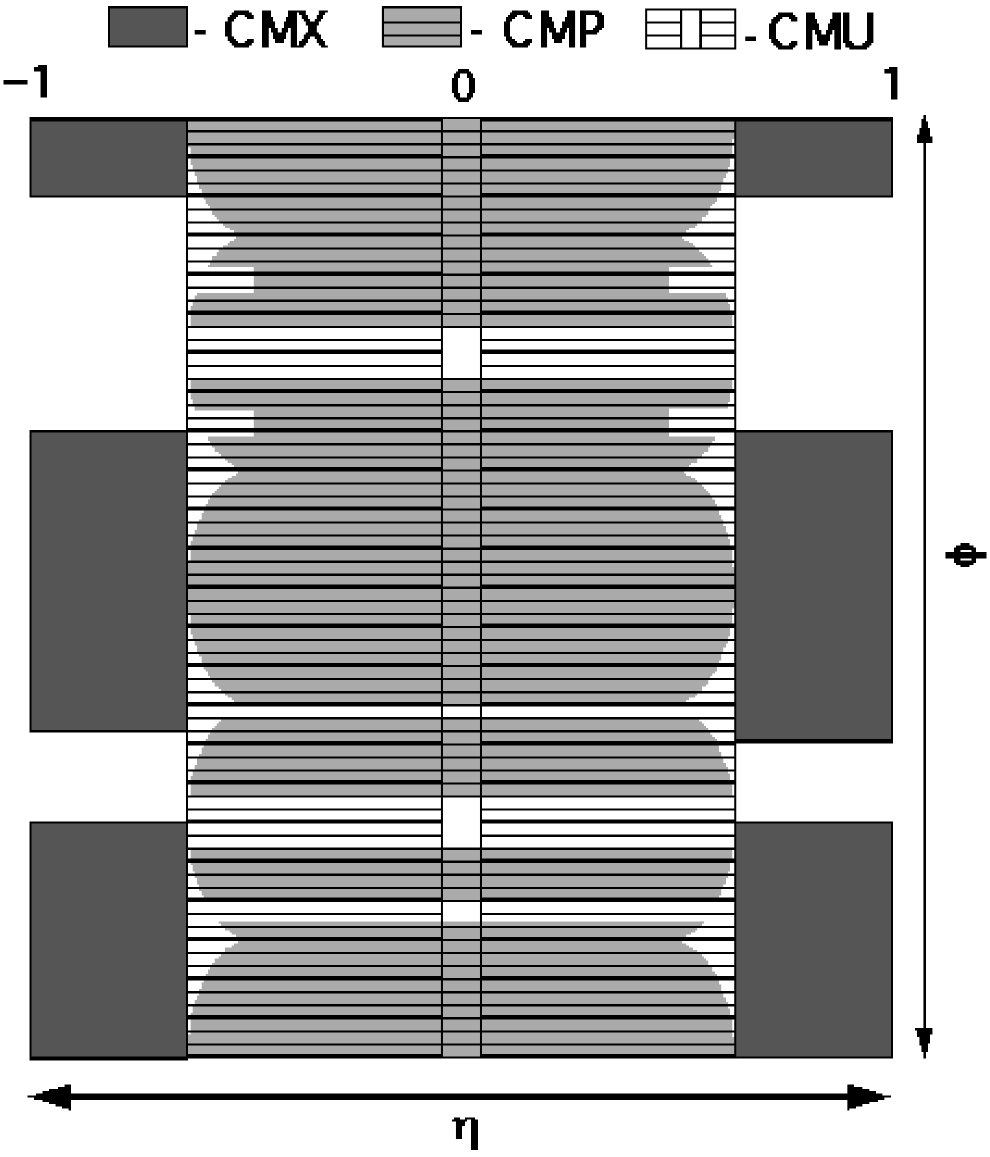

Figure 3.10: Map of muon eta-phi coverage.

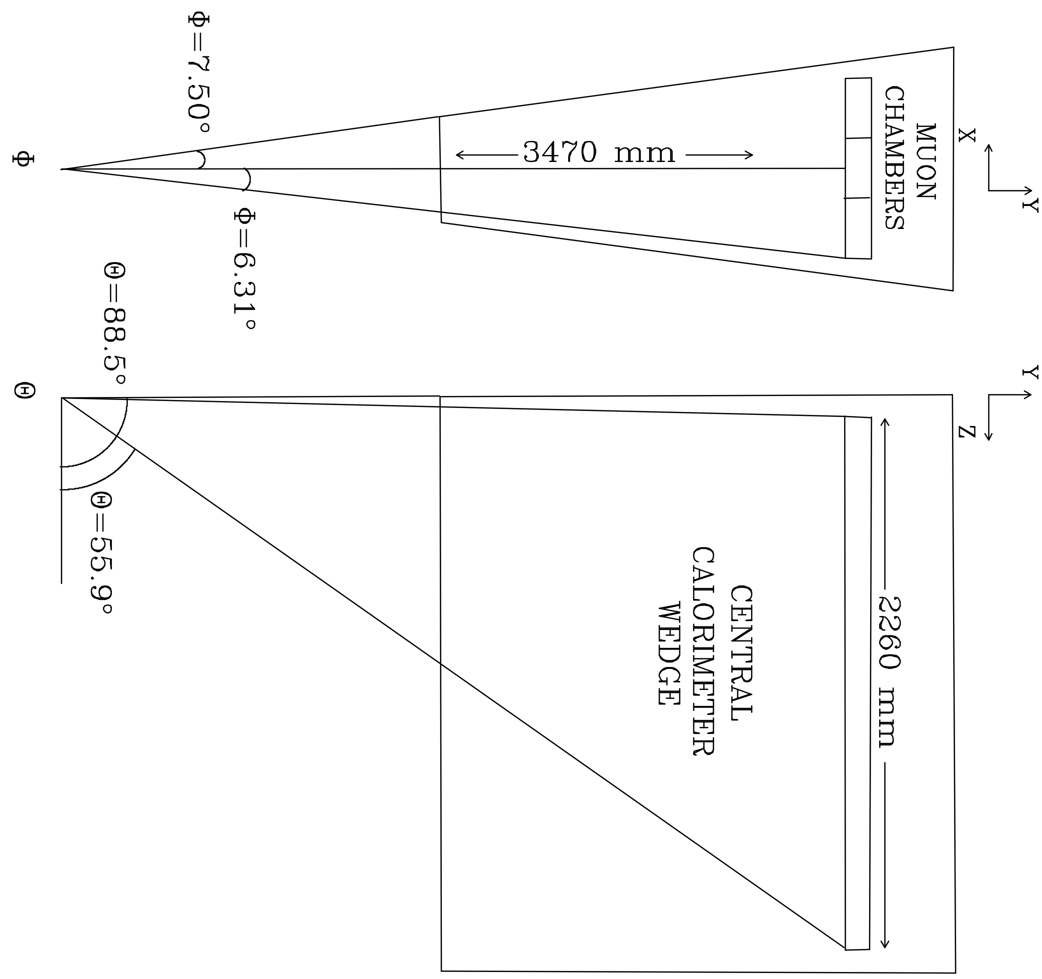

Figure 3.11: The layout of the central muon chambers in one of the central wedges.

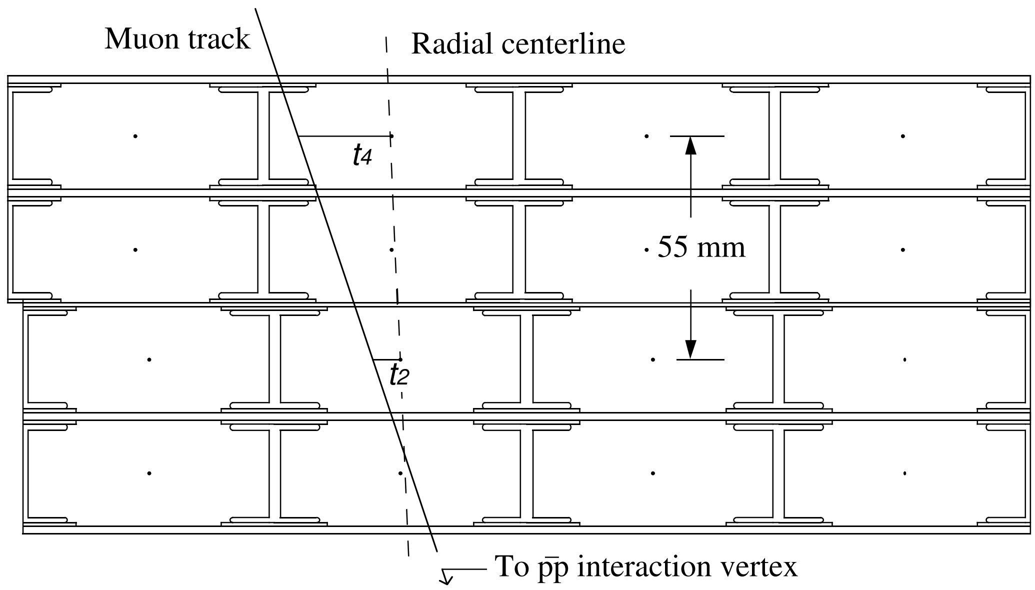

Figure 3.12: The arrangement of the four planes of central muon chambers in a view along the beam direction. The drift times t_2 and t_4 are used at the trigger level to determine a muon momentum cut off.

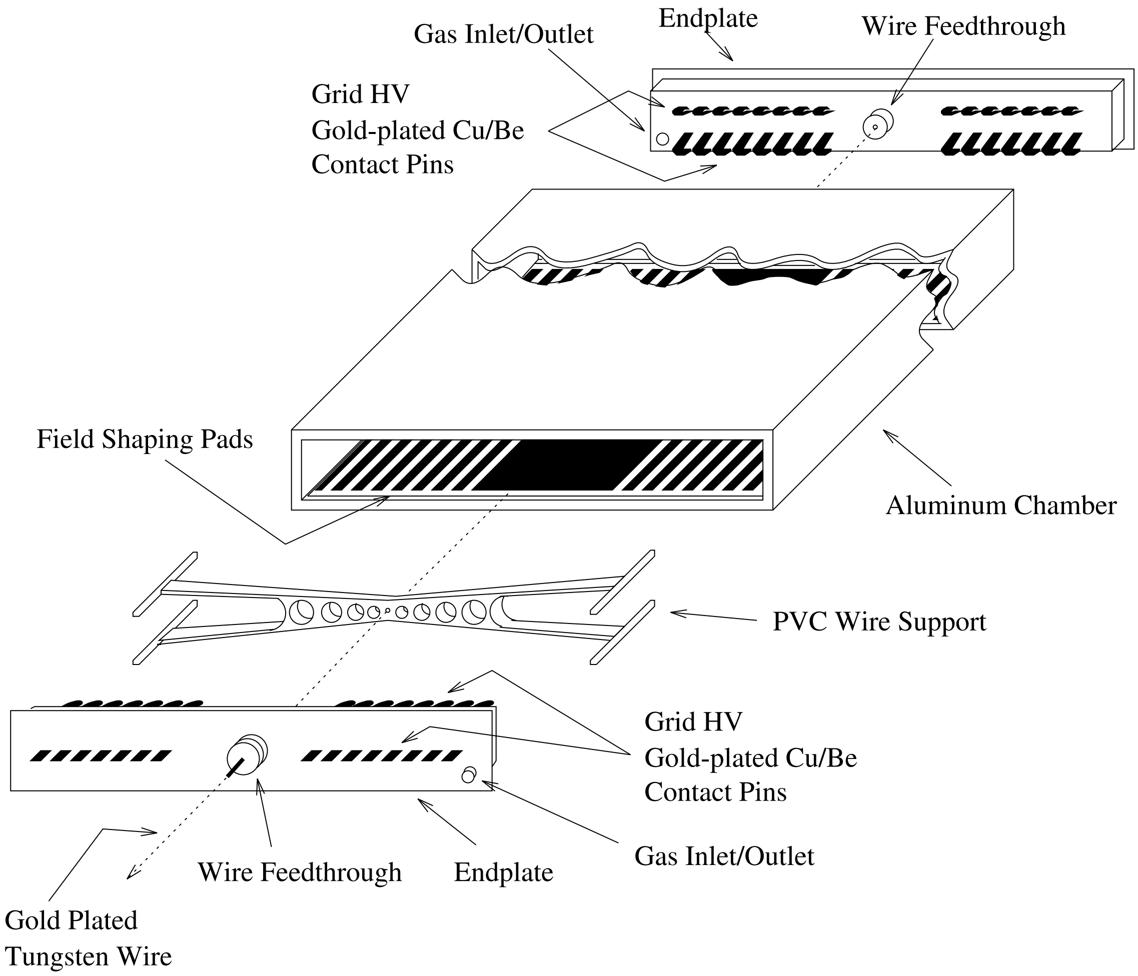

Figure 3.13: Schematic view of a CMP-CMX tube

Chapter 4

Analysis Outline and Data Reduction

4.1 Outline of the analysis

The mixing parameter, χ, can be estimated from Eq. (2.35) in Chapter 1 in principle, but several complications arise in actual analysis including consideration of sequential decays and backgrounds.

The important decay processes of $b\bar{b}$ events in this analysis are listed in Table 4.1. In Process 1, both b and $\bar{b}$ quarks decay to leptons directly, which is mentioned in Chapter 1. In Process 2 (3), the b ($\bar{b}$) quark decays to a lepton directly and the other $\bar{b}$ (b) quark to

$\left\{\begin{array}{lll} b & \rightarrow & l+X \\ \bar{b} & \rightarrow & l+X \end{array}\right.$	(Process 1)
$\left\{\begin{array}{lllll} b & \rightarrow & l+X & & \\ \bar{b} & \rightarrow & \bar{c}+X & \rightarrow & l+X \end{array}\right.$	(Process 2)
$\left\{\begin{array}{lllll} b & \rightarrow & c+X & \rightarrow & l+X \\ \bar{b} & \rightarrow & l+X & & \end{array}\right.$	(Process 3)

Table 4.1: Semileptonic decay processes.

	Process 1 $\left\{ \begin{array}{l} b \to l \\ \bar{b} \to l \end{array} \right.$	Process 2 $\left\{ \begin{array}{l} b \to l \\ \bar{b} \to \bar{c} \to l \end{array} \right.$	Process 3 $\left\{ \begin{array}{l} b \to c \to l \\ \bar{b} \to l \end{array} \right.$	Process 4 $\left\{ \begin{array}{l} c \to l \\ \bar{c} \to l \end{array} \right.$
Neither Q nor $\bar{Q}$ quark undergoes mixing.	OS	LS	LS	OS
One of Q $\bar{Q}$ quarks undergoes mixing.	LS	OS	OS	–
Both Q and $\bar{Q}$ quarks undergo mixing.	OS	LS	LS	–

Table 4.2: Charge combinations of e and μ for each Process. OS (LS) means opposite-sign (like-sign).

a lepton via $\bar{c}$ (c) quark.

The production of $c\bar{c}$ can contribute to $e\mu$ events through their semileptonic decay because we do not distinguish between leptons from $b\bar{b}$ and those from $c\bar{c}$. This process is taken into account in our analysis.

If there is no $B^0\bar{B}^0$ mixing, the charge signs of leptons are opposite in Process 1, as mentioned before. The charge signs of leptons are like in Process 2 and 3, because the charge of a sequentially produced lepton reverses.

Charge combinations of e and μ for each Process are summarized in Table 4.2. The process of $c\bar{c}$ production is included in the table as Process 4. If $e\mu$ events consist of Processes 1~4, the ratio of the number of LS events (N_{LS}) to that of OS events (N_{OS}) is written by

$$R = \frac{N_{LS}}{N_{OS}} = \frac{2\chi(1-\chi)N_D + [(1-\chi)^2 + \chi^2]N_S}{[(1-\chi)^2 + \chi^2]N_D + 2\chi(1-\chi)N_S + N_C} \tag{4.1}$$

$$= \frac{2\chi(1-\chi) + [(1-\chi)^2 + \chi^2]f_s}{(1-\chi)^2 + \chi^2 + 2\chi(1-\chi)f_s + f_c}, \tag{4.2}$$

where $f_s = N_S/N_D$ and $f_c = N_C/N_D$. The N_D and N_C are the numbers of events for Process 1 and 4, respectively. The N_S is the sum of the number of events for Processes 2 and 3. The probability for each mixing process is summarized in Table 4.3.

	Probability
Neither Q nor $\bar{Q}$ quark undergoes mixing.	$(1-\chi)^2$
One of Q $\bar{Q}$ quarks undergoes mixing.	$2\chi(1-\chi)$
Both Q and $\bar{Q}$ quarks undergo mixing.	χ^2

Table 4.3: Probability for each mixing process.

$\begin{cases} b \rightarrow l+X \\ \bar{b} \rightarrow J/\psi+X \rightarrow l+X \end{cases}$	(Process 5)
$\begin{cases} b \rightarrow J/\psi+X \rightarrow l+X \\ \bar{b} \rightarrow l+X \end{cases}$	(Process 6)
$\begin{cases} b \rightarrow l+X \\ \bar{b} \rightarrow \bar{c}+W; \quad W \rightarrow c+\bar{s}; \quad c \rightarrow l+X \end{cases}$	(Process 7)
$\begin{cases} b \rightarrow c+W; \quad W \rightarrow \bar{c}+s; \quad \bar{c} \rightarrow l+X \\ \bar{b} \rightarrow l+X \end{cases}$	(Process 8)

Table 4.4: Other semileptonic decay processes.

In addition to the above four processes, we have considered other processes listed in Table 4.4. In Process 5 (6), the b ($\bar{b}$) quark decays to a lepton directly and the other $\bar{b}$ (b) quark decays to a J/ψ and then one of the leptons from the $J/\psi \rightarrow l^+l^-$ decay is detected, while the other lepton misses detection. In Process 7 (8), the b ($\bar{b}$) quark decays to a lepton directly and the other $\bar{b}$ (b) quark to $\bar{c}+c+\bar{s}$ ($c+\bar{c}+s$) quarks and then the c ($\bar{c}$) quark decays to a lepton. The charge combinations of e and μ for the other processes are summarized in Tables 4.5 and 4.6. By looking at Eq. (4.2), it is not difficult to understand that inclusion of other b-decay processes does not change the shape of this equation. Since the most relevant definition of f_s is the ratio of all LS contributions to all OS contributions from $b\bar{b}$ events in the case of no mixing, the numbers of events for Process 5, 6, 7, and 8 are added to the N_D, and that for Process

	Process 5 $\left\{ \begin{array}{l} b \to l \\ \bar{b} \to J/\psi \to l \end{array} \right.$	Process 6 $\left\{ \begin{array}{l} b \to J/\psi \to l \\ \bar{b} \to l \end{array} \right.$
Neither Q nor $\bar{Q}$ quark undergoes mixing.	OS/LS	OS/LS
One of Q $\bar{Q}$ quarks undergoes mixing.	LS/OS	LS/OS
Both Q and $\bar{Q}$ quarks undergo mixing.	OS/LS	OS/LS

Table 4.5: Charge combinations of e and μ for Process 5 and 6. OS (LS) means opposite-sign (like-sign).

	Process 7 $\left\{ \begin{array}{l} b \to l \\ \bar{b} \to c \to l \end{array} \right.$	Process 8 $\left\{ \begin{array}{l} b \to \bar{c} \to l \\ \bar{b} \to l \end{array} \right.$
Neither Q nor $\bar{Q}$ quark undergoes mixing.	OS	OS
One of Q $\bar{Q}$ quarks undergoes mixing.	LS	LS
Both Q and $\bar{Q}$ quarks undergo mixing.	OS	OS

Table 4.6: Charge combinations of e and μ for Process 7 and 8. OS (LS) means opposite-sign (like-sign).

5 and 6 are added to the N_S. Contributions from the other decay processes, therefore, only change the value of f_s. The b-decay processes listed in Tables 4.1 and 4.4 account for most of the $e\mu$ events from $b\bar{b}$ production considered in this analysis. The effect of the other decay processes is relatively small.

Since the observed $e\mu$ events contain fake lepton events, the R is written in terms of the observed numbers of LS and OS $e\mu$ events, $N^{exp}(LS)$ and $N^{exp}(OS)$, by

$$R = \frac{N^{exp}(LS)(1 - F_{e\mu}(LS))}{N^{exp}(OS)(1 - F_{e\mu}(OS))}\,, \tag{4.3}$$

where $F_{e\mu}(LS)$ and $F_{e\mu}(OS)$ are the fake lepton fractions in the LS and OS samples. Fake leptons are caused by lepton mis-identification, photon conversion electrons, and muons from hadron decays in flight.

To determine χ, we need to know $F_{e\mu}(OS)$, $F_{e\mu}(LS)$, f_s and f_c in addition to $N^{exp}(OS)$ and $N^{exp}(LS)$. The studies of these quantities were carried out by using real data as much as possible, with minimum use of Monte Carlo's. The $F_{e\mu}$'s were obtained by studying the fake fraction for each lepton. For muons it was done by using $J/\psi \to \mu^+\mu^-$ decays, minimum bias data, $K_s^0 \to \pi^+\pi^-$ decays, and $\phi \to K^+K^-$ decays. Similarly, the study for electrons was done by using $J/\psi \to e^+e^-$, γ-hadron overlapped events, and Monte Carlo generated charged pions.

We used Monte Carlo programs to estimate the f_s. Direct quark pair productions were studied with ISAJET [41] + CLEOMC [42, 43]. Gluon splitting process was also taken into account by using ISALEP [44]+ CLEOMC. The ISAJET is a Monte Carlo program which simulates p-p and $\bar{p}$-p interactions at high energies. It is based on perturbative QCD plus phenomenological models for parton and beam jet fragmentation. The QFL is a Monte Carlo program which simulates bottom and charm particles decays. The ISALEP is a special version of ISAJET which is modified to generate higher order heavy quark events with high-P_T leptons effectively. Both generated events were passed through the QFL detector simulation package [45]. The CLEOMC is a detector simulation program for CDF detector. Since the philosophy of the package is to parameterize detector response rather than derive the response from first principles, the QFL Simulation package can provide a fast and reliable detector simulation for high statistics physics studies and acceptance calculations. We first considered processes listed in Table 4.1, and took into account of other processes separately as a correction.

A semileptonic decay of b and c quarks produces a jet associated with a lepton. The transverse momentum of the lepton to the jet axis, P_T^{rel}, defined in Fig. 4.1 is useful to estimate the fraction of the leptons from c quarks to those from b quarks because the mass difference between the quarks causes different P_T^{rel}-distributions. We derived the f_c by fitting a sum of the P_T^{rel}-distributions for different processes to an observed P_T^{rel} distribution.

4.2 Event selection

4.2.1 Muon selection

Muon candidates were selected by requiring the presence of a CTC track associated with a stub in muon chambers. The muon stub was reconstructed with the central muon chambers (CMU and CMP) and the muon momentum was derived from curvature of the CTC track. The energy deposit in calorimeter towers which a muon candidate traverses was required to correspond to a minimum ionizing particle. Muon identification was performed by applying the following cuts.

Track Quality Cuts

In order to make sure that the track of a muon candidate comes from a hard collision interaction and is not misreconstructed in the CTC, a set of track quality cuts is imposed as follows:

- A track must be reconstructed in 3 dimension.
- $|D_0| < 0.5$ cm.

- $|Z_{event} - Z_0| < 5.0$ cm
- number of hits in CTC chamber > 50

where D_0 is a radial distance of the track at the closest point to the beam axis, or the impact parameter. Z_{event} is the z position of the event vertex and Z_0 is the z position of the track at the closest point to the beam axis. The efficiency of these requirements for charged tracks should be quite high when the charged tracks are produced from $\bar{p}p$ collisions. Fig. 4.2, Fig. 4.3 and Fig. 4.4 show distributions of these parameters for muon candidates in J/ψ events and for non-interacting-punchthrough candidates in a jet sample. The J/ψ events are required to have two muon candidates and the invariant mass of them in a region $3 < M_{\mu\mu} < 3.15$ GeV. The jet sample consists of the events triggered by the pre-scaled jet trigger with an E_T threshold of 20 GeV. Since this sample is dominated by ordinary QCD jet events, most of the muon candidates in the sample can be considered as fake muons. To select non-interacting-punchthrough candidates, they are required to have a stub only in the CMU chamber even in the fiducial area of CMU and CMP chambers. We note that the position matching cuts described below are already imposed on the events shown in Fig. 4.2, Fig. 4.3 and Fig. 4.4. The cut values employed are indicated by arrows in the figures.

Position matching cuts

Muon selection requires that both CMU and CMP chambers have stubs. The $\Delta X(CMU)$ and $\Delta X(CMP)$ are defined position differences in $(r - \phi)$ space between the reconstructed CTC track and the reconstructed stub in CMU and CMP chamber. Fiducial cuts are applied to avoid cracks between the CMU chambers and regions uncovered with the CMP chambers. This fiducial area is well covered by the calorimeters. Figures 4.5 and 4.6 show $\Delta X(CMU)$ and $\Delta X(CMP)$ distributions for muon candidates in the J/ψ events and for non-interacting-punchthrough candidates in the jet sample.

The $\Delta X(CMU)$ and $\Delta X(CMP)$ distributions for muons can be explained by effects of multiple scattering in the material which muons traverse before reaching in the each muon chamber. Until muons reach the CMU chamber, they pass through material of 66 radiation lengths. The rms spread of ϕ will be

$$\Delta\phi_{\text{multiple scattering}}(CMU)\ [\text{rad}] = \frac{0.128}{P_T\ [\text{GeV/c}]}. \tag{4.4}$$

Since there is 60 cm steel (34 radiation lengths) between CMU and CMP chambers, the rms spread of ϕ in the CMP will be

$$\Delta\phi_{\text{multiple scattering}}(CMP)\ [\text{rad}] = \frac{0.158}{P_T\ [\text{GeV/c}]}. \tag{4.5}$$

Since the distance from the solenoid coil to the CMU is 203 cm, one standard deviation of ΔX at CMU is 5 cm at $P_T = 3$ GeV/c. For a typical distance of the CMP chambers from the coil of 400 cm (the distance change by the location of the CMP), one standard deviation of ΔX at the CMP is 12 cm at $P_T = 3$ GeV/c.

The $\chi^2(CMU)$ and $\chi^2(CMP)$ are a fit χ^2 of CTC and chambers track. The $\chi^2(CMU)$ and $\chi^2(CMP)$ distribution for muon candidates in the J/ψ events and the jet sample are shown in Figs. 4.7 and 4.8.

The position matching cuts used are:

- $\Delta X(CMU) < 7$ cm
- $\Delta X(CMP) < 30$ cm.
- $\chi^2(CMU) < 10$
- $\chi^2(CMP) < 30$

Minimum ionization cuts

The EM_{muon} and HAD_{muon} are the electromagnetic and hadronic energy of the calorimeter tower which a muon traverses. Figures 4.9 and 4.10 show the EM_{muon} and HAD_{muon} distribution for muons in the J/ψ events and the jet sample. The energy deposit by muons in the EM and HAD calorimeters was measured in a test beam to be $\mathrm{EM_{muon}} \sim$ 0.3 GeV and $\mathrm{HAD_{muon}} \sim$ 2 GeV, respectively. The distribution of the sum of the EM_{muon} and HAD_{muon} is shown in Fig. 4.11. We use the following minimum ionizing particle cuts:

- $EM_{muon} < 2$ GeV
- $HAD_{muon} < 4$ GeV
- $EM_{muon} + HAD_{muon} > 0.1$ GeV

Summary of the central muon selection

The central muon selection is summarized as follows:

1. Track quality cuts.

2. Position matching cuts.

3. Minimum ionization cuts.

4. $P_T > 3$ GeV/c

The cut values used in the selection are listed in Table 4.7. However, the muons selected by the above cuts, still include fake muons, which are mainly due to non-interacting-punchthrough of charged hadrons and decay-in-flight muons from hadrons. We will estimate the fraction of fake muons in Section 5.1.

4.2.2 Electron selection

Electron candidates are selected primarily by requiring the large energy deposit in the EM calorimeter and the presence of an associated track in the CTC.

Energy fraction cut

A ratio of hadronic energy to electromagnetic energy in a calorimeter cluster, HAD/EM, is used to discriminate charged hadrons, which have more energy deposited in the hadronic calorimeter than electrons. Figure 4.12 shows the HAD/EM distributions for $J/\psi \to ee$ events and the jet sample. The $J/\psi \to ee$ events are required to have two electron candidates and the invariant mass of them in a region $2.8 < M_{ee} < 3.2$ GeV. The jet sample consists of the events triggered by the pre-scaled jet trigger with an E_T threshold of 20 GeV. The EM clusters in the jet sample are used as fake electrons. We require that

- $HAD/EM < 0.04$

E/P

One of the sources which mimic the electron signature in the detector is a charged hadron overlapping with photon. This overlap of a photon and a charged hadron looks like an EM cluster associated with the track of the charged hadron. A ratio of transverse energy to transverse momentum, E/P, is used to distinguish an electron from this overlap. The E/P is not necessarily one in the overlap due to its accidental characteristics, while in the case of electrons it should be around one. Therefore, the E/P is useful to reject this type of backgrounds. Figure 4.13 shows the E/P distributions for electrons in $J/\psi \to ee$ events and for the EM clusters in the jet sample. We require that

- $E/P < 1.4$

Lateral shower shape, $\chi^2_{\mathbf{strip}}$, cut

Comparing a shower shape along the beam (Z) direction measured with the CES strip to that obtained from test beam electrons, one can check the consistency of the measured shower shape with the expected electron shower shape. We minimize the following function by varying two parameters, Z, the Z position of the center of a shower, and E, the electron energy.

$$\chi^2(Z,E) = \sum_{i-5}^{i+5} \frac{(E_i^{meas} - E \times q_i^{pred}(Z))^2}{\sigma_i^2(Z)}, \tag{4.6}$$

where E_i^{meas} is the measured energy on the strip channel i, q_i^{pred} is a normalized energy distribution on channel i predicted from 50 GeV/c test beam electrons, and σ_i denotes an energy fluctuation of a single-channel response. In the summation of i, neighboring eleven channels are examined corresponding to about 15 cm which is sufficient to contain a full electron shower. Based on 10 GeV/c electron test beam data [46], the response fluctuation σ_i for each channel is parameterized as

$$\sigma_i^2(Z) = 0.026^2 + 0.096^2 q_i^{pred}(Z). \tag{4.7}$$

Using the shower center position obtained above, χ^2_{strip} is defined as

$$\chi^2_{\text{strip}} = \frac{1}{4}\left(\frac{E_{CEM}}{10}\right)^{0.747} \sum_{i-5}^{i+5} \frac{(q_i^{meas} - q_i^{pred}(Z_{CES}))^2}{\sigma_i^2(Z_{CES})}, \tag{4.8}$$

where E_{CEM} is the energy measured by the central EM calorimeter, q_i^{meas} is the measured value of the normalized energy distribution on channel i. The energy obtained by minimizing function (4.6) is not used because the energy resolution of the strip chamber measurement is worse (20% and 30% for 50 GeV/c and 10 GeV/c electrons, respectively) than the one measured by the CEM. An energy dependence factor of $E^{0.747}$ is introduced to compensate for the energy dependence of the χ^2_{strip}, which comes from the fact that the CES is located at a fixed depth in the CEM and it therefore see a different age of the longitudinal shower development depending on the electron energy. The parameter was determined from test beam electrons of various energies from 10 GeV to 200 GeV. Figure 4.14 shows χ^2_{strip} distributions for the electrons from $J/\psi \to ee$ and for the EM cluster in the jet sample.

The χ^2_{strip} is useful to discriminate an EM cluster of an electron against an EM cluster in which more than one particle are contained. Photons from $\pi^0 \to \gamma\gamma$ decays have a minimum opening distance d (cm) at a radius R (cm) from the beam line that is related to the π^0 momentum as

$$d = \frac{2RM_\pi}{P_T(\pi)} \qquad\qquad (P_T \text{ in GeV/c}) \tag{4.9}$$

where $P_T(\pi)$ (GeV/c) and $M_\pi = 0.135$ GeV/c^2) are the transverse momentum and the mass of π^0. At the CES ($R = 184$ cm), we have $d \sim 50/P_T$. Since number of strips for calculation of $\chi_s^2 trip$ is eleven (~ 15 cm), two photons with $d < 7.5$ cm and two photons from π^0 of $P_T(\pi)$ above ~ 7 GeV/c will be contained in a same window for calculation of $\chi_s^2 trip$. The resulting χ^2_{strip} will have a large value due to the existence of an additional shower peak in the cluster. A typical CES shower has $\sim 99\%$ of the total CES energy in ± 2.5 cm around the shower center. Therefore the presence of two photons will be removed by a large value of χ^2_{strip} up to $P_T(\pi^0) \sim 20$ GeV/c. Above this momentum, the two photons get closer to make it difficult to recognize two showers in the CES.

This variable is also used to discriminate electrons against charged pions which interact and deposit mast of the energy in the CEM, since their shower shapes are different from those for electrons. We require that

- $\chi^2_{\text{strip}} < 10$

Position matching cut

The position difference in $(r - \phi)$ plane between the position measured by the CES and that of a CTC track extrapolated to the CES, $\Delta X(CES)$, is defined by

$$\Delta X(CES) = R\Delta\phi \qquad (R = 184 \text{ cm}) \tag{4.10}$$

where $\Delta\phi$ is the azimuthal difference between the ϕ position which is optimized in a similar way as in the χ^2_{strip} estimation and that of the extrapolated CTC-track at the CES, and R is the radius of the CES from the beam line. Figure 4.15 shows $\Delta X(CES)$

distributions for electrons from the $J/\psi \to ee$ events and for EM clusters of the jet sample.

The position difference along the beam direction, $\Delta Z(CES)$, is estimated from a position measurement in the CES and the extrapolated CTC-track position at the CES. The distributions of $\Delta Z(CES)$ for electrons from the $J/\psi \to ee$ events and for EM clusters of the jet sample are shown in Fig. 4.16. We require that

- $\Delta X(CES) < 1.5$ cm
- $\Delta Z(CES) < 2.5$ cm

This position matching is useful to remove the overlap of a photon with a charged hadron where an accidentally associated track of the charged hadron is expected to have a worse position matching than an electron track. In Section 5.1, we will use EM cluster events which have a worse position matching as overlap events of a photon with a charged hadron.

Lateral shower sharing, L_{shr}, cut

This variable, L_{shr}, describes a lateral sharing of the EM shower energy among the CEM towers in a cluster and is defined by

$$L_{\mathrm{shr}} = 0.14 \sum_i \frac{E_i^{meas} - E_i^{pred}}{\sqrt{(\Delta E)^2 + (\Delta E_i^{pred})^2}}, \tag{4.11}$$

where E_i^{meas} is the energy deposit in tower i, E_i^{pred} is the energy expected in tower i, ΔE is the uncertainty in the energy measurement with the CEM, and ΔE_i^{pred} is the error associated with E_i^{pred}. The sum runs over the two towers in η direction adjacent to the seed tower. The expected tower energy E_i^{pred} was determined from test beam electron data as a function of the seed tower energy and the direction of the CES shower center relative to the event vertex. The error ΔE_i^{pred} was determined by propagating an error of the shower center measurement in the CES to the predicted energy E_i^{pred}. Figure 4.17

shows L_{shr} distributions for the electrons from $J/\psi \to ee$ events and for the EM clusters in the jet sample. We require that

- $L_{\mathrm{shr}} < 0.2$

Photon conversion removal

Electrons from photon conversions have to be removed from the electron sample. A photon conversion can occur before entering the VTX, in the beam pipe material, in the layers of SVX and in the inner wall of the VTX. This type of photon conversions is called an inner photon conversion. Also a photon can convert after exiting the VTX, in the outer wall of the VTX and in the inner wall of the CTC. This is called an outer photon conversion. In both cases, the electron tracks can be detected in the CTC, but the outer photon conversions do not leave tracks in the VTX. A ratio of the number of VTX wire hits to the number of wires which are expected to be fired by a particle, VTX hit occupancy, can be used to discriminate charged particles from neutral particles in the VTX. Electrons from outer photon conversions have a low value of the VTX hit occupancy. In order to remove electrons from inner photon conversions, an additional oppositely charged CTC track is searched and the minimum invariant mass of them, $m_{e-track}$, is examined. Two electrons from inner photon conversions are expected to have a low mass. An electron which fails one of the following requirements is removed as a conversion electron,

- VTX hit occupancy > 0.5

- $m_{e-track} > 0.2$ GeV.

Figure 4.18 shows a distribution of conversion points for the conversion electron sample in terms of the radial distance from beam line, R. We see peaks around the SVX layers $R \sim$ 3-7 cm, the VTX inner wall $R \sim 22$ cm and the CTC inner wall $R \sim 28$ cm.

Summary of the central electron selection

The requirements for the central electrons are summarized as follows:

1. Energy fraction cut.

2. E/P cut.

3. Lateral shower shape cut.

4. Position matching cut.

5. Lateral shower sharing cut.

6. Photon conversion removal.

7. $E_T > 5$ GeV

The cut values used in the selection are listed in Table 4.7. The selected electrons still have fake electrons which are mainly charged hadrons, overlapped events with photon, and photon conversion events. We will study the fraction of fake electrons using real data and Monte Carlo data in Section 5.1.

4.2.3 $b\bar{b}$ event selection

Event vertex cut

In order to ensure that events are well covered by the tracking and calorimeter detectors, the Z position of event vertex, Z_{event}, required to be near the nominal event vertex. Figure 4.19 shows the Z position of event vertex for the J/ψ events as an example. We require that

- $Z_{\text{vertex}} < 60$ cm

in order to accept 90% of hard collision events.

$\not{E}_T$ cut

Missing transverse energy, $\not{E}_T$, is defined by the minus of the sum of transverse energies deposited in calorimeter towers over the range $|\eta| < 3.6$,

$$\not{E}_T \equiv | - \sum_{tower} \vec{E_T}^{tower} |, \tag{4.12}$$

where $\vec{E_T}^{tower}$ is a two-dimensional vector pointing from the event vertex to the tower centroid. For a tower included in the sum, its energy must be above a given threshold. The threshold is 0.1 GeV in the central electromagnetic and hadronic calorimeters, 0.3 GeV in the plug electromagnetic calorimeters, 0.5 GeV in the plug hadronic and forward electromagnetic calorimeters, and 0.8 GeV in the forward hadronic calorimeters. If there is no large-E_T neutrino nor jets escaping the detector, the distribution of the energy deposit in the transverse plane view in the calorimeters is expected to be balanced within jet energy resolutions and the $\not{E}_T$ is small.

Since W + fake lepton events followed by $W \to l\nu$ decays cause background to the $e\mu$ events, the $\not{E}_T$ is required not to be large. The following $\not{E}_T$ cut is imposed:

- $\not{E}_T < 15$ GeV

P_T^{rel} and jet axis distance cuts

For the $e\mu$ events we required each lepton to accompany one jet. The jet axis was determined by an algorithm shown in Fig. 4.21. We first pick up a seed track closes to the lepton within a cone size of $\Delta R = 0.8$. Tracks near the seed track are added to form a jet. The cone size in defining the jet is $\Delta R = 0.8$. The jet axis is calculated from momenta of tracks in the jet without the lepton momentum. Since each jet must come from different quarks, a distance between the jets axes associated to an electron and a muon in η-ϕ plane, $\Delta R(Jet(e) - Jet(\mu))$, was defined and was required to be greater than 0.1.

The distributions of the transverse momentum of the lepton relative to the jet axis,

P_T^{rel}, for $b\bar{b}$ and $c\bar{c}$ Monte Carlo events are shown in Figs. 4.22 and 4.23. The P_T^{rel} is related to a mass of the parent particle. A requirement of the P_T^{rel} to be greater than 1.5 GeV/c reduces the $c\bar{c}$ background. This P_T^{rel} cut is also expected to be effective in removing Process 2 and 3. The jet axis distance and P_T^{rel} cut employed are:

- $\Delta R(Jet(e) - Jet(\mu)) > 0.1$
- $P_T^{rel}(\mu) > 1.5$ GeV/c
- $P_T^{rel}(e) > 1.5$ GeV/c.

Azimuthal opening angle cut

A cut on an azimuthal opening angle $\Delta\phi(e\mu)$ between an electron and a muon removes cascade-decay events in which b ($\bar{b}$) quarks decay semileptonically to c ($\bar{c}$) quarks and successively the c ($\bar{c}$) quarks decay semileptonically,

$$\begin{array}{ll} b\ (\bar{b}) \rightarrow & c + \mu^- + X\ (\bar{c} + \mu^+ + X) \\ & \hookrightarrow e^+ + X\ (e^- + X) \end{array} \quad \text{or} \quad \begin{array}{ll} b\ (\bar{b}) \rightarrow & c + e^- + X\ (\bar{c} + e^+ + X) \\ & \hookrightarrow \mu^+ + X\ (\mu^- + X) \end{array}$$

Figures 4.24 (a) and (b) show Monte Carlo $\Delta\phi(e\mu)$ distributions for these semileptonic cascade decays and for $b\bar{b}$ production followed by Process 1$\sim$ 3. Semileptonic cascade decays events are distributed around $\Delta\phi(e\mu) \sim 0$. On the contrary, $b\bar{b}$ direct production events are distributed not at small $\Delta\phi(e\mu)$ but at large $\Delta\phi(e\mu)$. The $b\bar{b}$ production events from gluon splitting are distributed at small $\Delta\phi(e\mu)$ but their contribution to the $b\bar{b}$ events are small. The $\Delta\phi(e\mu)$ distribution for real data is shown in Fig. 4.24 (c). There is a bump at small $\Delta\phi(e\mu)$ for OS events but not for LS. This indicates the bump originates from the semileptonic cascade decays because they produce OS events. In order to remove the semileptonic cascade decay events, the following azimuthal opening angle cut is adopted:

- $\Delta\phi(e\mu) > 45°$

Muon ID	muon candidate has a CMU stub and a CMP stub CMU and CMP fiducial cut $EM < 2.0$ GeV $HAD < 4.0$ GeV $EM + HAD > 0.1$ GeV $P_T > 3$ GeV/c number of hits in CTC > 50 impact parameter < 0.5 cm $\mid Z_{\text{track}} - Z_{\text{vertex}} \mid < 5$ cm $\Delta X(\text{CMU}) < 10$ cm $\chi^2(\text{CTC/CMU}) < 10$ $\Delta X(\text{CMP}) < 30$ cm $\chi^2(\text{CTC/CMP}) < 30$
Electron ID	$E_T > 5$ GeV $HAD/EM < 0.04$ $L_{share} < 0.2$ number of 3D tracks $= 1$ $P_T > 3$ GeV/c $E_T/P_T < 1.4$ $\chi^2(CES) < 10$ $\Delta X(CES) < 1.5$ cm $\Delta Z(CES) < 2.5$ cm VTX hit fraction > 0.5 invariant mass of an e and each track > 0.2 GeV/c^2
$\mid Z_{\text{vertex}} \mid < 60$ cm $\not{E}_T < 15$ GeV each lepton accompanies one jet $P_T^{rel}(e) > 1.5$ GeV/c $P_T^{rel}(\mu) > 1.5$ GeV/c $\Delta R(Jet(e) - Jet(\mu)) > 0.1$ $\Delta\phi(e\mu) > 45^\circ$	

Table 4.7: Summary of the $e\mu$ event selection.

4.2.4 Results of event selection

After all the selection cut, we found 1710 opposite-sign and 861 like-sign $e\mu$ events in RUN-Ia data corresponding to 20 pb^{-1}. In the like-sign events, 420 $e^+\mu^+$ and 441$e^-\mu^-$ events were found. In the opposite-sign events, 850 $e^+\mu^-$ and 860 $e^-\mu^+$ events were found.

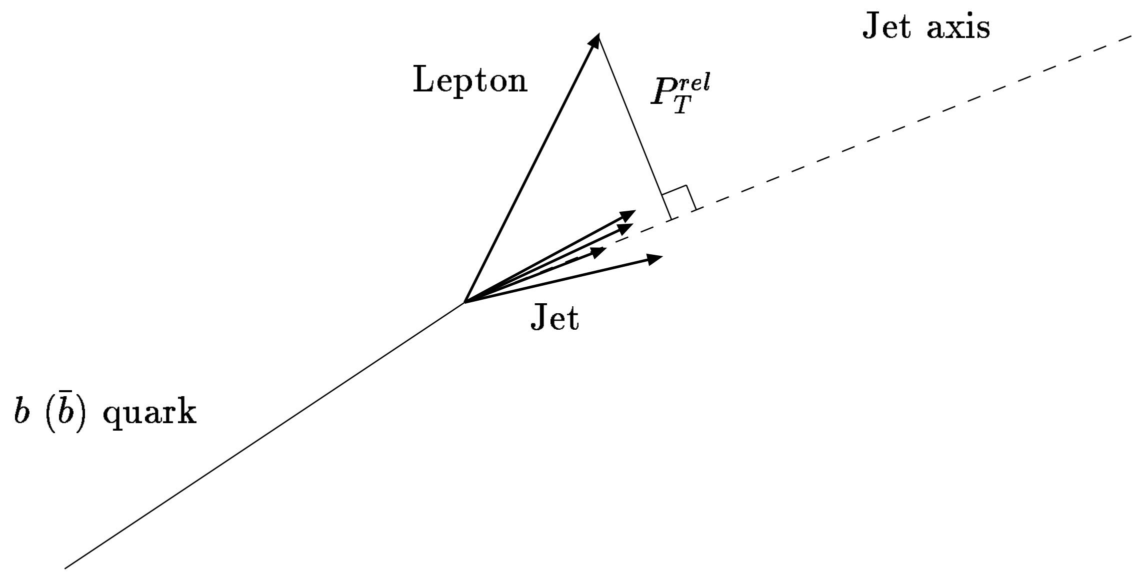

Figure 4.1: Definition of P_T^{rel}.

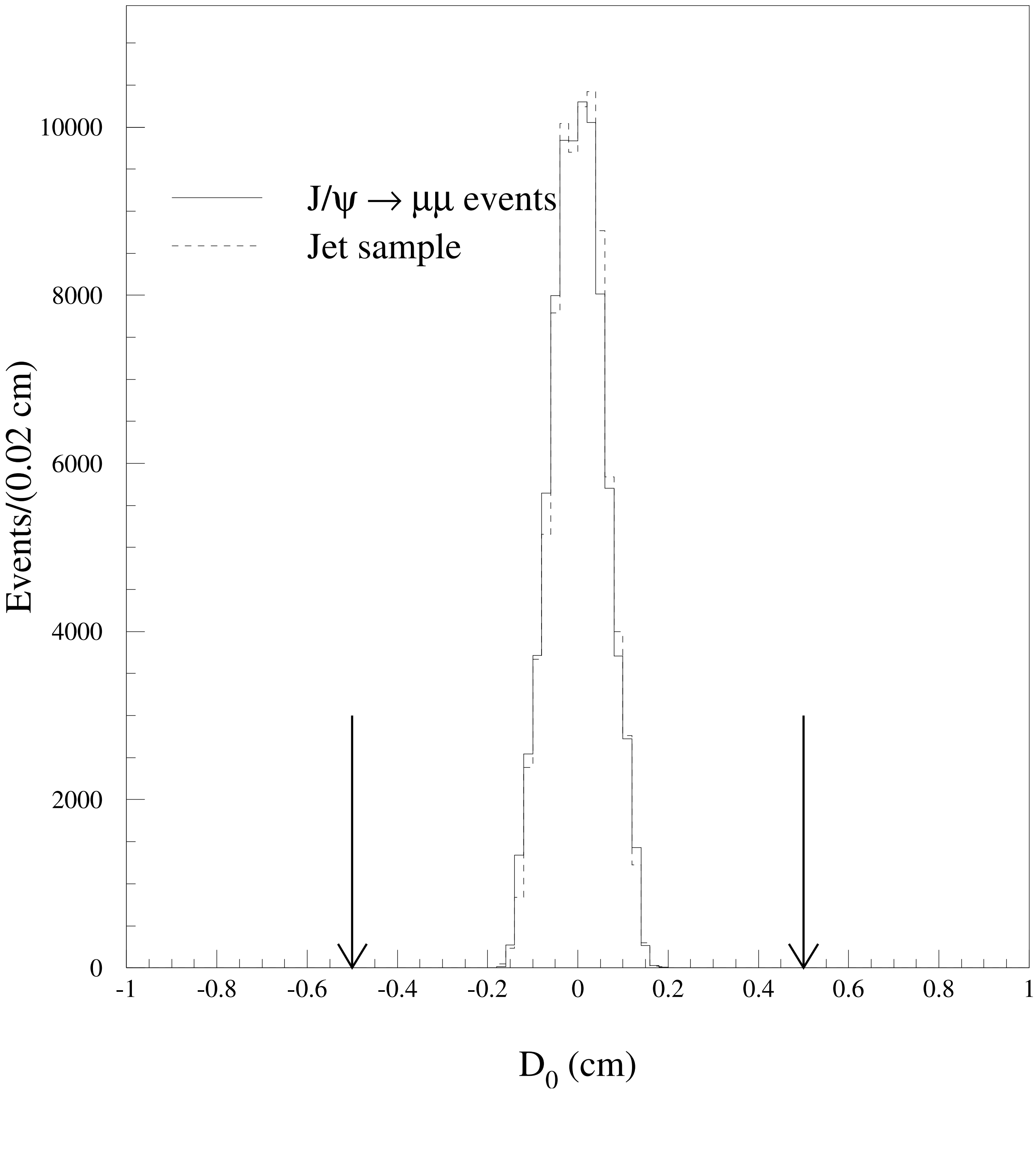

Figure 4.2: The distribution of the impact parameter of muon tracks; D_0. The distributions for muon candidates in the $J/\psi \rightarrow \mu\mu$ events (solid) and those for the jet sample (dotted) are shown.

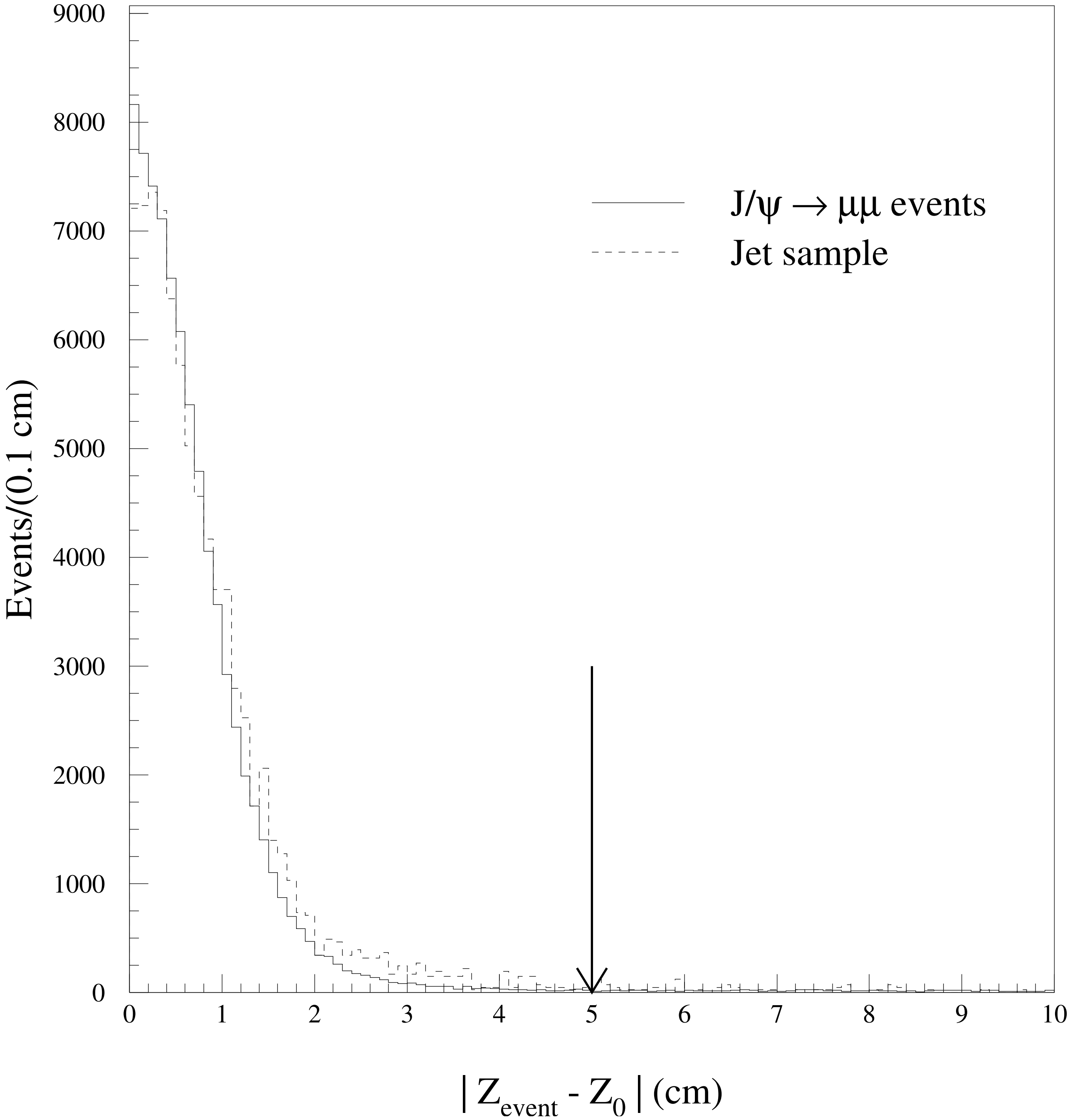

Figure 4.3: The distribution of the difference between the z position of event vertex and the z position of muon tracks; $|Z_{event} - Z_0|$. The distributions for muon candidates in the $J/\psi \to \mu\mu$ events (solid) and those for the jet sample (dotted) are shown.

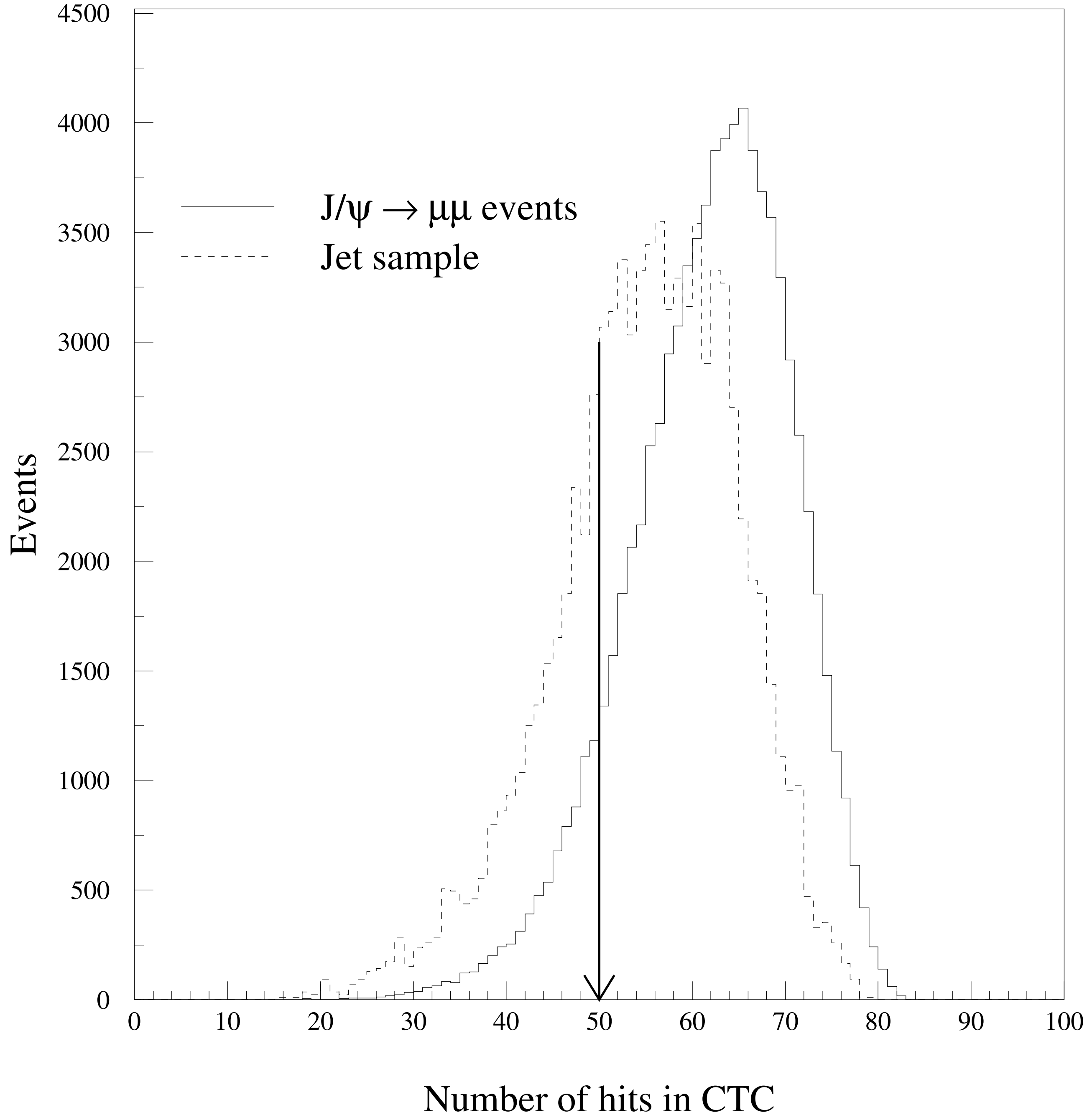

Figure 4.4: The distribution of the number of hits in CTC chamber. The distributions for muon candidates in the $J/\psi \rightarrow \mu\mu$ events (solid) and those for the jet sample (dotted) are shown.

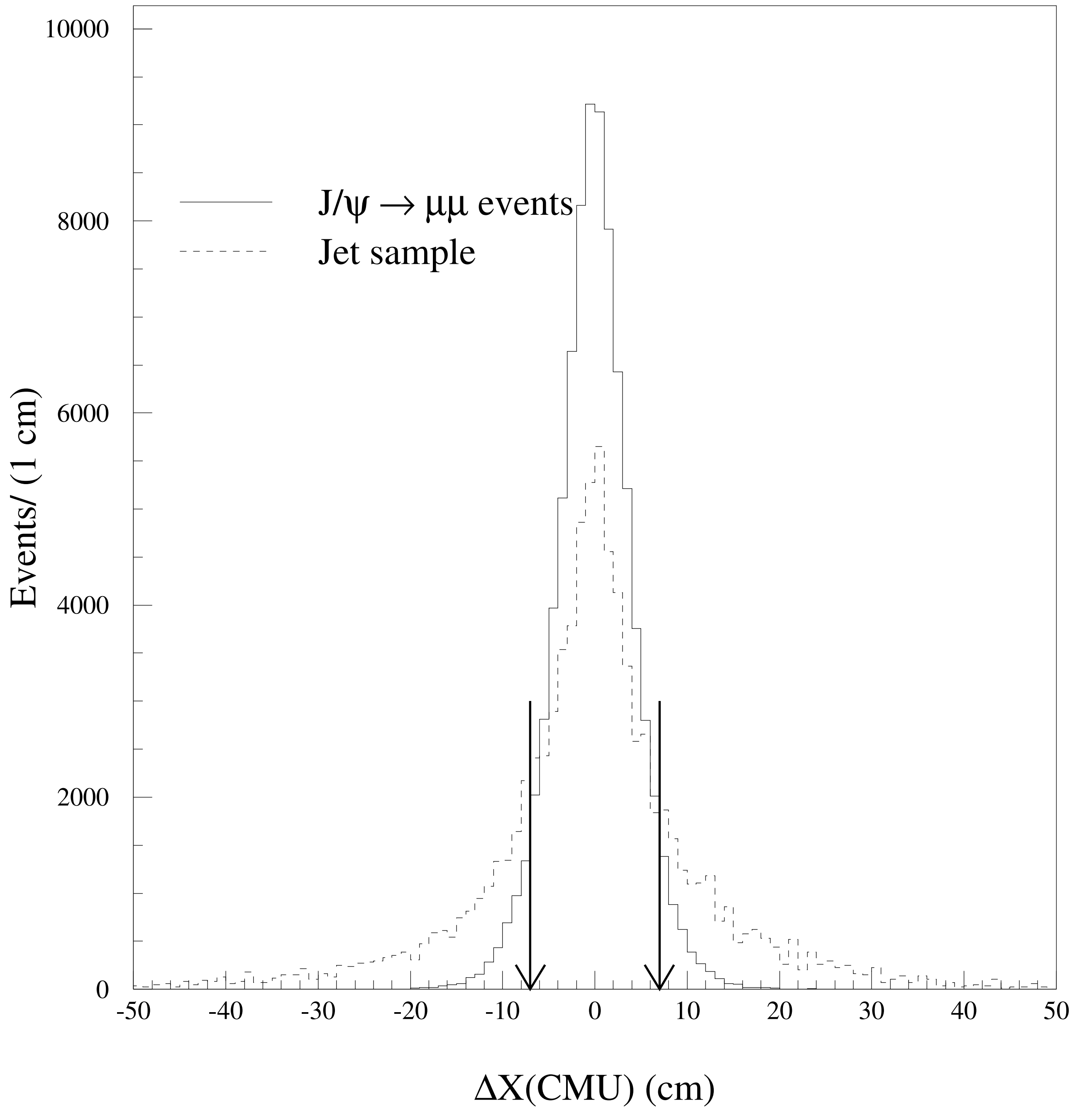

Figure 4.5: The distribution of position matching between a stub in the CMU chambers and an extrapolated CTC track to the CMU;$\Delta X(CMU)$. The distributions for muon candidates in the $J/\psi \rightarrow \mu\mu$ events (solid) and for the jet sample (dotted) are shown.

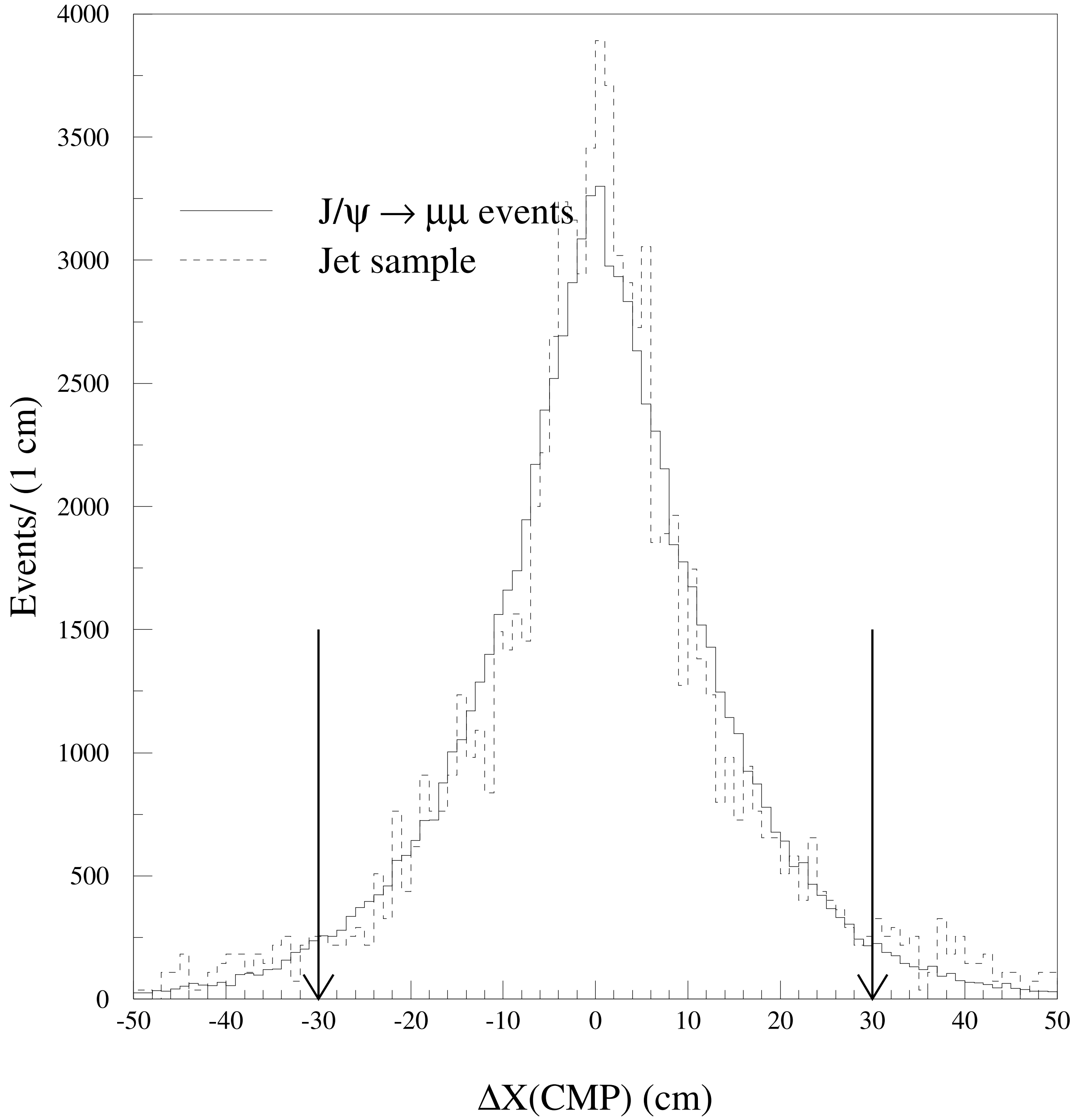

Figure 4.6: The distribution of position matching between a stub in the CMP chambers and an extrapolated CTC track to the CMP;$\Delta X(CMP)$. The distributions for muon candidates in the $J/\psi \to \mu\mu$ events (solid) and for the jet sample (dotted) are shown.

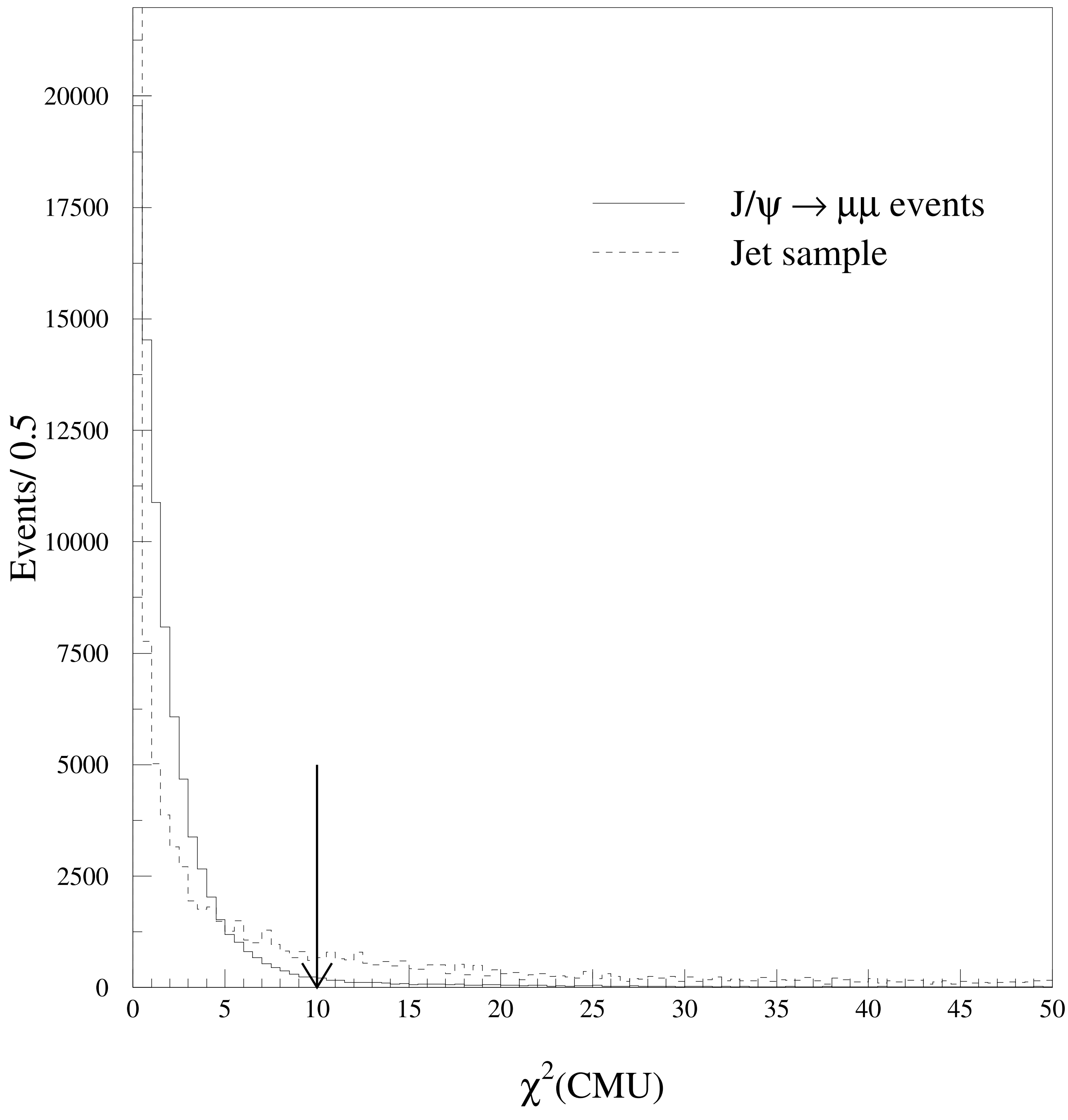

Figure 4.7: The distribution of χ^2 for position matching between a stub in the CMU chambers and an extrapolated CTC track to the CMU;$\chi^2(CMU)$. The distributions for muon candidates in the $J/\psi \to \mu\mu$ events (solid) and for the jet sample (dotted) are shown.

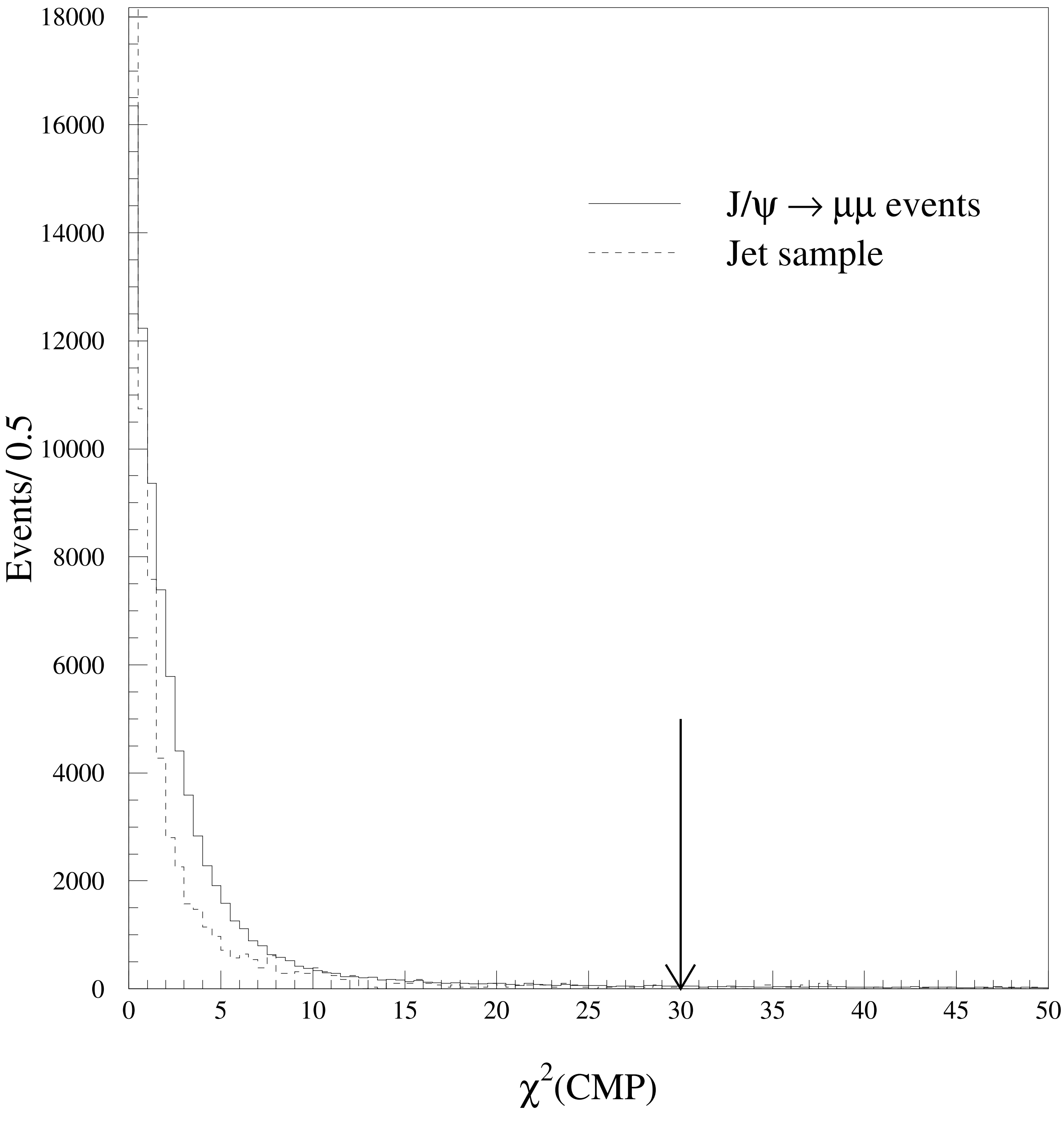

Figure 4.8: The distribution of χ^2 for position matching between a stub in the CMP chambers and an extrapolated CTC track to the CMP;$\chi^2(CMP)$. The distributions for muon candidates in the $J/\psi \rightarrow \mu\mu$ events (solid) and for the jet sample (dotted) are shown.

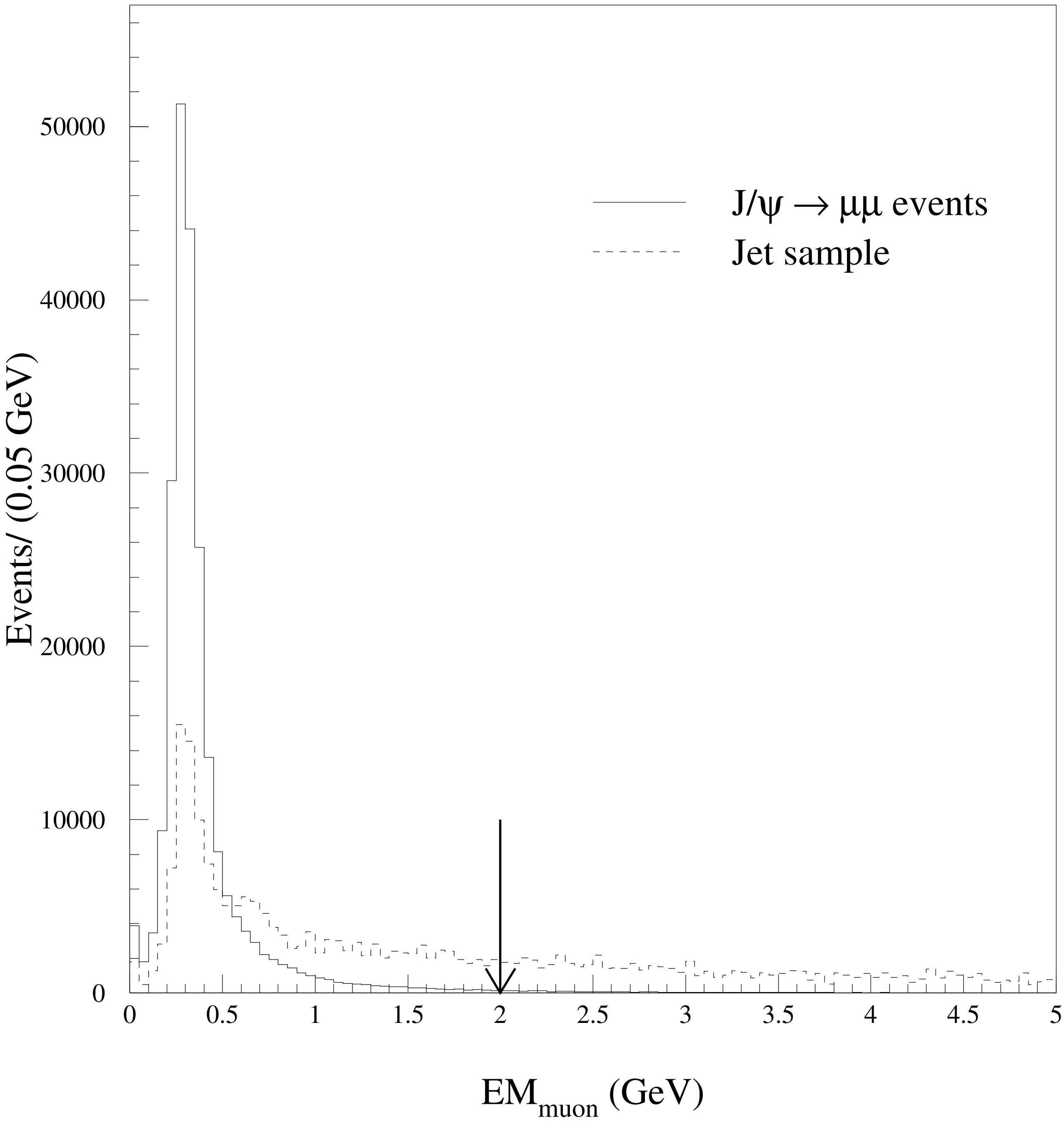

Figure 4.9: The energy of electromagnetic tower which a muon traverses. The distributions from the $J/\psi \to \mu\mu$ (solid) and the jet sample (dotted) are shown.

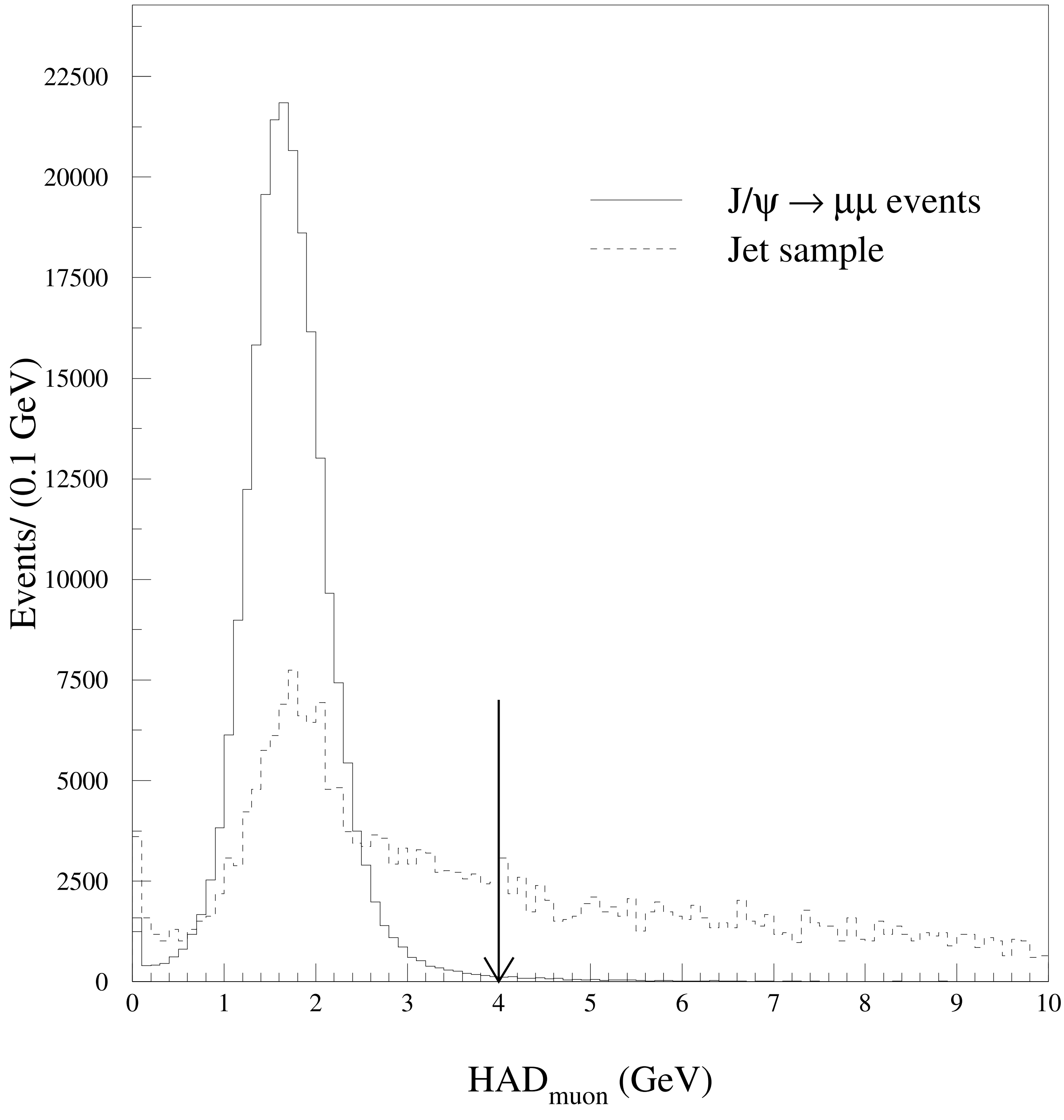

Figure 4.10: The energy of hadronic tower which a muon traverses. The distributions from the $J/\psi \rightarrow \mu\mu$ (solid) and the jet sample (dotted) are shown.

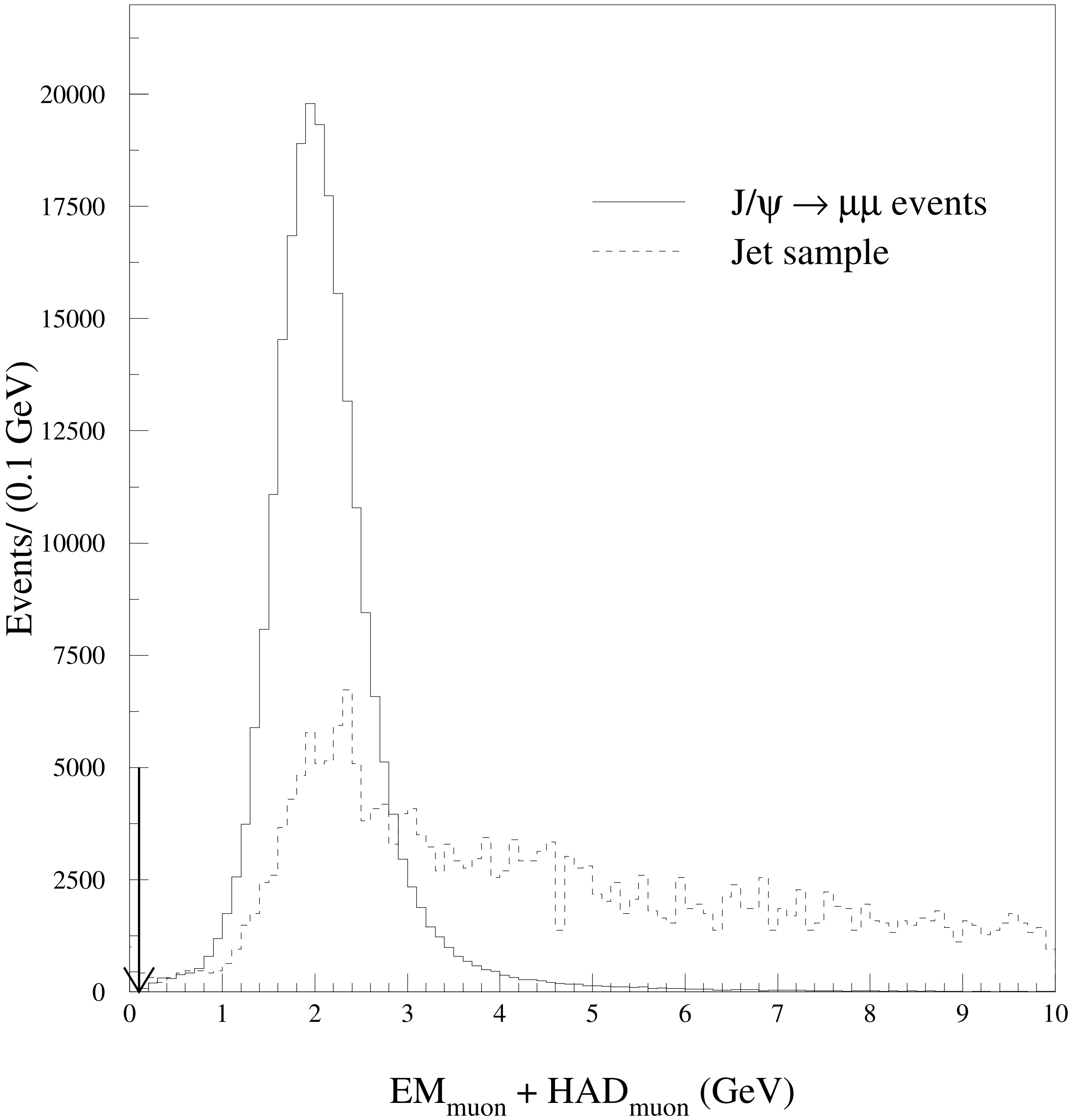

Figure 4.11: The energy sum of electromagnetic and hadronic tower which a muon traverses. The distributions from the $J/\psi \rightarrow \mu\mu$ (solid) and the jet sample (dotted) are shown.

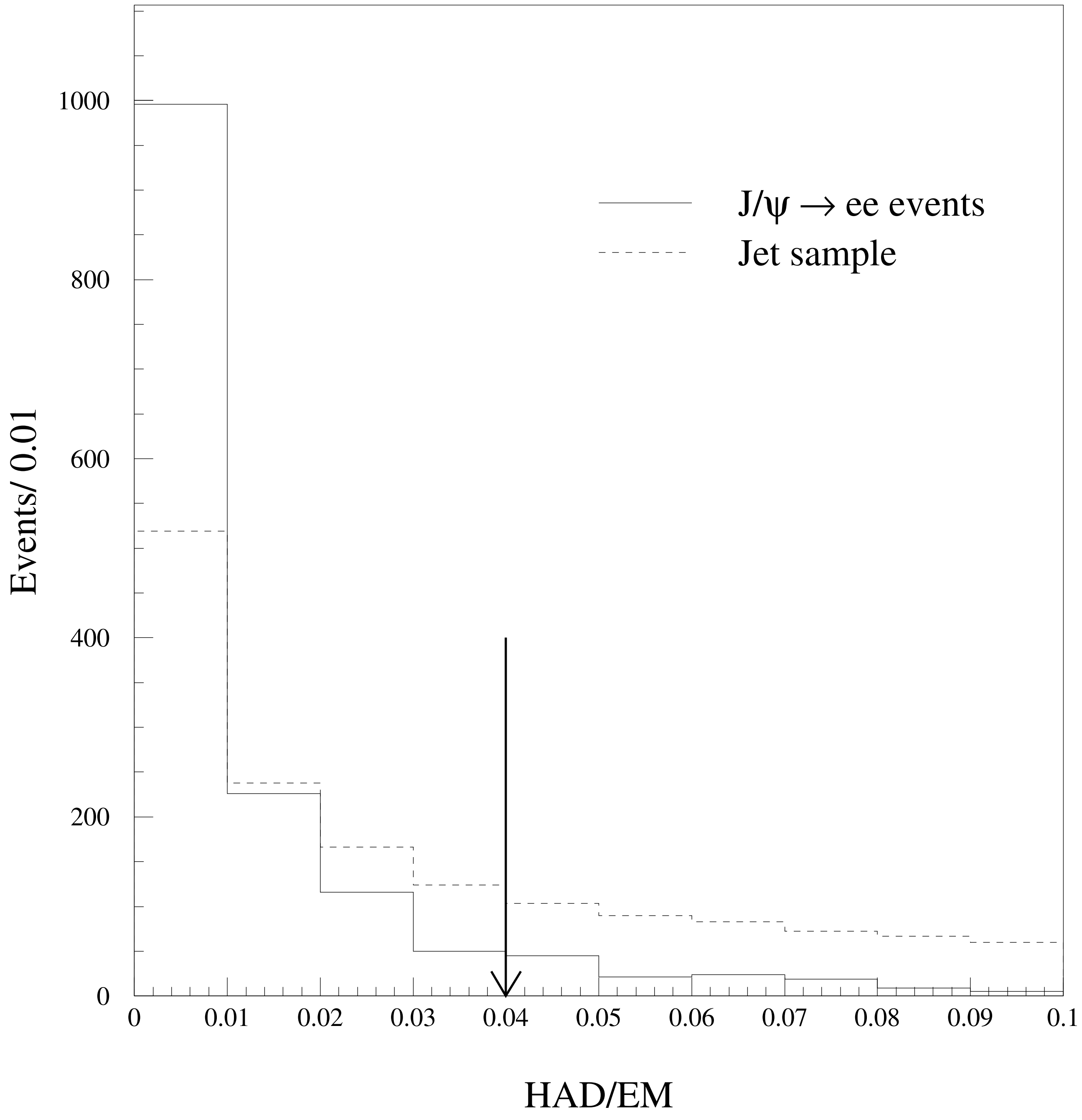

Figure 4.12: The HAD/EM distributions for central electrons in the $J/\psi \rightarrow ee$ (solid) and the jet sample (dotted).

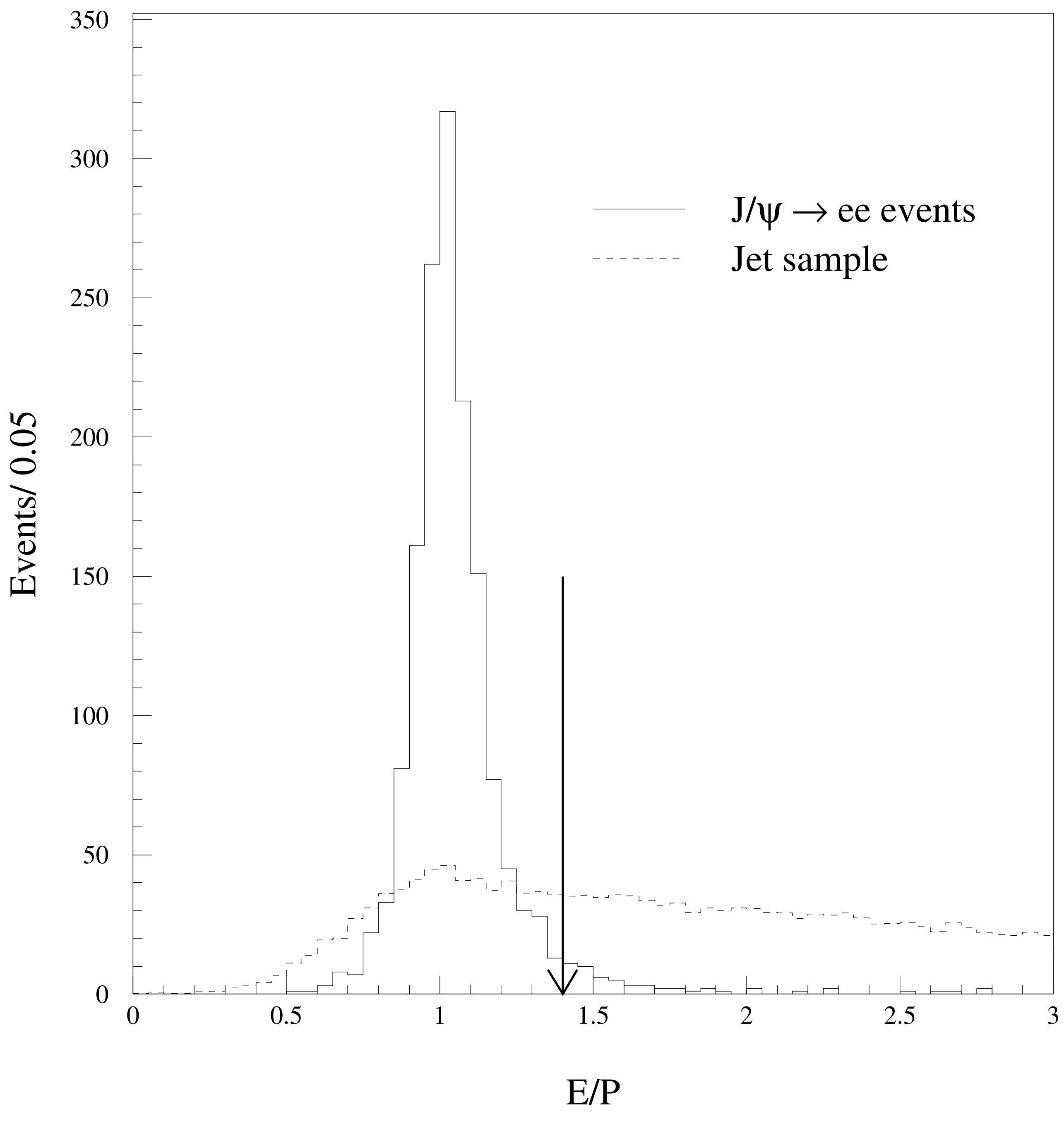

Figure 4.13: The E/P distributions for central electrons in the $J/\psi \rightarrow ee$ (solid) and the jet sample (dotted).

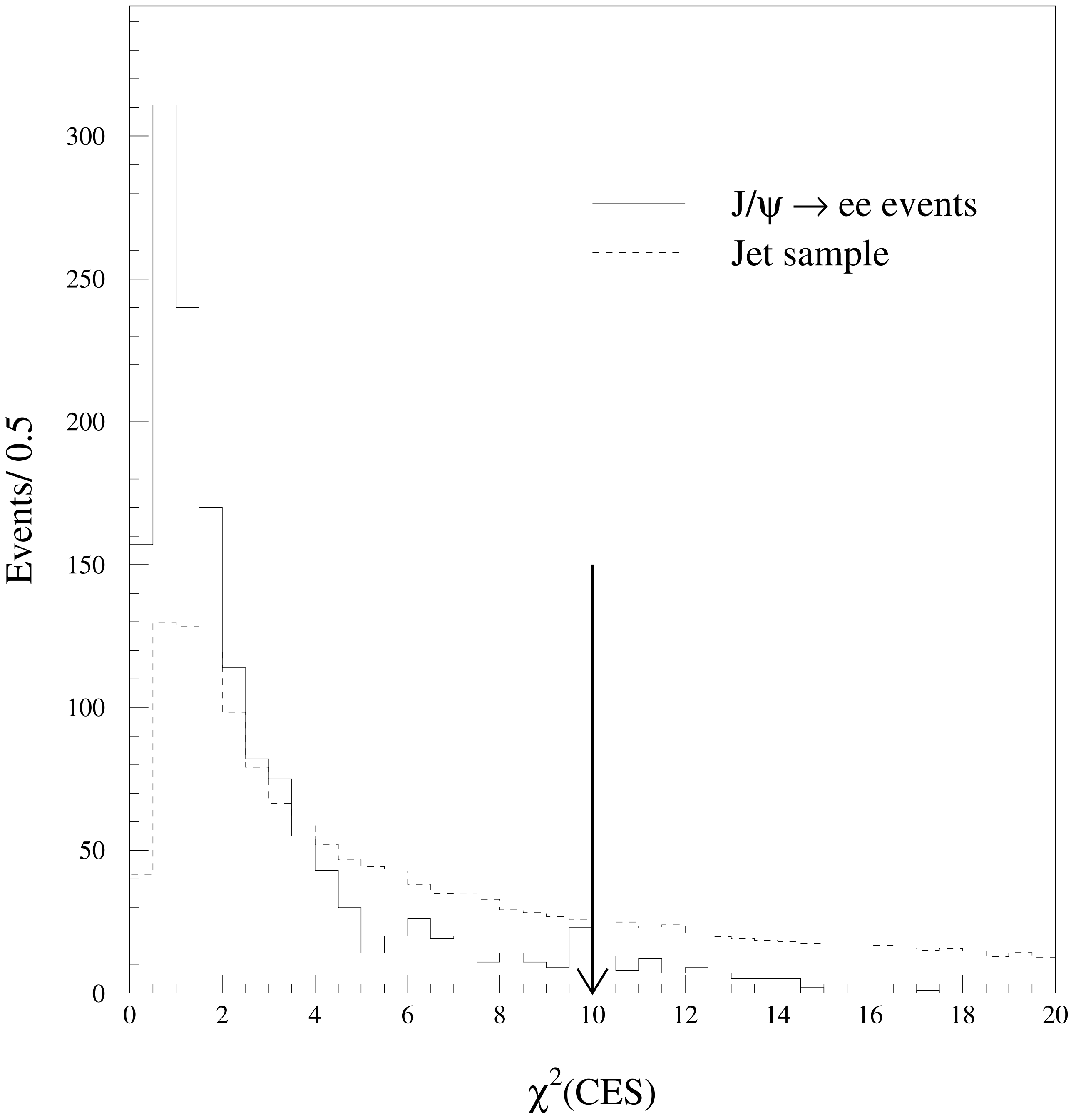

Figure 4.14: The lateral shower shape, $\chi^2_{\mathtt{strip}}$, distributions for electrons in the $J/\psi \to ee$ events (solid) and for EM clusters of the jet sample (dotted).

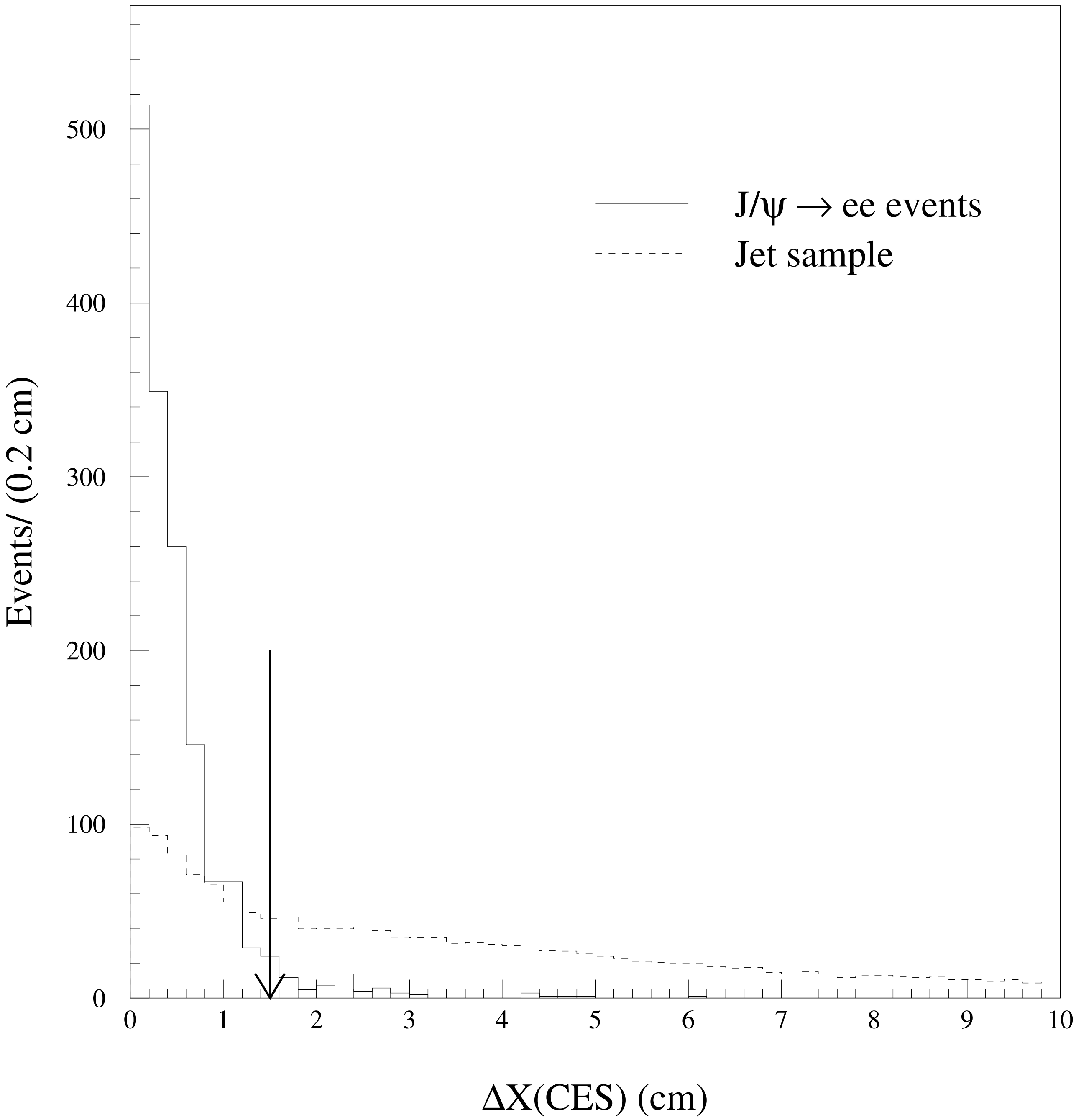

Figure 4.15: The position difference in $(r-\phi)$ plane between the position measured in the CES and that of a track extrapolated to the CES, $\Delta X(CES)$. The distributions for electrons in the $J/\psi \to ee$ events (solid) and for EM clusters of the jet sample (dotted).

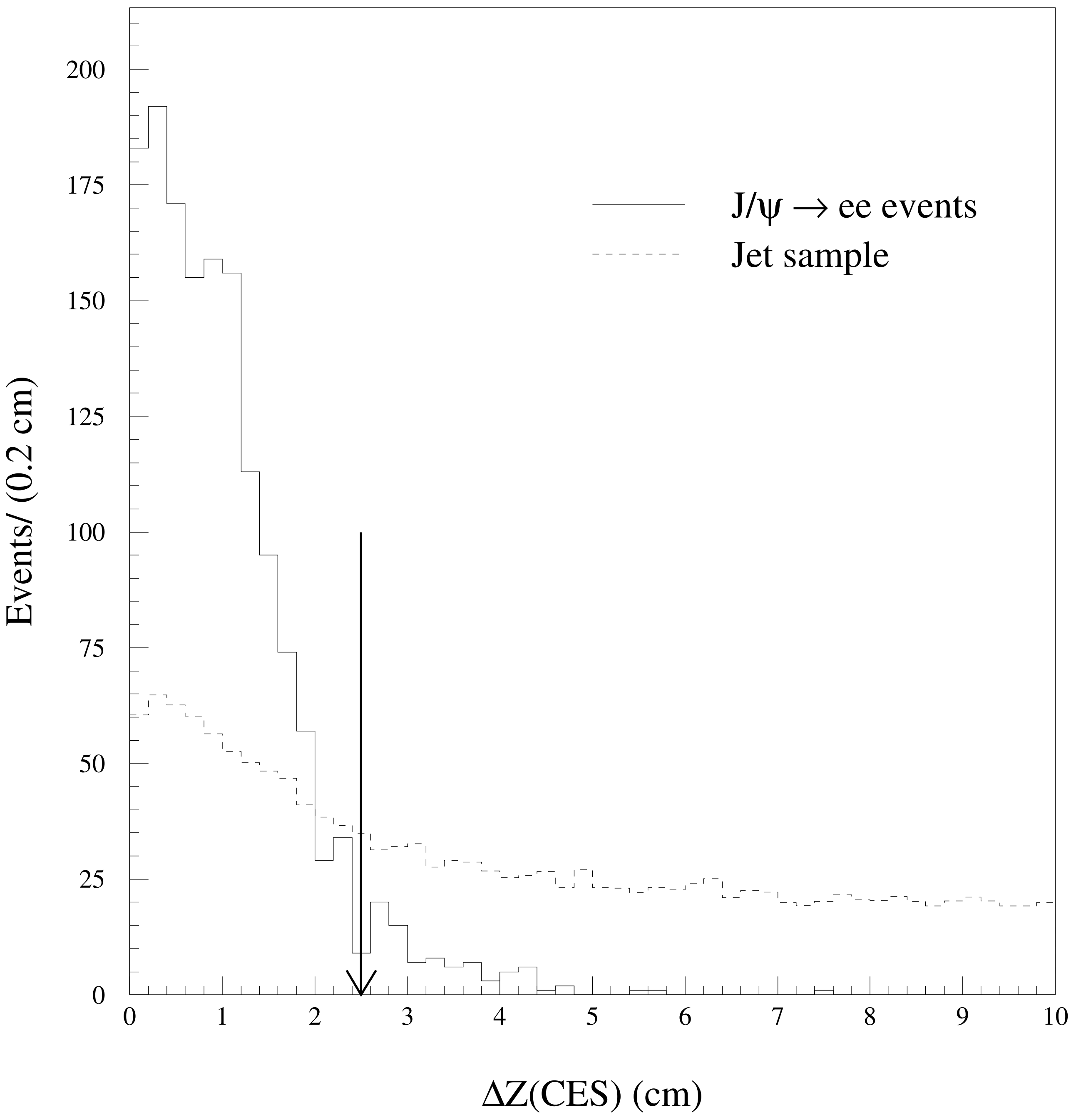

Figure 4.16: The position difference along the beam direction between the Z position measured in the CES and that of a track extrapolated to the CES, $\Delta Z(CES)$. The distributions for electrons in the $J/\psi \to ee$ events (solid) and for EM clusters in the jet sample (dotted).

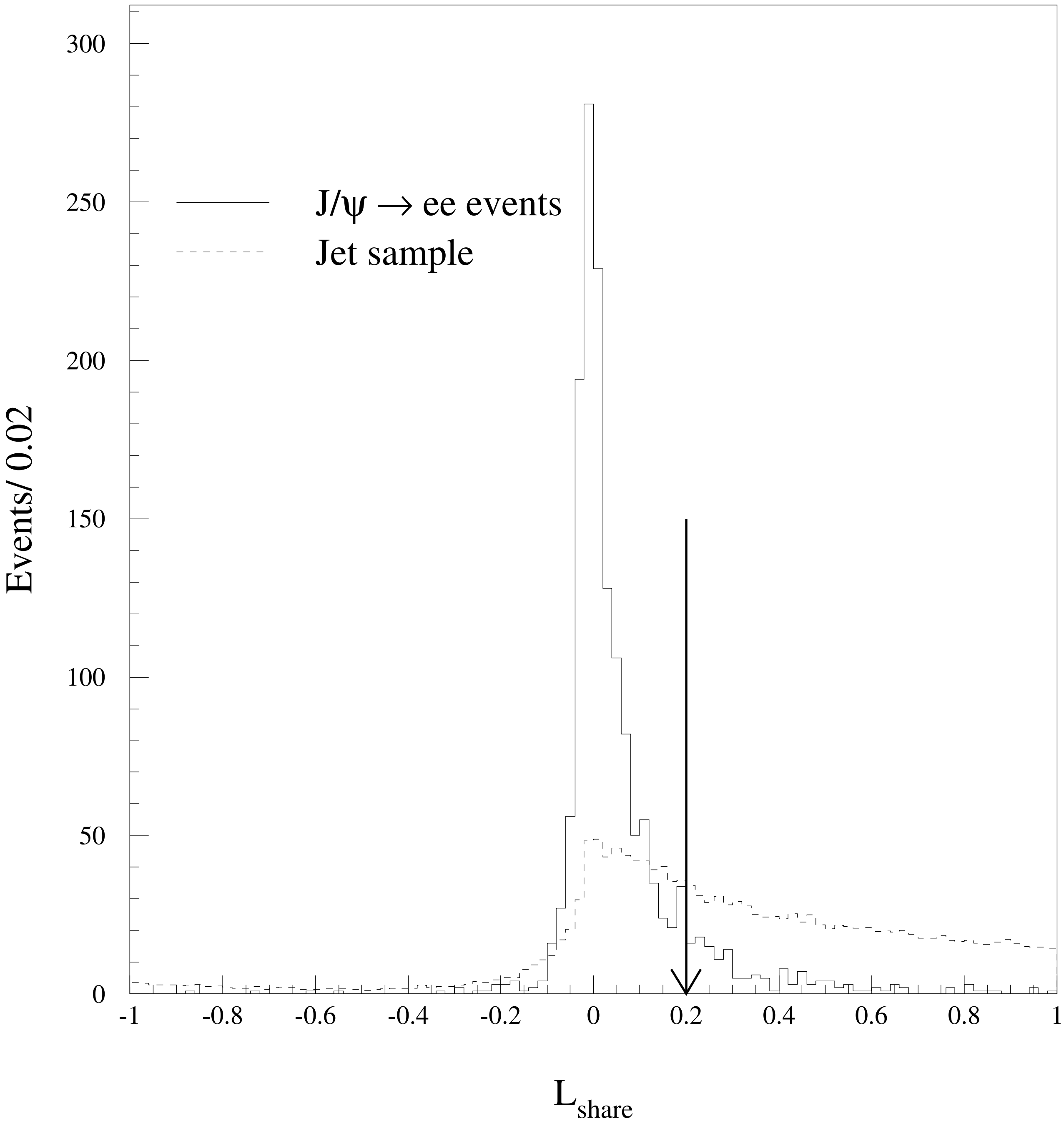

Figure 4.17: The lateral shower sharing, L_{shr}, for electrons in the $J/\psi \to ee$ (solid) and for EM clusters in the jet sample (dotted).

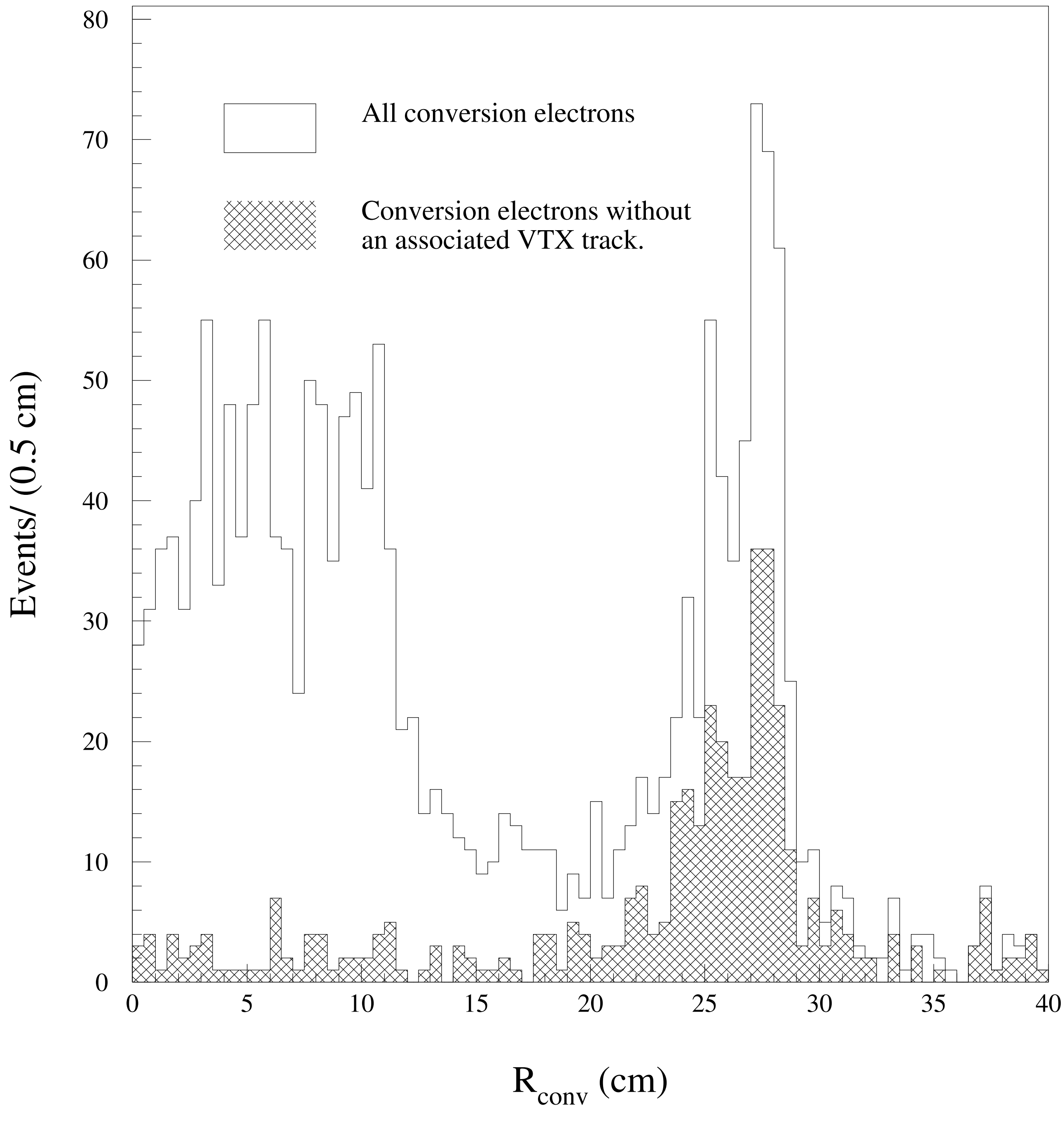

Figure 4.18: The radial distance of the conversion points from the central conversion electron sample.

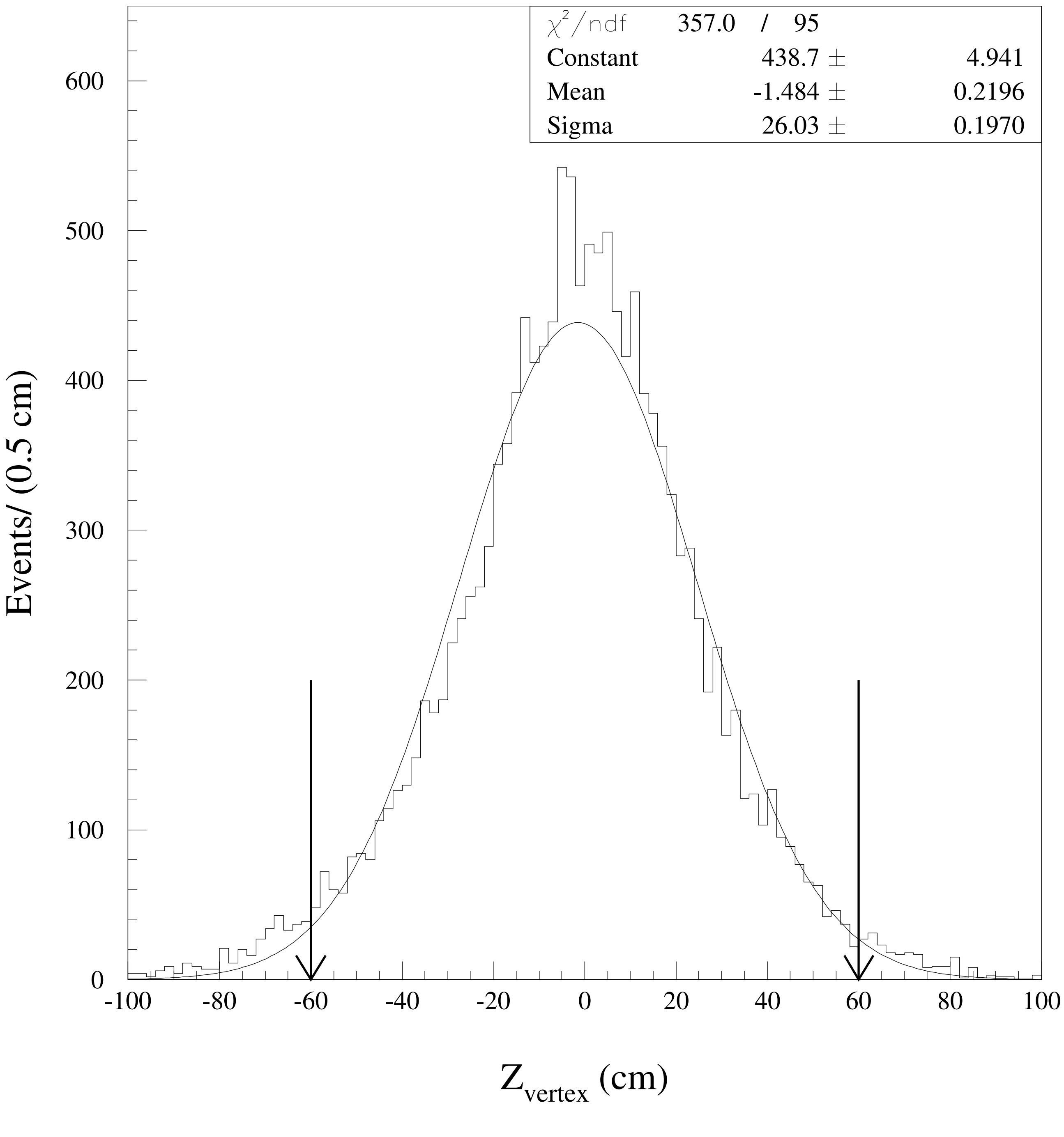

Figure 4.19: The z position of event vertex for $J/\psi \to \mu\mu$ events. The measured distribution and the fitted gaussian function are shown.

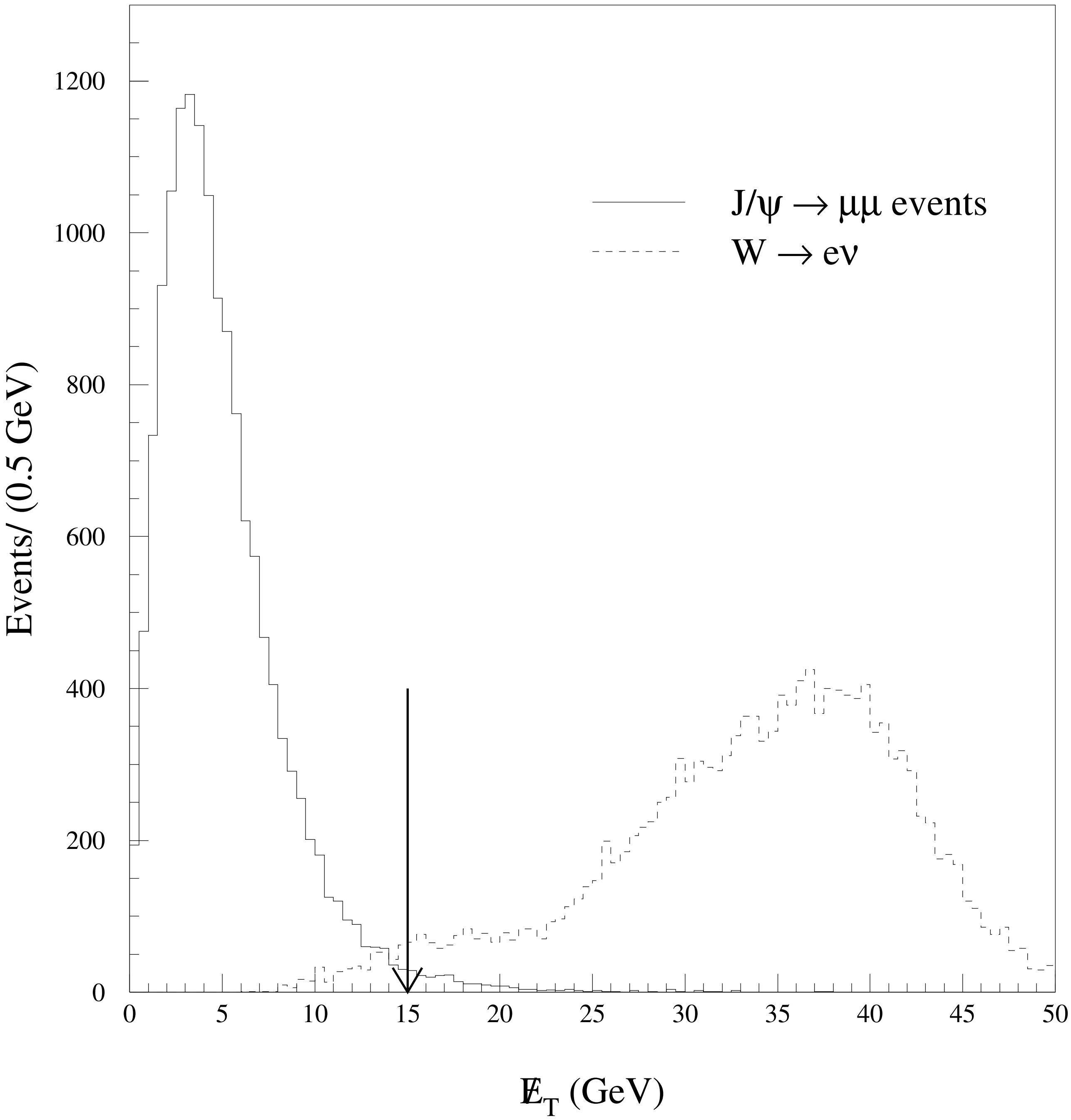

Figure 4.20: The missing transverse energy distributions for $J/\psi \to \mu\mu$ (solid) and $W \to e\nu$ events (dotted).

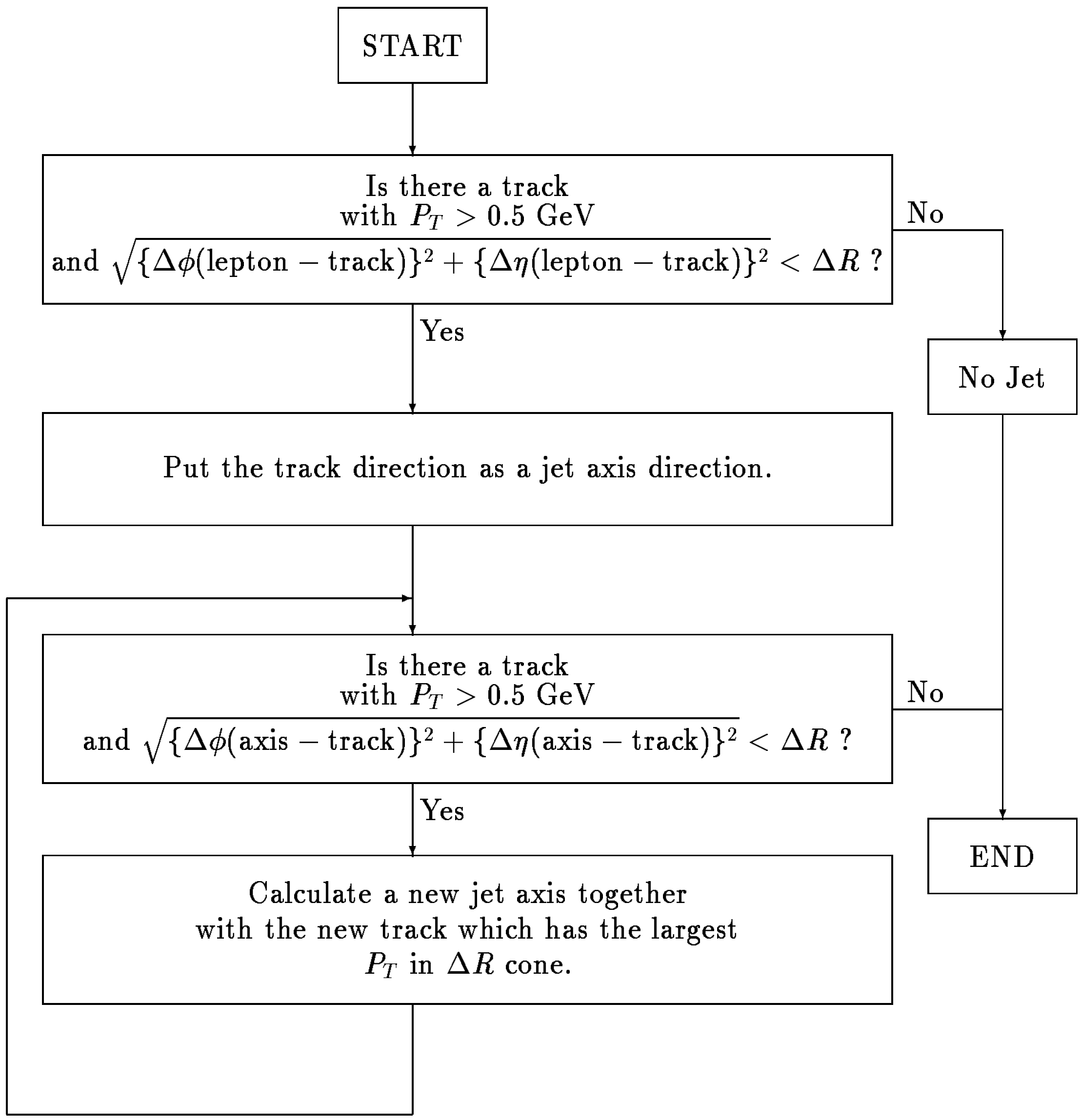

Figure 4.21: Jet axis finding algorithm.

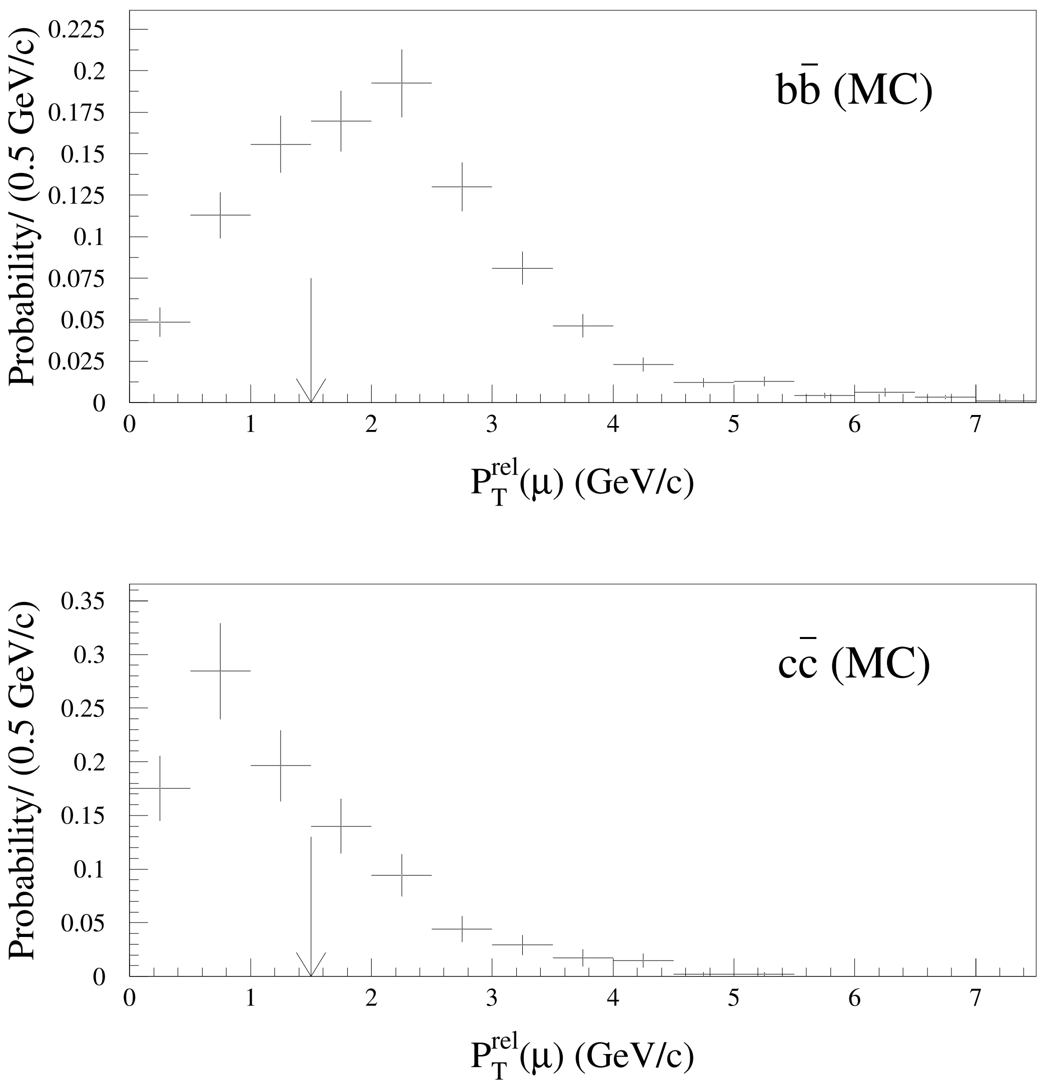

Figure 4.22: The muon P_T^{rel} distributions for $b\bar{b}$ and $c\bar{c}$ Monte Carlo events.

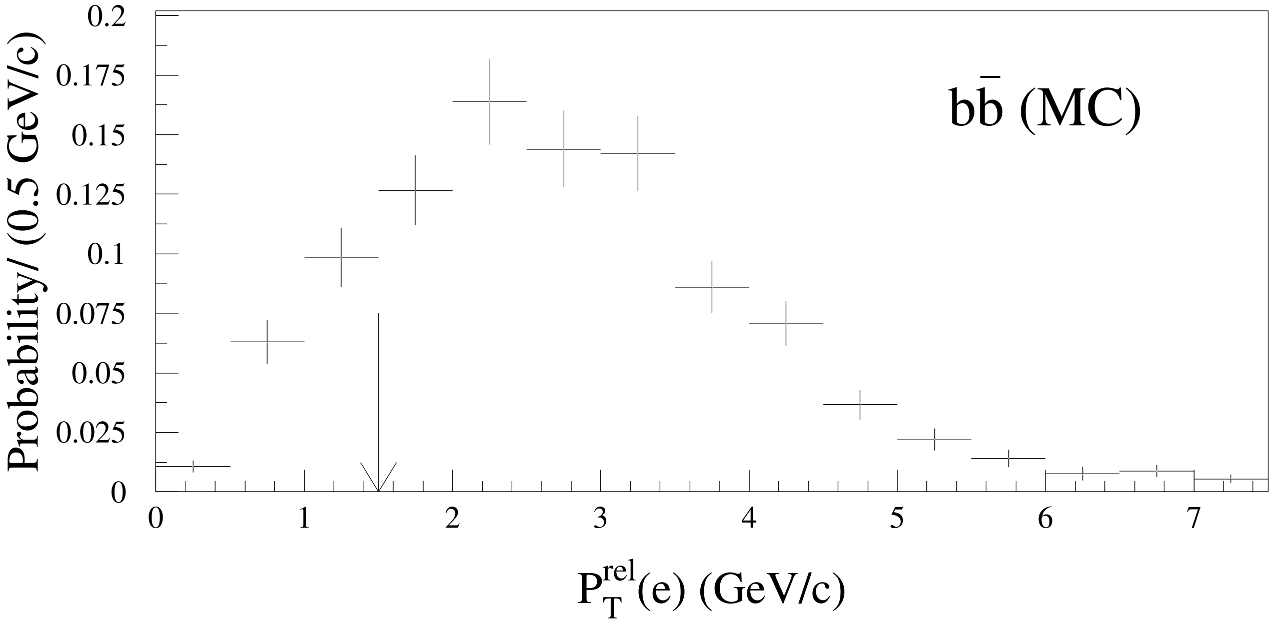

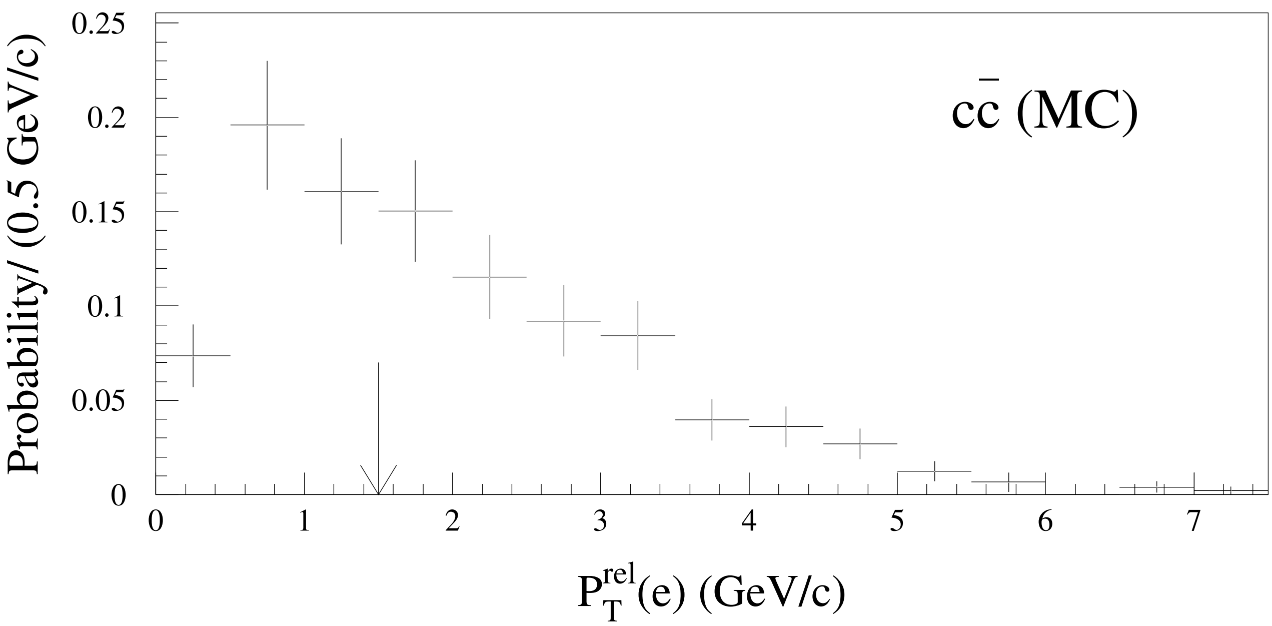

Figure 4.23: The electron P_T^{rel} distributions for $b\bar{b}$ and $c\bar{c}$ Monte Carlo events.

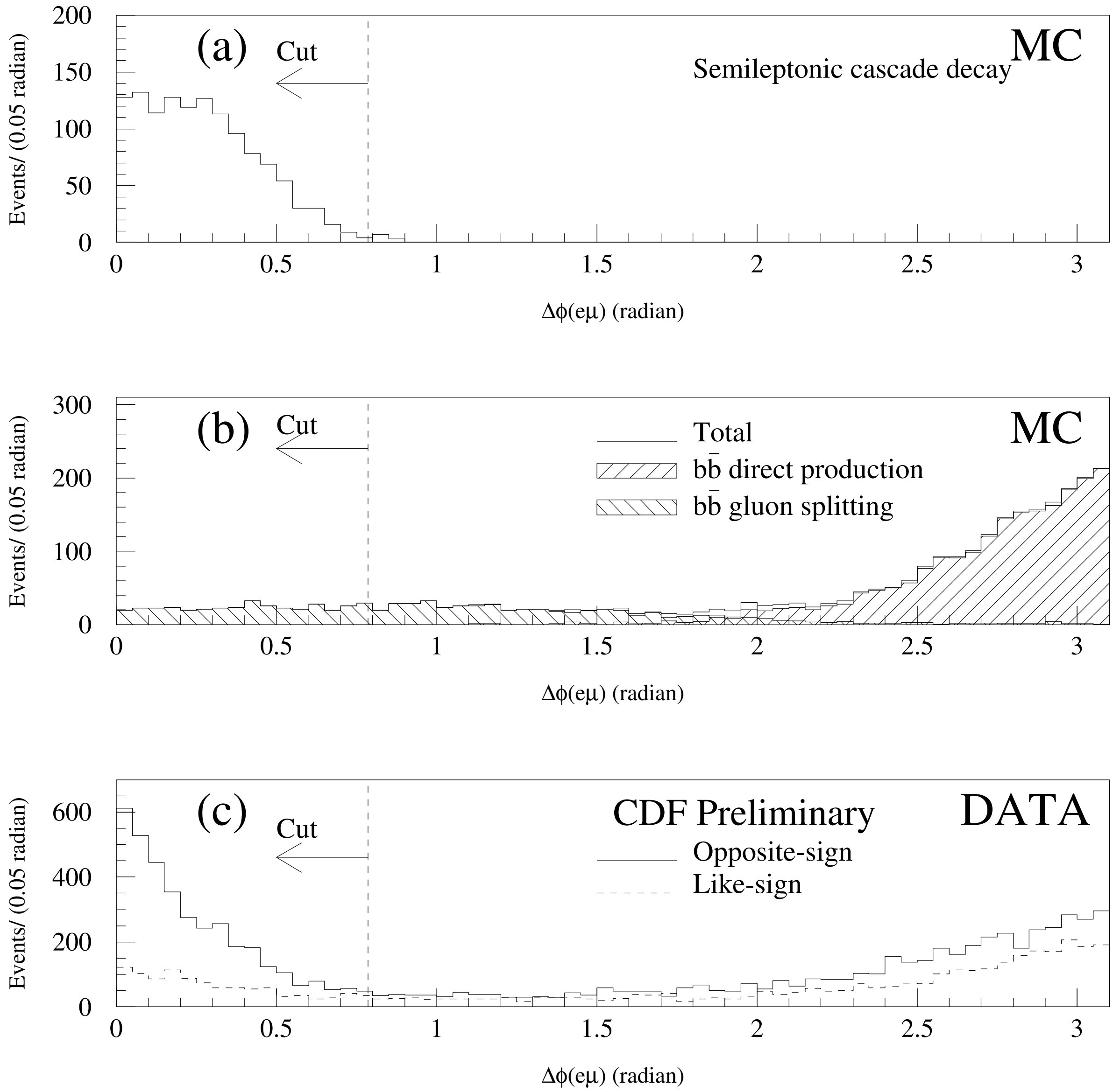

Figure 4.24: (a) Monte Carlo distribution of $\Delta\phi(e\mu)$ for semileptonic cascade decays. (b) Monte Carlo distribution of $\Delta\phi(e\mu)$ for $b\bar{b}$ direct production, $b\bar{b}$ production from gluon splitting and all (solid line). (c) The $\Delta\phi(e\mu)$ distribution for opposite-sign (solid line) and like-sign (dashed line) $e\mu$ events.

Chapter 5

Backgrounds and Systematic Uncertainties

5.1 Fraction of fake $e\mu$ events

The observed $e\mu$ events can be classified into four categories as listed in Table 5.1. In terms of them, the fake muon and the fake electron fractions of the observed $e\mu$ events are written as

$$F_\mu = \frac{(b) + (d)}{(a) + (b) + (c) + (d)} \,, \tag{5.1}$$

Muon–Electron		
Real –	Real	(a)
Fake –	Real	(b)
Real –	*Fake*	(c)
Fake –	*Fake*	(d)

Table 5.1: Four categories of the observed $e\mu$ events.

and

$$F_e = \frac{(c)+(d)}{(a)+(b)+(c)+(d)}\ , \tag{5.2}$$

respectively. The fake muon fraction of the fake electron sample is given by

$$F'_\mu = \frac{(d)}{(c)+(d)}. \tag{5.3}$$

Using the above equations, the fake $e\mu$ fraction of the observed $e\mu$ events is expressed as

$$\begin{aligned} F_{e\mu} &\equiv \frac{(b)+(c)+(d)}{(a)+(b)+(c)+(d)} \\ &= F_\mu + F_e - F_e \cdot F'_\mu. \end{aligned} \tag{5.4}$$

The fake muon and the fake electron fractions, F_μ and F_e, are estimated by the same method. We explain the method for muons as an example. Let us put N to be the number of observed $e\mu$'s which is 1710 for OS and 861 for LS. In order to estimate F_μ, we loosen the muon identification cut, and the new identification cut is called a loose muon identification cut. Then the event selection is performed again, resulting in a larger number of $e\mu$ events, N'. The N' can be written as

$$N' = N_f + N_r \tag{5.5}$$

where N_f and N_r are the numbers of fake and real muons which passed the loose identification cut. Putting P_f and P_r to be the probabilities that the fake and the real muons pass the original muon identification cut, N is expressed as

$$N = N_f \cdot P_f + N_r \cdot P_r. \tag{5.6}$$

Since N' and N are observed numbers, the N_f and N_r are estimated if P_f and P_r are known. Then the fake muon fraction is obtained as

$$F_\mu = \frac{N_f \cdot P_f}{N}. \tag{5.7}$$

Estimation of F'_μ is done similarly using low quality electrons as the fake electron sample.

5.1.1 Fake muon fraction

As the loose muon identification selection, we removed the requirement that muon candidates have a CMP stub and the other cut parameters were the same. Applying the $e\mu$ event selection to the data with the loose muon identification, we obtained $N'(OS) = 2122$ and $N'(LS) = 1175$. Estimation of P_f and P_r is done by using data samples different from the $e\mu$ sample.

Probability for fake muons P_f

Fake muons are considered to originate from two sources: (1) Non-interacting punchthrough (NIP) and (2) decay in flight (DIF) of hadrons. First we roughly estimate P_f before detailed analysis. We know from the previous CDF experiment [47] that the numbers of NIP and DIF particles are almost the same at the CMU chambers. The number of NIP particles at the CMP is almost zero due to hadron absorption in the steel walls between the CMU and the CMP chambers. And the efficiency of the CMP chambers for DIF muons is $\simeq 100\%$ for $P_T > 3$ GeV/c. Therefore $P_f \simeq \frac{(\mathrm{NIP} + \mathrm{DIF})_{\text{at CMP}}}{(\mathrm{NIP} + \mathrm{DIF})_{\text{at CMU}}}$ is expected to be $\simeq \frac{0+1}{1+1} = 0.5$.

To be more quantitative, the probability, P_f, was estimated in two different ways. Firstly, it was estimated from minimum-bias data corresponding to 18 pb^{-1} in RUN Ia. We assumed there was no real muon in the minimum bias data. We found 63 and 125 tracks which passed the muon identification cut and the loose one, respectively. Then we have $P_f = 63/125 = 0.504 \pm 0.045$.

Secondly, P_f was estimated by using $K_s^0 \to \pi\pi$ and $\phi \to KK$ decays in the low P_T

muon inclusive sample in JPSI STREAM 1. We reconstruct the $K_s^0 \to \pi\pi$ decay using a muon candidate track and one of oppositely charged 3D tracks, assuming that both tracks are pions. The oppositely charged 3D track which gives the $\pi\pi$ invariant mass closest to the K_s^0 mass was chosen. The secondary vertex of the two tracks was required to be more than 5 cm away from the primary vertex on r-ϕ plane. Figure 5.1 shows the invariant mass distribution. The dashed (solid) line histogram corresponds to the case where the muon candidate track passed the muon identification cut (the loose one). The P_f for pions is given by a ratio of the number of K_s^0 decays in the dashed histogram to that in the solid one. We fitted a Gaussian + cubic polynomial function to the invariant mass distribution in the region between 0.3 and 0.7 GeV/c^2. Defining a region between 0.45 and 0.55 GeV/c^2 as a K_s^0 signal region and subtracting background using the cubic polynomial function, we obtained $P_f = 0.498 \pm 0.011$ for pions.

We did a similar analysis for the $\phi \to KK$ decay. In this case, two tracks were assumed to be kaons and the secondary vertex cut was not required. The invariant mass distribution is shown in Fig. 5.2. We obtained $P_f = 0.498 \pm 0.016$ for kaons.

Assuming the K/π ratio in the sample to be 0.240 ± 0.120 [48, 49], we estimated $P_f = 0.498 \pm 0.010$ for hadrons.

The two independent methods described above using the minimum bias data and the invariant mass peaks of K_s^0 and ϕ give consistent values. We took the weighted average of them and obtained

$$P_f = 0.498 \pm 0.009 \qquad \text{for fake muons.} \tag{5.8}$$

Probability for real muons P_r

We used $J/\psi \to \mu\mu$ decays in the low P_T dimuon sample in order to estimate P_r. The invariant mass distribution for dimuons is shown in Figs. 5.3 (a) and (b). In Fig. 5.3 (a), one of the two muons passed the muon identification cut and the other muon passed the loose one. In Fig. 5.3 (b), both of the two muons passed the muon identification cut.

A Gaussian + constant function was fitted to these histograms in a region of invariant mass between 2.8 and 3.4 GeV/c^2. The probability for real muons, P_r, is given by

$$P_r = \frac{2N_b}{N_a + N_b}, \tag{5.9}$$

where N_a and N_b are the numbers of J/ψ decays in Figs. 5.3 (a) and (b) after subtracting backgrounds estimated from the constant term (See Appendix A for derivation of Eq. (5.9)). Looking at a region between 3.0 and 3.2 GeV/c^2 around the J/ψ mass, we obtained

$$P_r = 0.967 \pm 0.002 \qquad \text{for real muons.} \tag{5.10}$$

Fake muon fraction F_μ

Since we obtained N, N', P_r and P_f, we could solve Eqs. (5.5) and (5.6) for N_f, which was found 313 for OS and 271 for LS. Using Eq. (5.7), we obtained

$$F_\mu(OS) = 0.212 \pm 0.014(stat.) \pm 0.008(syst.) \tag{5.11}$$

and

$$F_\mu(LS) = 0.339 \pm 0.025(stat.) \pm 0.013(syst.), \tag{5.12}$$

where the statistical uncertainties come from N and N', and the systematic uncertainties come from P_r and P_f.

5.1.2 Fake electron fraction

We loosened the HAD/EM cut value from 0.04 to 0.1 for loose electron identification cut. The other cut parameters were left the same as those in Table 4.7. We obtained $N'(OS) = 1845$ and $N'(LS) = 969$.

Probability for fake electrons P_f

There are several sources of background which mimics electron signature in the detector. One of them is a charged pion interacting in the EM calorimeter. Most of charged pions are discriminated by the fact that the energy deposition in the hadronic calorimeter is large while that in the EM calorimeter is small. But some of charged pions interact and deposit a large part of their energy in the EM calorimeter. Since a charged pion leaves an associated track in the CTC, it looks like an electron. Another source of fake electrons is a photon with an overlapping charged track. The photon makes an energy deposition in the EM calorimeter, its track looks associated to that EM energy deposition. This also mimics the electron signature. On top of these fake electrons, there are electrons which are not related to hard collisions, such as electrons from photon conversions ($\gamma \to ee$).

In this selection, we consider two sources of fake electrons: (1) photons overlapped by charged hadrons in the EM calorimeter and (2) charged hadrons which deposited a significant amount of energy in the EM calorimeter. Photon conversions will be dealt with in the next section.

We studied photon + charged hadron overlap by removing the cut on position difference at the CES, $\Delta X(CES)$, from the electron identification, and estimated P_f for electron candidates with large $\Delta X(CES)$, most of which were considered to be the photon+ charged hadron overlap. Figure. 5.4 (a) shows the HAD/EM distribution for electron candidates with $\Delta X(CES) > 6$ cm. The probability, P_f, for a photon with an overlapping charged track to pass the electron identification cut was estimated from a ratio of the number of events in $HAD/EM < 0.04$ (hatched area) to that in $HAD/EM < 0.1$. We plot P_f as a function of the lower cut value of $\Delta X(CES)$ in Fig. 5.4 (b). We take the value of 0.606 ± 0.025 for $\Delta X(CES) > 6$ cm as P_f for photon + charged track overlap.

We used a Monte Carlo to study charged hadrons which deposited a significant amount of energy in the EM calorimeter. We generated charged pions with P_T = 5 and 7 GeV/c and let them pass through the CDFSIM detector simulation package.

Figures 5.5 (a) and (b) show the HAD/EM distributions for pions passing the loose electron identification selection for P_T of 5 and 7 GeV/c, respectively. We obtained $P_f = 0.482 \pm 0.036$ (0.394 ± 0.018) for pions with $P_T = 5$ (7) GeV/c.

Since we do not know the mixture ratio between the two sources, we assume the true value of P_f lies between the upper and lower extremes in the estimates, i.e., $0.606 + 0.025$ and $0.394 - 0.018$. That is, we take

$$P_f = 0.50 \pm 0.13 \qquad \text{for fake electrons.} \tag{5.13}$$

Probability for real electrons P_r

We estimated P_r for real electrons by a very similar way for muons. We reconstructed $J/\psi \to ee$ decays from two tracks of electrons in the dilepton sample. The invariant mass distribution is different from that for muons due to the bremsstrahlung of electrons. Since we are interested in the number of J/ψ's and not in the shape of the distribution itself, we did not correct it for the bremsstrahlung. We fitted a constant + an asymmetric Gaussian which has two different σ's on the right and left side of the peak to the distribution in the region between 2.3 and 3.8 GeV/c^2. We defined the signal region as the invariant mass region between 2.9 and 3.2 GeV/c^2, and from the numbers of backgrounds subtracted $J/\psi \to ee$ events, we obtained

$$P_r = 0.983 \pm 0.004 \qquad \text{for real electrons.} \tag{5.14}$$

Fake electron fraction

Putting the numbers for P_f, P_r, N and N' in Eqs. (5.5) and (5.6), N_f was found to be 72 for OS and 78 for LS. Then, from Eq 5.7 we obtained $F_e(OS) = 0.062 \pm 0.007(stat.) \pm 0.033(syst.)$ and $F_e(LS) = 0.110 \pm 0.013(stat.) \pm 0.059(syst.)$.

5.1.3 Contribution of photon conversions

We now consider photon conversion electrons as another fake electron source. Although most of photon conversion electrons were removed by the electron identification selection, some of them remain in the $e\mu$ sample when one of the two electron tracks is missed. Because one of the two conversion electrons have lower P_T than threshold P_T of track which is reconstructed by CTC data.

This contribution was estimated by using transverse momentum distributions for the photon conversion electron candidates in the $e\mu$ sample and a Monte Carlo [17, 50]. Photons in the Monte Carlo are generated with the transverse momentum spectra which is estimated by real photon conversion sample. The photons are converted to two electrons by a detector simulator.

Figure 5.7 shows the momentum distribution of an associated track with tagged electrons for the photon conversion in real data. The transverse momentum distribution of associated tracks for the Monte Carlo data in a region of $1 < P_T(track) < 5$ GeV/c is normalized to that for photon conversion events. The number of photon conversion events where one of two electrons is missed is estimated by subtracting the number of events for photon conversion from the normalized Monte Carlo events.

The contribution of γ conversion electrons to fake electrons is estimated as a fraction of the subtracted number to number of electron candidates and it turned out to be $(2.00 \pm 0.64)\%$. Adding this value to previous F_e's,

$$F_e(OS) = 0.082 \pm 0.010(stat.) \pm 0.034(syst.) \tag{5.15}$$

and

$$F_e(LS) = 0.111 \pm 0.015(stat.) \pm 0.059(syst.). \tag{5.16}$$

are obtained.

5.1.4 Fake $e\mu$ fraction $F_{e\mu}$

In order to estimate $F_{e\mu}$, we need to know the fake muon fraction in the fake electron sample, F'_{μ}, as can be seen in Eq. (5.4). We considered electron candidates with HAD/EM between 0.04 and 0.1 as a fake electron sample and estimated F'_{μ}. We counted N and N' in the fake electron sample and obtained $N = 135$ and $N' = 202$ for OS events; $N = 108$ and $N' = 171$ for LS events. Using N, N' and, $P_r = 0.967 \pm 0.002$ and $P_f = 0.498 \pm 0.009$ given in Eqs. 5.8 and 5.10, we obtained

$$F'_{\mu}(OS) = 0.474 \pm 0.078 \tag{5.17}$$

and

$$F'_{\mu}(LS) = 0.564 \pm 0.098. \tag{5.18}$$

Substituting F_{μ}, F_e and F'_{μ} into Eq. (5.4), we obtained

$$F_{e\mu}(OS) = 0.255 \pm 0.016(stat.) \pm 0.021(syst.), \tag{5.19}$$

and

$$F_{e\mu}(LS) = 0.396 \pm 0.028(stat.) \pm 0.031(syst.). \tag{5.20}$$

We summarize the fake lepton fractions in Table 5.2.

5.1.5 Asymmetry of fake $e\mu$ events

The number of fake $e\mu$ events is 436 for OS and 340 for LS, and there seems to be an asymmetry, $436/340 = 1.28 \pm 0.19$. In the fake $e\mu$ events, events of fake muon + real electron are dominant. Since the real electron P_T's are high enough to ensure that most of the real electrons are decay products of b hadrons, the main source of the fake $e\mu$ events is considered to be $b\bar{b}$ events. We study the origin of the asymmetry using $b\bar{b}$ Monte Carlo events.

	Opposite-sign		
	Muon	Electron	Muon (Fake electron sample)
N	1710		135
N'	2122	1845	202
$N_f \times P_f$	362 ± 17	140 ± 58	–
$N_r \times P_r$	1348 ± 45	1570 ± 71	–
F_μ, F_e	0.212 ± 0.016	0.082 ± 0.035	–
F'_μ	–	–	0.474 ± 0.078
$F_{e\mu}$	0.255 ± 0.026		
$N \times F_{e\mu}$	436 ± 44		

	Like-sign		
	Muon	Electron	Muon (Fake electron sample)
N	861		108
N'	1175	969	171
$N_f \times P_f$	292 ± 15	111 ± 51	–
$N_r \times P_r$	569 ± 33	750 ± 59	–
F_μ, F_e	0.339 ± 0.028	0.130 ± 0.060	–
F'_μ	–	–	0.564 ± 0.098
$F_{e\mu}$	0.396 ± 0.042		
$N \times F_{e\mu}$	340 ± 37		

Table 5.2: Summary of the fake lepton fraction estimation. The uncertainties include both the statistical and systematic uncertainties.

We generated $b\bar{b}$ events using ISAJET, and the b and $\bar{b}$ hadrons were decayed by CLEOMC. First, to simulate real lepton + fake lepton events, all b hadrons were forced to decay to leptons and all $\bar{b}$ hadrons were forced to decay to hadrons only. The P_Ts of leptons and charged hadrons were required to be greater than 3 GeV/c since the P_T threshold for leptons is 3 GeV/c in this analysis. The pseudo-rapidities of leptons and hadrons were required to be $|\eta| < 0.6$, corresponding to the central muon detector region. Since our electron-muon events are required that the azimuthal opening angle between the leptons is greater than 45°, the azimuthal opening angle of a lepton and a hadron is required to be greater than 45°. After these kinematical cuts were applied, the number of OS lepton-hadron pairs was 749 and that of LS lepton-hadron pairs was 518. Then the asymmetry in the OS and LS real lepton + fake lepton pairs is calculated to be $749/518 = 1.446 \pm 0.083$. Second, to simulate fake lepton + fake lepton events, we generated $b\bar{b}$ events and forced both the b and $\bar{b}$ quarks to decay to hadrons. After applying the same kinematical cuts for hadrons, the number of OS hadron-hadron pairs was 602 and that of LS hadron-hadron pairs was 561. The asymmetry in this case was $602/561 = 1.073 \pm 0.063$.

There is an asymmetry in the fake lepton + real lepton Monte Carlo $b\bar{b}$ events, but we can not say that there is an asymmetry in the fake lepton + fake lepton Monte Carlo $b\bar{b}$ events. Since the observed fake $e\mu$ events include fake lepton + real lepton events and fake lepton + fake lepton events in a certain ratio, we can expect the asymmetry will be in between 1 and 1.446. This result is consistent with the observed asymmetry of 1.28.

In order to see where the Monte Carlo asymmetry comes from, we studied multiplicities of charged particles from B and $\bar{B}$ mesons. For that end, $b\bar{b}$ events were generated and, b and $\bar{b}$ hadrons were decayed by the default branching ratio of CLEOMC. Then the multiplicities of charged particles were counted for each B meson. Figures 5.8 - 5.13 show the multiplicity distributions for B_u^-, $\bar{B}_d^0$, $\bar{B}_s^0$, B_u^+, B_d^0 and B_s^0 mesons, respectively. Histogram (a)'s in these figures show the multiplicity of charged particles before the

Quark	Meson	Charge asymmetry (+/−)
b	B_u^-	0.35 ± 0.01
	$\bar{B}_d^0$	0.74 ± 0.02
	$\bar{B}_s^0$	1.17 ± 0.06
$\bar{b}$	B_u^+	2.92 ± 0.10
	B_d^0	1.27 ± 0.04
	B_s^0	0.83 ± 0.05

Table 5.3: The daughter hadron charge asymmetry for each B meson. The uncertainties are due to the statistics of Monte Carlo events.

kinematical cut is applied. The number of charged particles produced from charged and neutral B mesons are odd and even, as they should be. The numbers of tracks (hadrons or leptons) after requiring the cuts on P_T and $|\eta|$ are almost 1 for any B mesons, as shown in histogram (b)'s. Histogram (c)'s are the same plots for hadrons only, and the distributions are essentially the same as for tracks. Since the charged hadron multiplicity after the cut is one most of the time, we calculate the daughter hadron charge asymmetry for each B meson using multiplicity-one event only. We summarize the asymmetries in Table 5.3. Assuming the production ratio of $B_u : B_d : B_s$ to be $1 : 1 : 0.3$ [51, 52, 53], the ratios of positive hadrons to negative hadrons are 0.63 and 1.40 for b and $\bar{b}$ quarks, respectively. When a b quark in $b\bar{b}$ events decays semileptonically to a negatively charged lepton and the other $\bar{b}$ quark decays into hadrons, we are more likely to find a positively charged hadron from the $\bar{b}$ quark. This creates the asymmetry in real lepton + fake lepton events. These studies show the asymmetry in fake $e\mu$ events originates from physical processes and our event selection.

5.2 Fraction of sequential decays

The fraction of sequential decays, f_s, was estimated from Monte Carlo events.

5.2.1 Monte Carlo of $b\bar{b}$ events

The $b\bar{b}$ events were generated by ISAJET (Version 7.06) with $P_T > 2.9$ GeV/c for both b and $\bar{b}$. The gluon splitting events were generated by ISALEP (Version 7.06) with $P_T > 9.8$ GeV/c for gluons that produced $b\bar{b}$ pairs. Quarks and gluons were hadronized and decayed in the ISAJET and ISALEP generators, but the B and $\bar{B}$ meson decays were replaced by those simulated using CLEOMC (Version 9.00). Finally the $b\bar{b}$ events were passed through the QFL (offline version 7.10) detector simulator.

5.2.2 Estimation of the f_s

To simulate Process 1 (Table 4.1), all b and $\bar{b}$ hadrons were forced to decay to leptons. For Process 2, all b hadrons were forced to decay to leptons and $\bar{b}$ hadrons were decayed following the CLEOMC decay table. In the decay products from $\bar{b}$ hadrons, $\bar{c}$ hadrons were forced to decay to leptons. Particles and anti-particles in Process 2 were exchanged for Process 3.

The numbers of Monte Carlo events that passed the $e\mu$ event selection are shown in Tables 5.4 to 5.12 for different structure functions and Peterson fragmentation parameters. The luminosities for generated events are also shown in the tables. The fraction of sequential decays is given by a ratio of the number of events for Processes 2 and 3 to that for Process 1, where the number of events is normalized by the luminosity, taking into account the branching ratio, $Br(b \to l + X) = 0.110 \pm 0.005$ [4] and $Br(c \to l + X)$. The branching ratio $Br(c \to l + X)$ for D^+ and D^0 are used 0.172 ± 0.019 and 0.0885 ± 0.0143 [4], respectively. For D_s^+ and c baryon, the branching ratio are estimated from $Br(D^+ \to e + \text{anything}) = 0.172 \pm 0.019$ and, the mean life, $\tau(D^+) = 1.057 \pm 0.015$, $\tau(D_s^+) = 0.467 \pm 0.017$ and $\tau(\Lambda_c^+) = 0.200 \pm 0.010$ [4]. The estimated branching ratio for D_s^+ and c baryon are 0.076 ± 0.019 and 0.033 ± 0.010, respectively.

The structure functions used in the above calculation are Martin-Roberts-Stirling (MRS) D0$-'$ structure function [54, 55], Eichten-Hinchliffe-Lane-Quigg (EHLQ) struc-

		ISAJET		ISALEP	
		Number of events	Luminosity (pb^{-1})	Number of events	Luminosity (pb^{-1})
Process 1		1024	0.742	59	0.309
Process 2	$\bar{b} \to \bar{D}^0 \to l$	33	0.729	5	0.336
	$\bar{b} \to D^- \to l$	16		0	
	$\bar{b} \to D_s^- \to l$	5		1	
	$\bar{b} \to baryon_{\bar{c}} \to l$	5		0	
Process 3	$b \to D^0 \to l$	24	0.663	2	0.296
	$b \to D^+ \to l$	10		1	
	$b \to D_s^+ \to l$	6		1	
	$b \to baryon_c \to l$	5		0	

Table 5.4: The numbers of $e\mu$ events which passed the $e\mu$ event selection and the corresponding luminosities. The structure function is MRSD0$-'$ and the Peterson parameter is set to 0.003.

		ISAJET		ISALEP	
		Number of events	Luminosity (pb^{-1})	Number of events	Luminosity (pb^{-1})
Process 1		1053	0.790	46	0.308
Process 2	$\bar{b} \to \bar{D}^0 \to l$	21	0.624	2	0.305
	$\bar{b} \to D^- \to l$	11		2	
	$\bar{b} \to D_s^- \to l$	2		0	
	$\bar{b} \to baryon_{\bar{c}} \to l$	5		0	
Process 3	$b \to D^0 \to l$	30	0.660	2	0.319
	$b \to D^+ \to l$	13		2	
	$b \to D_s^+ \to l$	6		0	
	$b \to baryon_c \to l$	2		0	

Table 5.5: The numbers of $e\mu$ events which passed the $e\mu$ event selection and the corresponding luminosities. The structure function is MRSD0$-'$ and the Peterson parameter is set to 0.006.

		ISAJET		ISALEP	
		Number of events	Luminosity (pb^{-1})	Number of events	Luminosity (pb^{-1})
Process 1		926	0.789	49	0.323
Process 2	$\bar{b} \to \bar{D}^0 \to l$	24	0.601	2	0.325
	$\bar{b} \to D^- \to l$	9		0	
	$\bar{b} \to D_s^- \to l$	2		0	
	$\bar{b} \to baryon_{\bar{c}} \to l$	3		1	
Process 3	$b \to D^0 \to l$	25	0.641	2	0.225
	$b \to D^+ \to l$	15		3	
	$b \to D_s^+ \to l$	3		0	
	$b \to baryon_c \to l$	4		0	

Table 5.6: The numbers of $e\mu$ events which passed the $e\mu$ event selection and the corresponding luminosities. The structure function is MRSD0$-'$ and the Peterson parameter is set to 0.009.

		ISAJET		ISALEP	
		Number of events	Luminosity (pb^{-1})	Number of events	Luminosity (pb^{-1})
Process 1		1169	0.589	203	0.586
Process 2	$\bar{b} \to \bar{D}^0 \to l$	34	0.627	14	0.586
	$\bar{b} \to D^- \to l$	21		5	
	$\bar{b} \to D_s^- \to l$	9		1	
	$\bar{b} \to baryon_{\bar{c}} \to l$	3		1	
Process 3	$b \to D^0 \to l$	34	0.512	9	0.586
	$b \to D^+ \to l$	16		1	
	$b \to D_s^+ \to l$	2		1	
	$b \to baryon_c \to l$	11		2	

Table 5.7: The numbers of $e\mu$ events which passed the $e\mu$ event selection and the corresponding luminosities. The structure function is EHLQ and the Peterson parameter is set to 0.003.

		ISAJET		ISALEP	
		Number of events	Luminosity (pb^{-1})	Number of events	Luminosity (pb^{-1})
Process 1		1252	0.706	216	0.587
Process 2	$\bar{b} \to \bar{D}^0 \to l$	25	0.606	6	0.587
	$\bar{b} \to D^- \to l$	26		5	
	$\bar{b} \to D_s^- \to l$	1		0	
	$\bar{b} \to baryon_{\bar{c}} \to l$	5		2	
Process 3	$b \to D^0 \to l$	45	0.563	6	0.587
	$b \to D^+ \to l$	25		4	
	$b \to D_s^+ \to l$	5		1	
	$b \to baryon_c \to l$	7		1	

Table 5.8: The numbers of $e\mu$ events which passed the $e\mu$ event selection and the corresponding luminosities. The structure function is EHLQ and the Peterson parameter is set to 0.006.

		ISAJET		ISALEP	
		Number of events	Luminosity (pb^{-1})	Number of events	Luminosity (pb^{-1})
Process 1		1129	0.705	204	0.585
Process 2	$\bar{b} \to \bar{D}^0 \to l$	39	0.705	8	0.585
	$\bar{b} \to D^- \to l$	34		2	
	$\bar{b} \to D_s^- \to l$	7		0	
	$\bar{b} \to baryon_{\bar{c}} \to l$	3		2	
Process 3	$b \to D^0 \to l$	39	0.705	5	0.557
	$b \to D^+ \to l$	22		5	
	$b \to D_s^+ \to l$	4		2	
	$b \to baryon_c \to l$	6		4	

Table 5.9: The numbers of $e\mu$ events which passed the $e\mu$ event selection and the corresponding luminosities. The structure function is EHLQ and the Peterson parameter is set to 0.009.

		ISAJET		ISALEP	
		Number of events	Luminosity (pb^{-1})	Number of events	Luminosity (pb^{-1})
Process 1		1217	0.662	71	0.233
Process 2	$\bar{b} \to \bar{D}^0 \to l$	39	0.588	3	0.229
	$\bar{b} \to D^- \to l$	13		2	
	$\bar{b} \to D_s^- \to l$	3		0	
	$\bar{b} \to baryon_{\bar{c}} \to l$	6		1	
Process 3	$b \to D^0 \to l$	44	0.523	1	0.227
	$b \to D^+ \to l$	18		0	
	$b \to D_s^+ \to l$	7		0	
	$b \to baryon_c \to l$	4		0	

Table 5.10: The numbers of $e\mu$ events which passed the $e\mu$ event selection and the corresponding luminosities. The structure function is DFLM and the Peterson parameter is set to 0.003.

		ISAJET		ISALEP	
		Number of events	Luminosity (pb^{-1})	Number of events	Luminosity (pb^{-1})
Process 1		995	0.586	57	0.233
Process 2	$\bar{b} \to \bar{D}^0 \to l$	27	0.485	2	0.218
	$\bar{b} \to D^- \to l$	14		1	
	$\bar{b} \to D_s^- \to l$	2		1	
	$\bar{b} \to baryon_{\bar{c}} \to l$	3		0	
Process 3	$b \to D^0 \to l$	39	0.596	2	0.215
	$b \to D^+ \to l$	15		0	
	$b \to D_s^+ \to l$	2		0	
	$b \to baryon_c \to l$	9		0	

Table 5.11: The numbers of $e\mu$ events which passed the $e\mu$ event selection and the corresponding luminosities. The structure function is DFLM and the Peterson parameter is set to 0.006.

		ISAJET Number of events	ISAJET Luminosity (pb^{-1})	ISALEP Number of events	ISALEP Luminosity (pb^{-1})
Process 1		1071	0.663	40	0.199
Process 2	$\bar{b} \rightarrow \bar{D}^0 \rightarrow l$	30	0.663	1	0.198
	$\bar{b} \rightarrow D^- \rightarrow l$	21		1	
	$\bar{b} \rightarrow D_s^- \rightarrow l$	6		0	
	$\bar{b} \rightarrow baryon_{\bar{c}} \rightarrow l$	7		0	
Process 3	$b \rightarrow D^0 \rightarrow l$	34	0.663	2	0.199
	$b \rightarrow D^+ \rightarrow l$	23		1	
	$b \rightarrow D_s^+ \rightarrow l$	5		0	
	$b \rightarrow baryon_c \rightarrow l$	4		0	

Table 5.12: The numbers of $e\mu$ events which passed the $e\mu$ event selection and the corresponding luminosities. The structure function is DFLM and the Peterson parameter is set to 0.009.

Structure function	f_s	Statistical uncertainty
MRSD0−′	0.1107	0.0084
EHLQ	0.1355	0.0050
DFLM 260	0.1124	0.0084

Table 5.13: The f_s for different structure functions where the Peterson parameter value is 0.006.

ture function [41, 56], and Diemoz-Ferroni-Longo-Martinelli (DFLM) structure function [54, 57] with $\Lambda_{QCD} = 260$ MeV. The f_s values calculated for three different structure functions are shown in Table 5.13, where the default value of the Peterson parameter, 0.006, was used. We take a center value of the minimum and the maximum values in Table 5.13: $f_s = 0.123$.

5.2.3 Correcting f_s for J/ψ and $b \to \bar{c} \to l$ events

We correct f_s for the contributions from other b-decay processes. Considering all of other possible decay processes, we have found that the following two processes have a sizable effect:

$$\text{Process 5} \quad \begin{cases} b \to & l^- \\ \bar{b} \to & J/\psi \to \quad l^+(\text{ or } l^-) \end{cases} \qquad \text{Process 6} \quad \begin{cases} b \to & J/\psi \to \quad l^+(\text{ or } l^-) \\ \bar{b} \to & l^+ \end{cases} \tag{5.21}$$

and

$$\text{Process 7} \quad \begin{cases} b \to & l^- \\ \bar{b} \to & \bar{c}W; \quad W \to c\bar{s}; \quad c \to l^+ \end{cases} \qquad \text{Process 8} \quad \begin{cases} b \to & cW; \quad W \to \bar{c}s; \quad \bar{c} \to l^- \\ \bar{b} \to & l^+ \end{cases} \tag{5.22}$$

We call the first process $b \to J/\psi \to l$ events and the second $b \to \bar{c} \to l$ events. The $b \to J/\psi \to l$ events produce tri-leptons. Since we are rejecting events with three or more good leptons, the $b \to J/\psi \to l$ events come into our sample only when one of the two leptons from J/ψ decays fails the selection cuts. Depending on which lepton

	Direct $b\bar{b}$ production (ISAJET)		Gluon splitting (ISALEP)	
	Number of events	Luminosity (pb^{-1})	Number of events	Luminosity (pb^{-1})
$\begin{cases} b \to l^- \\ \bar{b} \to J/\psi \to l^\pm \end{cases}$	195	0.720	12	0.295
$\begin{cases} b \to l^- \\ \bar{b} \to c \to l^+ \end{cases}$	14	0.491	5	0.481

Table 5.14: The numbers of $b \to J/\psi \to l$ and $b \to \bar{c} \to l$ events which passed the $e\mu$ event selection and the corresponding luminosities, where the structure function is MRSD0$-'$ and the Peterson parameter is set to 0.006.

fails, $b \to J/\psi \to l$ events produce OS or LS pairs. On the other hand, $b \to \bar{c} \to l$ events contribute to OS. We generated these events in the same way as for the case of Processes 1$\sim$3. This time, b mesons were forced to decay to leptons, and $\bar{b}$ mesons were forced to decay to J/ψ for $b \to J/\psi \to l$ events, and to c mesons for $b \to \bar{c} \to l$ events in the CLEOMC. The structure function was MRSD0$-'$ and the Peterson parameter was set to 0.006. The number of Monte Carlo events that passed the $e\mu$ event selection, together with the integrated luminosities are summarized in Table 5.14. As in the case of Processes 1$\sim$3, the luminosities are not corrected for having forced b-decays to specific channels. The corresponding branching ratios used for the correction of the luminosities are $Br(b \to l + X) = 0.110$ which is the same as before, and $Br(b \to J/\psi) = 0.019$ and $Br(b \to \bar{c}) = 0.12$.

A summary of the numbers of events from Processes 1$\sim$3, $b \to J/\psi \to l$ and $b \to \bar{c} \to l$ events corresponding to the integrated luminosity of 20 pb^{-1} is given in Table 5.15. Note that $b \to J/\psi \to l$ events are considered to have an equal contribution to OS and LS. Processes 1$\sim$3 gave $f_s = 0.1107$ for MRSD0$-'$ as already shown in Table 5.13.

	OS	LS
$\begin{cases} b \to l^- \\ \bar{b} \to l^+ \end{cases}$	1630.0 ± 124.3	–
$\begin{cases} b \to l^- \\ \bar{b} \to \bar{c} \to l^- \end{cases}$ $\begin{cases} b \to c \to l^+ \\ \bar{b} \to l^+ \end{cases}$	–	180.5 ± 20.8
$\begin{cases} b \to l^- \\ \bar{b} \to J/\psi \to l^\pm \end{cases}$ $\begin{cases} b \to J/\psi \to l^\pm \\ \bar{b} \to l^+ \end{cases}$	26.0 ± 1.9	26.0 ± 1.9
$\begin{cases} b \to l^- \\ \bar{b} \to c \to l^+ \end{cases}$ $\begin{cases} b \to \bar{c} \to l^- \\ \bar{b} \to l^+ \end{cases}$	41.1 ± 9.4	–

Table 5.15: The numbers of Monte Carlo events which passed the $e\mu$ selection for OS and LS at the integrated luminosity of 20 pb^{-1}. The structure function is MRSD0$-'$ and Peterson parameter is set to 0.006.

Inclusion of $b \to J/\psi \to l$ and $b \to \bar{c} \to l$ events changed f_s to 0.1231, which was a correction by a factor of 1.112 ± 0.012. The uncertainty is estimated from the statistics of $b \to J/\psi \to l$ and $b \to \bar{c} \to l$ Monte Carlo events. Multiplying 1.112 to 0.123 which was obtained only from Processes 1$\sim$3 as the center value for the three different structure functions, we obtained $f_s = 0.137$.

5.2.4 Systematic uncertainties in f_s

We discuss the uncertainties of f_s in what follows. The relatively small contributions from $b \to J/\psi \to l$ and $b \to \bar{c} \to l$ events were not included in the Monte Carlo data used in estimation of this uncertainties.

First of all, our estimation of the uncertainty due to the structure function is already included in Table 5.13. The uncertainty due to b quark fragmentation was estimated by changing the Peterson parameter, $\epsilon = 0.006 \pm 0.003$ [7], by one sigma. The results for the MRSD0$-'$ structure function of are shown in Table 5.16. Figure 5.14 shows the f_s

Peterson parameter (ϵ)	f_s	uncertainty
0.003	0.1055	0.0075
0.006	0.1107	0.0084
0.009	0.1190	0.0091

Table 5.16: The f_s for different values of the Peterson parameter (ϵ), where the structure function is MRSD0$-'$. The uncertainties are due to the statistics of the Monte Carlo events.

Fraction of gluon splitting	f_s
0%	0.1004
11.2%	0.1107
22.4%	0.1128

Table 5.17: The f_s for different ratios of gluon splitting events to $b\bar{b}$ direct productions, where the structure function is MRSD0$-'$ and the Peterson parameter is set to 0.006.

values for different structure functions and different values of the Peterson parameter. Due to the statistical uncertainty of the Monte Carlo events, we can not separate the uncertainties from the structure function and the fragmentation. Instead, we simply looked at the minimum and the maximum of center values of f_s in Fig 5.14, which are -14.3% and 12.9% of our f_s, respectively. We took 14.3% conservatively as the combined uncertainty of f_s due to the statistics, the structure function and the fragmentation. The uncertainties due to the branching ratios, $Br(b \to l + X)$ and $Br(c \to l + X)$, were estimated to be 4.5% and 9.1%, respectively, by propagating their uncertainties to f_s. We estimated a ratio of gluon splitting events to direct production events to be 11.2% from the Monte Carlo data where the structure function was MRSD0$-'$ and the Peterson parameter was set to the default value of 0.006. When we changed the ratio from 11.2% to 0% and 22.4%, f_s varied by -9.3% and $+1.8\%$, respectively, as shown in Table 5.17. We took 9.3% as the uncertainty due to the ratio of gluon splitting events to direct production events. The uncertainty due to the correction factor for $b \to J/\psi \to l$

Source	Uncertainties
$\left\{\begin{array}{l}\text{Monte Carlo statistics}\\ \text{Fragmentation}\\ \text{Structure function}\end{array}\right.$	14.3%
$Br(b \to l + X)$	4.5%
$Br(c \to l + X)$	9.1%
Fraction of gluon splitting	9.3%
J/ψ, $b \to \bar{c} \to l$	1.1%
Total	19.9%

Table 5.18: Uncertainties in f_s.

and $b \to \bar{c} \to l$ events was 1.1%.

As a final result, we obtained

$$f_s = 0.137 \pm 0.027. \tag{5.23}$$

The uncertainties in f_s are summarized in Table 5.18.

5.3 Fraction of direct $c\bar{c}$ background

5.3.1 Method of f_c estimation

The fraction of direct $c\bar{c}$ background was estimated by fitting P_T^{rel} distributions for $b\bar{b}$ Monte Carlo, $c\bar{c}$ Monte Carlo and fake leptons from the real data to the observed distribution. The $b\bar{b}$ Monte Carlo was already described in the previous section. The $c\bar{c}$ direct production events were generated by ISAJET with $P_T > 2.9$ GeV/c for both c and $\bar{c}$, and $c\bar{c}$ events from gluon splitting were generated by ISALEP with $P_T > 2.9$ GeV/c for gluons. These events were processed by the QFL detector simulator.

We can rewrite $N^{exp}(LS)$ and $N^{exp}(OS)$ as

$$N^{exp}(LS) = 2\chi(1-\chi)N_D + [(1-\chi)^2 + \chi^2]N_S + N_f(LS) \tag{5.24}$$

and

$$N^{exp}(OS) = [(1-\chi)^2 + \chi^2]N_D + 2\chi(1-\chi)N_S + N_f(OS) + N_C, \tag{5.25}$$

where N_D, N_S, N_C and N_f are the numbers of events for Process 1+5+6, Process 2+3+5+6+7+8, Process 4 in Tables 4.1 and 4.4, and fake leptons. The difference between the numbers of OS and LS is written by

$$N^{exp}(OS) - N^{exp}(LS) = (1-2\chi)^2(N_D - N_S) + N_C + \Delta N_f. \tag{5.26}$$

where the last term, $\Delta N_f \equiv N_f(OS) - N_f(LS)$. There is a similar relation among P_T^{rel} distributions,

$$\begin{aligned} &N^{exp}(OS)H^{exp}_{OS}(P_T^{rel}) - N^{exp}(LS)H^{exp}_{LS}(P_T^{rel}) = \\ &\quad (1-2\chi)^2[N_D H_d(P_T^{rel}) - N_S H_s(P_T^{rel})] + N_C H_c(P_T^{rel}) + \Delta N_f H_f(P_T^{rel}), \end{aligned} \tag{5.27}$$

where $H(P_T^{rel})$ represents the P_T^{rel} distribution function and is normalized to be one. This relation holds for muons and electrons separately. We fitted

$$n_b(H_d(P_T^{rel}) - \frac{N_S}{N_D}H_s(P_T^{rel})) + n_c H_c(P_T^{rel}) + \Delta N_f H_f(P_T^{rel}) \tag{5.28}$$

to

$$H^{exp}_{OS}(P_T^{rel}) - H^{exp}_{LS}(P_T^{rel}) \tag{5.29}$$

taking n_b and n_c are fitting parameters and setting ΔN_f to the observed value. Since we defined Eq. (5.27) for muons and electrons separately, the ΔN_f can be defined to be a difference of number of fake leptons. Then the ΔN_f is calculated to be 70 ± 23 and 29 ± 77 for fake muons and fake electrons, respectively, from Table 5.2 in Section 5.1.

The P_T^{rel} distributions for $b\bar{b}$ and $c\bar{c}$ were obtained from the Monte Carlo's. As fake muons, we used muon candidates which had a stub only in CMU chambers within the CMU and CMP fiducial region. As fake electrons, we used electron candidates with

$\Delta X(CES) > 6$ cm which were considered as photons overlapped by charged hadrons in the EM calorimeter. We here assume that the P_T^{rel} distribution for photons overlapped by charged hadrons and that for other sources of fake electrons are the same. One should note that the magnitude of ΔN_f for fake electrons itself is small compared to the total number of the fitted distribution, that is $N^{exp}(OS) - N^{exp}(LS) = 849$ derived from Table 5.2. The result, therefor, does not significantly depend on it. The number of direct $c\bar{c}$ background is given by $N_C = n_c \int H_c dP_T^{rel}$ in the region of $P_T^{rel} > 1.5$ GeV/c. The fraction of direct $c\bar{c}$ background is obtained by

$$f_c = \frac{N_C}{N_D} = \frac{N_C}{[N^{exp}(OS)(1 - F_{e\mu}(OS)) + N^{exp}(LS)(1 - F_{e\mu}(LS)) - N_C] \cdot \frac{1}{1+f_s}}. \quad (5.30)$$

5.3.2 Estimation of f_c

The fitted P_T^{rel} distributions for muons and electrons are shown in Fig. 5.15, where the structure function is used MRSD0$-'$ In Fig. 5.15 (a) ((b)), we did not apply the P_T^{rel} cut to muons (electrons) while P_T^{rel} of electrons (muons) was required to be greater than 1.5 GeV/c. The shape difference between the P_T^{rel} distributions for muons and electrons comes from the different lepton P_T thresholds, which was confirmed by raising up the P_T threshold for muons. The number of direct $c\bar{c}$ background N_C was estimated to be -6 ± 26 from the fit of electron P_T^{rel} distribution and 34 ± 18 from muon P_T^{rel}. These numbers are consistent with each other within the statistical uncertainties. The weighted average of the numbers, 21 ± 15, was used in this analysis.

We estimated f_c for two other structure functions as in the case of f_s. The fitted P_T^{rel} distributions for EHLQ and DFLM structure functions are shown in Figs. 5.16 and 5.17, respectively. The results for three structure functions are shown in Table 5.19. We take as f_c the center value of the minimum and the maximum values in Table 5.19, which is 0.007.

Structure function	f_c	Statistical uncertainty
MRSD0$-'$	0.013	0.010
EHLQ	0.009	0.010
DFLM 260	0.001	0.012

Table 5.19: The f_c for different structure functions.

Difference between the numbers of fake leptons in OS and LS		f_c
Fake muon	Fake electron	
70	29	0.013
$70 + 23$	$29 + 77$	-0.002
$70 - 23$	$29 - 77$	0.031

Table 5.20: The f_c for values of difference between the numbers of fake leptons in OS and LS.

5.3.3 Systematic uncertainties in f_c

The uncertainty due to the structure function was obtained in the same way as for f_s. The combined uncertainty in f_c due to statistics and the structure function is taken to be 85.7% which is half of the difference between the minimum and the maximum values in Table 5.19.

The uncertainty in f_c caused by the uncertainty in n_f was estimated by changing the n_f by one sigma around the center value of n_f in the fitting. The default structure function, MRSD0$-'$, was used for the Monte Carlo data. From Table 5.20 showing the results, we estimated the uncertainty to be 139.6%, where we took the largest deviation from the center value divided by the center value.

Finally, we got

$$f_c = 0.007 \pm 0.011. \tag{5.31}$$

The uncertainties in f_c are summarized in Table 5.21

Source	Uncertainties
Statistics Structure function	85.7%
Fake leptons	139.6%
Total	163.4%

Table 5.21: Uncertainties in f_c.

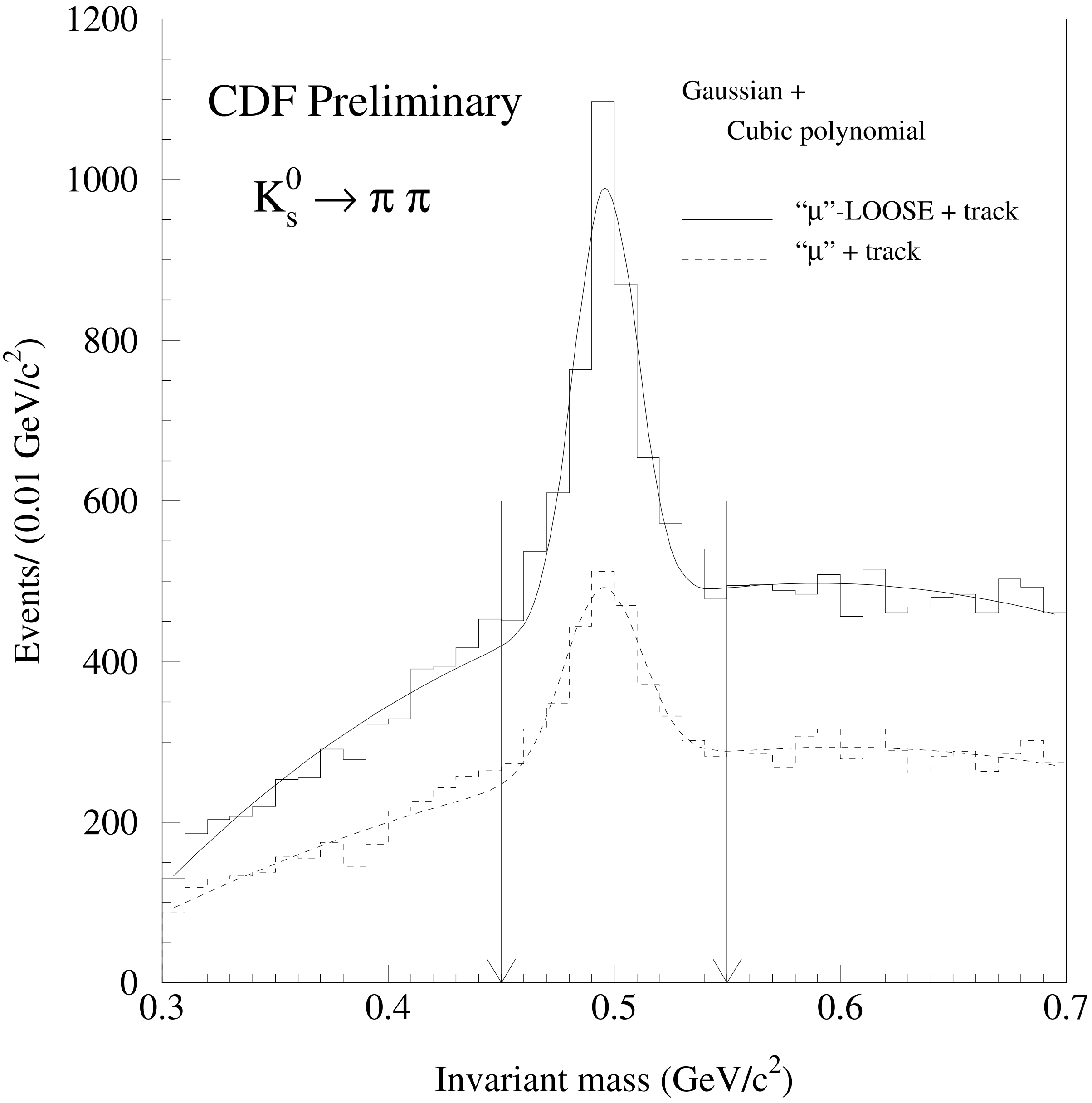

Figure 5.1: Invariant mass of a muon candidate track and an oppositely charged hadron track with a π-π mass assignment. The dashed (solid) histogram is for the case where the muon candidate track passed the muon identification cut (the loose cut).

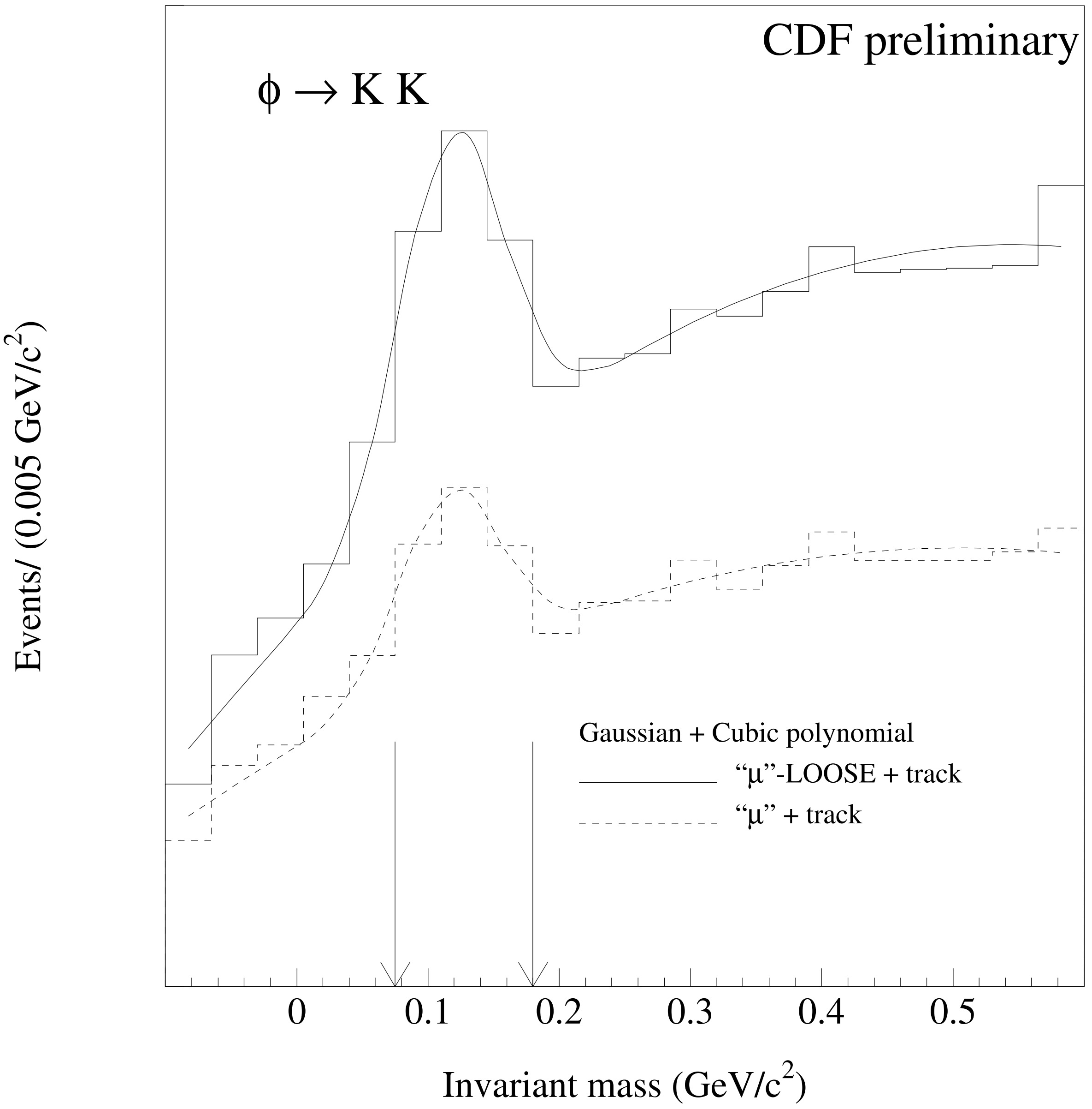

Figure 5.2: Invariant mass of a muon candidate track and an oppositely charged hadron track with a K-K mass assignment. The dashed (solid) histogram is for the case where the muon candidate track passed the muon identification cut (the loose cut).

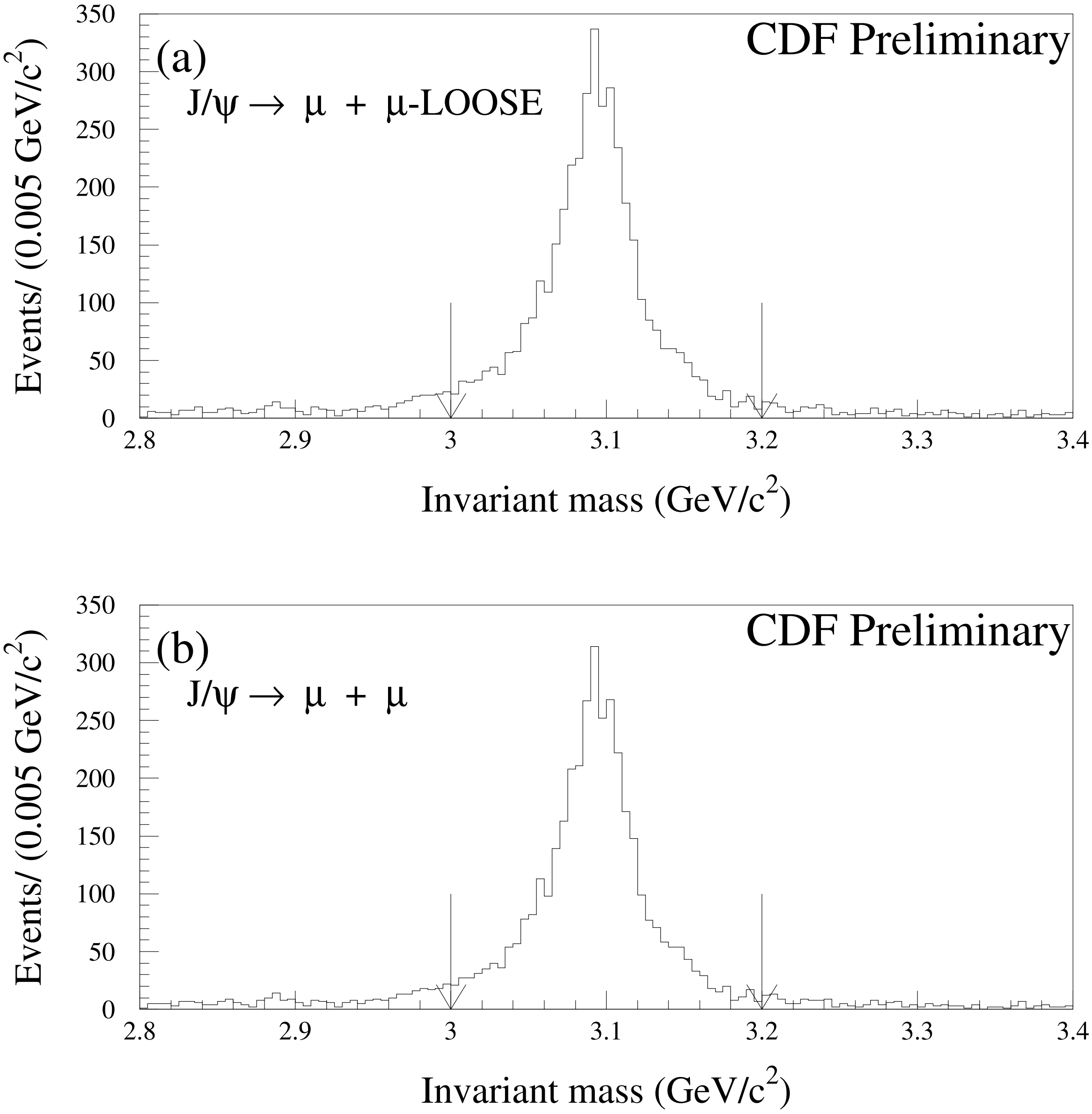

Figure 5.3: Invariant mass distributions for dimuons. (a) One of the two muons passed the muon identification cut and the other muon passed the loose one. (b) Both of the two muons passed the muon identification cut.

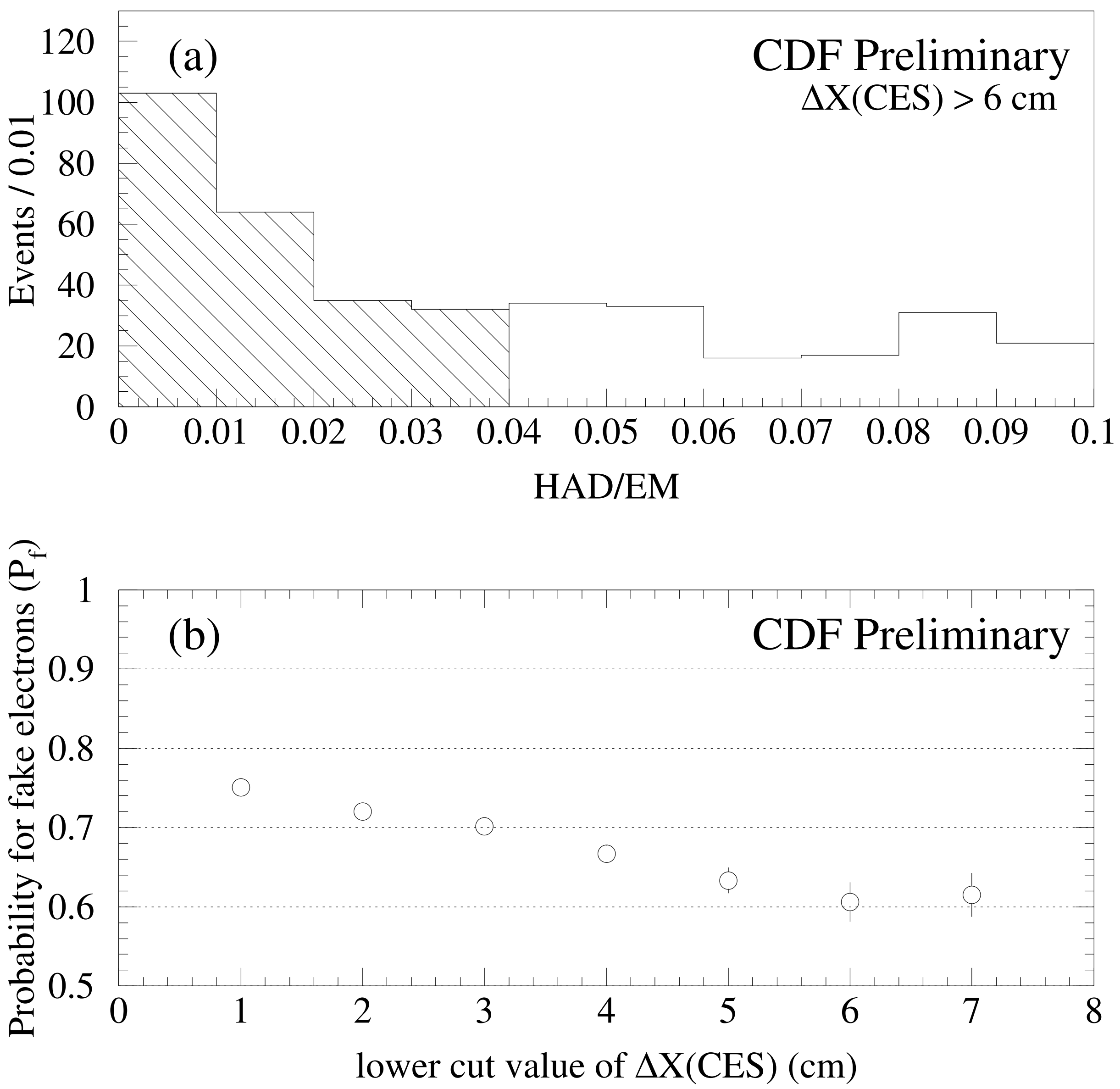

Figure 5.4: (a) HAD/EM distribution for electron candidates with $\Delta X(CES) > 6$ cm. Electron candidates in the hatched area pass the electron identification cut except $\Delta X(CES)$ cut. (b) Probabilities for fake electrons (photon + charged hadron overlap) as a function of the lower cut value of $\Delta X(CES)$.

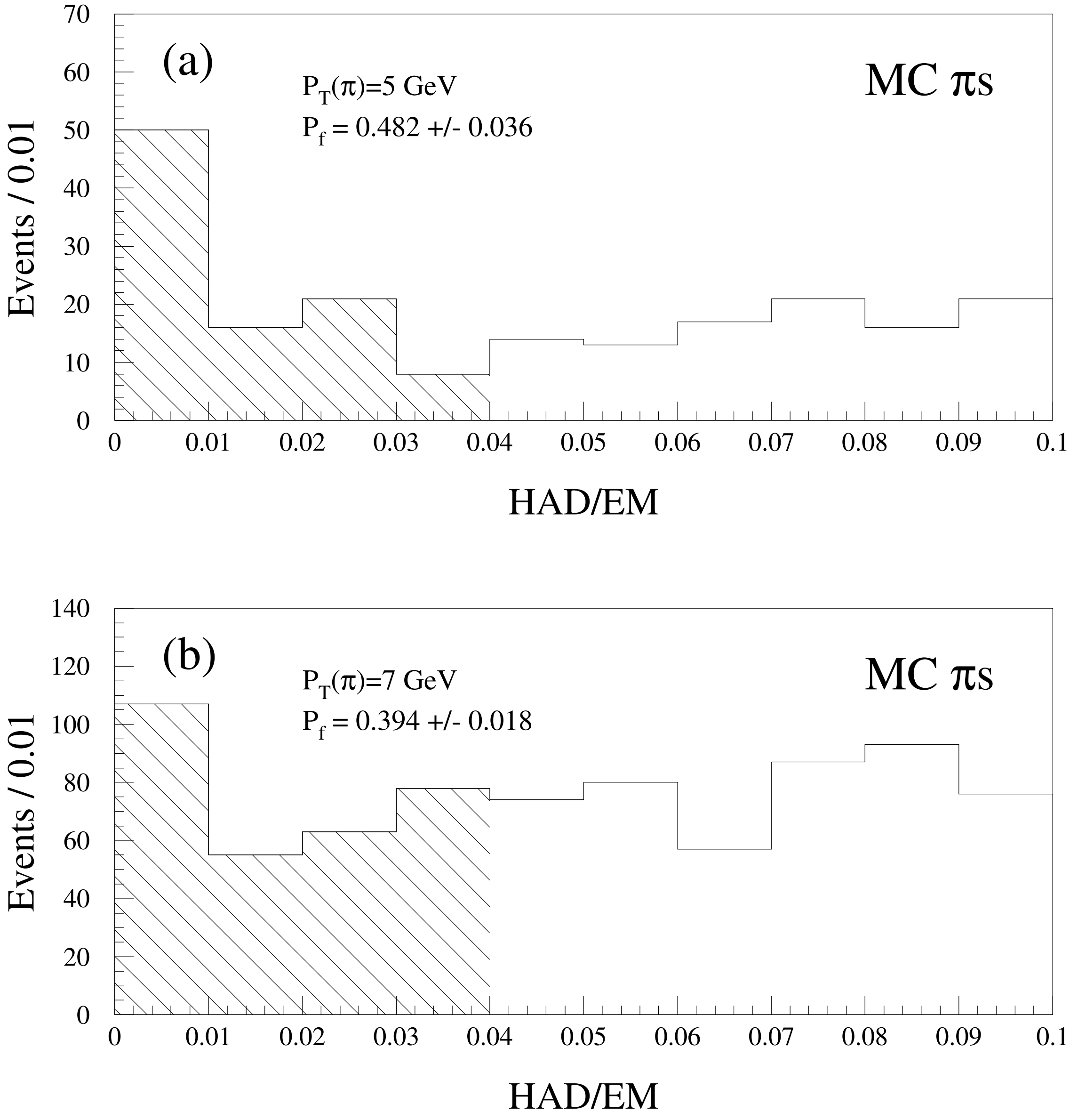

Figure 5.5: HAD/EM distributions for generated pions passing the loose electron identification cut for (a) $P_T = 5$ GeV/c and (b) $P_T = 7$ GeV/c. Pions in the hatched area pass the electron identification cut.

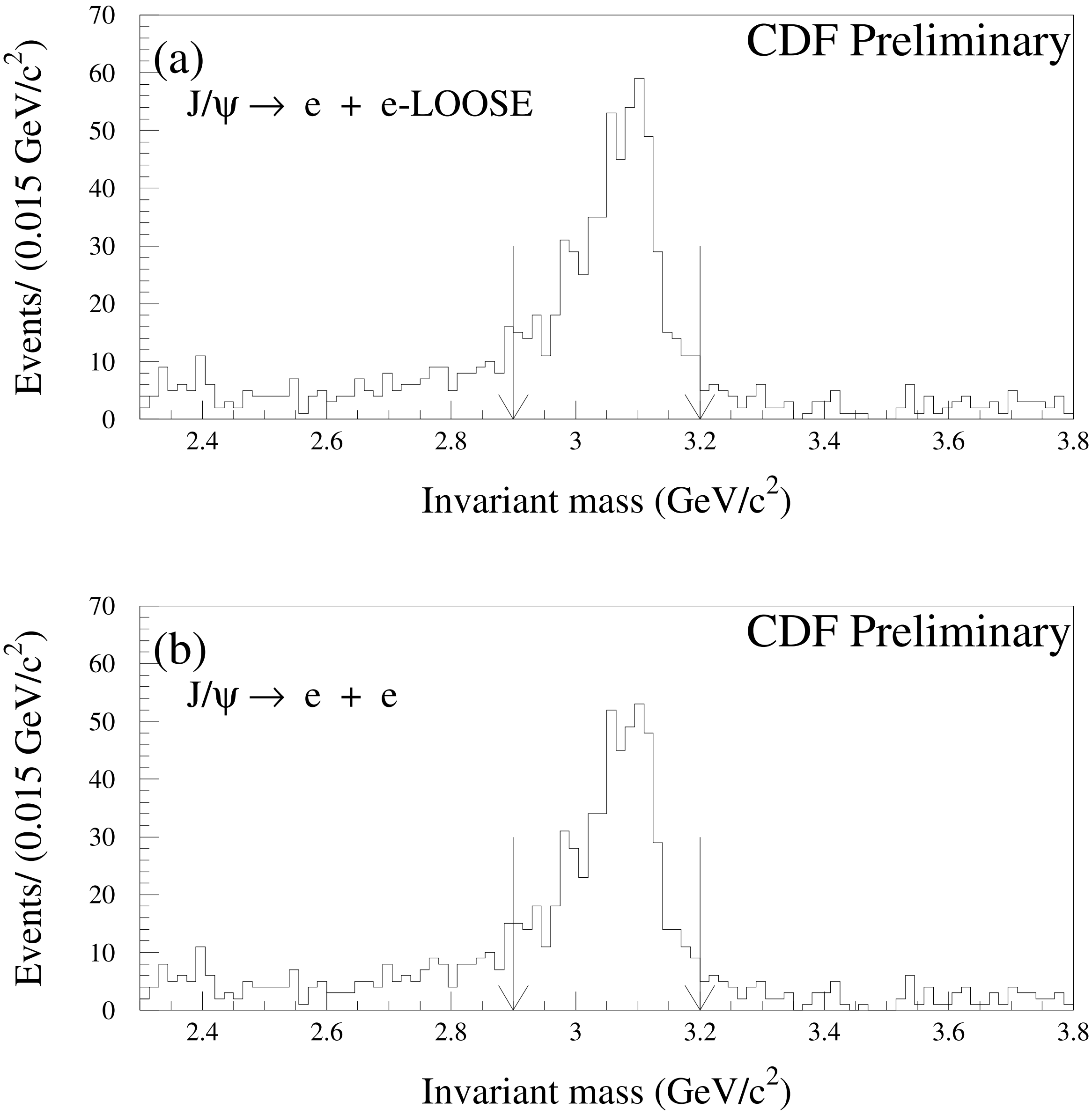

Figure 5.6: Invariant mass distributions for dielectrons. (a) One of the two electrons passed the electron identification selection and the other electron passed the loose one. (b) Both of the two electrons passed the electron identification selection.

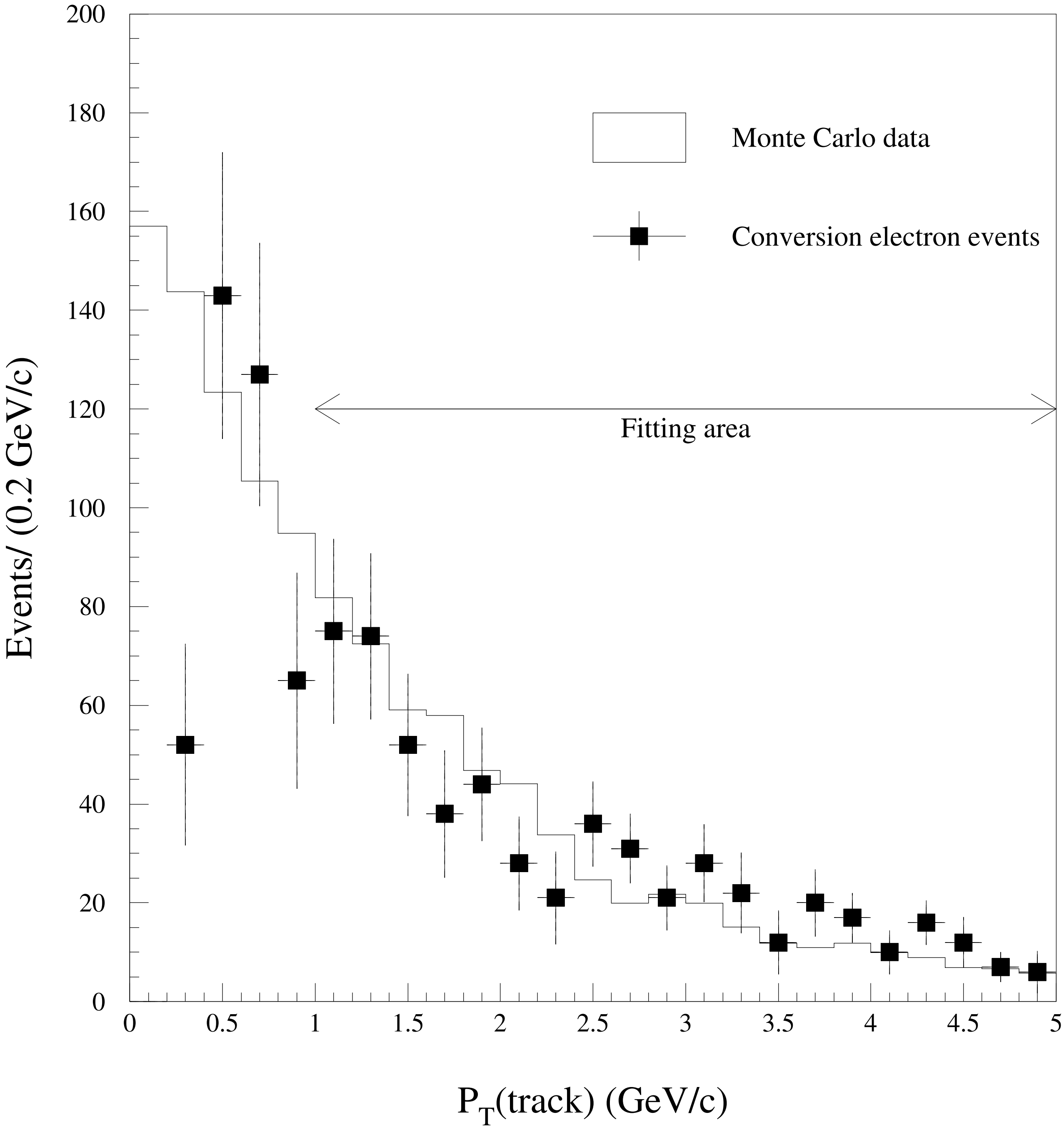

Figure 5.7: Transverse momentum distributions of electrons for conversion electron sample and the Monte Carlo data. The Monte Carlo data is normalized in a region of $1 < P_T(track) < 5$ GeV/c.

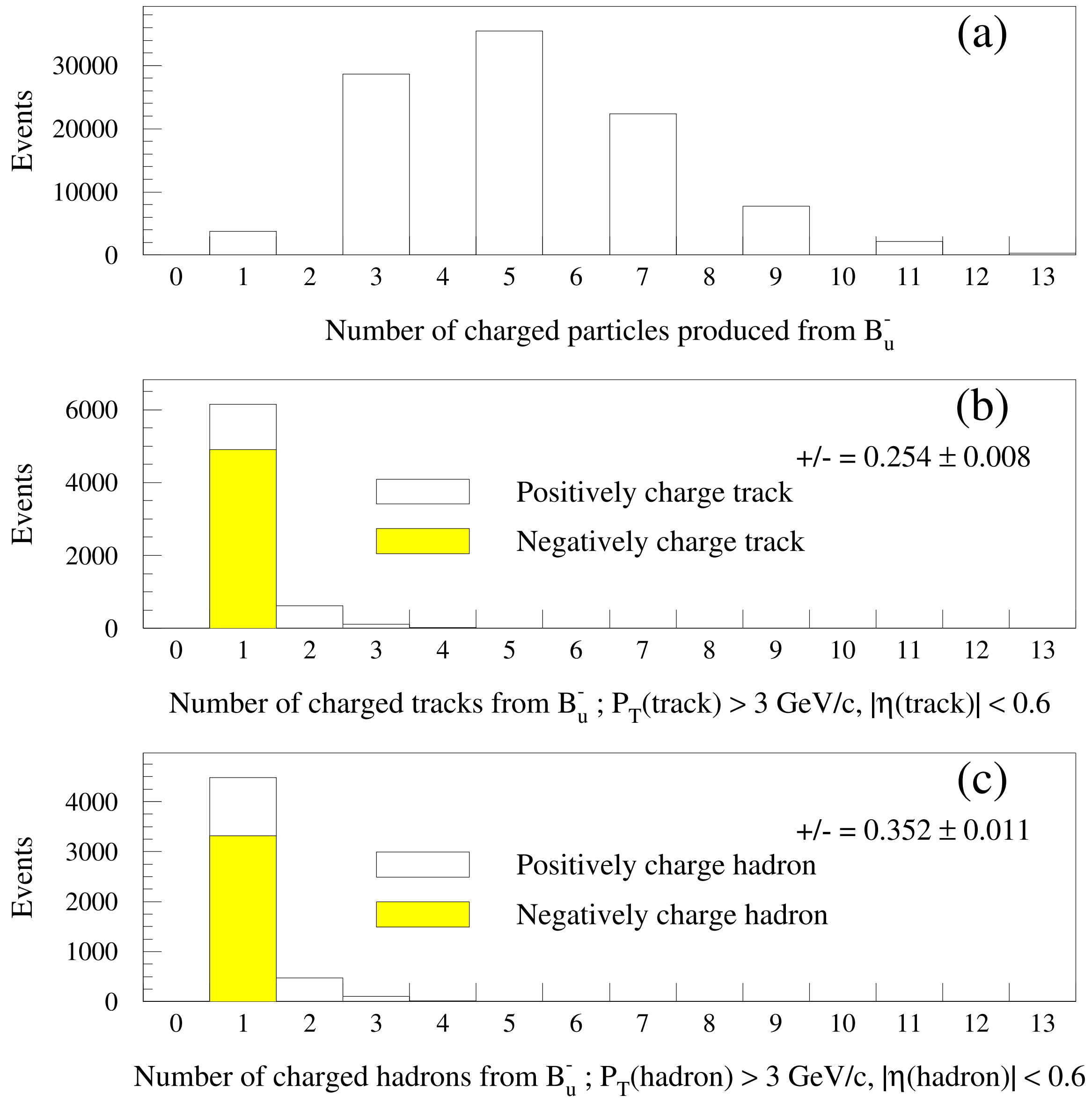

Figure 5.8: Charged particle multiplicities from the B_u^- meson. (a) Multiplicity of charged particles produced from B_u^- mesons. (b) Multiplicity of charged tracks (hadron or lepton) with $P_T > 3$ GeV/c and $|\eta| < 0.6$. (c) Multiplicity of charged hadrons with $P_T > 3$ GeV/c and $|\eta| < 0.6$. The leptons are removed in this distribution. The hatched area in multiplicity one bin in (b) and (c) represents negatively charged tracks and hadrons.

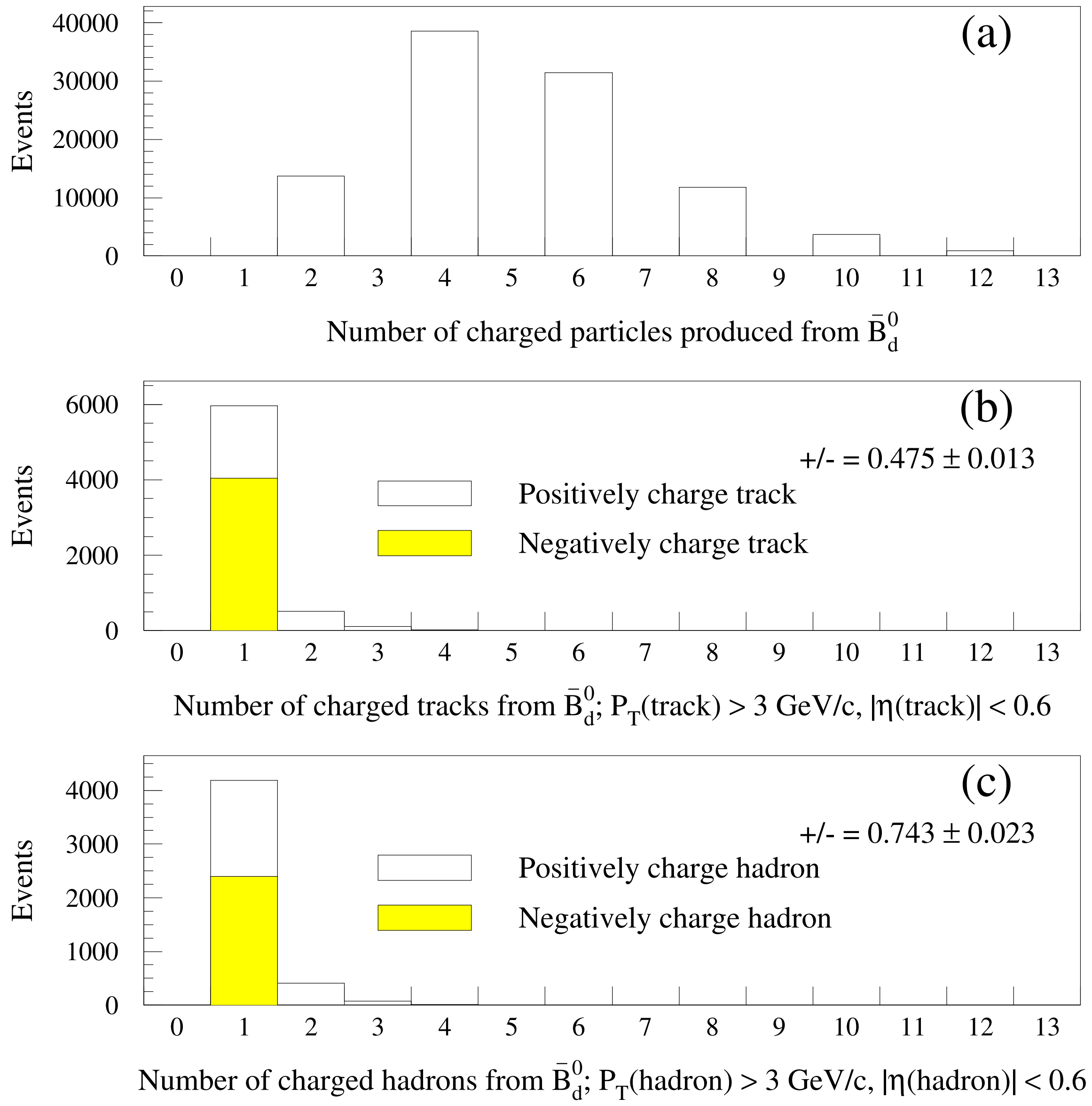

Figure 5.9: Charged particle multiplicities from the $\bar{B}^0_d$ meson. (a) Multiplicity of charged particles produced from $\bar{B}^0_d$ mesons. (b) Multiplicity of charged tracks (hadron or lepton) with $P_T > 3$ GeV/c and $|\eta| < 0.6$. (c) Multiplicity of charged hadrons with $P_T > 3$ GeV/c and $|\eta| < 0.6$. The leptons are removed in this distribution. The hatched area in multiplicity one bin in (b) and (c) represents negatively charged tracks and hadrons.

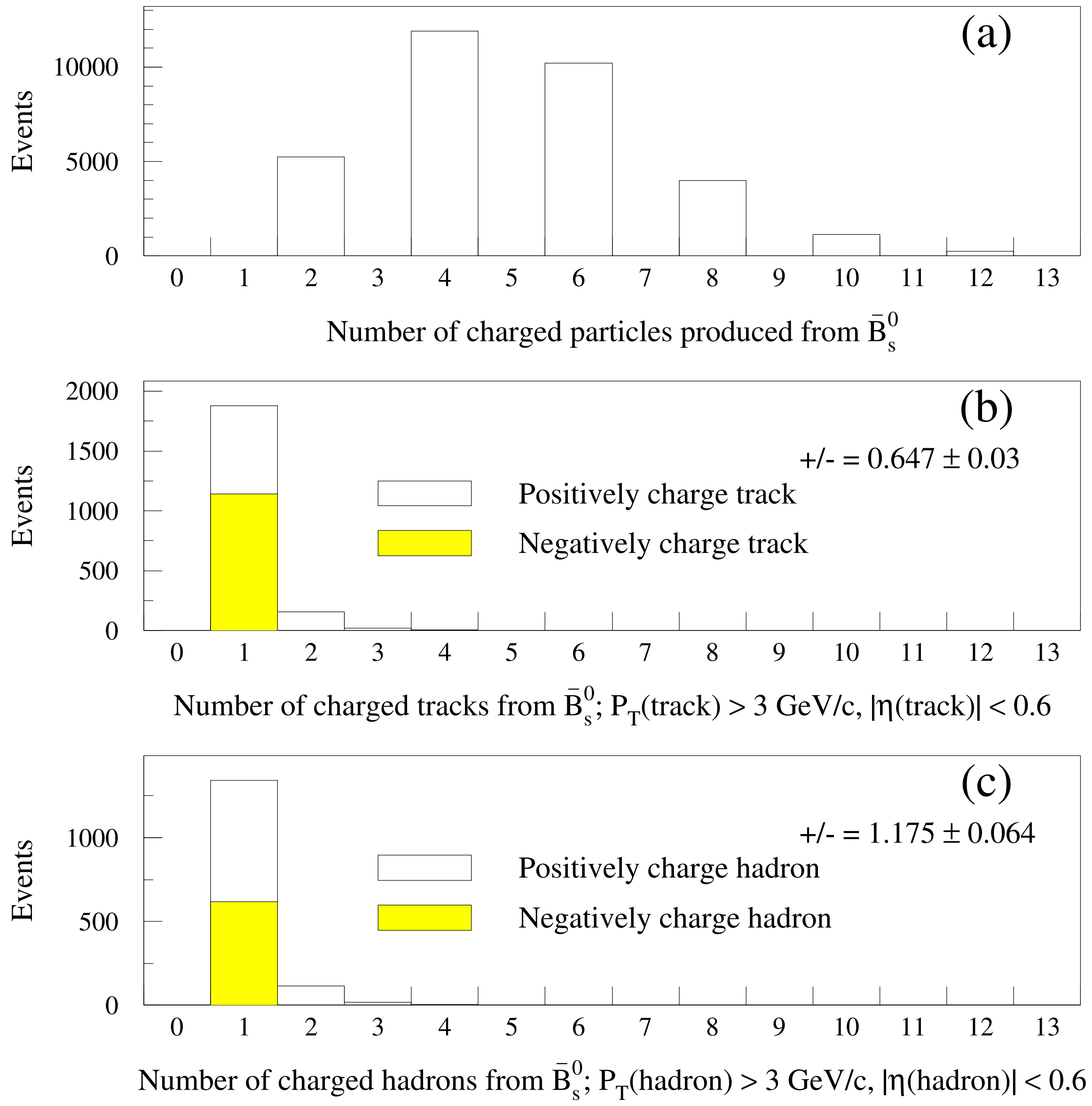

Figure 5.10: Charged particle multiplicities from the $\bar{B}_s^0$ meson. (a) Multiplicity of charged particles produced from $\bar{B}_s^0$ mesons. (b) Multiplicity of charged tracks (hadron or lepton) with $P_T > 3$ GeV/c and $|\eta| < 0.6$. (c) Multiplicity of charged hadrons with $P_T > 3$ GeV/c and $|\eta| < 0.6$. The leptons are removed in this distribution. The hatched area in multiplicity one bin in (b) and (c) represents negatively charged tracks and hadrons.

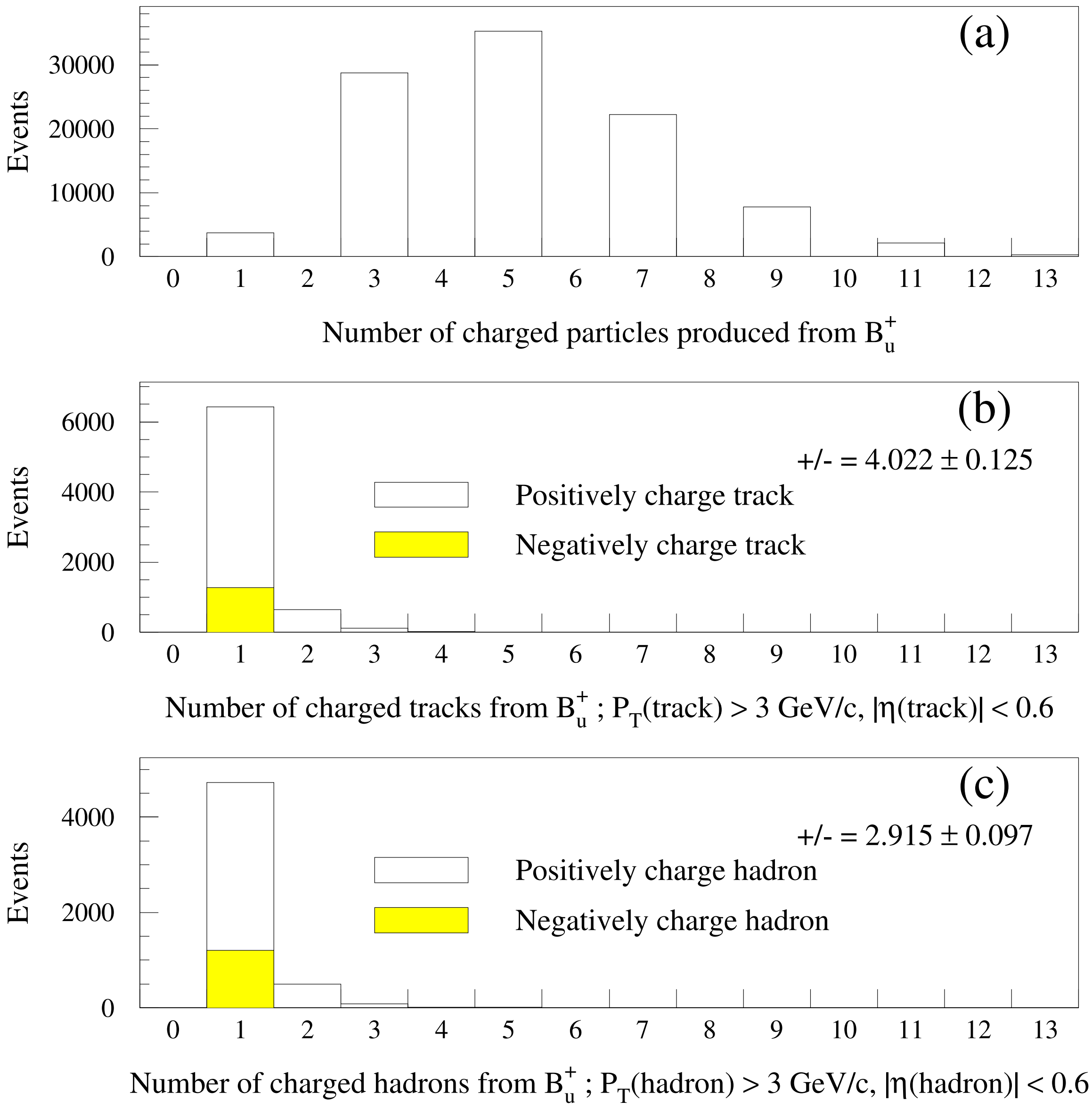

Figure 5.11: Charged particle multiplicities from the B_u^+ meson. (a) Multiplicity of charged particles produced from B_u^+ mesons. (b) Multiplicity of charged tracks (hadron or lepton) with $P_T > 3$ GeV/c and $|\eta| < 0.6$. (c) Multiplicity of charged hadrons with $P_T > 3$ GeV/c and $|\eta| < 0.6$. The leptons are removed in this distribution. The hatched area in multiplicity one bin in (b) and (c) represents negatively charged tracks and hadrons.

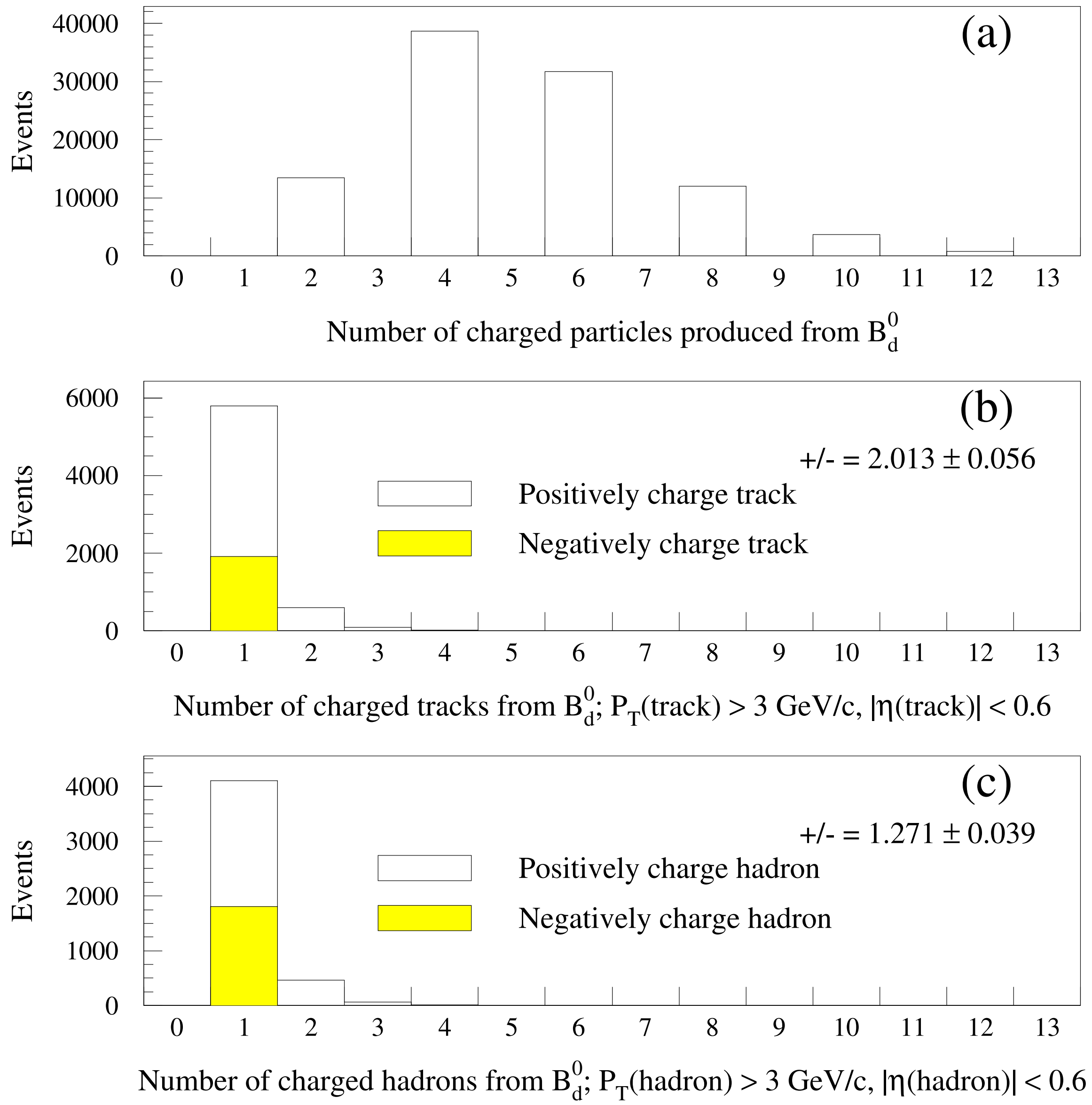

Figure 5.12: Charged particle multiplicities from the B_d^0 meson. (a) Multiplicity of charged particles produced from B_d^0 mesons. (b) Multiplicity of charged tracks (hadron or lepton) with $P_T > 3$ GeV/c and $|\eta| < 0.6$. (c) Multiplicity of charged hadrons with $P_T > 3$ GeV/c and $|\eta| < 0.6$. The leptons are removed in this distribution. The hatched area in multiplicity one bin in (b) and (c) represents negatively charged tracks and hadrons.

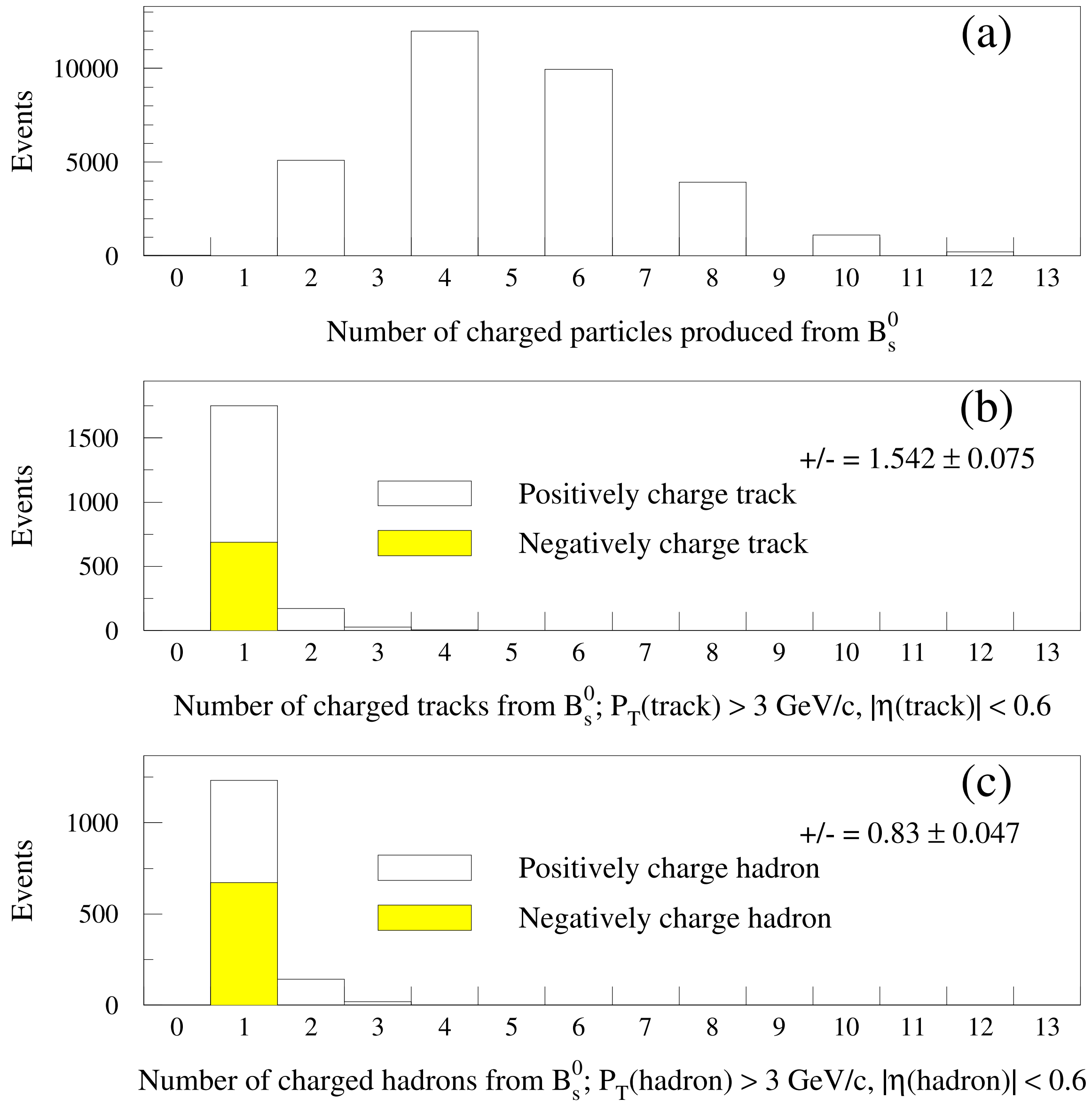

Figure 5.13: Charged particle multiplicities from the B_s^0 meson. (a) Multiplicity of charged particles produced from B_s^0 mesons. (b) Multiplicity of charged tracks (hadron or lepton) with $P_T > 3$ GeV/c and $|\eta| < 0.6$. (c) Multiplicity of charged hadrons with $P_T > 3$ GeV/c and $|\eta| < 0.6$. The leptons are removed in this distribution. The hatched area in multiplicity one bin in (b) and (c) represents negatively charged tracks and hadrons.

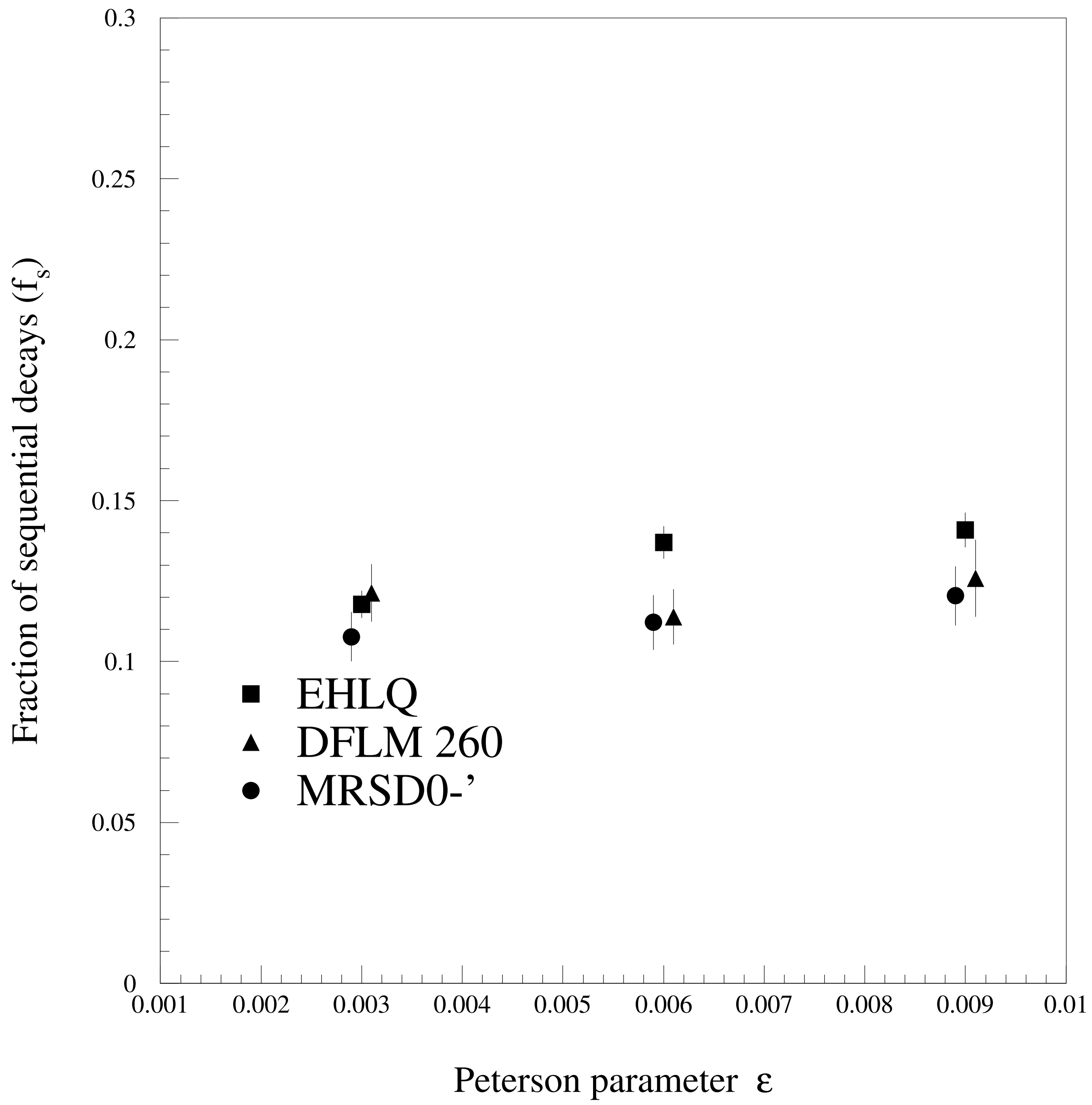

Figure 5.14: The fraction of the sequential decays for different Peterson parameter values and structure functions.

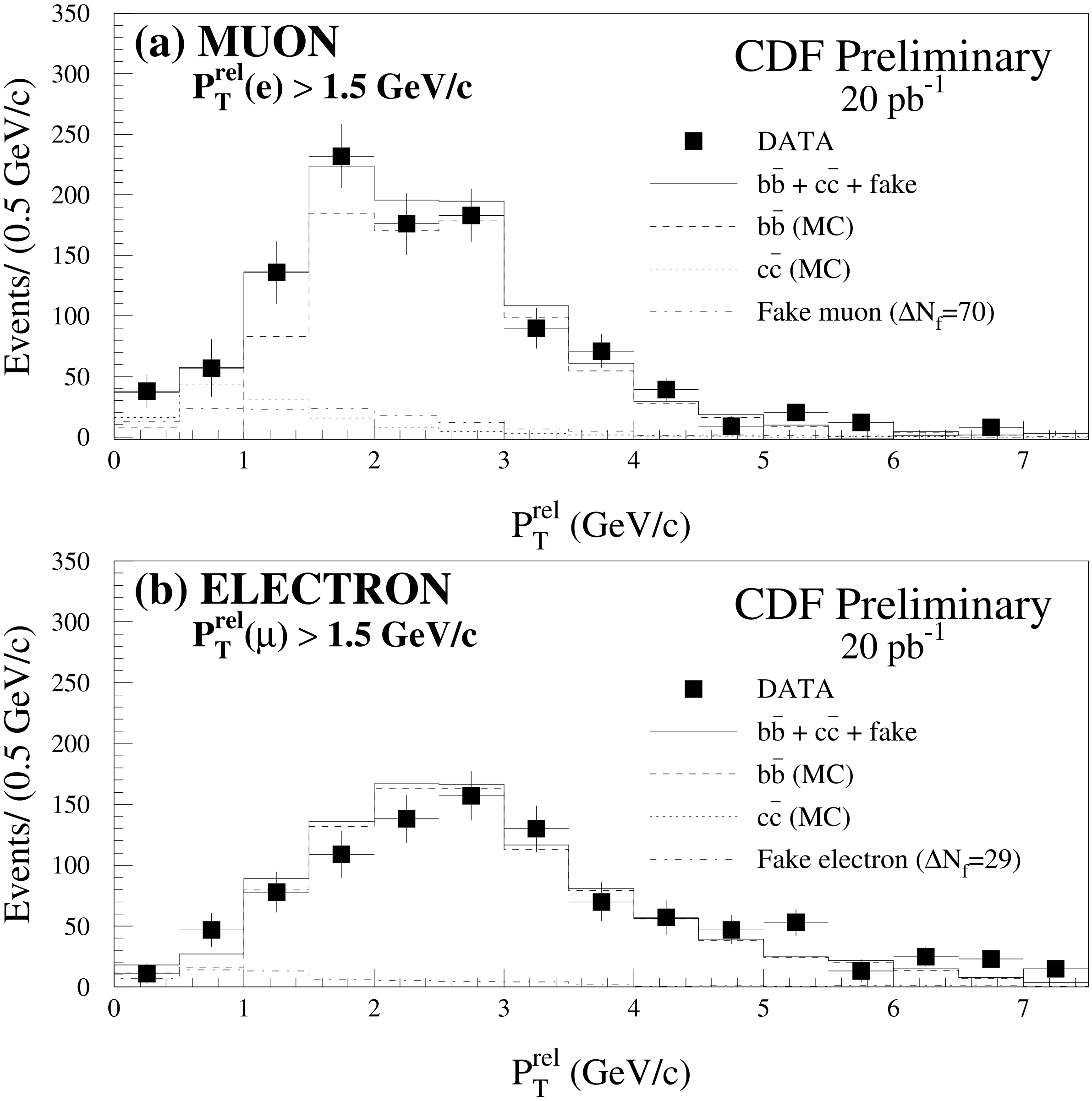

Figure 5.15: The difference between the numbers of OS and LS events as a function of P_T^{rel} (a) for muons and (b) for electrons. The points are observed data. The bashed line represents $b\bar{b}$ Monte Carlo data, the dotted line $c\bar{c}$ Monte Carlo data, the dot-dashed line fake lepton events, the solid line the sum of these three. The Monte Carlo data are generated using MRSD0$-'$ structure function set. The contributions from $c\bar{c}$ and fake lepton events are not clear by visible for the electron case.

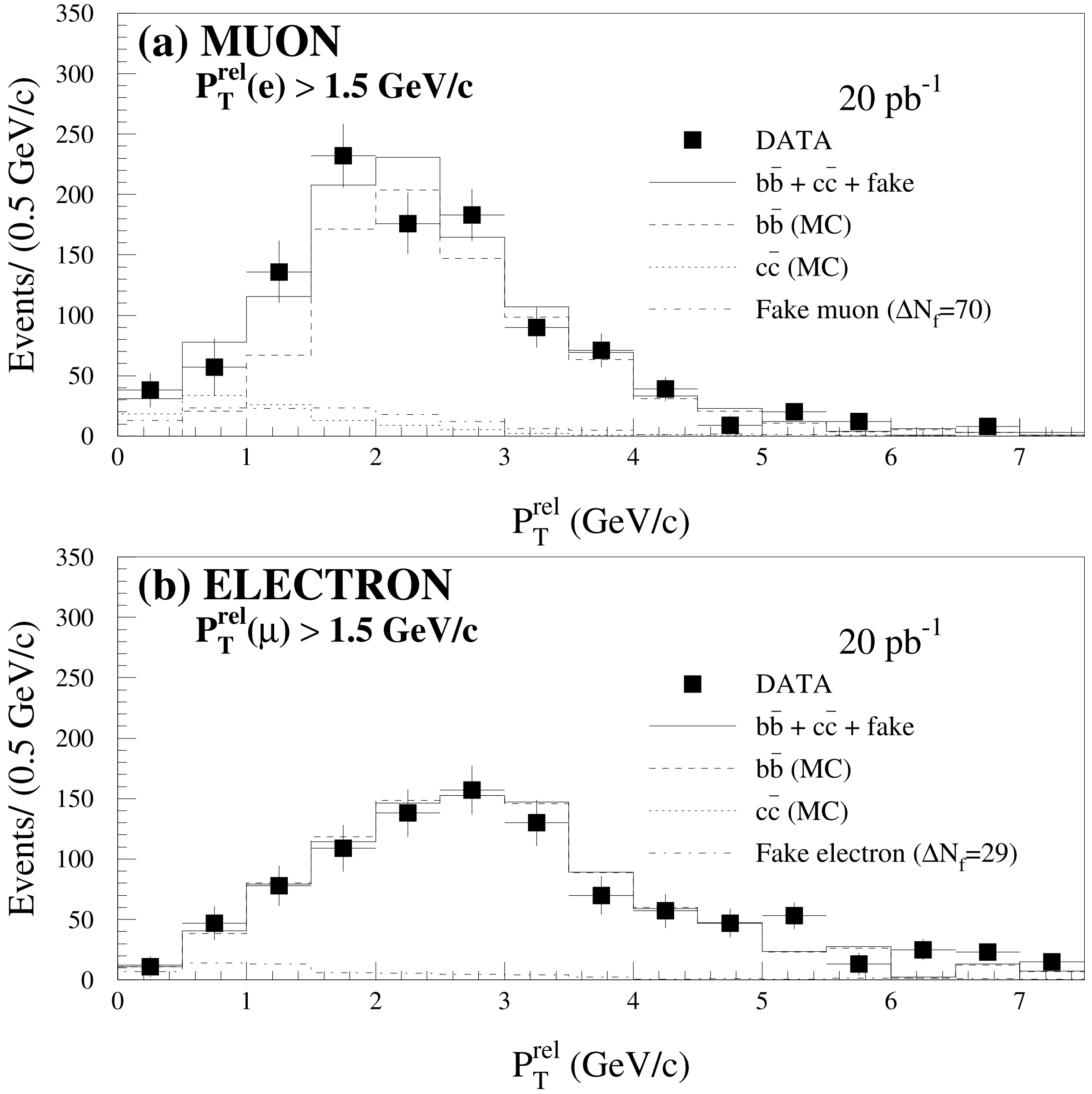

Figure 5.16: The difference between the numbers of OS and LS events as a function of P_T^{rel} (a) for muons and (b) for electrons. The points are observed data. The bashed line represents $b\bar{b}$ Monte Carlo data, the dotted line $c\bar{c}$ Monte Carlo data, the dot-dashed line fake lepton events, the solid line the sum of these three. The Monte Carlo data are generated using EHLQ structure function set. The contributions from $c\bar{c}$ and fake lepton events are not clear by visible for the electron case.

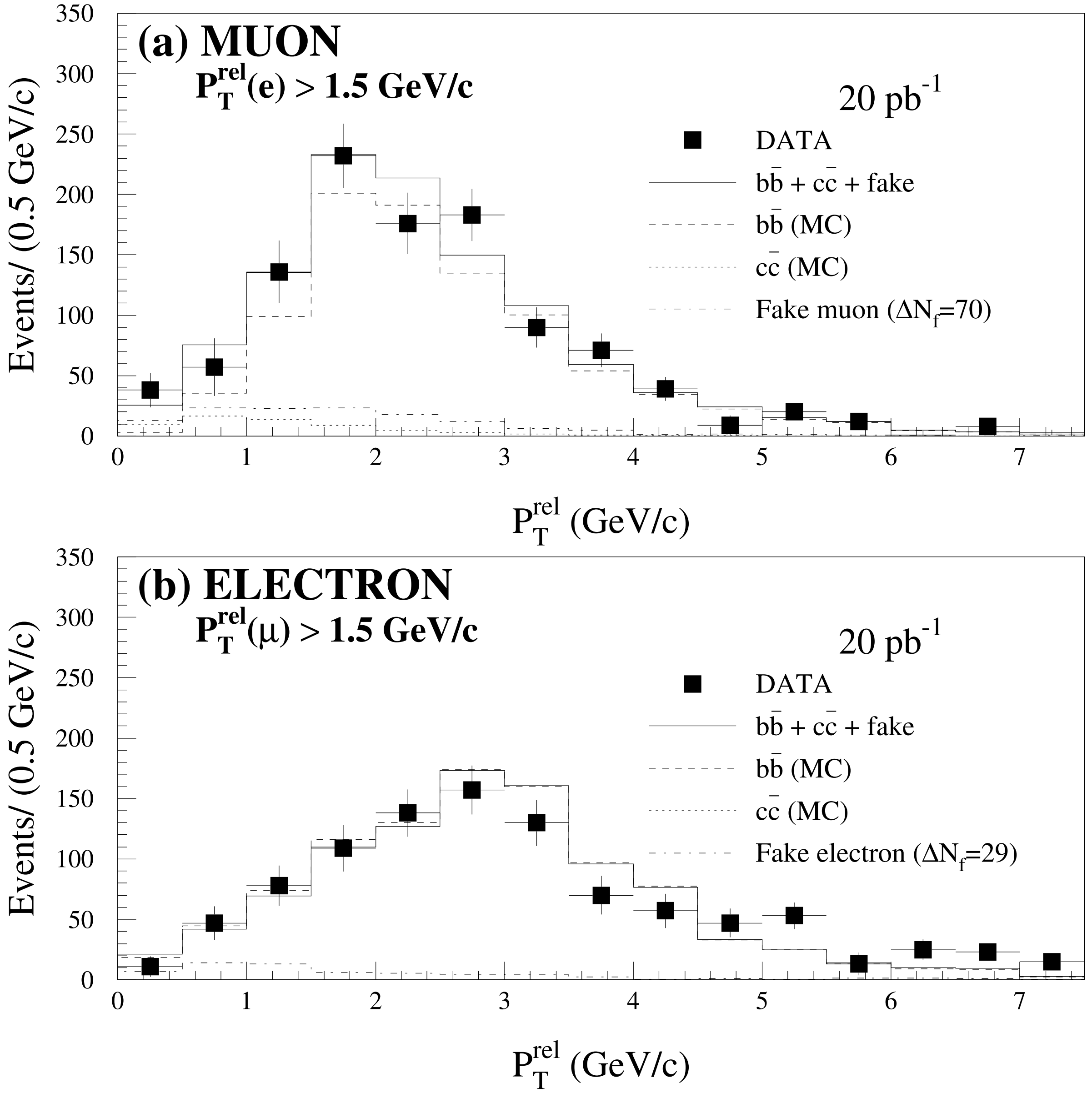

Figure 5.17: The difference between the numbers of OS and LS events as a function of P_T^{rel} (a) for muons and (b) for electrons. The points are observed data. The bashed line represents $b\bar{b}$ Monte Carlo data, the dotted line $c\bar{c}$ Monte Carlo data, the dot-dashed line fake lepton events, the solid line the sum of these three. The Monte Carlo data are generated using DFLM 260 structure function set. The contributions from $c\bar{c}$ and fake lepton events are not clear by visible for the electron case.

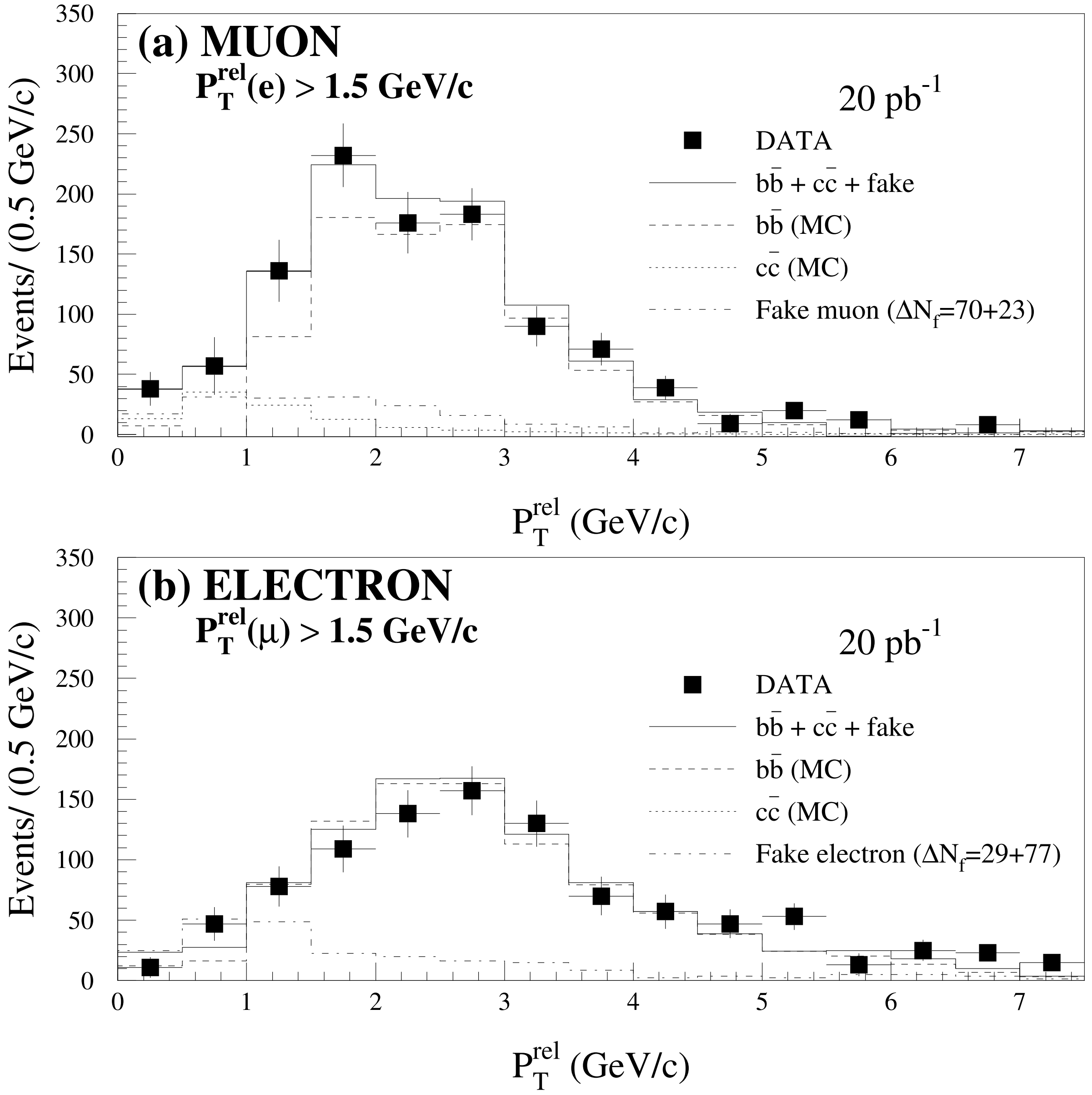

Figure 5.18: The difference between the numbers of OS and LS events as a function of P_T^{rel} (a) for muons and (b) for electrons. The points are observed data. The bashed line represents $b\bar{b}$ Monte Carlo data, the dotted line $c\bar{c}$ Monte Carlo data, the dot-dashed line fake lepton events, the solid line the sum of these three. The Monte Carlo data are generated using MRSD0$-'$ structure function set. In this distributions, numbers of fake muons and electrons are normalized to $70 + 23$ and $29 + 77$, respectively. The contributions from $c\bar{c}$ and fake lepton events are not clear by visible for the electron case.

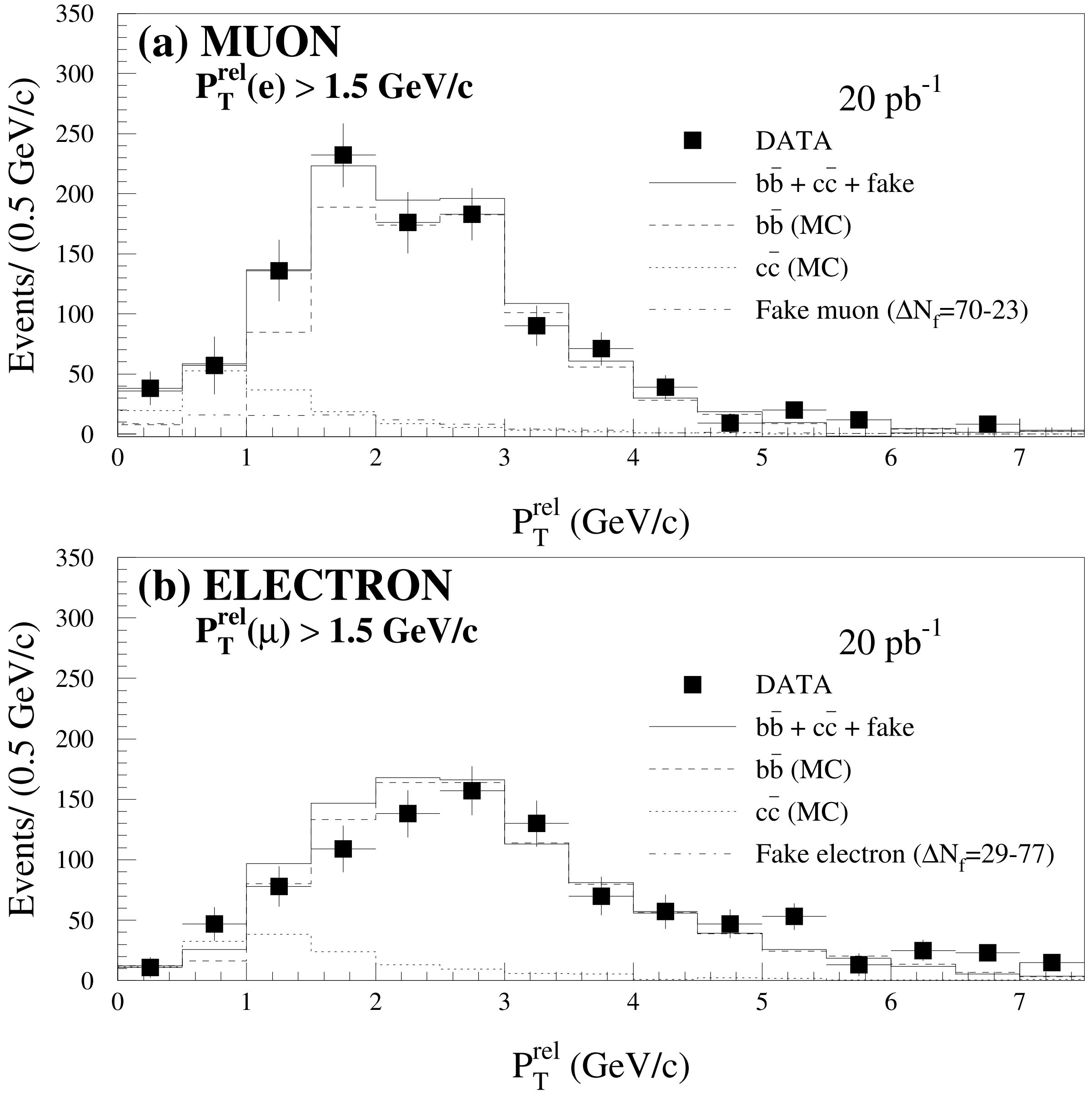

Figure 5.19: The difference between the numbers of OS and LS events as a function of P_T^{rel} (a) for muons and (b) for electrons. The points are observed data. The bashed line represents $b\bar{b}$ Monte Carlo data, the dotted line $c\bar{c}$ Monte Carlo data, the dot-dashed line fake lepton events, the solid line the sum of these three. The Monte Carlo data are generated using MRSD0$-'$ structure function set. In this distributions, numbers of fake muons and electrons are normalized to $70-23$ and $29-77$, respectively. The contributions from $c\bar{c}$ and fake lepton events are not clear by visible for the electron case.

Chapter 6

Results and Discussion

6.1 Mixing parameter, χ

From Eqs. (4.2) and (4.3), the mixing parameter χ is related to the ratio R of the number of LS events to that of OS events by

$$R = \frac{N^{exp}(LS)(1 - F_{e\mu}(LS))}{N^{exp}(OS)(1 - F_{e\mu}(OS))} = \frac{2\chi(1-\chi) + [(1-\chi)^2 + \chi^2]f_s}{(1-\chi)^2 + \chi^2 + 2\chi(1-\chi)f_s + f_c}. \tag{6.1}$$

Substituting the numerical values, $F_{e\mu}(OS) = 0.255 \pm 0.021$, $F_{e\mu}(LS) = 0.395 \pm 0.031$, $f_s = 0.137 \pm 0.027$ and $f_c = 0.007 \pm 0.011$, together with the observed $N^{exp}(OS) = 1710$ and $N^{exp}(LS) = 861$, we obtained

$$\chi = 0.130 \pm 0.010(stat) \pm 0.010(syst). \tag{6.2}$$

The uncertainties in χ are shown in Table 6.1. The obtained result (Eq. (6.2)) is consistent with the 88/89 CDF result and also with other experiments as shown in Fig. 6.1.

Source	Uncertainties
Statistical	0.010
Fake lepton events	0.004
Fraction of sequential decays	0.009
Fraction of $c\bar{c}$ events	0.002
Total	0.014

Table 6.1: Uncertainties in χ.

6.2 Mixing parameter for B_s mesons, χ_s

To obtain the value of χ_s, we used the relation $\chi = P_d\chi_d + P_s\chi_s$. The B_d^0 and B_s^0 fractions, P_d and P_s, are inferred from measurements of the relative production rates of kaons and pions. We have assumed $P_d = 0.391$ and $P_s = 0.117$. These values correspond to a strange quark suppression factor $P_s/P_d = 0.3$ consistent with measurements at LEP [51] and lower energy e^+e^- colliders [52, 53]. The mixing parameter, χ, gives a constraint on the χ_d-χ_s plane as shown in Fig. 6.2. The dotted line represents the ARGUS and CLEO combined result of χ_d:

$$\chi_d = 0.15 \pm 0.03 \tag{6.3}$$

which was measured by ARGUS (1992 and 1994) and CLEO (1993) [9, 10, 58]. The shaded region is allowed by the standard model (see Eq. (2.19)). The B_s^0 meson is expected to be maximally mixed from the ARGUS & CLEO results combined with the Standard Model prediction. Our result is consistent with this expectation.

We combined our result and the world average value in the Particle Data Book (1994) to obtain a new world average

$$\chi = 0.132 \pm 0.008 \tag{6.4}$$

Assuming that the errors in χ_d (Eq. (6.3)) and χ (Eq. (6.4)) are independent and represent 1σ uncertainty of the Gaussian error function, we derive a limit on χ_s:

$$\chi_s > 0.447 \qquad (68.3\% C.L.). \tag{6.5}$$

The contour in the $\chi_s - \chi_d$ plane is shown in Fig. 6.3.

The value of χ_s is sensitive to the relative production fractions of B_d^0 and B_s^0 mesons. The dependence of χ_s on P_s/P_d is shown in Fig. 6.4, up to the SU(3) flavor symmetry limit of $P_s/P_d = 1$.

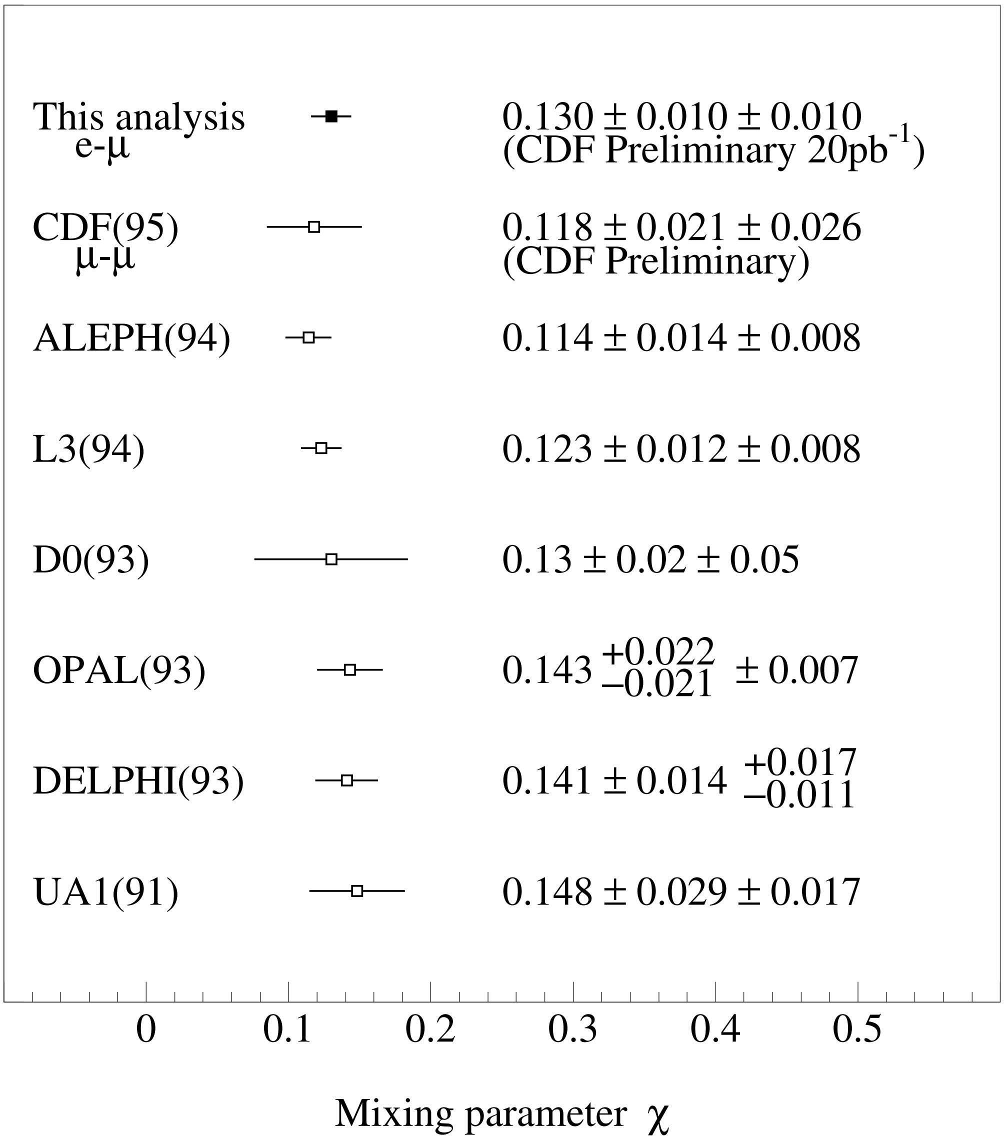

Figure 6.1: Comparison with other experiments.

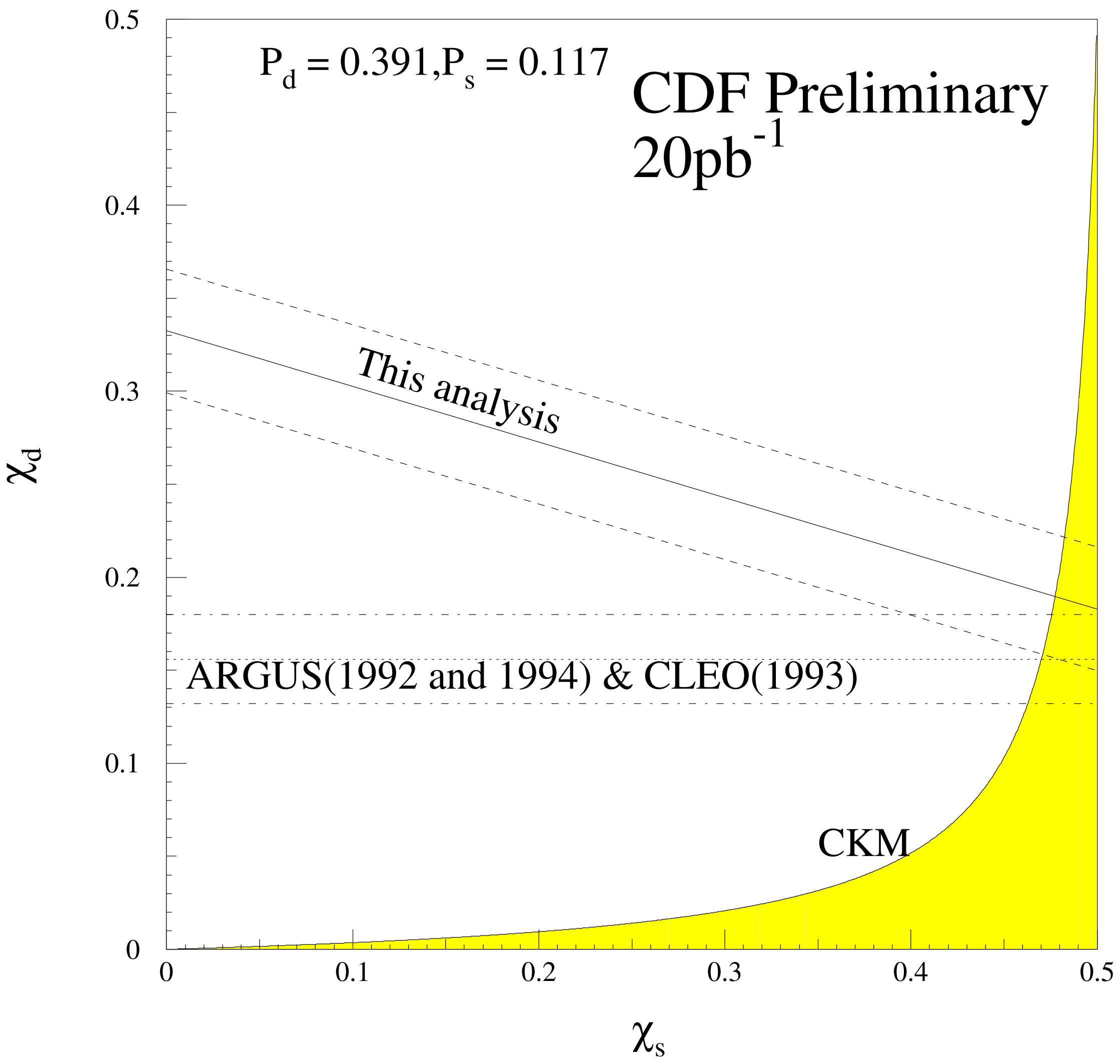

Figure 6.2: The mixing parameter for B_d^0 versus that for B_s^0 assuming that P_d and P_s are 0.391 and 0.117. The χ_d range is the ARGUS (1992&1994) and CLEO (1993) combined result of 0.15 ± 0.03. The bands represent $\pm 1\sigma$ uncertainty.

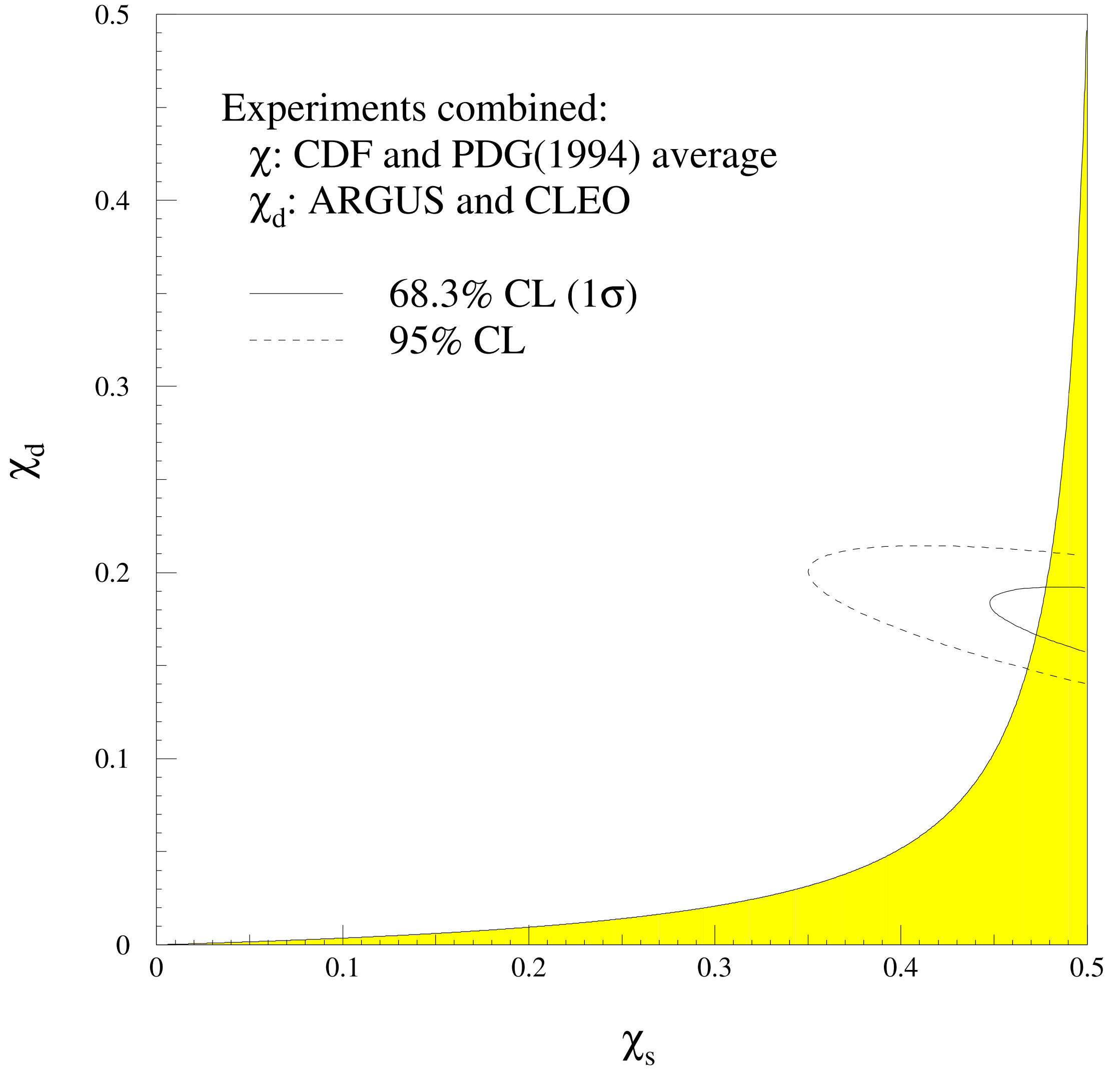

Figure 6.3: The mixing parameter for B_d^0 versus that for B_s^0 assuming P_d and P_s are 0.391 and 0.117. The χ was calculated from our result and average value in the Particle Data Book. The χ_d is estimated by the ARGUS (1992&1994) and CLEO (1993) combined result of 0.15 ± 0.03. The 68.3% (solid) and 95% (dashed) confidence areas are shown.

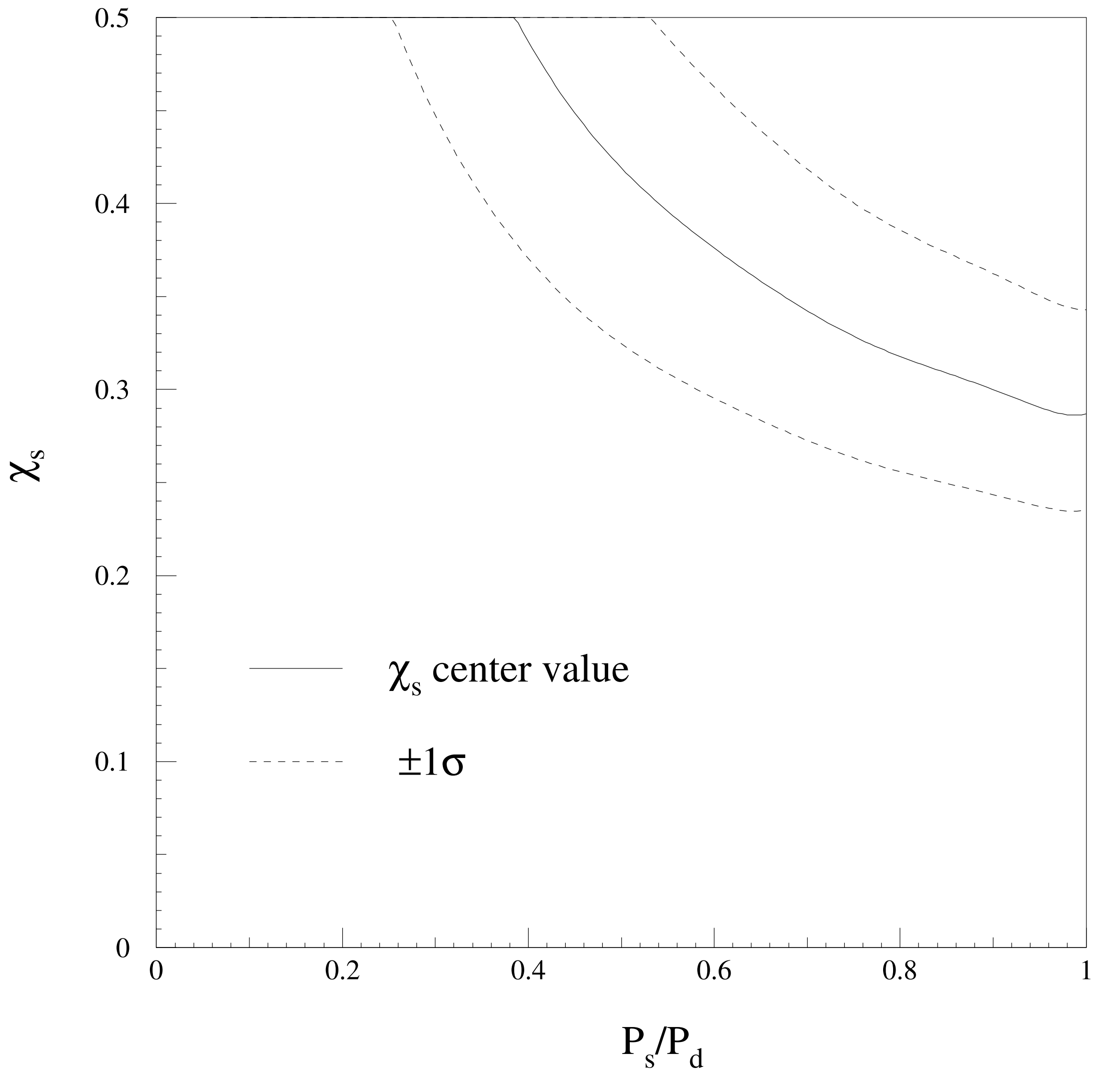

Figure 6.4: χ_s as a function of P_s/P_d.

Chapter 7

Conclusion

We measured $B^0\bar{B}^0$ mixing parameter, χ, in electron muon events in proton antiproton collisions at $\sqrt{s} = 1.8$ TeV using the CDF detector. The data were collected in the 1992-1993 CDF run. The corresponding integrated luminosity was 20 pb^{-1}. We have exploited the good electron and muon identification capabilities of the CDF detector to measure the $B^0\bar{B}^0$ mixing parameter. We obtained the mixing parameter as

$$\chi = 0.130 \pm 0.010(stat.) \pm 0.010(syst.). \tag{7.1}$$

This result improves the previous CDF result by a factor of 3 and is one of the most accurate measurements of χ at the present time. The result is consistent with other measurements of χ and also with the expectations from the standard model using other experimental results.

Since both neutral B mesons, B_d^0 and B_s^0, are produced in $p\bar{p}$ collisions, the mixing parameter for B_s^0, χ_s, is estimated by using the mixing parameter for B_d^0 measured by the ARGUS and the CLEO groups in e^+e^- collisions and by assuming the fractions of B_d^0 and B_s^0 mesons produced in $b\bar{b}$ events. The value of the mixing parameter for B_s mesons is consistent with the expectations from the standard model.

Appendix A

Estimation of Probabilities for Real Leptons from $J/\psi \to ll$ Events

In this appendix, we derive Eq. (5.9) used to estimate the P_r.

Before to discuss $J/\psi \to ll$ events, We first consider the definition of the probability, P_r, for a single lepton. Let N_r be the total number of real leptons. Call N_t the number of leptons which pass the original identification cut, and N_l the number of leptons which pass the loose identification cut. We write ϵ_t for the probability that the lepton passed the original cut, and ϵ_l for the probability that leptons which fail the original cut, pass the loose cut. The numbers N_t and N_l are related to N_r, ϵ_t and ϵ_l by

$$N_t = N_r \epsilon_t \tag{A.1}$$

$$N_l = N_t + N_r(1-\epsilon_t)\epsilon_l \tag{A.2}$$

$$= [\epsilon_t + (1-\epsilon_t)\epsilon_l] N_r \tag{A.3}$$

Since the probability P_r is defined by a ratio of number of leptons which pass the original cut to number of leptons which pass the loose cut, the P_r can be written by

$$P_r = \frac{N_t}{N_l} \tag{A.4}$$

$$= \frac{\epsilon_t}{\epsilon_t + (1-\epsilon_t)\epsilon_l} \tag{A.5}$$

When N is the number of $J/\psi \to ll$ events produced, let N_1 be the number of J/ψ's for which at least one lepton passes the original identification cut, and N_2 be the number of J/ψ's for which both leptons pass the cut. We write the N_1 and N_2 using ϵ_t and ϵ_l as

$$N_1 = N\epsilon_t^2 + 2N\epsilon_t(1-\epsilon_t)\epsilon_l \tag{A.6}$$

$$N_2 = N\epsilon_t^2 \tag{A.7}$$

From these equations and Eq. (A.5), we get.

$$P_r = \frac{2N_2}{N_1 + N_2} \tag{A.8}$$

Appendix B

Uncertainty in f_S due to Monte Carlo Statistics, Structure Function and Peterson Parameter

The uncertainty in f_s due to Monte Carlo statistics, structure functions and Peterson fragmentation parameter was estimated by using minimum and maximum of center values for each Monte Carlo data set. Is this estimation reasonable?

The center values and statistical uncertainties of f_s for different structure function sets and Peterson parameters are listed in Table B.1. We made the probability distributions of f_s using the center value and uncertainties assuming the Gaussian distributions where the center value and the statistical uncertainty were used as the mean value and sigma of the Gaussian distribution. The probability distributions for different structure function sets and Peterson parameters are shown in Fig. B.1.

We assume that each of the nine probability distributions represent and independent measurement of f_s. Then we make the sum of the nine distributions to determine the center value and its error (Fig. B.2). The sum probability distribution is fitted by a Gaussian function and the results are listed in the figure. From the results, the relative uncertainty in f_s due to structure functions, Peterson parameter and Monte

Structure function	Peterson parameter ϵ	f_s	Statistical uncertainty
MRSD0$-'$	0.003	0.1055	0.0075
	0.006	0.1107	0.0084
	0.009	0.1190	0.0092
EHLQ	0.003	0.1158	0.0041
	0.006	0.1355	0.0050
	0.009	0.1390	0.0053
DFLM 260	0.003	0.1196	0.0089
	0.006	0.1124	0.0084
	0.009	0.1242	0.0118

Table B.1: Fraction of sequential decays with MRSD0$-'$, EHLQ and DFLM 260 structure functions and, with Peterson parameter $\epsilon = 0.003, 0.006, 0.009$.

Carlo statistics is 10.2%. This is consistent with the uncertainty which is estimated in Section 5.2.4.

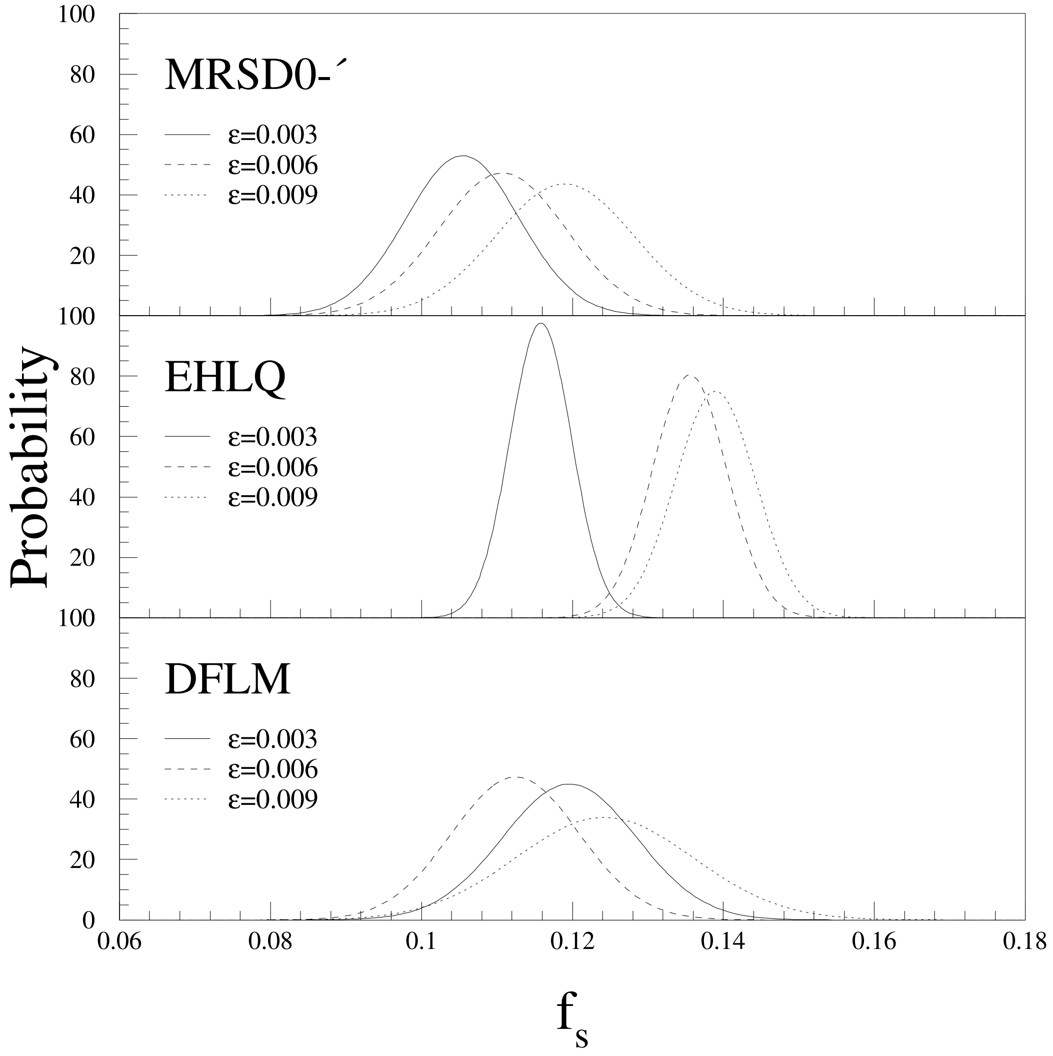

Figure B.1: The probability distributions of f_s. The structure functions for the top, middle and bottom figures are MRSD0$-'$, EHLQ and DFLM, respectively. In each figure, the solid (dashed or dotted) line represents the probability with Peterson fragmentation parameter $\epsilon = 0.003$ (0.006 or 0.009).

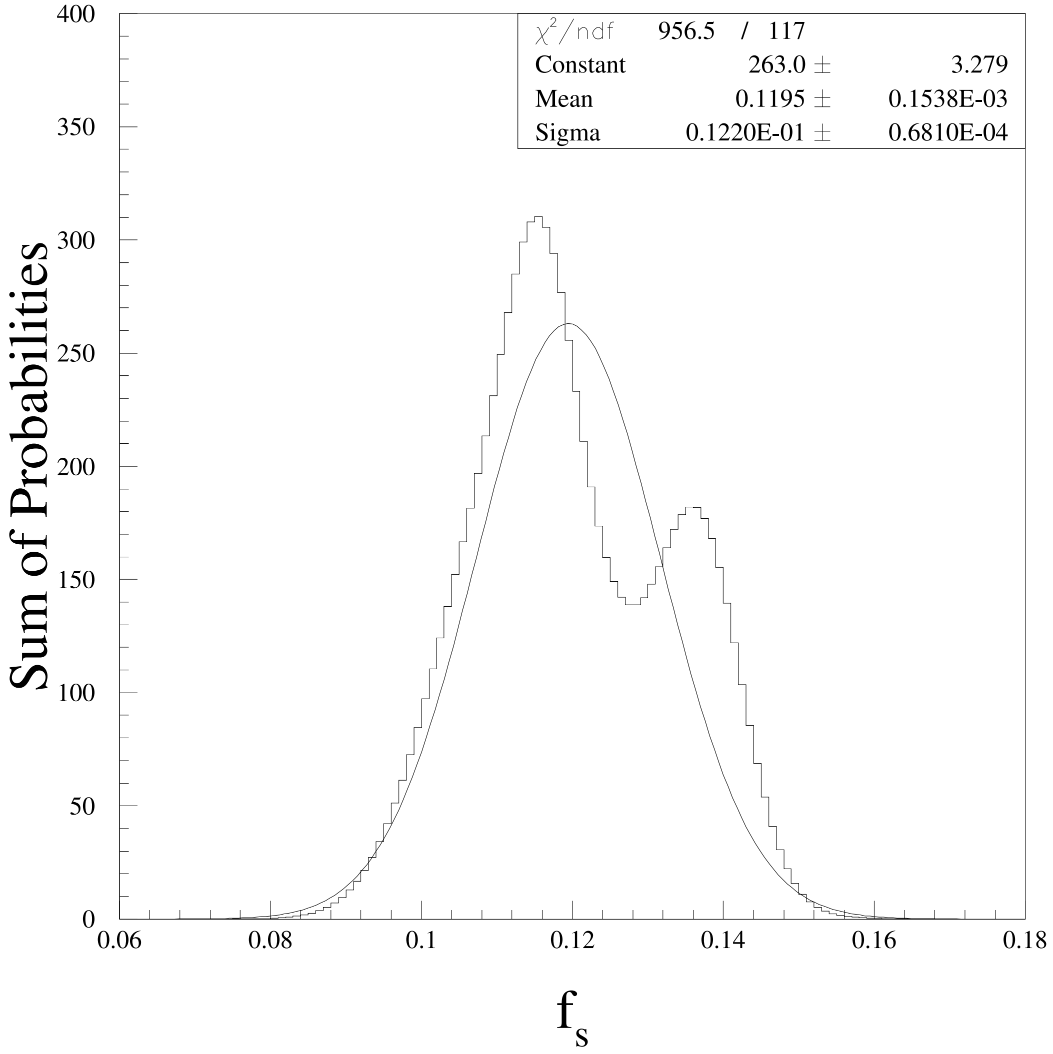

Figure B.2: The sum of probability distributions for f_s. The distribution is fitted by a Gaussian distribution. The fitted parameters of the Gaussian distribution are listed in the figure.

Bibliography

[1] F. Abe *et al.* (CDF collab.), Phys. Rev. Lett. **74**, 2626, (1995)

[2] S. Abachi *et al.* (D0 collab.), Phys. Rev. Lett. **74**, 2632, (1995)

[3] M. Kobayashi and T. Maskawa, Prog. Theor. Phys. **49**, 652 (1973).

[4] Particle Data Group, Review of Particle Properties, Phys. Rev. **D50**, 1173 (1994).

[5] L. Wolfenstenin, Phys. Rev. Lett. **51**, 1945 (1983)

[6] Sheldon Stone, "B DECAYS", 460 (1994).

[7] J. Chrin, Z. Phys. **C36**, 165 (1987).

[8] P. J. Franzini, Phys. Rept. **173** 1 (1989).

[9] H. Albrecht *et al.* (ARGUS collab.), Phys. Lett. **B324**, 249 (1994).

[10] J. Bartelt *et al.* (CLEO collab.), Phys. Rev. Lett. **71**, 1680 (1993).

[11] D. Buskulic *et al.* (ALEPH collab.), Z. Phys. **C62** 179 (1994).

[12] M. Acciarri *et al.* (L3 collab.), Phys. Lett. **B335** 542 (1994).

[13] S. Abachi *et al.* (D0 collab.), Proceedings of the 9th Topical Workshop on Proton-Antiproton Collider Physics, Tsukuba, Japan (1993).

[14] P. D. Acton *et al.* (OPAL collab.), Phys. Lett. **B276**, 379 (1992).

[15] P. Abreu *et al.* (DELPHI collab.), Phys. Lett. **B301**, 145 (1993).

[16] C. Albajar *et al.* (UA1 collab.), Phys. Lett. **B262**, 171 (1991).

[17] F. Abe *et al.* (CDF collab.), Phys. Rev. Lett. **67**, 3351 (1991).

[18] D. Amidei *et al.*, Nucl. Instrum. Methods **A350**, 73, (1994).

[19] F. Bedeschi *et al.*, Nucl. Instrum. Methods **A268**, 50 (1988).

[20] L. Balka *et al.*, Nucl. Instrum. Methods **A267**, 272 (1988).

[21] L. Balka *et al.*, Nucl. Instrum. Methods **A267**, 272 (1988).

[22] S. Bertolucci *et al.*, Nucl. Instrum. Methods **A267**, 301 (1988).

[23] S. Bertolucci *et al.*, Nucl. Instrum. Methods **A267**, 301 (1988).

[24] Y. Fukui *et al.*, Nucl. Instrum. Methods **A267**, 280 (1988).

[25] F. Abe *et al.*, Nucl. Instrum. Methods **A271**, 387 (1988).

[26] Y. Fukui *et al.*, Nucl. Instrum. Methods **A267**, 280 (1988).

[27] W. C. Carithers *et al.*, "Performance and calibration studies of the CDF endplug hadron calorimeter", CDF note 368.

[28] G. Ascoli *et al.*, Nucl. Instrum. Methods **A268**, 33 (1988).

[29] A. Gauthier *et al.*, "Design and performance of drift chambers for the central muon upgrade of the CDF detector", CDF internal note 1500, to be submitted to Nucl. Instrum. Methods.

[30] D. Amidei *et al.*, Nucl. Instrum. Methods **A269**, 51 (1988).

[31] G. Ascoli *et al.*, Nucl. Instrum. Methods **A269**, 63 (1988).

[32] J. T. Carrol *et al.*, Nucl. Instrum. Methods **A300**, 552 (1991).

[33] G. W. Foster *et al.*, Nucl. Instrum. Methods **A269**, 93 (1988).

[34] E. Barsotti *et al.*, Nucl. Instrum. Methods **A269**, 82 (1988).

[35] G. Drake *et al.*, Nucl. Instrum. Methods **A269**, 68 (1988).

[36] H. Brafman *et al.*, IEEE Trans. Nucl. Sci. **NS-32**, 336 (1985).

[37] M. Bozzo *et al.*, Phys. Lett. **147B**, 392 (1984).

[38] M. Bozzo *et al.*, Phys. Lett. **198B**, 583 (1987).

[39] F. Abe *et al.*, Phys. Rev. **D44**, 29 (1991).

[40] F. Abe *et al.*, Phys. Rev. **D50**, 5550 (1994).

[41] F. E. Paige and S. D. Protopopescu, "ISAJET 5.20: A Monte Carlo event generator for $p\bar{p}$ and $p\bar{p}$ interactions.", BNL Report No. BNL-38034, 1986 (unpublished). ISAJET version 7.06 (1994) was used, specially modified fro the CDF analysis system and modified to include the parton distribution functions, using the CERN PDFLIB interface package from ref [54].

[42] Paul Avery, Ken Read and Garry Trahern, "QQ: A Monte Carlo Generator", CLEO Software Note CSN-212, March 25, 1985.

[43] Jonathan Lewis and Paul Avery, "CLEOMC: THe CDF Interface to the CLEO Monte Carlo (QQ)", CDF internal note 2724, 1994.

[44] ISALEP is a special version of ISAJET which is modified to generate heavy quark events with high-P_T leptons effectively.

[45] M. Shapiro *et al.*, "A User's Guide to QFL", CDF internal note 1810.

[46] N. Solomey and A. B. Wicklund, "Study of Electromagnetic Showers In the CDF Central Electromagnetic", CDF internal note 247 (1984).

[47] D.A. Smith and H.B. Jensen, "Pion Punchthrough Probability of the Central Calorimeter Wedges", CDF internal note 707 (1988).

[48] F. Abe *et al.* (CDF collab.), Phys. Rev. **D40**, 3791 (1989).

[49] G.J. Alner *et al.* (UA5 collab.), Nucl. Phys. **B258**, 505 (1985).

[50] P. Kesten, L. Kirsch, and S. Tarem, "A measurement of $B\bar{B}$ Mixing Using Di-electrons", CDF internal note 1314 (1991).

[51] B. Adeva *et al.* (OPAL collab.), Phys. Lett. **B264**, 467 (1991).

[52] W. Bartel *et al.* (JADE collab.), Z. Phys. **C20**, 187 (1983).

[53] M. Althoff *et al.* (TASSO collab.), Z. Phys. **C27**, 27 (1985).

[54] H. Plothow-Besch, "PDFLIB: a library of all available parton density functions of the nucleon, the pion and the photon and the corresponding α_s calculations", Comp. Phys. Comm. **75**, 396 (1993) This reference provides the interface to the parton distribution functions found in Ref. [57] and [55].

[55] A.D. Martin, R. G. Roberts and W. J. Stirling, Phys. Lett. **B306**, 145 (1993) and Phys. Lett. **B309**, 492 (1993).

[56] E. Eichiten, I. Hinchliffe, K. Lane and C. Quigg, Rev. Mod. Phys. **56**, 579 (1984) and Rev. Mod. Phys. **58**, 1065 (1985).

[57] M. Diemoz, F. Ferroni, E. Longo and G. Martinelli, Z. Phys. **C39**, 21 (1988)

[58] H. Albrecht *et al.* (ARGUS collab.), Z. Phys. **C55**, 357 (1992).